Synthesis, Photo-Physical Properties, and Applications of Nitrogen-doped Carbon Dots

A dissertation submitted in partial fulfilment of requirements

for the degree of

Doctor of Philosophy

by

Nilanjana Nandi

Roll No. 176122012

Department of Chemistry

Indian Institute of Technology Guwahati

Guwahati-781039, Assam, India

July 2022

Statement

I do hereby declare that the work incorporated in this thesis entitled, "**Synthesis, Photo-Physical Properties, and Applications of Nitrogen-doped Carbon Dots**" is the result of investigations carried out by me under the guidance of Prof. Kalyanasis Sahu, at the Department of Chemistry, Indian Institute of Technology Guwahati, Guwahati, Assam, India.

In keeping with the general practice of reporting scientific observations, acknowledgments have been made wherever the work described is based on the findings of other investigators. I further declare that this work has not been submitted in part or full to any other university or institute for the award of any degree or diploma.

Nilanjana Nandi

IIT Guwahati
July 2022

Nilanjana Nandi

Prof. Kalyanasis Sahu
Professor, Department of Chemistry
Indian Institute of Technology Guwahati
Guwahati-781039, Assam, India
http://www.iitg.ac.in/chemistry/fac/ksahu/

Phone : +91-361-2583302
E-mail : ksahu@iitg.ac.in

Certificate

This is to certify that the work included in this thesis entitled "**Synthesis, Photo-Physical Properties, and Applications of Nitrogen-doped Carbon Dots**" by Nilanjana Nandi, Department of Chemistry, Indian Institute of Technology Guwahati has been carried out under my supervision. I further certify that this work has not been submitted to any other University or Institution in part or full for the award of any degree or diploma.

IIT Guwahati
July 2022

Kalyanasis Sahu
Thesis supervisor
Department of Chemistry
Indian Institute of Technology Guwahati
Guwahati – 781039, Assam, India

Dedicated to my parents

and Rabi

Table of Contents

Acknowledgement

I am pleased to put across my heartfelt obligation and appreciation to everyone whoever have contributed in the completion of this thesis. Many individuals have supported me in this truly remarkable and amazing journey. I have tried to list everyone who have sincerely helped and guided me in the completion of this thesis. I thank each person from the bottom of my heart.

First of all, I am extremely obliged to my supervisor and mentor Prof. Kalyanasis Sahu for providing me with a valuable opportunity to work in his group. His constant support, valuable suggestions, scientific guidance, deep perceptions, and inspiration have encouraged me to take up the tasks and familiarized me with a field that I knew little about. I solemnly thank him for having trust in me and giving me the freedom in choosing the way of my research. I feel blessed to have him as my guide who has always motivated me with his hard work, enthusiasm, and optimism. He has been ever patient with me and was always available to provide his very useful opinion regarding my thesis work.

Besides my supervisor, I am highly grateful to my doctoral committee members, Prof. Gopal Das, Prof. Anumita Paul, and Prof. Debasis Manna for assessing my research work regularly. Their precious suggestions and essential comments during all my seminars helped me expand my research from various perspectives and improve my thesis.

I sincerely express my gratitude to all my teachers at Midnapore College and IIT (ISM) Dhanbad for imbibing good values and knowledge in me.

I had the best of times working with Priyanka, and Neha who were my core team members. Both of them deserve the best and extreme respect for their hard work, assiduousness, and obligatory input into the overall research work. Further, the research experience gathered along with Dillip da, Tousif da, and Aparajita di is also worth mentioning.

I extend my special thanks to my friends Priyanka, Retwik, Rabi, Rituparna, Santa, Nikita, and Ritesh from the bottom of my heart for the discussions beyond work. Thank you, guys, for helping me right from the beginning of knowing each other providing all the moral support and time. I am also very thankful to Ruma di and Soutick da for them I have learned many things during my research journey.

Finally, I would like to express admiration towards my go to person, Rabindranath Garai, who has always support me especially in the tough phases of my life. At the end, I want to

thank my parents and Shuvendu uncle for their prayers, sacrifice and struggle. It is because of them I am able to fulfill my dream and complete my higher education from a prestigious institute. They have always given me the strength to chase my dreams which was immensely needed.

I am also thankful to all the research scholars and staff of the Department of Chemistry, IIT Guwahati for their kind cooperation and support. Further, I am grateful to the Central Instrument Facility, IIT Guwahati for allowing me to access their facility for the various experimentations as and when required. I am indebted to the staff of Student Affairs, Academic Affairs, and Finance sections of IIT Guwahati for being kind enough to advise and help in their respective roles.

I express gratitude towards each individual for extending their support, encouragement and remembering me in their prayers.

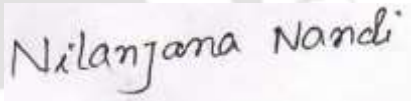

Nilanjana Nandi

Thesis Abstract

The thesis addressed various strategies to regulate the photo-physical property and applicability of carbon dots (CDs) by heteroatom (especially Nitrogen(N)) incorporation approach. This thesis pursues a detailed analysis of the structural and optical properties of newly developed N-doped CDs (NCDs). Till now, the source of emission property of CDs is not explained properly, which is the main inspiration of the thesis to explore each detailed photo-physical characteristic of synthesized NCDs and executed the same in the sensing and biological platform.

In *chapter 1*, the systematic development of carbon-based quantum dots (carbon and graphene quantum dots) as potential luminescent materials is discussed along with their synthesis procedures, photoluminescent properties, and vast application. This chapter also includes various modification and doping strategies to tune the optical properties of CDs and their application in diverse fields. *Chapter 2* provides a broad description of the various materials, instrumental techniques, and experimental methodology. In *chapter 3*, the specific detection of Pb^{2+} and ClO^{-} by using surface-functionalized graphene quantum dot (F-GQD) is successfully achieved. The surface modification of graphene quantum dot (GQD) was done by a simple coupling reaction between 2,6-diaminopyridine moiety, and GQD which is further applied to imaging and recognition of ClO^{-} in living cells and Pb^{2+} detection occurred by aggregation induced emission enhancement manner whereas the ClO^{-} detection consists of energy migration through H-bonding network between amino group of F-GQD and ClO^{-}. *Chapter 4* refers to the hydrothermally synthesized highly blue-emissive NCDs (quantum yield 22.7 % in an aqueous medium) from 3,6-diaminoacridine hydrochloride and L-aspartic acid for the detection of two analytes i.e., vitamin-B_{12} and bilirubin. Herealso, the mechanism of detection of two analytes are totally opposite in nature. For vitamin-B_{12}, inner filter effect plays the key role for emission suppression, whereas, H-bonding induced energy transfer was operated for detection of bilirubin. Moreover, the NCD was further applied in living cell imaging and successfully recognize vitamin-B_{12} in HeLa cells. In *chapter 5*, cover a brief detection strategy to recognize 4-nitroaniline (4-NA) by two different emissive NCD-1 (blue) and NCD-2 (green). Here, the sensing mechanism highly depends on the emission wavelength and solvent system. *Chapter 6*, contains unique optical properties of newly developed NCD with three different color emissions (blue, green, and red) under different excitation windows and their application of Fe^{3+} and ascorbic acid detection as well as logic gate preparation. In *chapter*

7, we synthesized a dual-emissive N-doped carbon dot (NCD) for very specific ratiometric detection of pH and Fe^{3+} with a distinct ratiometric property. Furthermore, this NCD act as pretty good anti-cancerous agent, and it was recognized intracellular pH as well as exogenous Fe^{3+} in the breast cancer cell line (MCF-7). A solution-phase white light also constructed by considering the emission property of NCD. *Chapter 8* encompasses the whole summary of the existing thesis and future scenarios of this thesis.

List of Figures

List of Schemes

List of Tables

[This page was intentionally left blank]

CHAPTER 1

Introduction

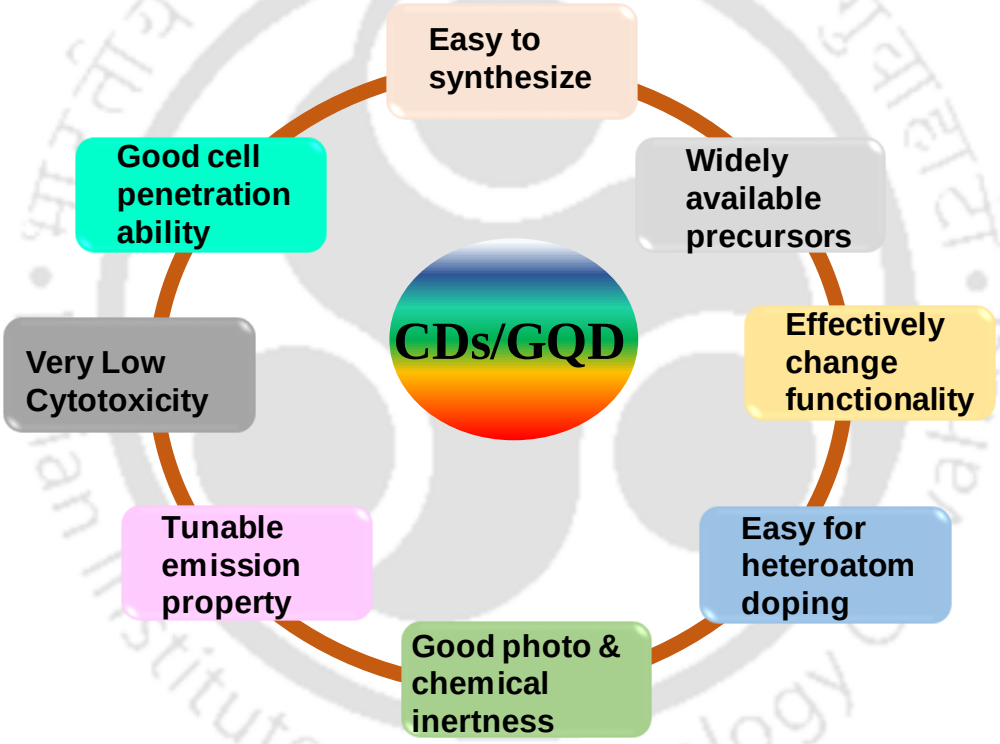

[This page was intentionally left blank]

1.1 Overview

Fluorescent nanomaterials usually denote the particular materials whose average size falls on 1–100 nm in three-dimensional space. Over time, nanomaterials have now played a supreme part in engineering and science fields. Nano-fluorescent materials include metal nanoclusters, semiconductor quantum dots, and carbon-based quantum dots (carbon and graphene). Carbon dots (CDs) are mainly carbon-based luminescent nanomaterial with quasi-spherical shapes and narrow size distributions (1 to 20 nm).[1] It mainly contains a carbogenic core (sp^3 and/or sp^2 carbon atom), various functional groups, and/or polymer chains at the surface.[2, 3] While graphene quantum dot (GQD) is the subgroup of CD[4] which can be obtained from graphene-like reacting materials and contain one or some few-layered graphene.[5] In contrast to CD, GQD shows a more crystalline structure due to its graphitic lattice plane.[6, 7] CDs and GQDs are bio- and eco-friendly and possess great potential in various applications.

1.2 Discovery of Carbon and Graphene Quantum Dot

In 2004, Xu et al. first fortuitously discovered the CDs during the purification of single-wall carbon nanotube (SWCNT).[8] Later, Sun et al. synthesized CDs through laser ablation of a carbon target.[9] Another masterpiece synthesis was achieved by the Liu group through combustion oxidation generating luminescent CDs (<2 nm) in 2007.[10] Following the Xu et al. work, Geim and Ponomarenko fabricated GQD in 2008.[11] After that, both the GQD and CDs fields gained intense limelight by researchers due to their enormous advantages.

1.3 Structural Analysis of CDs and GQDs

The CD and GQD contain two essential elements, carbon (C) and oxygen (O). As the base is carbon and presents in large amounts (atomic percentage), it is called a "carbon dot". There may be another important element, nitrogen (N), depending on starting precursors. [12] The contribution of each element depends on the synthesis procedure, precursors, and reaction time. Carbon dots are zero-dimensional materials containing carbogenic core and surface states. The intrinsic carbogenic core consists of sp^2 (C=C) or sp^3 (C-C) carbon atoms and other functional moieties (-COOH, -OH, and $-NH_2$, etc.) present at the surface. Although GQD also belongs to a class of carbon dots, there are some structural differences; the core of GQD consists of sp^2 hybridized graphitic carbon atoms and other functionality

present at the basal plane and edge sides. The epoxy (C-O-C) groups are mainly found at the basal plane, and other groups (-COOH, -OH, -COR) are mainly situated at edge sites.[13] CDs and GQDs have lattice spacing ranging from 0.18 to 0.25 nm, whereas the graphitic interlayer spacing ranges from 0.32 to 0.40 nm.[14, 15] This interlayer spacing largely depends on the degree of oxidation.[16] The schematic illustration of carbon based quantum dots is represented in **Figure 1.1**.

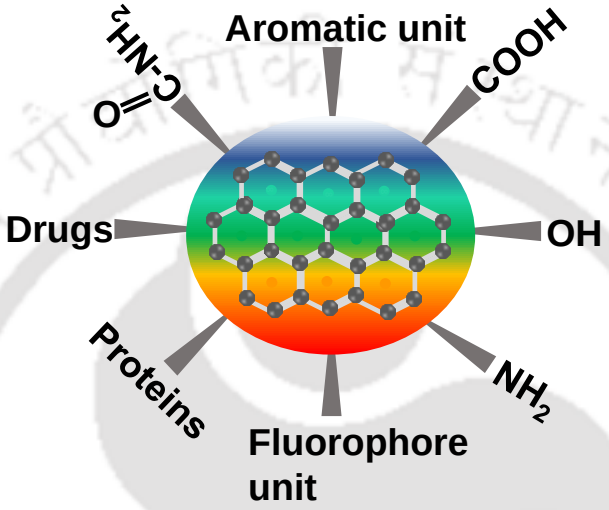

Figure 1.1. Schematic illustration of carbon-based quantum dots.

1.4 Synthesis Procedure

For the preparation of CDs and GQD, many chemical and physical techniques are developed in the last few decades. But overall synthesis procedures are classified into two categories (1) top-down and (2) bottom-up approaches. The former involves disintegrating the bulk carbon material into ultrasmall fluorescent carbon products. While the latter produces CDs from a primary carbon source (glucose, small organic precursors, citric acid, etc.) where dehydration and carbonization are the main routes.[17] Detail of the synthesis route is represented in **Figure 1.2**.

The phrase "top-down" simply refers to "top" to "down" movement by breaking down bonds.[18] Some large-size carbon precursors such as graphene, graphene oxide, carbon nanotube, and carbon fiber are used as a starting material to produce nano-size luminescent CDs via various methodologies, including laser ablation, chemical oxidation, electrochemical oxidation, arc-discharge, and ultrasonication.[19] Sun group first pioneered the laser ablation (Nd: YAG laser, 1064 nm, 10 Hz) method to synthesize the CDs from

carbon precursors using argon as the carrier gas with the existence of water vapor.[9] In the electrochemical degradation, graphite was the working electrode, while platinum (Pt) and Ag/AgCl were the counter, and reference electrodes, respectively, and several water-soluble electrolytes, like, phosphate buffer (PBS), 1-butyl-3-methylimidazolium tetrafluoroborate, and NaH_2PO_4 was used.[20, 21] The first electrochemical approach of synthesis blue emissive CDs from multi-walled CNTs was reported by the Ding group.[16] The green-emitting GQD was also prepared by electrochemical method in a high redox potential (±1.5 to ±3V) window with a size distribution of 3-5 nm.[22] Chemical oxidation is a widely used method to prepare CD and GQD. Dong et al. prepared GQDs by a chemical oxidizing method, treating carbon black (CX-72) with concentrated nitric acid.[23] The several kinds of carbon soot obtained from candles, graphite flakes, etc. were also chemically oxidized by strong nitric acid to produce luminescent CDs.[10, 24] Like other synthesis methods, ultrasonication is also adopted for the CDs and GQDs preparation. The vibration of the solvent molecules during sonication is responsible for disintegrating the large carbon source. Keep in mind that the top-down synthesis approach suffers from some drawbacks, including hazardous conditions (strong acids) or some electrolytes, requiring a series of extra purification and surface passivating agents to enhance fluorescence properties.

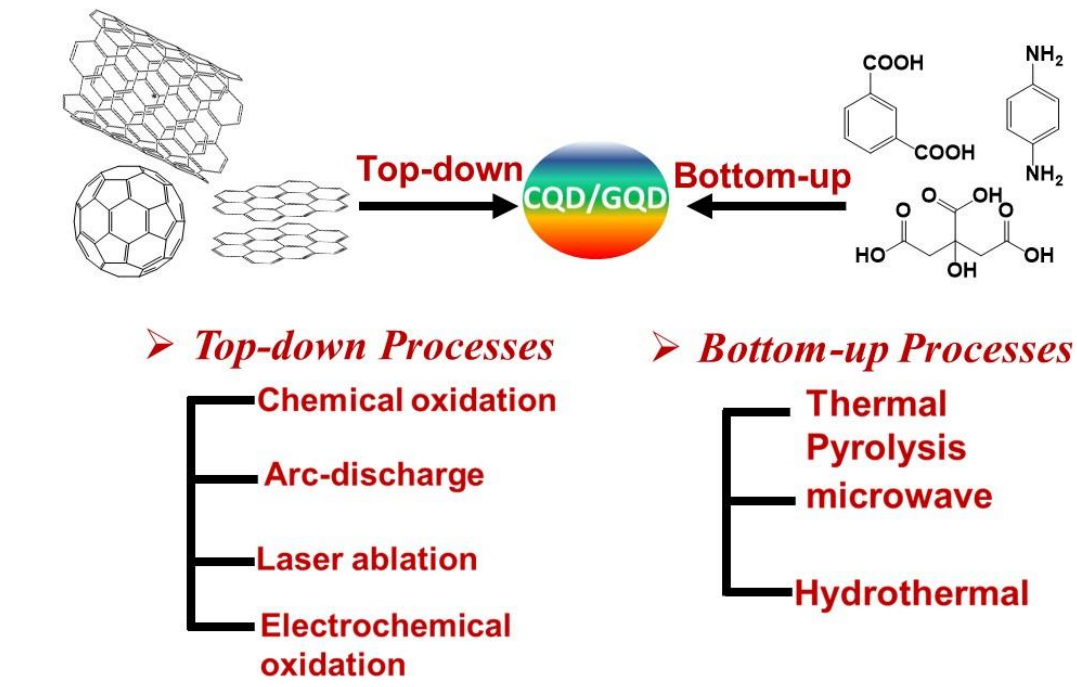

Figure 1.2. Schematic illustration of synthesis procedures of the carbon-based quantum dots.

Due to the various obstacles of earlier discussed methods, the researchers tried synthesizing CDs via the "bottom-up" approaches. Here, hydrothermal, microwave, and thermal pyrolysis procedures are mainly involved. Among them, the most popular hydrothermal method is one pot self-passivated and very simplistic technique for preparation of highly fluorescent CDs which contain multiple heterogeneous functionalities induced by precursors and solvent chosen. The main motif of hydrothermal reaction is the process that occurs in elevated pressure and temperature. In 2011, the first hydrothermally synthesized CDs were discovered by the Wang group.[25] Here, the monopotassium phosphate and glucose were poured in deionized water in a particular molar ratio, and an additional nitrogen source was further employed in that reaction mixture. After that, the whole mixture was transferred into a Teflon-lined autoclave and placed in the hydrothermal oven at 200° C for 12 h. After this, the journey of GQD and CDs expanded exponentially. The CDs with tunable emission can also be prepared by varying only temperature.[26] The CD synthesized from citric acid and 2-Imidazolidinethione (2-IZT) under 180° C and 200° C for 24 h display blue and green emissions, respectively. The cause of spectral nature shifts with reaction time variation was the amount of sulfur heteroatom. As the reaction time increases, the atomic percentage of sulfur also increases from 6 % (blue) to 18 % (green), which directly facilitates the formation of more H-bonding networks and leads to the shifting of emission maxima in the green region. Moreover, solvent also played a crucial role in hydrothermal synthesis.[27] By adjusting the type of solvent during hydrothermal synthesis, the photoluminescence also varies for the CD. Lei's research groups recently reported multi-emissive CDs i.e., blue, green, and red using phenylalanine and o-phenylenediamine as nitrogen and carbon source.[28] The blue and green CDs were obtained in formamide, N, N-dimethylacetamide, respectively, while red emissions were found when the precursor mixture was treated with a mixture of concentrated sulfuric acid and water. Later, various CDs are derived from various green sources i.e., lemon juice,[29] beetroots,[30] amino acids,[31] jute[32] etc. to enhance their biocompatible nature. This synthesis procedure is comparably considered green, cost-effective, and rapid for CD synthesis. The obtained CD becomes more bio-friendly and sometimes possesses a high quantum yield.

Yang's research group revealed and confirmed the fascinating microwave method of CDs synthesis.[33] Here, saccharides (fructose and glucose, etc.) and PEG-200 (poly (ethylene glycol)) were fully dissolved in deionized water, and then the whole transparent mixture was placed in a microwave oven (500 W) for 2 to 10 min. As the heating time is changed

from 2 min to 10 min the average size was also altered from 2.57±0.45 nm to 3.65±0.6 nm. There are numerous merits of this method like quick synthesis, low cost, homogeneous radiation, etc.[34, 35] Another step CDs synthesis method is thermal pyrolysis which was invented by Emmanuel P. Giannelis's research group.[36] Recently, the Gong group just reported CDs obtained from pyrolysis of ionic liquid (1-butyl-3-methylimidazolium chloride) in presence of both citric acid and o-phenylenediamine which emits blue, green, yellow, and red emissions with different size distributions.[37] All the above precisely described the commonly utilized synthetic approach to produce CDs.

1.5 Origin of fluorescence

The origination of luminescence property of CDs is still under investigation. Several precursors, synthetic approaches, and post-synthetic purification processes of CDs usually have been taken to produce dissimilar luminescence features. As per the literature report, the unique photoluminescence properties of CDs may be coined from the surface functional moieties, degree of surface oxidations, molecular type fluorescence, quantum confinement effect (QCE), and synergistic effect of QCE and surface states, etc.[38]

1.5.1 Surface functional moieties, degree of surface oxidations

A lot of studies disclosed that the luminescence of CDs results from their degree of surface oxidation and surface functional groups which are directly linked up with the CDs. As the increase of surface oxidative groups and various functional moieties, the defect sites increase, leading to produce different energy levels of CDs. Liang's group demonstrated multicolor nitrogen-doped CDs (NCDs) with various emission signals from blue to red to even white emissions (**Figure 1.3a**).[39] The full-color emission depended solely on surface functional groups, not the surface oxidation since they found oxygen contents are the same for every emissive NCDs. Recently, Li at al. synthesized CDs (CDs and GQDs) with the same size distribution but different in nature of surface oxidation. With the upsurge of surface oxidation, the wavelength of emission showed a red shift from 518 nm to 543 nm, leading to the decrease of the band gaps (**Figure 1.3b**).[40]

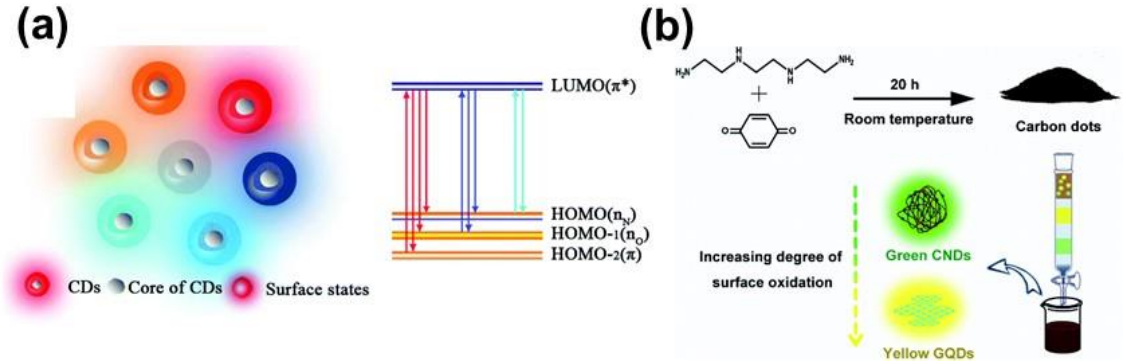

Figure 1.3. (a) Core and surface state emissions of carbon-based dots, Permission taken from ref 39. Copyright 2017, Royal Society of Chemistry. (b) Surface oxidation dependent emission properties of carbon-based dots. Permission taken from ref 40. Copyright 2017, Royal Society of Chemistry

1.5.2 Quantum confinement effect (QCE)

The quantum size of CDs also influenced the optical properties.[41] Choi et al. invented GQDs with different sizes, ranging from 5 nm to 35 nm, with unlike morphologies, and investigated size-dependent fluorescence and absorption spectra. As the size increases, the absorption energy decreases, and the emission peak gradually undergoes red-shift attributing to the QCE effect (**Figure 1.4**).[42]

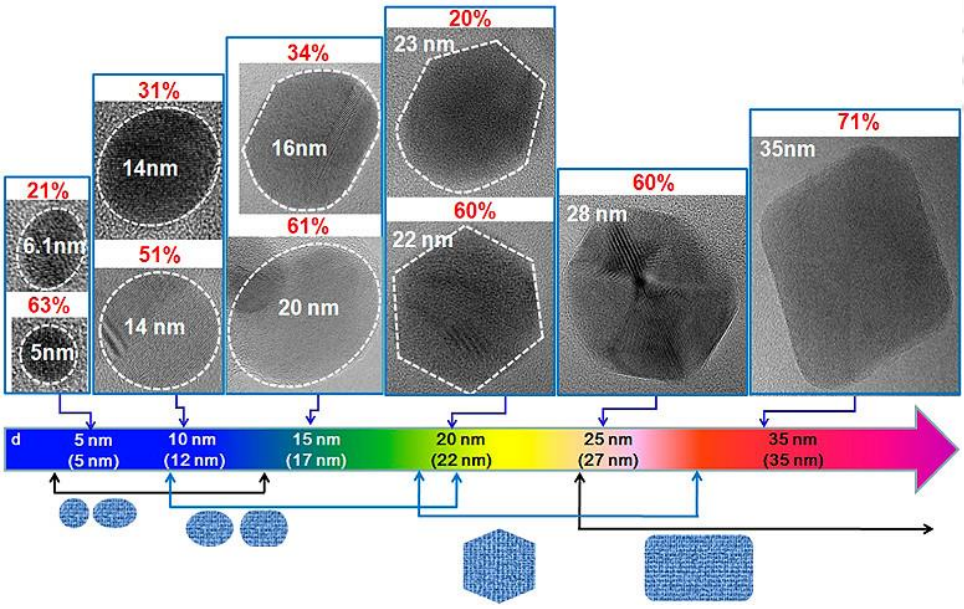

Figure 1.4. Quantum confinement effect of carbon-based dots. Permission taken from ref 42. Copyright 2012, American Chemical Society.

1.5.3 The synergistic effect of the quantum confinement effect and surface state

Presently, both the surface state and quantum confinement effect synergistically control the emission of CDs.[43] Pang et al. proposed that the surface states and QCE governed the fluorescence property of CDs. A sequence of CDs with diverse emissions was produced by changing the size, and degree of surface oxidation. The results showed that the increase of surface oxidation or the π-conjugated electronic systems, leads to a smaller energy gap in the CDs which is also influenced to shift the emission maxima in the red side.[44]

1.5.4 Molecular type fluorescence

Current studies demonstrate that during the synthesis, the formation of some emissive impurities (called molecular fluorescence) also contributes to the emission of CDs. The clarification the role of different molecular fluorescence in the spectral property of CDs, Rogach's group prepared three types of citric acid-based CDs. The authors also proved that the molecular fluorophores were not free in the solution, rather they are directly attached to the CDs and influenced the optical properties.[45] Baker's group evidently proved that the emissive impurities formed as the side-products during CDs synthesis largely contribute to the emission by eliminating the molecular fluorophores (**Figure 1.5**).[46]

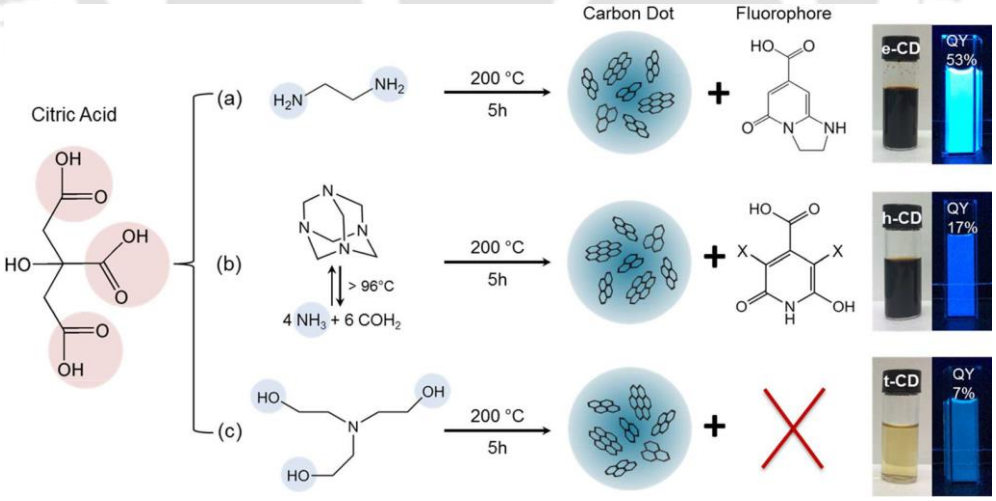

Figure 1.5. Various emissive impurities of carbon-based quantum dots. Permission taken from ref 46. Copyright 2012, American Chemical Society.

1.6 Heteroatom doping

As discussed earlier, many synthesis approaches exist to synthesize CDs effectively. However, some common drawbacks also persist for CDs; bare CDs show relatively low

fluorescence quantum yield compared to quantum dots and organic fluorophores even though various surface passivated or edge functional groups are present in CDs.[47] To overcome the challenges and enhance the biomedical applicability, most CDs and GQDs need further functionalization or more passivating groups. Hence, doping is promising for producing CDs and GQD with high emission efficiency (**Figure 1.6**). The doping method can be categorized into two parts: metal-doping (selenium, cobalt, iron, etc.) and non-metal doping (boron, nitrogen, sulfur, phosphorous, etc.). Moreover, effective surface functionalization by more heterogeneous groups also improves their chemical and optical properties and applicability. The percentage of dopant is also vital to modulate emission efficacy. A linear response is usually found between dopant percentage and fluorescence quantum yield.[48] This thesis is mainly focused on non-metal doping and surface functionalization in CDs and GQDs.

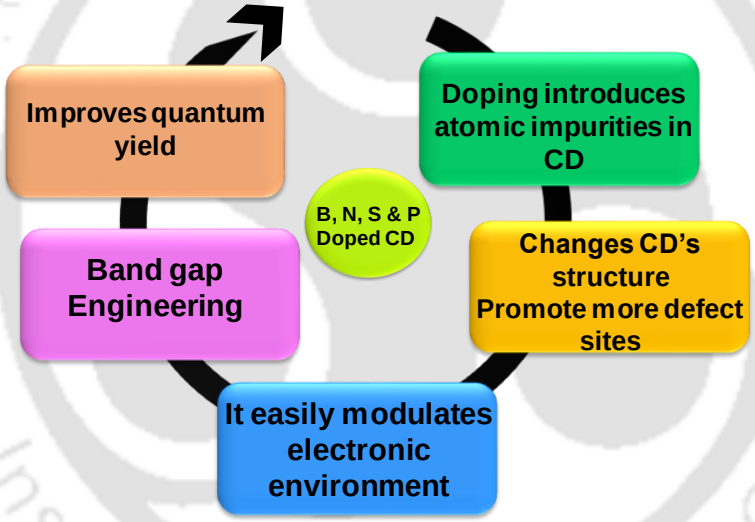

Figure 1.6. Advantages of heteroatom doping in carbon dots.

1.6.1 Nitrogen (N) doping

N doping is the most beneficial, significant, and commercially low-cost strategy. With the positive mesomeric effect, the lone pair electrons of N atoms trim down the excitation energy level (π^*) of CDs and generate a more electronic environment, resulting in π and π^* levels being close enough and emission signals coming from longer wavelength sides. Simultaneously, N atoms can also modulate the decay time; the percentage of fast emission decay in the intrinsic state increases and the percentage of slow emission in the surface state decreases.[48-50] Thus, a strong and effective emission signal can be achieved. The doping of N mostly leads to three kinds of N-containing structures, i.e., pyridinic-N,

pyrrolic-N, graphitic-N, etc. Chen et al. synthesized blue emissive NCDs from hydrothermally treating folic acid (used as both C and N sources) in 2014.[51] Several natural sources and other organic compounds are used to dope the CDs.[52-54]

1.6.2 Sulfur (S) doping

The Group 16 element S containing a vacant 3d orbital and a slightly larger size can also be doped into CDs. It can also excellently tune the optical properties of CDs by inducing a more electronegative effect which can modulate the electronic bandgap. It is not easy to insert an S atom into a carbon framework.[50] In 2014, the S-doped CDs were reported by straightforward hydrothermal synthesis, which exhibits 67 % quantum yield.[55] S-doped GQD was also developed by Li's research via electrolysis of graphite in a solution of sodium p-toluenesulfonate.[56] Moreover, various sources of sulfur can be used for doped of CDs, such as dimethyl sulfoxide, thiomalic acid, cysteine, glutathione, etc.[57-60]

1.6.3 Phosphorus (P) doping

The n-type semiconductor, P, belongs to Group 15 and is relatively larger than the N atom. It can provide much more defect sites on carbon lattice, which helps to tune the electronic levels and photophysical properties of CDs. The fluorescent P-doped CDs were prepared by Chandra et al. in 2011 by microwave treatment (100 W for 3 min 40 s) of sucrose and phosphoric acid.[61] Later, P-doped GQD synthesis was achieved using a graphite rod and sodium phytate by an electrochemical technique.[62] However, other P sources like phytic acid, adenosine 5′-monophosphate, triethyl phosphonoacetate, and adenosine triphosphate were also used for P-doping.[63-65]

1.6.4 Boron (B) doping

Being a vacant P orbital, ‘B’ is a typical p-type semiconductor. As the B atom is smaller in size, thus it is easily inserted into the carbon cluster. The effectiveness of p-type doping is the opposite of n-type doping because of the generation of holes.[50] Various B-containing moieties (boric acid, borax, B_2O_3, BBr_3, etc.) are used as boron sources.[66, 67] In 2014, the Feng research group reported blue emissive B-doped CD using BBr_3 and hydroquinone.[68] In this same year, the first-time blue emissive B-doped GQD was discovered from boron-doped graphene sheets by hydrothermal method.[69]

1.7 Surface functionalization

There is another possible method that also helps to improve the heterogeneity, and efficiently tune the energy levels of CDs/GQD and quantum yield of the synthesized materials called surface functionalization. In this method, the edge groups (-COOH and –OH and NH_2) of CDs and GQD can be functionalized by various organic moieties, bio-molecule, metal nanoclusters, and polymers, etc.[70-77]

1.8 Optical Properties

1.8.1 Absorbance

Generally, the absorbance spectra of CDs and GQDs are very broad and extensive in nature. Mostly synthesized CDs and GQDs have shown a very strong absorbance band in the range 230 nm to 290 nm (UV-region) due to the π to π* transition of C=C moieties. Moreover, it may also have a broad and extended absorbance tail from 300 nm to 700 nm for n to π* transition of surface functional groups (C=O, C=N, etc.). The absorbance spectra are directly related to the bandgap; hence it can be directly governed by changing surface states.

1.8.2 Photoluminescence

The most enthralling part of CDs and GQDs is their photoluminescence. The observed luminescence properties of the nanomaterials can be classified into three categories: (1) excitation-dependent emission (**Figure 1.7a**), (2) excitation-independent emission (**Figure 1.7b**), and (3) step-wise emission under separate excitation windows (**Figure 1.7c**).

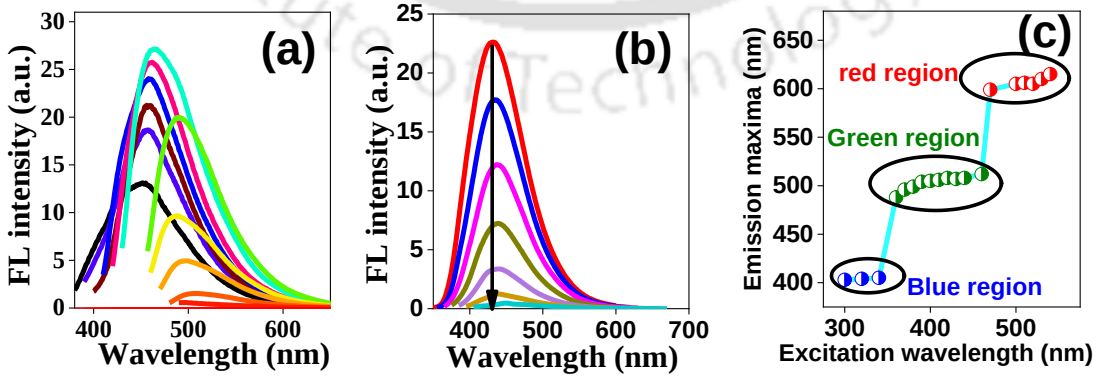

Figure 1.7. (a) Excitation dependent emission, (b) Excitation independent emission, (c) Step-wise emissions under different excitation windows.

1.8.3 Excitation-dependent emission

CDs mainly possess excitation-dependent emission characteristics, i.e., as the excitation wavelength increases, the emission maxima continuously shift to the red side, gradually decreasing the emission intensity. Many research groups suggested that this phenomenon was observed due to (1) the quantum confinement effect, (2) size, and (3) largely distributed surface emissive trap states.[78, 79] When the particles size on a nanometer scale, the whole electronic arrangement has influenced by grain boundaries which leads to the exhibit of different characteristics like bandgap and the size-dependent energy relaxation dynamics.[2] Another consequence is the size-dependent emission; as the size of synthesized nanomaterials increases, the emission continuously shifts to the red end.[80] Li et al. prepared CDs via the electrochemical method and purified the CDs by column chromatography. The prepared CDs are different in size and emission properties; the small ones (1.2 nm) provide UV light emission, the medium ones (1.5-3 nm) exhibit emission in the visible range, and the large ones (3.8 nm) give near-infrared emissions.[6] Like CDs, different sizes of GQDs were also prepared by Peng and his team with a size distribution of 1-4 nm (small), 4-8 nm (medium), and 7-11 nm (large) with emission maxima changing from blue, green, and yellow, respectively.[81] Moreover, the effect of abundant surface functional groups cannot be ignored. The various functional moieties produce several emissive trap states, each containing a particular excitation wavelength. When the CDs or GQDs are excited through the channel of wavelengths, the corresponding surface emissive trap becomes predominant, resulting in an excitation-dependent red shift of emission maxima.

1.8.4 Excitation-independent emission

Another side of the photoluminescence behavior of CDs and GQDs is excitation-independent emission, where the emission peak positions do not change with excitation wavelength. The property may depend on narrow size distributions directly related to the distinct separation of energy states.[82, 83] Recently, research uses the chromatography technique to separate the different emissive CDs depending on surface oxidation. Xiong et al. reported various emissive CDs via silica column chromatography and found that as surface oxidation increases, the emission shifts to the higher wavelength side (**Figure 1.8a** and **1.8b**).[84] Later, much literature is reported on such kinds of emission properties.[85-87]

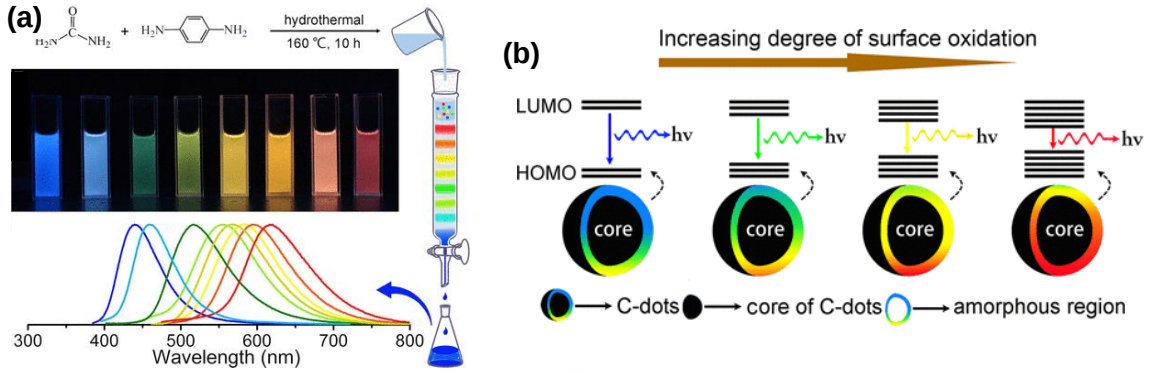

Figure 1.8. (a) Purification of CDs through column chromatography, (b) Schematic illustration of tunable emissions of CDs with different oxidation. Permission taken from ref 84. Copyright 2012, American Chemical Society.

1.8.5 Step-wise emission under particular excitation windows

Recently, researchers have found a different kind of luminescence property of carbon dot, called step-wise emission. Here, CDs may possess a different emission position but a distinct emission location at the particular excitation window, which is not dependent on the excitation wavelength. This type of behavior may originate from inherent carbon-core state emission and extrinsic surface state emission.[88] Naccache research group derived CDs from glutathione and formamide, which exhibits dual fluorescent emission, blue and red (**Figure 1.9**).[89] The blue emission originated from the carbon-core state, and the red emission signal came from various surface states.

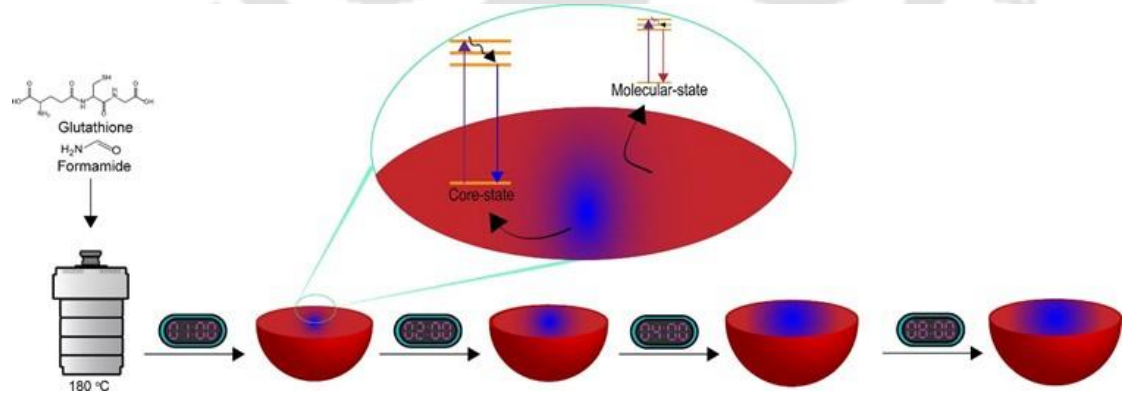

Figure 1.9. Two different emission centres of carbon dots, Permission taken from ref 89. Copyright 2012, American Chemical Society.

1.8.6 Up-conversion Properties

From conventional fluorescence down-conversion, the up-conversion technique is fully the opposite phenomenon. Here, anti-stoke shifts are observed, i.e., the molecule excited at the

higher wavelength and the emission signal comes at the lower wavelength region. In this process, the absorption of multiple photons can lead to emission at a lower wavelength. It was first invented by Cao et al. where CDs exhibit visible emission upon excitation of 800 nm laser pulse.[90] This technique is very much useful in the biological platform as it can effectively reduce auto-fluorescence and deep tissue permeability.[91, 92]

1.9 Theory of fluorescence quenching

Basically, suppression of emission intensity happens only presence of a particular quencher, i.e., effective interactions between nanoprobe and quencher may lead to fluorescence quenching. In the quenching procedure, the determination of the rate of quenching is an important factor[93]. The quenching rate constant can be determined by plotting the ratio of emission intensity against the concentration of the quencher which mostly shows a linear plot, called the Stern-Volmer (S-V) plot. This can be defined by the following equation

$$\frac{F}{F_0} = 1 + K_{sv}[Q]$$

Here, F and F_0 are the emission intensities of synthesized nanoprobe before and after the addition of quencher. Q is the concentration of the quencher. K_{sv} is called the S-V constant.

This plot also helps to determine the number of quenching mechanisms involved in the process. If the plot is linear, then only one quenching mechanism is operating, and any deviation from the linearity may indicate the involvement of two or more quenching processes.

There are various mechanisms responsible for fluorescence quenching: ground-state complex formation, Photo-induced electron transfer, Forster resonance energy transfer, Inner filter effect, etc.[94]

1.9.1 Ground-state complex formation

A non-fluorescent ground state complex may form between fluorophore (F) and analytes (A) which displays a distinguishable absorbance spectrum and undergoes some non-radiative decay. Here, the emission intensity depends upon analyte concentration and also temperature. As the temperature increases, the complex may break down; hence, the association constant decreases (K_{ass}). Here, the intensity ratio plot against quencher

concentration shows linearity, and fluorescence lifetime also remains unchanged[93] (**Figure 1.10a** and **1.10b**)

$$F + A \xrightarrow{K_{ass}} [F \cdots A]\ (nonfluorescent\ complex)$$

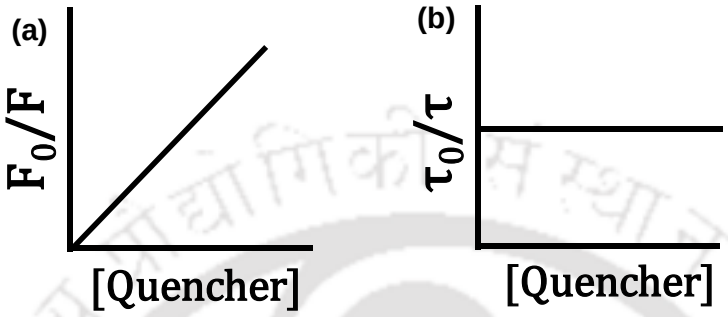

Figure 1.10. (a) The ratio of emission intensity, and (b) The ratio of average lifetime vs. quencher concentration plot.

1.9.2 Photo-induced electron transfer (PET)

The well-known fluorescence quenching mechanism, PET is generally occurred between the donor (D) and acceptor (A) via complex formation.[95, 96] Mostly, excited nano-fluorescent probes (CDs or GQDs) donate an electron to the ground-state acceptor molecules (here metal ion) by forming [D^+-A^-] pair as depicted in **Figure 1.11**. This complex reverted again into the ground state via non-radiative transitions. This is a major phenomenon for fluorescence quenching by various metal ions.

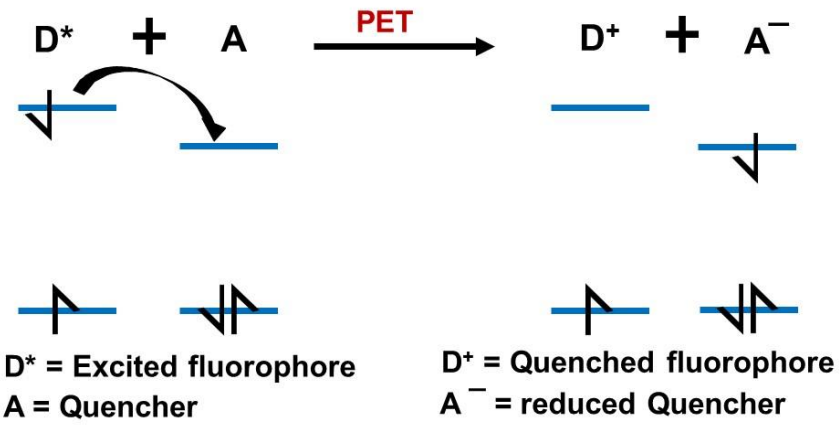

Figure 1.11. Schematic illustration of PET process.

1.9.3 Inner filter effect (IFE)

IFE is another significant phenomenon in a spectrofluorometric area where the absorber or quencher absorbs the emission and/or excitation energy of the nanoprobe.[93, 97] The spectral overlap between quencher absorption spectra and fluorophore emission-excitation spectra is presented in **Figure 1.12**.

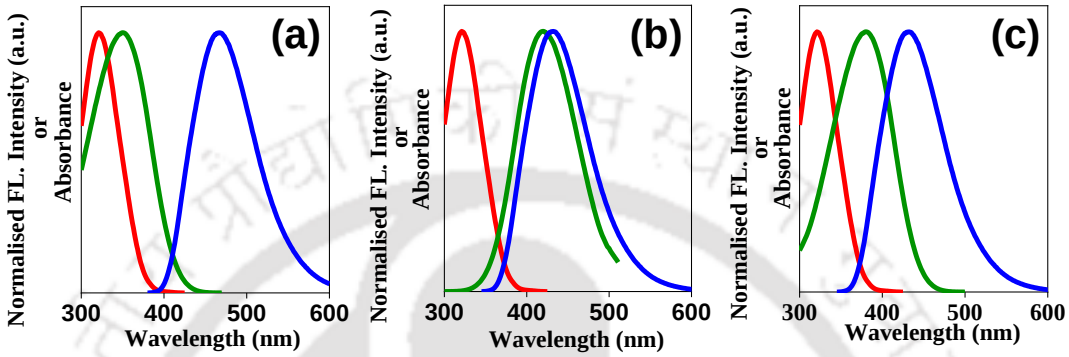

Figure 1.12. Various conditions for IFE: the overlap of the absorption spectrum of the quencher with (a) the excitation spectrum, (b) the emission spectrum and (c) both the excitation and emission spectra of the fluorophore. [red line: Excitation spectra of fluorophore, green line: Absorption spectra of quencher, and blue line: Emission spectra of fluorophore]

It is a straightforward process and did not involve nanoprobe-quencher interactions. IFE can be divided into two subcategories (1) primary-IFE (P-IFE) and (2) secondary-IFE (S-IFE). The former and later stem from absorption of the excitation and emission energy, respectively. Various sensors have been developed by considering this theory. For IFE calculation following formula is used[98]

$$\frac{F_{corrected}}{F_{observed}} = \frac{2.3dA_{ex}}{1-10^{-dA_{ex}}} 10^{gA_{em}} \frac{2.3sA_{em}}{1-10^{-sA_{em}}}$$

Here, $F_{corrected}$, $F_{observed}$, A_{ex}, and A_{em}, are the corrected emission intensity after removing the IFE, actual emission intensity, the absorbance value of nanomaterials at the excitation wavelength, and absorbance value at emission wavelength, respectively. The ‘d’, and ‘s’ are the is the thickness of the cuvette and the width of the excitation beam. The ‘g’ is the distance between the edges of the cuvette and the excitation beam.

1.9.4 Forster resonance energy transfer (FRET)

The mechanism of FRET is summarized in **Figure 1.13**. Here, the donor-fluorophore molecule at first excited (D*), and while coming back to the ground state it releases energy. By absorbing this energy, the acceptor molecule goes up to a higher energy level (A*).

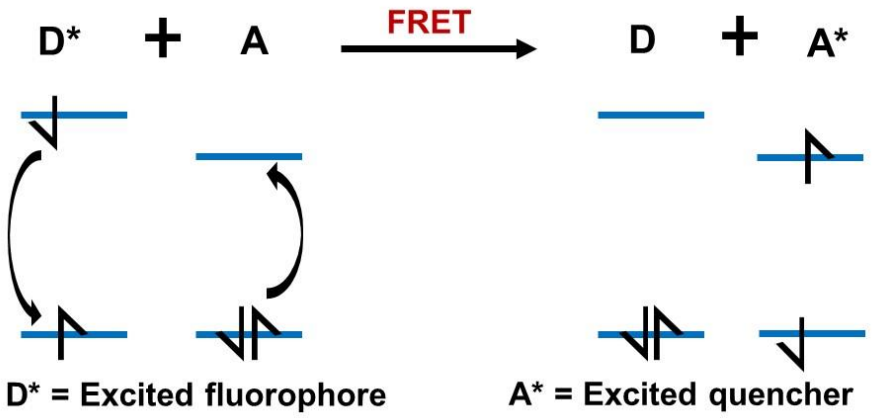

Figure 1.13. Schematic illustration of FRET process.

There are three main factors which are controlled the rate of this process (1) the distance between the donor-acceptor pair, (2) the dipole orientation, and, (3) the extent of spectral overlap i.e., the donor emission and acceptor absorption. The extent of overlap i.e., overlapping integral (J(λ)) is calculated by the following formula[99, 100]

$$\text{Overlapped Integral J}(\lambda) = \frac{\int_0^\infty F_D(\lambda)\varepsilon(\lambda)\lambda^4 d\lambda}{\int_0^\infty F_D(\lambda)d\lambda}$$

here $F_D(\lambda)$ denoted for corrected FL intensity of the donor in the range λ to λ + Δλ and ε(λ) represented the molar extinction coefficient of the acceptor. The effective FRET efficacies are also calculated by the following equation[93]

$$\text{FRET Efficiency (E)} = 1 - \frac{\tau_{D-A}}{\tau_D}$$

Here, τ_D and τ_{D-A} denote the lifetimes of the quantum dots in the presence and absence of a quencher.

The distance (r_0) between the pair of donor-acceptor also governers for the FRET pair and the effective Förster distance was also calculated using the equations

$$\text{Förster distance } (R_0) = 8.8 \times 10^{-25}\kappa^2 n^{-4}\varphi\, J(\lambda) \quad \text{in nm}$$

$$E = \frac{1}{1 + (r_0/R_0)^6} \qquad (r_0 \text{ value in nm})$$

where κ^2 is described as the orientation factor between the donor and the transition dipole acceptor, φ is the measured quantum yield of synthesized nanomaterials, n is the refractive index of the solvent, and J(λ) stands for the overlapping integral.

1.10 Application

CDs and GQDs have several applications in diverse filed. The utilization of these carbon-based quantum dots in various platform is elucidated here.

1.10.1 Sensing

The sensing application mainly focuses on two criteria, i.e., transduction and recognition. The specific analyte (which to be detected) interacts with the specific site of the sensor (here CDs/GQDs) and the degree of this interaction largely depends on analyte concentrations. By evaluating the alteration of the chemical or physical property of the CDs/GQDs, the analyte concentration is determined. In another way, a method of converting concentration variations into practical data is called signal transduction. In chemical sensors, both the sensing analyte and signal transducer are incorporated together. The photoluminescence-based optical sensors are highly superior owing to its fast, sensitive spectral changes, cost-effective, and precise detection of analyte.[101] Depending on the sensor-analyte interactions, the emission signal may vary mainly in three ways; (1) signal-on (here, the emission intensity enhances manyfold by adding analyte, called 'turn-on sensing'), (2) signal-off (the emission intensity gradually goes down with changing analyte concentration, called 'turn-off' sensing), (3) ratiometric sensing (here either one emission band increase and other decreases or remain constant. The nanoscale size, numerous surface functional groups, and outstanding spectroscopic property allow the CDs/GQDs to detect several kinds of analytes.

1.10.2 Metal ion detection

Every metal ion has some threshold limit, beyond that, it becomes very harmful for physiological systems and environments. Hence, a CDs/GQDs-based good, simple, and economical sensor is crucial to develop. Specific metal ion are binds only specific types of carbon dots. Many metal ions can be detected using CDs/GQDs, such as Fe^{3+},[102-104] Pb^{2+},[105] Hg^{2+},[106, 107] Cu^{2+},[108, 109] Cr^{6+},[110, 111] Al^{3+},[112] As^{3+},[113, 114] Zn^{2+},[115, 116] Pb^{2+},[105] Au^{3+},[117] PO_4^{3-},[118] I^-,[119] CN^-,[120] etc. Mostly, metal ion sensing is accomplished by complex formation with GQDs/CDs, and electron transfer process.

1.10.3 pH sensing

pH is extremely essential in the living organism for proper functioning physiological processes. The different types of surface functional groups (-NH_2, -COOH, -OH, pyridinic-N, etc.) or edge functionalization of CDs/GQDs helps to grow up pH-sensitive performance.[121] Mainly protonation and deprotonation of surface functionality boosts the pH dependent behaviour of CDs. For example, various N-doped GQD (NGQD) was reported by Kurniawan et al. where they found that the combined effect of –OH and pyrrolic N would be responsible for a wide range of pH sensing behavior (1.8 to 13.6) with the red shifting of emission maxima.[122] In another report, a wide range of pH (1 to 9) and intracellular pH recognition were reported by red emissive CDs. This pH-responsive performance is achieved by aggregation-disaggregation of synthesized CDs materials.[123]

1.10.4 Biomolecule detection

The biocompatible nature of CDs/GQDs endorses its applicability in the area of biomolecule detection. Several kinds of biomolecules such as vitamins,[124] jaundice biomarkers,[125] glutathione,[126] cysteine,[127] adenosine triphosphate,[128] glucose,[129] uric acid,[130] etc. carbon-based quantum dot also able to bind with DNA which helps in the treatment of life-threatening diseases.[131, 132]

1.10.5 Other Sensing

Hitherto, the exceptional spectroscopic properties of CDs/GQDs have been expansively used to design or develop new novel nanoprobe for recognizing various chemical regents like dopamine,[133] fingerprint,[134] valine,[135] picric acid,[136] 4-nitroaniline,[137] nerve agents,[138] H_2S,[139] hazardous dye,[140] pesticides,[141] H_2O_2,[142] moisture,[143] temperature,[144] formaldehyde,[145] tetracycline,[146] reactive oxygen species (ROS)[147] etc.

1.10.6 Bioimaging

CDs are a suitable candidate for bioimaging. The very low-cytotoxic behavior and nanoscale range size make them appropriate nanoprobe for biological applications. Two photon fluorescence microscopy have been used in 2007 by Cao et al. for cancer cell imaging.[90] Later CDs are introduced in mice model by Yang et al. at 2009 for showing the

non-toxic behavior, and biocompatible nature.[148] Afterward, CDs are applied for the specifically targeted living organs like mitochondria,[149] lysozyme,[150] and nucleus.[151]

1.10.7 Drug delivery

The CDs/GQDs are promising materials for traceable drug release due to its bio-friendly nature and very tiny size which helps to act as a nano-carrier for drugs. The plausible reasons behind drug loading are the non-covalent interactions between drug and the surface of CDs/GQDs.[49] Sometimes hollow cavity presents at the center of the carbon-based dots facilitating abundant space for drug molecules.[152] Recently, amino acid mimicking NIR-emitting CDs was invented by Li et al. with many paired amino and α-carboxyl groups present at the edge site which prompt multivalent interactions with large neutral amino acid transporter 1 (LAT1).[153] This CDs specifically detects and provides imaging of the cancerous cell, tumor, and its locations. The aromatic domain of NIR-CDs helps to load topotecan hydrochloride (TPTC) drug via π–π interactions and deliver the drug to the brain tumors through penetrating the blood-brain barrier. Sung and his co-workers also develop GQD-based drug delivery systems where docetaxel (DTX), a hydrophobic drug loaded with GQD via sp^2-sp^2 interactions (GQD/DTX). This system was further coated with large pores mesoporous sponge-like silica and capping with Cetuximab (Ct) and RBC membrane (named as Ct-RBC@GQD-D/NS). Finally, when Ct-RBC@GQD-D/NS reached the tumor-targeted locations, GQD/DTX was discharged upon significant NIR radiation, subsequent to tumor ablation.[154]

1.10.8 Solar cells

Carbon-based quantum dots can absorb the entire spectral region i.e., from UV to NIR. This phenomenon can be utilized to devise photovoltaics such as solar cells. In this recent times, various composites of CDs/GQDs are reported for dye-sensitized solar cells (DSSC), and perovskite solar cells (PSCs), due to it can be enhanced the photovoltaic performance. GQDs and CDs can applied as very efficient counter electrode (CE) for the dye dye-sensitized solar cells (DSSCs) in replacement of Pt CE. The nanocomposite made with reduced graphene oxide (rGO), MoS2, and N-doped graphene quantum dot can be used as a potential CE for the DSSC devices and reveals very good power conversion efficiency (PCE).[155] In another work, CDs is being dopped in the heterojunction of n-ZnO/p-NiO to diminish the electron/hole potential barrier at respective edge of n-ZnO/Cdot and

Cdot/pNiO.[156] CDs and GQDs can also be utilized as a passivation additive for perovskite solar cells. In a recent study, two different CDs with varied functional groups has been utilized to passivate the $MAPbI_3$ perovskite and carbon electrode interface. This surface passivation strategy will enhance the defect states of perovskite and also enhance the hydrophobicity of the layer that results in highly efficient and stable solar cell devices.[157] Novel GQDs can also be used as a passivation molecule to improve the device efficiency and stability.[158]

1.10.9 Catalysis

CDs are also used as an electrochemical and photocatalysis. Till now, many metal-based catalysis and nano-composites are described to enhance the reaction kinetics. Due to the complicated reaction technique of metal catalysis, CD-based compounds are incorporated here as well. The bi-functional CDs are reported for measuring the electro-catalytic behavior in an oxidation-reduction reaction.[159] The CD with 1 to 4 nm size was prepared, which exhibited catalytic activity of conversion of alcohols to benzaldehyde in NIR irradiation. The efficiency of conversion was reported at 92 % with almost 100 % selectivity.

1.10.10 White Light generation

White light generation is a hot topic in the modern research world. As the CDs have broad emission ranges, they can be successfully used to generate white light. For white light production, various emission (blue, green, and red) colors are required to recreate the visible spectral range (400-700 nm).[160] Very recently, Chen et al. reported multicolor emissive CDs/epoxy composite i.e, blue, green, and red CDs in some for making multicolor LEDs. Furthermore, they mixed the multicolor emissive epoxy/CDs composite in a 1:2:2 (red: green: blue) weight ratio to produce a bright white light.[161]

1.11 Motivation

In the thesis, I am inclined to prepare several novel N-functionalized carbon dots and investigate their optical properties and applications, considering the different fascinating facets of carbon-based quantum dots discussed in this introduction section. Carbon dots represent a highly flourishing research domain exposing versatile newer applications. As the circle of time expands, the overall toxicity in nature increases; many hazardous

chemicals and heavy metal ions are found at abnormal levels in the environment, causing many serious health issues in the human body and aquatic animals. The primary motivation of the thesis is to identify low levels of hazardous chemicals and metal ions by implementing biocompatible N-doped/functionalized carbon dots as an excellent nano-optical sensor. Detecting harmful analytes by the simple fluorometric method is also challenging. So far, all the criteria of recognizing hazardous materials through switching of emission signal can be easily achieved by N-doped/functionalized carbon dots.

1.12 Thesis Overview

This thesis emphasizes the facile synthesis of new and biocompatible N-doped carbon dots with fascinating optical characteristics and robust sensing performance. This thesis contains eight chapters, and a brief description of each chapter is given below.

Chapter 1 briefly introduces carbon dots, its classification, various synthesis techniques, doping strategy, surface functionalization, photoluminescence properties, and enormous applications.

Chapter 2 describes the details of materials and methods adopted during the synthesis. The synthetic procedures and the instruments used for characterizing the nanomaterial are thoroughly explained in this chapter.

Chapter 3 presents surface functionalized graphene quantum dot by 2,6-diaminopyridine molecule (F-GQD) for the multimode detection of Pb^{2+} and ClO^{-} via totally distinct emission properties. The fluorescence quantum yield and surface heterogeneity increase manifold by incorporating 2,6-diaminopyridine. For Pb^{2+}, the emission signal was amplified because of the aggregation-induced emission enhancement effect. However, a turn-off fluorescence behavior was observed in the case of ClO^{-}. The mechanism for the detection of ClO^{-} was unique in nature. In the presence of ClO^{-}, an H-bonding interaction between –H from amine functionality and ClO^{-} leads to energy migration from nanosensors to ClO^{-}. The effect of amine functionality in sensing performance was also clarify undertaking only 2-aminopyridine functionalized graphene quantum dots. The functionalized nanodot is further applied for detecting ClO^{-} in the HeLa cell line with excellent outcomes.

Chapter 4 discusses multi-heteroatomic N-doped carbon dot (NCD) prepared from 3,6-diaminoacridine hydrochloride and L-aspartic acid in a 1:1000 molar ratio. This nanodot is

highly blue-emissive and has solid-state emission properties. The two well-known bio-analytes, e.g., bilirubin and vitamin-B_{12} are easily recognized by the NCD with contrasting detection mechanisms. The bilirubin detection consists of H-bonding induced energy transfer from donor-NCD to acceptor-BR, whereas the inner filter effect was responsible for vitamin-B_{12} detection. Furthermore, the NCDs show excellent biocompatibility and detect vitamin-B_{12} in the living systems.

In ***Chapter 5***, two different emissive (blue and green) NCDs were prepared by considering two different precursors, 5-aminoisopthalic acid and 3,5-diaminobenzoic acid. With increasing the atomic percentage of nitrogen from 8.3% to 15.8 % the emission center was shifted from 430 nm (NCD-1; blue emission) to 490 nm (NCD-2: green emission). NCD-1 has solid-state emission and centre at 521 nm, which is 91 nm red-shifted from solution-state. Both the NCDs recognize 4-nitroaniline (4-NA) with good sensitivity and selectivity. The sensing mechanism depends on the emission wavelength and solvent system. In an aqueous medium, the inner filter effect and electron transfer are primarily responsible for sensing 4-NA by NCD-1, whereas both energy and electron transfer are responsible for 4-NA detection by NCD-2. In DMSO medium, multiple mechanisms act together, e.g., inner filter effect, electron, and energy transfer. A paper-strip-based 4-NA detection was also achieved for fast on-site detection of 4-NA.

Chapter 6 reports a triple mode emissive N-doped carbon dot (NCD) synthesized from 3,5-diaminobenzoic acid and hydrazine hydrate. Here, the NCD shows three different emissions in three different blue, green and red emissions when excitation windows fall on 300-340 nm, 380-460 nm, and 500-540 nm, respectively. We established that the blue emission arises from the carbon core, and the rest of the emission stems from surface states. The surface-state emissions are very sensitive to Fe^{3+}, showing turn-off quenching, whereas the off-state emission signals are restored after adding ascorbic acid. Finally, a multi-input logic gate was established to transform the molecular information as fluorescence signal outputs.

In ***Chapter 7***, a dual-emissive N-doped carbon dot (NCD) was prepared from 3,4-diaminobenzoic acid and hydrazine hydrate, where emission signal appears at 490, and 570 under 410 nm excitation. This NCD is highly sensitive to pH and Fe^{3+} in a ratiometric manner. As the pH increases from 2 to 7.6, the emission intensity gradually increases; after that, it levels off (pH 8 to 12). The fluorescence decay profile depends on pH. For Fe^{3+}, the 490 nm peak intensity gradually decreases while the 570 nm peak intensity increases in a

distinct ratiometric manner. The complexation between various heterophilic surface functional groups and Fe^{3+} plays a central role in such ratiometric sensing performance. Moreover, the NCD shows a noteworthy anti-cancerous property. This bi-color emitting NCD can effectively recognize the intracellular pH and exogenous Fe^{3+} in the breast cancer cells (MCF-7). Finally, a solution-phase white light was also prepared by considering the emission characteristic of NCDs.

Chapter 8 summarises the thesis and furnishes future perspectives for the works presented in the thesis.

References

1. J. Wan, X. Zhang, K. Fu, X. Zhang, L. Shang and Z. Su, *Nanoscale*, 2021, **13**, 17236-17253.

2. S. Zhu, Y. Song, X. Zhao, J. Shao, J. Zhang and B. Yang, *Nano Res.*, 2015, **8**, 355-381.

3. S. Tao, S. Zhu, T. Feng, C. Xia, Y. Song and B. Yang, *Mater. Today Chem.*, 2017, **6**, 13-25.

4. Y. Xu, J. Liu, C. Gao and E. Wang, *Electrochem. commun.*, 2014, **48**, 151-154.

5. X. Li, M. Rui, J. Song, Z. Shen and H. Zeng, *Adv. Funct. Mater.*, 2015, **25**, 4929-4947.

6. H. Li, X. He, Z. Kang, H. Huang, Y. Liu, J. Liu, S. Lian, C. H. A. Tsang, X. Yang and S.-T. Lee, *Angew. Chem., Int. Ed.*, 2010, **49**, 4430-4434.

7. S. Qu, X. Wang, Q. Lu, X. Liu and L. Wang, *Angew. Chem., Int. Ed.*, 2012, **51**, 12215-12218.

8. X. Xu, R. Ray, Y. Gu, H. J. Ploehn, L. Gearheart, K. Raker and W. A. Scrivens, *J. Am. Chem. Soc.*, 2004, **126**, 12736-12737.

9. Y.-P. Sun, B. Zhou, Y. Lin, W. Wang, K. A. S. Fernando, P. Pathak, M. J. Meziani, B. A. Harruff, X. Wang, H. Wang, P. G. Luo, H. Yang, M. E. Kose, B. Chen, L. M. Veca and S.-Y. Xie, *J. Am. Chem. Soc.*, 2006, **128**, 7756-7757.

10. H. Liu, T. Ye and C. Mao, *Angew. Chem., Int. Ed.*, 2007, **46**, 6473-6475.

11. L. A. Ponomarenko, F. Schedin, M. I. Katsnelson, R. Yang, E. W. Hill, K. S. Novoselov and A. K. Geim, *Science*, 2008, **320**, 356-358.

12. S. Y. Lim, W. Shen and Z. Gao, *Chem. Soc. Rev.*, 2015, **44**, 362-381.

13. S. Wang, I. S. Cole, D. Zhao and Q. Li, *Nanoscale*, 2016, **8**, 7449-7458.

14. J. Shen, Y. Zhu, X. Yang and C. Li, *Chem. Commun.*, 2012, **48**, 3686-3699.

15. X. T. Zheng, A. Ananthanarayanan, K. Q. Luo and P. Chen, *Small*, 2015, **11**, 1620-1636.

16. J. Zhou, C. Booker, R. Li, X. Zhou, T.-K. Sham, X. Sun and Z. Ding, *J. Am. Chem. Soc.*, 2007, **129**, 744-745.

17. M. Li, T. Chen, J. J. Gooding and J. Liu, *ACS Sens.*, 2019, **4**, 1732-1748.

18. M. K. Kumawat, M. Thakur, R. B. Gurung and R. Srivastava, *ACS Sustain. Chem. Eng.*, 2017, **5**, 1382-1391.

19. H. Li, Z. Kang, Y. Liu and S.-T. Lee, *J. Mater. Chem.*, 2012, **22**, 24230-24253.

20. L. Zheng, Y. Chi, Y. Dong, J. Lin and B. Wang, *J. Am. Chem. Soc.*, 2009, **131**, 4564-4565.

21. J. Lu, J.-x. Yang, J. Wang, A. Lim, S. Wang and K. P. Loh, *ACS Nano*, 2009, **3**, 2367-2375.

22. Y. Li, Y. Hu, Y. Zhao, G. Shi, L. Deng, Y. Hou and L. Qu, *Adv. Mater.*, 2011, **23**, 776-780.

23. Y. Dong, C. Chen, X. Zheng, L. Gao, Z. Cui, H. Yang, C. Guo, Y. Chi and C. M. Li, *J. Mater. Chem.*, 2012, **22**, 8764-8766.

24. R. Sekiya, Y. Uemura, H. Murakami and T. Haino, *Angew. Chem., Int. Ed.*, 2014, **53**, 5619-5623.

25. Z.-C. Yang, M. Wang, A. M. Yong, S. Y. Wong, X.-H. Zhang, H. Tan, A. Y. Chang, X. Li and J. Wang, *Chem. Commun.*, 2011, **47**, 11615-11617.

26. J. Velusamy, G. Ramos-Ortiz, M. Rodríguez, O. Hernández-Cruz and A. Ponce, *J. Colloid. Interf. Sci.*, 2018, **528**, 237-247.

27. X. Xu, G. Hu, L. Mo, Y. Li, H. Wei, B. Lei, X. Zhang, C. Hu, J. Zhuang and Y. Liu, *Nanoscale*, 2021, **13**, 6846-6855.

28. X. Lei, D. Li, Y. Chen, Q. Liu, Q. Yan, J. Wang, B. Han, G. He and B. An, *New J. Chem.*, 2022, **46**, 4979-4982.

29. A. Tadesse, M. Hagos, D. RamaDevi, K. Basavaiah and N. Belachew, *ACS Omega*, 2020, **5**, 3889-3898.

30. V. Singh, K. S. Rawat, S. Mishra, T. Baghel, S. Fatima, A. A. John, N. Kalleti, D. Singh, A. Nazir, S. K. Rath and A. Goel, *J. Mater. Chem. B*, 2018, **6**, 3366-3371.

31. S. Pandit, P. Behera, J. Sahoo and M. De, *ACS Appl. Bio Mater.*, 2019, **2**, 3393-3403.

32. A. Deb, A. Konwar and D. Chowdhury, *ACS Sustain. Chem. Eng.*, 2020, **8**, 7394-7402.

33. H. Zhu, X. Wang, Y. Li, Z. Wang, F. Yang and X. Yang, *Chem. Commun.*, 2009, DOI: 10.1039/B907612C, 5118-5120.

34. M. Larhed, C. Moberg and A. Hallberg, *Acc. Chem. Res.*, 2002, **35**, 717-727.

35. F. Li, C. Li, J. Liu, X. Liu, L. Zhao, T. Bai, Q. Yuan, X. Kong, Y. Han, Z. Shi and S. Feng, *Nanoscale*, 2013, **5**, 6950-6959.

36. A. B. Bourlinos, A. Stassinopoulos, D. Anglos, R. Zboril, M. Karakassides and E. P. Giannelis, *Small*, 2008, **4**, 455-458.

37. M. Cao, X. Zhao and X. Gong, *Small*, 2022, **18**, 2106683.

38. L. Bao, Z.-L. Zhang, Z.-Q. Tian, L. Zhang, C. Liu, Y. Lin, B. Qi and D.-W. Pang, *Adv. Mater.*, 2011, **23**, 5801-5806.

39. Y. Zhang, R. Yuan, M. He, G. Hu, J. Jiang, T. Xu, L. Zhou, W. Chen, W. Xiang and X. Liang, *Nanoscale*, 2017, **9**, 17849-17858.

40. M. L. Liu, L. Yang, R. S. Li, B. B. Chen, H. Liu and C. Z. Huang, *Green Chem.*, 2017, **19**, 3611-3617.

41. X. Yan, B. Li and L.-s. Li, *Acc. Chem. Res.*, 2013, **46**, 2254-2262.

42. S. Kim, S. W. Hwang, M.-K. Kim, D. Y. Shin, D. H. Shin, C. O. Kim, S. B. Yang, J. H. Park, E. Hwang, S.-H. Choi, G. Ko, S. Sim, C. Sone, H. J. Choi, S. Bae and B. H. Hong, *ACS Nano*, 2012, **6**, 8203-8208.

43. S. Zhu, Y. Song, J. Wang, H. Wan, Y. Zhang, Y. Ning and B. Yang, *Nano Today*, 2017, **13**, 10-14.

44. L. Bao, C. Liu, Z.-L. Zhang and D.-W. Pang, *Adv. Mater.*, 2015, **27**, 1663-1667.

45. J. B. Essner, J. A. Kist, L. Polo-Parada and G. A. Baker, *Chem. Mater.*, 2018, **30**, 1878-1887.

46. J. Schneider, C. J. Reckmeier, Y. Xiong, M. von Seckendorff, A. S. Susha, P. Kasák and A. L. Rogach, *J. Phys. Chem. C*, 2017, **121**, 2014-2022.

47. X. Kou, S. Jiang, S.-J. Park and L.-Y. Meng, *Dalton Trans.*, 2020, **49**, 6915-6938.

48. Q. Xu, T. Kuang, Y. Liu, L. Cai, X. Peng, T. Sreenivasan Sreeprasad, P. Zhao, Z. Yu and N. Li, *J. Mater. Chem. B*, 2016, **4**, 7204-7219.

49. Y. Park, Y. Kim, H. Chang, S. Won, H. Kim and W. Kwon, *J. Mater. Chem. B*, 2020, **8**, 8935-8951.

50. L. Li and T. Dong, *J. Mater. Chem. C*, 2018, **6**, 7944-7970.

51. R. Zhang and W. Chen, *Biosens. Bioelectron.*, 2014, **55**, 83-90.

52. J. Feng, W.-J. Wang, X. Hai, Y.-L. Yu and J.-H. Wang, *J. Mater. Chem. B*, 2016, **4**, 387-393.

53. R. Atchudan, T. N. J. I. Edison, D. Chakradhar, S. Perumal, J.-J. Shim and Y. R. Lee, *Sens. Actuators B Chem.*, 2017, **246**, 497-509.

54. S. A. Shaik, S. Sengupta, R. S. Varma, M. B. Gawande and A. Goswami, *ACS Sustain. Chem. Eng.*, 2021, **9**, 3-49.

55. Q. Xu, P. Pu, J. Zhao, C. Dong, C. Gao, Y. Chen, J. Chen, Y. Liu and H. Zhou, *J. Mater. Chem. A*, 2015, **3**, 542-546.

56. S. Li, Y. Li, J. Cao, J. Zhu, L. Fan and X. Li, *Anal. Chem.*, 2014, **86**, 10201-10207.

57. R. Das, S. Parveen, A. Bora and P. K. Giri, *Carbon*, 2020, **160**, 273-286.

58. S. Chandra, P. Patra, S. H. Pathan, S. Roy, S. Mitra, A. Layek, R. Bhar, P. Pramanik and A. Goswami, *J. Mater. Chem. B*, 2013, **1**, 2375-2382.

59. C. J. Reckmeier, Y. Wang, R. Zboril and A. L. Rogach, *J. Phys. Chem. C*, 2016, **120**, 10591-10604.

60. M. Tang, B. Zhu, Y. Wang, H. Wu, F. Chai, F. Qu and Z. Su, *Microchim Acta*, 2019, **186**, 604.

61. S. Chandra, P. Das, S. Bag, D. Laha and P. Pramanik, *Nanoscale*, 2011, **3**, 1533-1540.

62. Y. Li, S. Li, Y. Wang, J. Wang, H. Liu, X. Liu, L. Wang, X. Liu, W. Xue and N. Ma, *Phys. Chem. Chem. Phys.*, 2017, **19**, 11631-11638.

63. Y. Su, M. Zhang, N. Zhou, M. Shao, C. Chi, P. Yuan and C. Zhao, *Microchim Acta*, 2017, **184**, 699-706.

64. M. Wang, Y. Li, J. Fang, C. J. Villa, Y. Xu, S. Hao, J. Li, Y. Liu, C. Wolverton, X. Chen, V. P. Dravid and Y. Lai, *Adv. Energy Mater.*, 2020, **10**, 1902736.

65. Y. Li, H. Lin, C. Luo, Y. Wang, C. Jiang, R. Qi, R. Huang, J. Travas-sejdic and H. Peng, *RSC Adv.*, 2017, **7**, 32225-32228.

66. Y. Ma, A. Y. Chen, Y. Y. Huang, X. He, X. F. Xie, B. He, J. H. Yang and X. Y. Wang, *Carbon*, 2020, **162**, 234-244.

67. T. Li, C. Wu, M. Yang, B. Li, X. Yan, X. Zhu, H. Yu, M. Hu and J. Yang, *Langmuir*, 2022, **38**, 2287-2293.

68. X. Shan, L. Chai, J. Ma, Z. Qian, J. Chen and H. Feng, *Analyst*, 2014, **139**, 2322-2325.

69. L. Zhang, Z.-Y. Zhang, R.-P. Liang, Y.-H. Li and J.-D. Qiu, *Anal. Chem.*, 2014, **86**, 4423-4430.

70. R. Guo, S. Zhou, Y. Li, X. Li, L. Fan and N. H. Voelcker, *ACS Appl. Mater. Interfaces*, 2015, **7**, 23958-23966.

71. M. Rong, X. Yang, L. Huang, S. Chi, Y. Zhou, Y. Shen, B. Chen, X. Deng and Z.-Q. Liu, *ACS Appl. Mater. Interfaces*, 2019, **11**, 2336-2343.

72. W. Zhao, Y. Li, S. Yang, Y. Chen, J. Zheng, C. Liu, Z. Qing, J. Li and R. Yang, *Anal. Chem.*, 2016, **88**, 4833-4840.

73. Y. Yan, J. Chen, N. Li, J. Tian, K. Li, J. Jiang, J. Liu, Q. Tian and P. Chen, *ACS Nano*, 2018, **12**, 3523-3532.

74. T. Scharl, A. Ferrer-Ruiz, A. Saura-Sanmartín, L. Rodríguez-Pérez, M. Á. Herranz, N. Martín and D. M. Guldi, *Chem. Commun.*, 2019, **55**, 3223-3226.

75. H. Xie, J. Dong, J. Duan, G. I. N. Waterhouse, J. Hou and S. Ai, *Sens. Actuators B Chem.*, 2018, **259**, 1082-1089.

76. Z. Qu, N. Li, W. Na and X. Su, *Talanta*, 2019, **192**, 61-68.

77. T. G. Novak, J. Kim, S. H. Song, G. H. Jun, H. Kim, M. S. Jeong and S. Jeon, *Small*, 2016, **12**, 994-999.

78. A. Sharma, T. Gadly, A. Gupta, A. Ballal, S. K. Ghosh and M. Kumbhakar, *J. Phys. Chem. Lett.*, 2016, **7**, 3695-3702.

79. S. Khan, A. Gupta, N. C. Verma and C. K. Nandi, *Nano Lett.*, 2015, **15**, 8300-8305.

80. S. Kumar Thiyagarajan, S. Raghupathy, D. Palanivel, K. Raji and P. Ramamurthy, *Phys. Chem. Chem. Phys.*, 2016, **18**, 12065-12073.

81. J. Peng, W. Gao, B. K. Gupta, Z. Liu, R. Romero-Aburto, L. Ge, L. Song, L. B. Alemany, X. Zhan, G. Gao, S. A. Vithayathil, B. A. Kaipparettu, A. A. Marti, T. Hayashi, J.-J. Zhu and P. M. Ajayan, *Nano Lett.*, 2012, **12**, 844-849.

82. K. Mishra, S. Koley and S. Ghosh, *J. Phys. Chem. Lett.*, 2019, **10**, 335-345.

83. D. Gao, H. Zhao, X. Chen and H. Fan, *Mater. Today Chem.*, 2018, **9**, 103-113.

84. H. Ding, S.-B. Yu, J.-S. Wei and H.-M. Xiong, *ACS Nano*, 2016, **10**, 484-491.

85. H. Wang, C. Sun, X. Chen, Y. Zhang, V. L. Colvin, Q. Rice, J. Seo, S. Feng, S. Wang and W. W. Yu, *Nanoscale*, 2017, **9**, 1909-1915.

86. V. Hinterberger, C. Damm, P. Haines, D. M. Guldi and W. Peukert, *Nanoscale*, 2019, **11**, 8464-8474.

87. Y. Zheng, K. Arkin, J. Hao, S. Zhang, W. Guan, L. Wang, Y. Guo and Q. Shang, *Adv. Opt. Mater.*, 2021, **9**, 2100688.

88. M. Shamsipur, A. Barati, A. A. Taherpour and M. Jamshidi, *J. Phys. Chem. Lett.*, 2018, **9**, 4189-4198.

89. J.-R. Macairan, T. V. de Medeiros, M. Gazzetto, F. Yarur Villanueva, A. Cannizzo and R. Naccache, *J. Colloid. Interf. Sci.*, 2022, **606**, 67-76.

90. L. Cao, X. Wang, M. J. Meziani, F. Lu, H. Wang, P. G. Luo, Y. Lin, B. A. Harruff, L. M. Veca, D. Murray, S.-Y. Xie and Y.-P. Sun, *J. Am. Chem. Soc.*, 2007, **129**, 11318-11319.

91. S. Zhu, J. Zhang, S. Tang, C. Qiao, L. Wang, H. Wang, X. Liu, B. Li, Y. Li, W. Yu, X. Wang, H. Sun and B. Yang, *Adv. Funct. Mater.*, 2012, **22**, 4732-4740.

92. Y. Song, S. Zhu and B. Yang, *RSC Adv.*, 2014, **4**, 27184-27200.

93. in *Principles of Fluorescence Spectroscopy*, ed. J. R. Lakowicz, Springer US, Boston, MA, 2006, DOI: 10.1007/978-0-387-46312-4_2, pp. 27-61.

94. L. K. Fraiji, D. M. Hayes and T. C. Werner, *J. Chem. Educ.*, 1992, **69**, 424.

95. M. S. Meaney and V. L. McGuffin, *Anal. Chim. Acta*, 2008, **610**, 57-67.

96. B. Valeur and M. N. Berberan-Santos, *Molecular Fluorescence: Principles and Applications*, Wiley, 2012.

97. S. Chen, Y.-L. Yu and J.-H. Wang, *Anal. Chim. Acta*, 2018, **999**, 13-26.

98. T. D. Gauthier, E. C. Shane, W. F. Guerin, W. R. Seitz and C. L. Grant, *Environ. Sci. Technol.*, 1986, **20**, 1162-1166.

99. X. Sun, Y. Wang and Y. Lei, *Chem. Soc. Rev.*, 2015, **44**, 8019-8061.

100. S. W. Thomas, G. D. Joly and T. M. Swager, *Chem. Rev.*, 2007, **107**, 1339-1386.

101. F. G. Banica, *Chemical Sensors and Biosensors: Fundamentals and Applications*, Wiley, 2012.

102. M. Liu, Y. Xu, F. Niu, J. J. Gooding and J. Liu, *Analyst*, 2016, **141**, 2657-2664.

103. F. Niu, Y. Xu, M. Liu, J. Sun, P. Guo and J. Liu, *Nanoscale*, 2016, **8**, 5470-5477.

104. J. Shangguan, J. Huang, D. He, X. He, K. Wang, R. Ye, X. Yang, T. Qing and J. Tang, *Anal. Chem.*, 2017, **89**, 7477-7484.

105. H. Lu, S. Xu and J. Liu, *ACS Sens.*, 2019, **4**, 1917-1924.

106. A. Gupta, A. Chaudhary, P. Mehta, C. Dwivedi, S. Khan, N. C. Verma and C. K. Nandi, *Chem. Commun.*, 2015, **51**, 10750-10753.

107. Y. H. Yuan, R. S. Li, Q. Wang, Z. L. Wu, J. Wang, H. Liu and C. Z. Huang, *Nanoscale*, 2015, **7**, 16841-16847.

108. S. Yang, J. Sun, X. Li, W. Zhou, Z. Wang, P. He, G. Ding, X. Xie, Z. Kang and M. Jiang, *J. Mater. Chem. A*, 2014, **2**, 8660-8667.

109. Y. Wang, C. Zhang, X. Chen, B. Yang, L. Yang, C. Jiang and Z. Zhang, *Nanoscale*, 2016, **8**, 5977-5984.

110. L. Fang, L. Zhang, Z. Chen, C. Zhu, J. Liu and J. Zheng, *Mater. Lett.*, 2017, **191**, 1-4.

111. Y. Meng, Y. Jiao, Y. Zhang, Y. Li, Y. Gao, W. Lu, Y. Liu, S. Shuang and C. Dong, *Talanta*, 2020, **210**, 120653.

112. H. Rao, W. Liu, K. He, S. Zhao, Z. Lu, S. Zhang, M. Sun, P. Zou, X. Wang, Q. Zhao, Y. Wang and T. Liu, *ACS Sustain. Chem. Eng.*, 2020, **8**, 8857-8867.

113. S. Rajendran, D. V. Ramanaiah, S. Kundu and S. K. Bhunia, *ACS Appl. Nano Mater.*, 2021, **4**, 10931-10942.

114. S. Pathan, M. Jalal, S. Prasad and S. Bose, *J. Mater. Chem. A*, 2019, **7**, 8510-8520.

115. Z. Zhang, W. Sun and P. Wu, *ACS Sustain. Chem. Eng.*, 2015, **3**, 1412-1418.

116. Z. Zhang, Y. Shi, Y. Pan, X. Cheng, L. Zhang, J. Chen, M.-J. Li and C. Yi, *J. Mater. Chem. B*, 2014, **2**, 5020-5027.

117. J. Gu, D. Hu, W. Wang, Q. Zhang, Z. Meng, X. Jia and K. Xi, *Biosens. Bioelectron.*, 2015, **68**, 27-33.

118. Z. Wu, H. Yang, S. Pan, H. Liu and X. Hu, *ACS Sens.*, 2020, **5**, 2211-2220.

119. R. Jiang, Y. Zhang, Q. Zhang, L. Li and L. Yang, *ACS Appl. Nano Mater.*, 2021, **4**, 9760-9767.

120. Y. Dong, R. Wang, W. Tian, Y. Chi and G. Chen, *RSC Adv.*, 2014, **4**, 3701-3705.

121. M. Zhang, R. Su, J. Zhong, L. Fei, W. Cai, Q. Guan, W. Li, N. Li, Y. Chen, L. Cai and Q. Xu, *Nano Res.*, 2019, **12**, 815-821.

122. D. Kurniawan, B. A. Anjali, O. Setiawan, K. K. Ostrikov, Y. G. Chung and W.-H. Chiang, *ACS Appl. Mater. Interfaces*, 2022, **14**, 1670-1683.

123. X. Ye, Y. Xiang, Q. Wang, Z. Li and Z. Liu, *Small*, 2019, **15**, 1901673.

124. W. He, W. Weng, X. Sun, Y. Pan, X. Chen, B. Liu and J. Shen, *ACS Appl. Nano Mater.*, 2020, **3**, 7420-7427.

125. L. Bao and S. Liu, *Spectrochim. Acta A Mol. Biomol. Spectrosc.*, 2022, **267**, 120513.

126. N. Sohal, B. Maity and S. Basu, *ACS Appl. Nano Mater.*, 2020, **3**, 5955-5964.

127. X. Yang, F. Cui, R. Ren, J. Sun, J. Ji, F. Pi, Y. Zhang and X. Sun, *ACS Omega*, 2019, **4**, 12575-12583.

128. R. S. Li, J. Liu, Y. Yan, C. Su, T. Lai, Y. Liao, Y. F. Li, N. Li and C. Z. Huang, *Anal. Chem.*, 2021, **93**, 11878-11886.

129. H. Zhao, X. Yuan, X. Yang, F. Bai, C. Mao and L. Zhao, *Inorg. Chem.*, 2021, **60**, 15485-15496.

130. J. Yang, Z. Huang, Y. Hu, J. Ge, J. Li and Z. Li, *New J. Chem.*, 2018, **42**, 15121-15126.

131. S. Pramanik, S. Chatterjee, G. Suresh Kumar and P. Sujatha Devi, *Phys. Chem. Chem. Phys.*, 2018, **20**, 20476-20488.

132. D. Wu, B. L. Li, Q. Zhao, Q. Liu, D. Wang, B. He, Z. Wei, D. T. Leong, G. Wang and H. Qian, *Small*, 2020, **16**, 1906975.

133. P. K. Pandey, Preeti, K. Rawat, T. Prasad and H. B. Bohidar, *J. Mater. Chem. B*, 2020, **8**, 1277-1289.

134. X.-Y. Dong, X.-Q. Niu, Z.-Y. Zhang, J.-S. Wei and H.-M. Xiong, *ACS Appl. Mater. Interfaces*, 2020, **12**, 29549-29555.

135. L. Qian, Z. Zhen, S. Tang, C. Zhou, M. Ji, B. Liu, Y. Fang, S. Ou and R. Cheng, *Sens. Actuators B Chem.*, 2022, **367**, 132168.

136. A. Kathiravan, A. Gowri, V. Srinivasan, T. A. Smith, M. Ashokkumar and M. Asha Jhonsi, *Analyst*, 2020, **145**, 4532-4539.

137. L. Cai, Z. Zhang, H. Xiao, S. Chen and J. Fu, *RSC Adv.*, 2019, **9**, 41383-41391.

138. Q. Chen, Y. Sun, S. Liu, J. Zhang, C. Zhang, H. Jiang, X. Han, L. He, S. Wang and K. Zhang, *Sens. Actuators B Chem.*, 2021, **344**, 130278.

139. Y. Xu, H. Yu, L. Chudal, N. K. Pandey, E. H. Amador, B. Bui, L. Wang, X. Ma, S. Deng, X. Zhu, S. Wang and W. Chen, *Mater. Today Phys.*, 2021, **17**, 100328.

140. Y. Hu, Z. Gao and J. Luo, *Food Chem.*, 2021, **335**, 127677.

141. W.-K. Li, J.-T. Feng and Z.-Q. Ma, *Carbon*, 2020, **161**, 685-693.

142. P. K. Yadav, V. K. Singh, S. Chandra, D. Bano, V. Kumar, M. Talat and S. H. Hasan, *ACS Biomater. Sci. Eng.*, 2019, **5**, 623-632.

143. M. Ö. Alaş and R. Genç, *ACS Appl. Nano Mater.*, 2021, **4**, 7974-7987.

144. C. Yao, Y. Xu and Z. Xia, *J. Mater. Chem. C*, 2018, **6**, 4396-4399.

145. Y. Liu, H. Yang, C. Ma, S. Luo, M. Xu, Z. Wu, W. Li and S. Liu, *ACS Appl. Mater. Interfaces*, 2020, **12**, 36628-36638.

146. Z. Shen, C. Zhang, X. Yu, J. Li, Z. Wang, Z. Zhang and B. Liu, *J. Mater. Chem. C*, 2018, **6**, 9636-9641.

147. S. Mandal, S. R. Prasad, D. Mandal and P. Das, *ACS Appl. Mater. Interfaces*, 2019, **11**, 33273-33284.

148. S.-T. Yang, L. Cao, P. G. Luo, F. Lu, X. Wang, H. Wang, M. J. Meziani, Y. Liu, G. Qi and Y.-P. Sun, *J. Am. Chem. Soc.*, 2009, **131**, 11308-11309.

149. X. Geng, Y. Sun, Z. Li, R. Yang, Y. Zhao, Y. Guo, J. Xu, F. Li, Y. Wang, S. Lu and L. Qu, *Small*, 2019, **15**, 1901517.

150. H. Liu, Y. Sun, Z. Li, J. Yang, A. A. Aryee, L. Qu, D. Du and Y. Lin, *Nanoscale*, 2019, **11**, 8458-8463.

151. W. Pang, P. Jiang, S. Ding, Z. Bao, N. Wang, H. Wang, J. Qu, D. Wang, B. Gu and X. Wei, *Adv. Healthc. Mater.*, 2020, **9**, 2000607.

152. Z. Zhang, Y. Lei, X. Yang, N. Shi, L. Geng, S. Wang, J. Zhang and S. Shi, *J. Mater. Chem. B*, 2019, **7**, 2130-2137.

153. S. Li, W. Su, H. Wu, T. Yuan, C. Yuan, J. Liu, G. Deng, X. Gao, Z. Chen, Y. Bao, F. Yuan, S. Zhou, H. Tan, Y. Li, X. Li, L. Fan, J. Zhu, A. T. Chen, F. Liu, Y. Zhou, M. Li, X. Zhai and J. Zhou, *Nat. Biomed. Eng*, 2020, **4**, 704-716.

154. S.-Y. Sung, Y.-L. Su, W. Cheng, P.-F. Hu, C.-S. Chiang, W.-T. Chen and S.-H. Hu, *Nano Lett.*, 2019, **19**, 69-81.

155. K. Silambarasan, S. Harish, K. Hara, J. Archana and M. Navaneethan, *Carbon*, 2021, **181**, 107-117.

156. T. A. Geleta and T. Imae, *ACS Appl. Nano Mater.*, 2021, **4**, 236-249.

157. H. Tang, T. Xu, X. Qin, K. Zou, S. Lv, J. Fan, T. Huang, L. Chen and W. Huang, *ACS Appl. Nano Mater.*, 2021, **4**, 13339-13351.

158. J. Zhang, T. Tong, L. Zhang, X. kLi, H. Zou and J. Yu, *ACS Sustain. Chem. Eng.*, 2018, **6**, 8631-8640.

159. H. Li, R. Liu, S. Lian, Y. Liu, H. Huang and Z. Kang, *Nanoscale*, 2013, **5**, 3289-3297.

160. N. Muhamad Sarih, P. Myers, A. Slater, B. Slater, Z. Abdullah, H. A. Tajuddin and S. Maher, *Sci. Rep.*, 2019, **9**, 11834.

n,161. M. Chen, C. Liu, Y. An, Y. Li, Y. Zheng, H. Tian, R. Shi, X. He and X. Lin, *Nanoscale Adv.*, 2022, **4**, 14-18.

CHAPTER 2

Materials, Methods, and Instrumentation

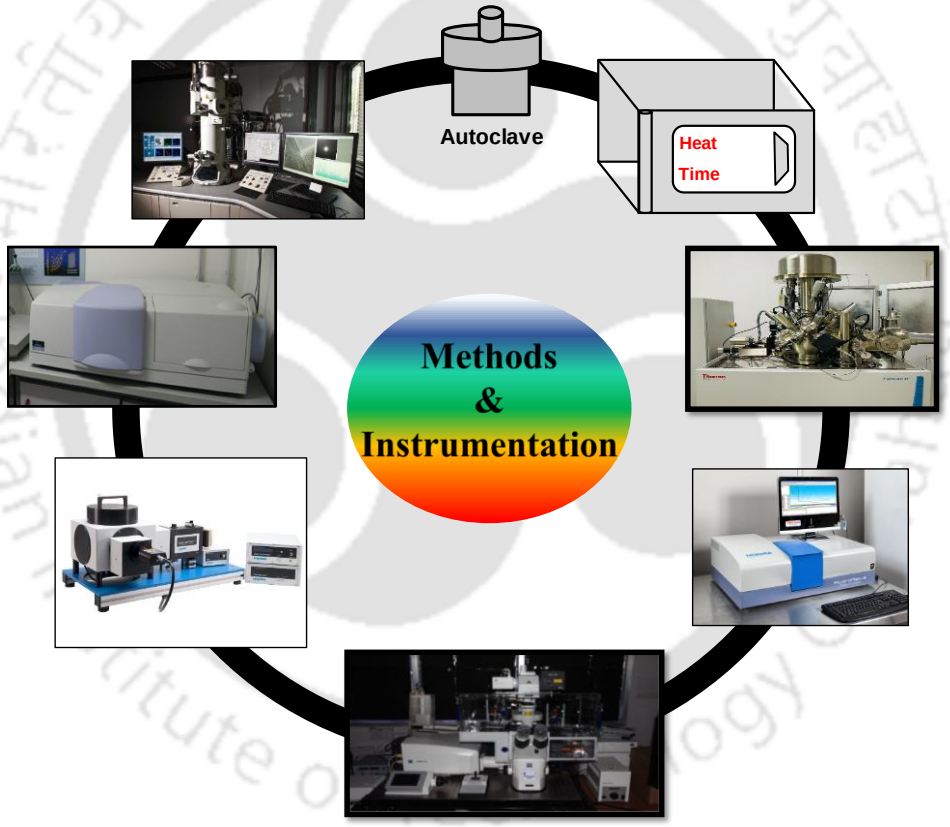

[This page was intentionally left blank]

2.1 Overview

In this chapter, we have thoroughly focused on the material used and synthesis technique for the preparation of CD and GQD. Additionally, the instrumentation specifications for characterizing the novel nano-fluorescent material are completely described. The surface and morphological analysis are performed by transmission electron microscope (TEM), atomic fluorescent microscope (AFM), X-ray photoelectron spectroscopy (XPS), Raman spectroscopy, Fourier transformed infrared spectroscopy (FTIR), and powder X-ray diffraction (p-XRD). For spectrofluorometric characterization, UV-visible absorption (UV), steady-state fluorescence, and time-correlated single photon counting (TCSPC) are used. Lastly, the confocal laser scanning microscope (CLSM) is used for biological purpose.

2.2 Materials and Synthetic Procedures

Graphite flake, 2-aminopyridine (2AP), 2,6-diaminopyridine (DAP), 3,6-diaminoacridine hydrochloride, L-ascorbic acid, L-aspartic acid, vitamin B12, vitamin B1, vitamin B3, vitamin B5, vitamin B6, vitamin B7, vitamin B9, vitamin B12, bilirubin, haemoglobin, human serum albumin, bovine serum albumin, creatinine, lysine, histidine, threonine, dopamine, urea, glutathione, cysteine, 5-aminoisopthalic acid, 3,5-diaminobenzoic acid 3,4-diaminobenzoic acid, dialysis kits (MWCO 1000 Da), PBS tablet, Tris(hydroxymethyl)aminomethane hydrochloride, and metal salts (Cr^{3+}, Mn^{2+}, Fe^{3+}, Co^{2+}, Ni^{2+}, Cu^{2+}, Zn^{2+}, Hg^{2+}, Pb^{2+}, Cd^{2+}, Al^{3+}, Li^{+}, Na^{+}, K^{+} Fe^{2+}, SCN^{-}, PO_4^{3-}, $S_2O_8^{2-}$, and CN^{-}) were purchased from Sigma-Aldrich Chemicals. 1-ethyl-3-(3-(dimethylamino)propyl) carbodiimide (EDC), N-Hydroxysuccinimide (NHS), $NaClO{\cdot}5H_2O$, glucose, sucrose, hydrazine hydrate were bought from Alfa Aesar. The absolute ethanol, other solvents (DMSO, DMF, THF, and acetonitrile) concentrated H_2SO_4, and HNO_3 were received from Merck and used without any kind of purification. The aqueous solution was prepared using Mili-Q deionized water (18.2 $M\Omega^{-cm}$).

2.2.1. Preparation of functionalized GQD

For ***chapter 3***, GQDs were produced from non-emissive graphite flakes (GF) considering an earlier reported literature.[1] Briefly, the GF were poured into the mixture of concentrated acid (HNO_3:H_2SO_4: = 1:3) and sonicated for 2 h. Then the mixture was heated at 120 °C

for 24 h. After naturally cooling down to normal temperature, the full solution was neutralized by adding an appropriate amount of NaOH solution in a dropwise manner with continuous checking the pH of the medium. Then the solution was filtered by 0.22 μm PTFE membrane and dialyzed (using MWCO 1000 Da) against water (1L). After lyophilisation, a brownish solid GQD powder was obtained.

For edge-modified GQDs (F-GQD) preparation, simple carbodiimide chemistry is followed. In 2 mg/mL aqueous solution of GQD, 10 mM EDC and 10 mM NHS was added and vigorously stirred 30 min for the activation of carboxylic acid groups present at the GQD edges. After that, DAP solution (10 equivalents with respect to GQD) was added into the activated GQD solution in a dropwise manner. The total mixture was simply stirred for 2 days and purified by adopting dialysis methods. The powder F-GQD sample was achieved by lyophilising the solutions. The same synthetic process was followed by the synthesis of 2AP-GQDs where instead of DAP, 2AP was used for edge functionalization.

2.2.2. Preparation of N-doped carbon dots (NCDs)

For the preparation of novel NCD in ***chapter 4***, L-aspartic acid and 3,6-diaminoacridine hydrochloride were preferred for the starting precursors where the molar ratio was maintained at 1000:1 (L-aspartic acid; 3,6-diaminoacridine hydrochloride). In this molar ratio of precursors were dissolved into 50 mL of absolute ethanol and placed in sonication for 1 h followed by 30 min continuous stirring to produce a well homogeneous mixture. The homogeneous solution was then moved into the Teflon-lined autoclave and transferred in a hydrothermal oven at diverse temperatures ranging from 150 to 180 °C with variable reaction times from 2 to 6 h. After cooling, the NCDs solutions were filtered with a 0.22 μm poly(tetrafluoroethylene) (PTFE) membrane to remove unwanted by-products. Then, each NCD solution was further dialyzed (MWCO 1000 Da) for 5 days and finally dried the solution at 50 °C. On the basis of fluorescence emission intensity, it was found that the maximum emission signal was noticed for the NCDs prepared at 170 °C and 5 h reaction time.

2.2.3. Synthesis Procedure of two different emissive NCDs

In this ***chapter 5***, two different types of NCDs were demonstrated i.e., NCD-1 and NCD-2 which were synthesized by considering two different starting materials i.e., 5-aminoisopthalic acid and 3,5-diaminobenzoicacid, respectively. Each of the precursors was

separately dissolved into 15 ml absolute ethanol followed by 30 min stirring and 1h sonication process. The whole solution was shifted into a Teflon-lined autoclave inner vessel and placed in an oven at 160 °C for 12 hours. All the resultant NCDs solution was naturally cooled to room temperature and then filtered (0.22 μm PTFE membrane) to eliminate any large particles. After that, each NCD solution was poured into a dialysis tube (MWCO 1000Da) for 3 days. Lastly, the solid purified product was gained after drying at 50 °C.

2.2.4 Synthesis of triple mode excitation-emission NCDs

Herein, in ***chapter 6*** the NCDs were also prepared by accepting eco-friendly, cost-effective hydrothermal techniques. In the 20 ml of absolute ethanol, 3,5-diaminobenzoic acid (100 mg) was poured and placed in ultra-sonication for 1 hour. Then, dropwise hydrazine hydrate (100 μL) was added to the above mixture with continuous stirring. Afterward, the full reactant mixtures were poured into an autoclave vessel and placed in an oven with a temperature 170°C for 5 h. After finishing the reaction, the autoclave cooled to normal temperature and the purified the full solution by following three procedures in a step-wise manner (1) centrifugation (10000 rpm for 15 min), (2) fitration (0.22 μm membrane filter) and (3) dialysis (MWCO 1000 Da). Ultimately, the clear brown color solid product of NCDs was achieved via freeze-drying.

Here also, the same preparation technique was also followed for the preparation of CD_{Blank} where only 3,5-diaminobenzoic acid was considered as a starting precursor.

2.2.5. Synthesis of dual-emitting NCD

The well-known hydrothermal method was also used in ***chapter 7*** for the preparation of bright yellow emissive NCDs. In short, 100 mg of 3,4-diaminobenzoic acid and 100 μL of hydrazine hydrate were firstly poured into absolute ethanol (20 ml) and treated in a sonication method for 30 min. Then, the reactant mixture was heated in an autoclave at 170°C for 5 hours. After cooling the reaction, the complete solution was centrifuged for 15 min at 10000 rpm and dialyzed against deionized water. Next, the filtration technique for more purification. In the end, a dark-brown color solid of yellow emissive NCDs was obtained from freeze-drying.

2.3 Biological Analysis

In ***chapter 3***, cytotoxicity of nanoprobe F-GQD, the MTT (3-(4,5-dimethylthiazol-2-yl)-2,5-diphenyltetrazolium bromide) assay was performed using HeLa (human cervical cancer cell line) cells. The freshly trypsinized cells were seeded in Dulbecco's Modified Eagle Medium (DMEM) with 10% fetal bovine serum in 96-well flat-bottom plates and incubated at 37°C in 5% CO_2 atmosphere. A range of concentrations of F-GQD (50 µg/mL to 400 µg/mL) was accordingly introduced into the culture media and incubated for 24 h. Afterward, 10 µl of MTT solution (stock solution of 50 µM MTT reagent in phosphate buffer saline) was added over the cells. Following an incubation of 4 hours at 37°C, excess MTT solution was discarded, and 100 µl of DMSO (dimethyl sulfoxide) was introduced for dissolving formazan. Finally, the absorbance value was measured at 570 nm by using a microplate reader for cell viability measurement. For the purpose of cell imaging, 1×10^5 HeLa cells were seeded on clean and clear coverslips and incubated overnight at standard conditions (37 °C and 5% CO_2). A 200 µg/ml F-GQDs solution was subsequently introduced into the culture media and incubated for 2 h at the same standard condition. Thereafter, the cells are prudently washed two times with PBS buffer (pH 7) and fixed with 4% formaldehyde before mounting over a glass slide with glycerol. The fluorescence images were captured using a confocal laser scanning microscope (CLSM) with an excitation laser source of wavelength 405 nm. Here the emission range are fixed from 420 to 480 nm

In ***chapter 4***, the method of evolution of cytotoxicity study and cell imaging of nanoprobe NCDs is quite similar to earlier procedure. But there are some differences, here, range of concentration of NCDs (50 µg/mL to 500 µg/mL) were consequently introduced into the culture media and incubated for 24h to discover the cytotoxic behavior. For cell imaging purpose, 200 µg/ml NCDs solution was subsequently introduced into the culture media and incubated for 2h at the same standard condition. The fluorescence images were captured using a confocal laser scanning microscope (CLSM) with an emission range 420 to 470 nm and excitation laser source of 405 nm.

For ***chapter 7***, the cell viability assay using MTT [3-(4,5-dimethylthiazol-2-yl)-2,5-diphenyltetrazolium bromide] was carried out on MCF-7 and HEK-293 cells (normal cell line). Cells were seeded at a density of 5×10^3 per well into a 96-well plate and treated with varying concentrations of NCD for 48 h. The control study was also done with the

concentration of PBS not exceeding 0.1% in the cell culture medium. Following treatment, an MTT assay was performed where the respiratory mitochondrial enzyme in the live cell reduces MTT to an insoluble formazan product which when dissolved in DMSO, can be detected spectro-photometrically at 570 nm with the reference filter at 655 nm. The amount of formazan formed is directly proportional to the number of live cells. The percentage (%) of cell viability was calculated as follows.

$$\frac{(Abs\ 570 - Abs\ 655)\ treated\ cells}{(Abs\ 570 - Abs\ 655)\ control\ cells}\ X\ 100 = \%\ Cell\ viability$$

The inhibitory concentration, and IC_{50} values were determined from the sigmoidal dose-response curves, using the GraphPad Prism. (Version 6.0.0 for Windows, GraphPad Software, San Diego, California USA, www.graphpad.com). The MCF-7 was treated with three different pH solutions (3, 5.5, and 7), and a 450 µg/ml NCD compound was used for cell imaging. For Fe^{3+}, 200 µM solution was added to the NCD-treated MCF-7 cell line, and check the images under Leica DMi 8 confocal microscope at a laser excitation of 405 nm. The uptake study was carried out by treating the MCF-7 cells with NCD at the IC_{50} concentration and incubating for 7 h at 37 °C. The cells were viewed under a Leica DMi 8 confocal microscope at a laser excitation of 405 nm and emission at 490 nm and 570 nm. To analyse the cell surface morphology, the treated and control MCF-7 cells were imaged using FESEM. Cells were treated with the IC_{50} value of NCD. Both treated and untreated cells were incubated at 37 °C for 12 h. Following that, cells were washed using PBS and trypsinized. They were fixed with 4% formaldehyde followed by washing with PBS. The final cell pellet was dispersed in deionized water. To an aluminium foil-covered glass slide, 20 µl of the diluted cells was drop-casted and air-dried overnight, following which images were captured.

2.4 Sensing study

2.4.1. Fluorescence Assay of Pb^{2+} and ClO^- for *chapter 3*

Fluorescence studies were carried out for detection of Pb^{2+} where various concentrations of Pb^{2+} were added to the Phosphate buffer solution (PBS, 10 mM pH 7), containing F-GQD (20 $\mu g \cdot mL^{-1}$). All emission spectra were recorded after mixing of ClO^- in 1 cm × 1 cm quartz cuvette. In PBS buffer, F-GQD has maximum absorbance located at 420 nm and emission maximum was at 470 nm (λ_{ex} = 420 nm).

Fluorescence studies were carried out for detection of ClO^- where various concentrations of ClO^- were added to the Phosphate buffer solution (10 mM PBS buffer, pH 7), containing F-GQD (50 $\mu g \cdot mL^{-1}$). All emission spectra were recorded after mixing of ClO^- in 1 cm × 1 cm quartz cuvette in the dark. In PBS buffer, F-GQD has maximum absorbance located at 420 nm and emission maximum was at 470 nm (λ_{ex} = 420 nm).

2.4.2. Fluorescence Sensing of Bilirubin (BR) for *chapter 4*

Bilirubin is not soluble in an aqueous medium, but it becomes soluble after adding an adequate alkaline solution. Here, 2ml of 1mM of BR stock solution was prepared in PBS buffer, including 5µL of 1M NaOH solution. Fluorescence titration with BR (0 to 92µM) was carried out in low light. For the selectivity experiment, 1mM of analytes was introduced into 2.5ml PBS buffer containing 80µg/ml NCD. Before recording each spectrum, the fluorescence response time of NCD towards BR was measured.

2.4.3. Fluorescence Sensing of VB12 for *chapter 4*

For fluorometric detection of VB12, 2500µL of 80µg/ml NCD PBS solution (pH 7.4, 10mM) was thoroughly mixed with different concentrations of VB12, and the fluorescence spectra were monitored at an excitation wavelength of 360 nm. The emission spectra are recorded at room temperature with 2 min incubation time after each titration. Fluorescence spectra were also measured with various other vitamins, amino acids, and some metal ions to investigate the anti-interference adequacy and selectivity.

2.4.4. Fluorescence assay of Fe^{3+} for *chapter 6*

250 µg/ml NCDs solution was used for performing the fluorescence assay in a Tris-HCl buffer of pH 6. For Fe^{3+} titration, different amounts (in µL) of 1 mM Fe^{3+} stock solution were injected into the 2 ml NCD solution to vary the Fe^{3+} concentration. Similarly, 5 mM AA stock solution was prepared, and different amounts (in µL) of the stock solution were injected into the NCD+Fe^{3+} solution to vary the ascorbic acid concentration. Emission spectra were recorded under 420 nm and 500 nm excitation wavelengths.

2.4.5. Fluorescence assay of of Fe^{3+} for *chapter 7*

100 µg/ml NCDs solution was used for performing the fluorescence assay in a Tris-HCl buffer. For Fe^{3+} titration. Different concentrations of Fe^{3+} solution was inserted into the 2

ml of NCD solution. All emission spectra were recorded under 410 nm excitation wavelength.

2.5 Instrumentation

2.5.1. UV-visible spectroscopy

UV-absorption spectroscopy is one of most beneficial spectroscopic method which can provides valuable evidence about the electronic transition of various functional moieties. During all the experiments, UV-Vis spectra were recorded in Perkin-Elmer Lamda-750 spectrophotometers. The instrument consists of tungsten, deuterium, halogen light source, high sensitivity R928 PMT and double holographic grating monochromator,

2.5.2 Steady-state fluorescence

Jobin Yvon Fluoromax4 is used for recording all the fluorescence spectra of all the synthesized samples. Here is, the high-pressure 150 W xenon (ozone-free) arc lamp is used as a light source. The emission signal is collected by placing the cuvette at a 90^{o} angle with respect to the incident beam and the emitted signal is identified through a monochromator by an R928P photomultiplier (PMT).

2.5.3. Quantum yield

Quantum yield (QY) can be described as the ratio of the number of emitted photons and the number of absorbed photons.

$$\phi_f = \frac{\text{Number of photons emitted}}{\text{Number of photons absorbed}}$$

QY of the synthesized nano-fluorescent material was taken in a relative manner with the following formula.

$$QY = (I/I_R) \times (A_R/A) \times \eta^2/(\eta_R^2) \times QY_R \text{---- (1)}$$

Here QY is the calculated quantum yield of synthesized material. I and I_R are integrated emission intensities of nanomaterials and the references, respectively. η is the refractive index of the solvent used. A_R and A is the optical density at the excitation wavelength of the reference and the quantum dots. QY_R is the reference quantum yield. While measuring the QY, the absorbance was always kept below 0.1 at the excitation wavelength.

For *Chapter 3*, rhodamine-6G in ethanol (Q= 95%), and *chapter 4 to chapter 6*, quinine sulfate was used (QY = 54.4% in 0.1 M H_2SO_4). In *chapter 7*, rhodamine-6G was used as a reference (Q = 95% in ethanol).

2.5.4. Time correlated single photon counting (TCSPC)

The fluorescence lifetime of all newly developed materials is measured by a time-correlated single-photon-counting (TCSPC) instrument which has a broad time resolution range from picoseconds to nanosecond scale. In ***chapter 3***, ***chapter 4***, and ***chapter 5*** DeltaDiode-375L pulsed laser is used. The full width at half-maximum (FWHM) of these setups was typically ~100 ps measured using a liquid scatter. DeltaDiode-290, DeltaDiode-405 and DeltaDiode-515 are used in ***chapter 6***. In the ***chapter 7*** only DeltaDiode-405 is used to record the emission decay. All the decay curves are fitted into tri-exponential functions

$$I(t) = A_1 e^{(-t/\tau_1)} + A_2 e^{(-t/\tau_2)} + A_3 e^{(-t/\tau_3)}$$

Where τ_i is the decay time of components and A_i is the corresponding contribution.

The average lifetime is calculated in every chapter by the following formula.

$$\tau_{average} = A_1\tau_1 + A_2\tau_2 + A_3\tau_3$$

2.5.5. Field Emission Transmission electron microscope (FETEM)

To know the formation of quantum dots, TEM measurement is a very powerful technique which is accomplished by a JEOL JEM 2100 electron microscope with an operating voltage of 200 kV. Every TEM sample was prepared by drop-casting a very diluted solution of CDs to a copper grid and allowing it to dry in a cleaned desiccator. For analyzing the size of the samples and calculation of 'd' spacing, Image-J software, and Gatan software are used, respectively.

2.5.6. Fourier transformed infrared spectroscopy (FTIR)

The FTIR spectra of all samples are recorded in attenuated total reflectance or ATR mode with a scanning range from 4000 to 400 cm^{-1} with an average of 4 scans. Here, all the solid samples are placed into the incident IR-light chamber followed by applying the force gauge 45 and recording the spectra. Here, the sample is directly in contact with the incident IR beam which is very advantageous for detecting functional groups.

2.5.7. Atomic fluorescence microscopy (AFM)

The roughness and surface area were thoroughly analyzed by AFM characterization. Here, The AFM images of ***chapter 3***, ***chapter 6***, and ***chapter 7*** were taken by the asylum cypher oxford instrument.

2.5.8. X-ray photoelectron spectroscopy (XPS)

XPS is the most useful method for quantum dot-based nanomaterials for anticipating chemical bonding via analyzing the binding energy values. In this thesis, all XPS characterization was done by ESCALAB Xi+ (Thermo Fisher Scientific Pvt. Ltd., UK) photoelectron spectrometer. For full range XPS measurement the pass energy 200.00 eV and for high resolution XPS analysis pass energy was 50.00 eV. For the XPS deconvoluting, XPSPEAK4.1 software was used.

2.5.9. Powder X-ray diffraction (p-XRD)

The amorphous nature of synthesized quantum dots (***chapter 3, chapter 4,*** and ***chapter 6***) was identified by Bruker D2 PHASER X-ray diffractometer with the generation of Cu¬Kα (λ = 1.54 Å) with a 9-kW power. The spacing (d) is calculated using the following formula

$$n\lambda = 2d\sin\theta$$

Here d, θ, and λ are is the spacing between diffracting planes, the incident angle, and the wavelength of the beam, respectively. The 'n' is the integer.

2.5.10. Raman Analysis

Raman spectroscopy is a commendable technique to study carbon-based dots. This analysis can also be helpful for the prediction of some functional groups. All the Raman spectra of the as-prepared materials (***chapter 3, chapter 4,*** and ***chapter 5***) were recorded in the Horiba Jobin Vyon Micro Raman System (Model-LabRam HR) with the excitation laser source of 488 nm.

2.5.11. Field emission scanning electron microscope (FESEM)

For ***chapter 7***, the FESEM of the biological sample was investigated by Zeiss (model-Sigma 300) instrument with an operating voltage at 5 kV.

2.5.12. Confocal laser scanning microscope

For confocal analysis, two different kind of instrument was used. For ***chapter 3*** and ***chapter 4***, the cell images are collected by using Zeiss, LSM 880 instrument. The Leica DMi 8 instrument was used in ***chapter 7*** for the cell imaging study.

Reference

1. R. Sekiya, Y. Uemura, H. Murakami and T. Haino, *Angew. Chem., Int. Ed.*, 2014, **53**, 5619-5623.

[This page was intentionally left blank]

CHAPTER 3

Hit Multiple Targets with One Arrow: Pb^{2+} and ClO^- Detection by Edge Functionalized Graphene Quantum Dot and Its Applications in Living Cells

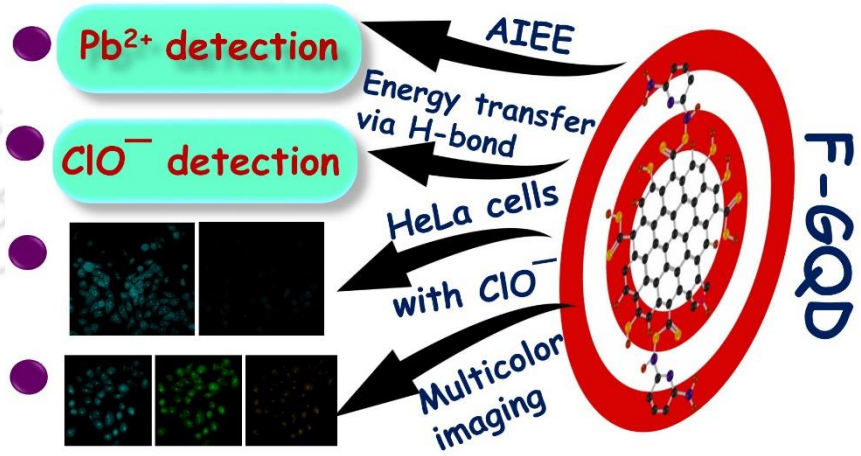

Manuscript: Nilanjana Nandi, Shubham Gaurav, Priyanka Sarkar, Sachin Kumar, Kalyanasis Sahu, "Hit Multiple Targets with One Arrow: Pb^{2+} and ClO^- Detection by Edge Functionalized Graphene Quantum Dots and Their Applications in Living Cells" *ACS Appl. Bio Mater*. 2021, **4**, 10, 7605–7614

[This page was intentionally left blank]

Abstract

Recently, multimodal detection of analytes through a single nanoprobe has become an eminent approach for researchers. Herein a fluorescent nanoprobe, functionalized-GQDs (F-GQD), has been designed through edge functionalization of GQDs by 2,6-diaminopyridine molecules. The fluorescence of F-GQD is quite sensitive to the pH, making it a suitable pH sensor within the pH range 2–6. Interestingly, F-GQD shows dual sensing of Pb^{2+} and ClO^- via entirely dissimilar pathways; Pb^{2+} exhibits fluorescence turn-on performance while ClO^- triggers turn-off fluorescence quenching. The emission enhancement of F-GQD may originate from the Pb^{2+}-induced aggregation of the nanodots. For ClO^-, the detailed mechanistic investigations reveal that both dynamic and static quenching effects simultaneously operate together. The dynamic quenching was attributed to the energy migration from F-GQD to ClO^- through hydrogen bonding interaction (static quenching) between the amine group at the F-GQD surface and ClO–. The limit of detection (LOD) was also impressive, 1.2 μM and 12.6 nM for Pb^{2+} and ClO^-, respectively. Moreover, the F-GQDs also serve as multicolor fluorescent probes for cell imaging; the nanoprobe can easily permeate the cell membrane and successfully detect intracellular ClO^- .

2.1 Overview

The heavy metal lead ion is a crucial environmental pollutant with an extreme carcinogenic effect on human health via complexation with multiple heteroatomic groups like, oxygen, sulfur, and nitrogen groups present in various bio-ligands[1, 2]. The complexation can break the hydrogen bond of proteins which accelerates the damage of numerous tissues and inhibits their work-functions[3]. Several endogenous pathways and oxidative stress are responsible for generating reactive oxygen species (ROS)[4-6]. Any abnormality of the ROS level can cause several diseases like arthritis, cardiovascular irregularity, degeneration of neurons, stress production, chronic inflammation, cell membrane, and DNA damage[7]. During cellular homeostasis, various oxygen-containing ROS, e.g., hydroxyl radical ($^{\cdot}OH$), singlet oxygen ($^1O_2$), hypochlorite (ClO^-), and superoxide anion ($O_2^{\cdot-}$) are generated[8]. Among these, hypochlorite (ClO^-) is a powerful oxidizer that has been applied extensively in various industrial processes such as deodorization and disinfection of water, bleaching, sanitizing, etc[9, 10]. High consumption of hypochlorite can produce an extremely poisonous side product, trihalomethane[11], which causes numerous diseases like infertility, renal disease, etc[12]. Endogenic ClO^- is produced by a catalytic reaction between chloride ions (Cl^-) and hydrogen peroxide (H_2O_2) catalysed by myeloperoxidase (MPO)[13]. Therefore, it is essential to develop a sensitive and selective sensor for monitoring the level of ClO^- in water and its uptake level in living cells.
Significant advancements have been achieved for Pb^{2+} and ClO^- detection through various techniques, such as atomic absorption[14] and emission spectroscopy[15], electrochemical[16], chemiluminescence[17], and chromatography[18]. However, fluorescence-based methods deliver the most promising results in several organisms with extraordinary sensitivity and selectivity. So far, many fluorescent sensors have been reported for Pb^{2+}, and ClO^- recognition, including organic fluorophores, rare earth metal co-ordinate complexes[19], metal-organic frameworks[20], and nanoclusters[21]. However, these materials need a vigorous time-consuming synthesis technique and cannot effectively penetrates into cell. Thus, it is imperative to develop a fluorescence-based nanosensor for recognition of Pb^{2+} and ClO^- with excellent sensitivity and low cytotoxicity.

Graphene quantum dots (GQDs) are the most suitable materials due to facile synthesis, inexpensive precursors, large surface area, outstanding solubility, and biocompatibility[22, 23]. Recently, functionalized GQDs, with improved photophysical and chemical properties,

have attracted considerable attention.[24, 25] Kwon et al. reported red, orange, and green-emitting GQDs by effectively functionalizing the surface groups by 4-methoxythioaniline, 4-methoxyaniline, and 6-aminoquinoline.[26] Tetsuka et al. synthesized various nitrogen-functionalized GQDs to tailor the energy levels and emission colour for optoelectronic devices[27]. Moreover, sulphur-doped GQD was reported for the detection of Pb^{2+} via fluorescence quenching mechanism[28]. The surface of GQD modified by coupling with o-phenylenediamine (o-PD) was successfully applied for the detection of ClO^-. The ClO^- first oxidizes the aromatic amine promoting an effectual photo-induced electron transfer (PET) from the excited-state of GQDs to the oxidized form of o-PD [29].

In this work, we adopt a two-step synthesis approach to develop a novel bluish-green emissive fluorescent nanoprobe F-GQD, where the edge of GQD is successfully functionalized by 2, 6-diaminopyridine moiety via a facile coupling reaction. This edge-modification plays an essential role in enhancing quantum yield, improving heterogeneity, controlling bandgap, physical-chemical characteristics, and pH regulation. This functionalization allowed F-GQD to become a very superior nanoprobe for detection of Pb (II) and ClO^- through aggregation-induced emission enhancement (AIEE) and H-bonding induced energy transfer (ET). The role of the amine group was further elucidated by examining the sensing behaviour of 2-aminopyridine functionalized GQD (2AP-GQD). Furthermore, F-GQD was applied for HeLa cell imaging, where the nanoprobe exhibits negligible toxicity and multicolour emission depending on the excitation wavelength. Moreover, the exogenic ClO^- was also well recognized by F-GQD in HeLa cells.

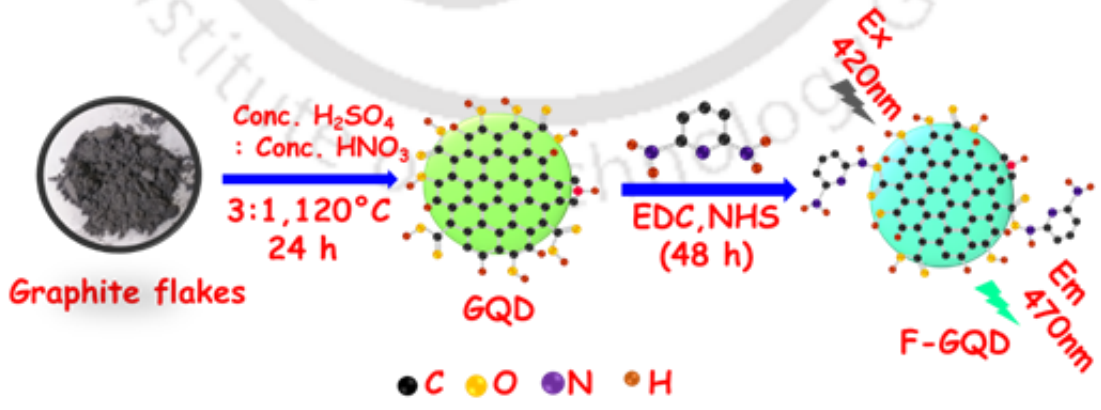

Scheme 3.1. The schematics of the synthesis procedure of F-GQD.

3.2. Results and Discussions

3.2.1 Characterization of F-GQD

Scheme 3.1 denotes the synthesis methodology of the target F-GQD nanoprobe, and details are supplied in the supporting information. Morphological characterization and surface functionality of F-GQD were investigated extensively using various analytical techniques such as transmission electron microscope (TEM), X-ray photoelectron spectroscopy (XPS), powder X-ray diffraction (pXRD), and Fourier-transformed infrared spectroscopy (FTIR). The TEM images of F-GQD show well dispersed, spherical particles without any agglomeration (**Figure 3.1a**). The lateral size of synthesized nanomaterial was 2.9 ± 0.2 nm, which is quite bigger than the bare GQD (1.5±0.4 nm) (**Figure 3.1b**). The high-resolution TEM (HRTEM) image reveals the interplanar distance of F-GQD is 0.24 nm (**inset of Figure 3.1a**), indicating (1120) amorphous graphitic lattice fringes[30]. The functionalization was further confirmed by FTIR analysis. A broad spectral range from 3360 cm^{-1} to 3200 cm^{-1} indicates the existence of –OH/–NH_2 functionality (**Figure 3.1c**). In contrast to GQD, some new peaks emerge at 1608 cm^{-1}, 1554 cm^{-1}, 1494 $cm^{-1,}$ and 1343 cm^{-1} relating to the stretching vibrations of the amide linkage, N-H bending, aromatic C-N stretching, and single bond (C-N)[31, 32] stretching vibrations, respectively. Furthermore, the Raman spectrum of F-GQD exhibits two sharp peaks at 1364 cm^{-1} and 1572 cm^{-1}, symbolized as D and G bands, respectively, which account for the structural defects of sp^2 carbon material and C=C in-plane phonon vibration (**Figure 3.1d**). The observed intensity ratio of Raman-G and D band (I_G/ I_D) for F-GQD and GQD are 0.56 and 1.05, respectively, suggesting that F-GQD contains a lower degree of the graphitic surface. Importantly, the Raman-D band of F-GQD is blue-shifted by ~14 cm^{-1} from GQD, suggesting distortion of the lattice by introducing nitrogen functionality. In contrast to bare GQD, the deconvoluted Raman spectra of F-GQD (**Figure 3.1e**) in the 1050-1820 cm^{-1} range show a prominent Raman peak at 1643 cm^{-1} designated for C–N vibration[33, 34]. The results also imply that the DAP molecule successively functionalized the surface of GQD. The pXRD diffractogram of the synthesized nanodot shows a prominent sharp peak at 27.8°, attributed to (002) Bragg's reflection plane (**Figure 3.1f**).[35] The bare GQD exhibits a broad (002) plane peak at 26.4°. Interestingly, the characteristic peak position of the (002) plane is slightly shifted to a higher degree and became more prominent in F-GQD than in GQD, suggesting that the interlayer spacing is much more compact in F-GQD. Moreover, the distance of two

successive layers is found to be 3.2 Å and 3.4 Å, respectively, for F-GQD and GQD[36]. The variation of interlayer distance may be different due to strain[37].

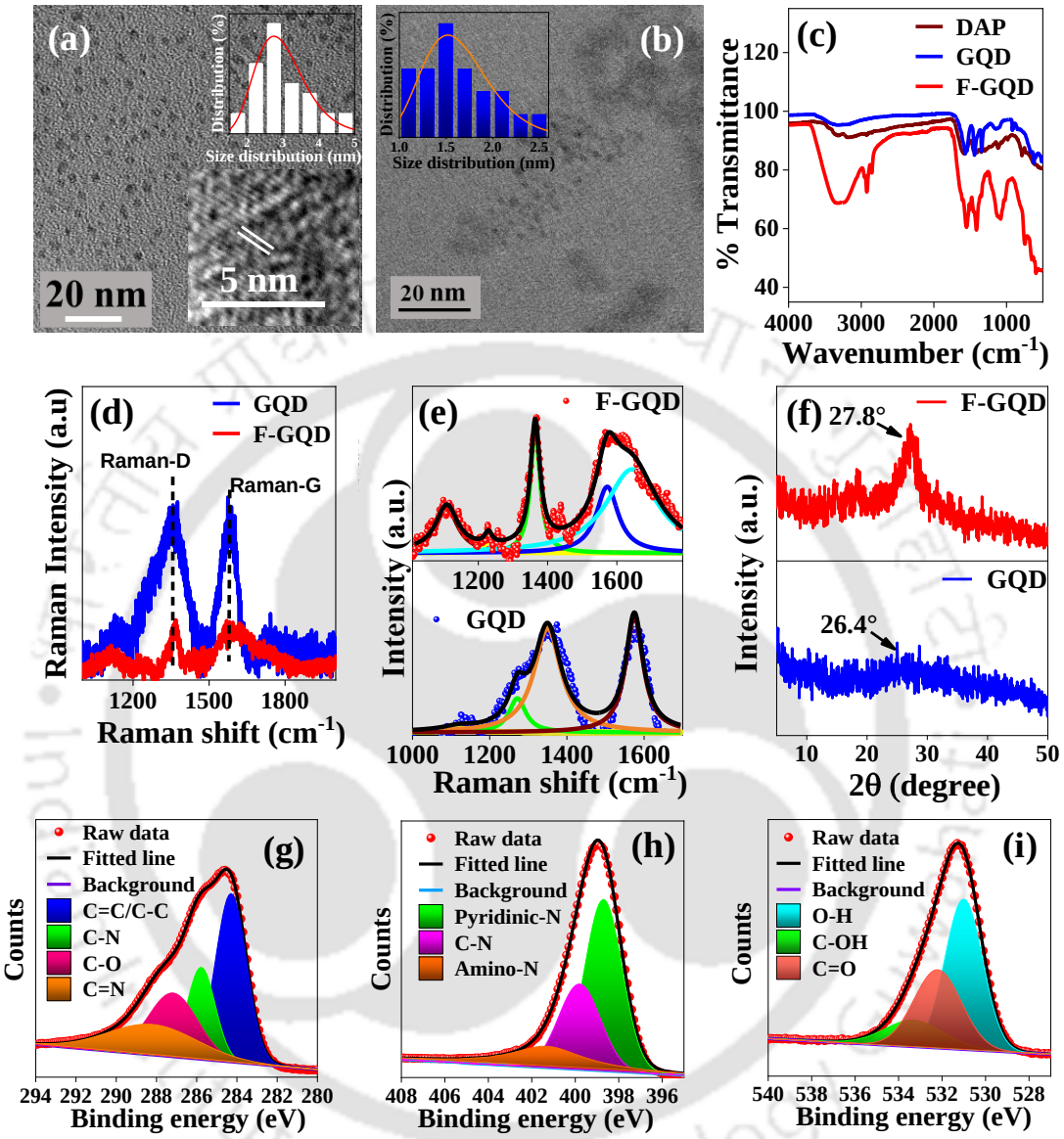

Figure 3.1. (a) TEM image of F-GQD (size distribution and HRTEM images in the inset); (b) TEM image of GQD (inset graph shows size distribution); (c) FTIR spectra of F-GQD, GQD and DAP; (d) full range Raman spectra of F-GQD and GQD; (e) Deconvoluted Raman spectrum of F-GQD and GQD; (f) Powder-XRD pattern of F-GQD and GQD; (g-i) Deconvoluted XPS spectra: C 1s, N 1s, and O 1s of F-GQD.

All these features signify that the DAP molecule successfully functionalizes the edge groups of GQD. XPS measurements add further support to the effective functionalization. The XPS survey of F-GQD depicts three prominent peaks at ~284 eV, ~400 eV, and ~532 eV for C 1s, N 1s, and O 1s, respectively (**Figure A. 3.1a**). The deconvoluted C1s spectrum of F-GQD exhibits four characteristic peaks at 284.2 eV (C=C/C−C), 285.8 eV (C−N), 287.2 eV (C−O) and 288.4 eV (C=N)[38] (**Figure 3.1g**). The high-resolution spectrum of N

1s can also be resolved into three components- pyridinic-N (398.7 eV), C-N bond (399.8 eV), and amino-N (401.5 eV) (**Figure 3.1h**).[39] Additionally, the high-resolution O 1s spectrum reveals that F-GQD consists of O-H (530.9 eV), C-OH (532.1 eV), and C=O (533.4 eV) functional groups (**Figure 3.1i**).[38, 40] Overall, the characterizations signify that the DAP molecule successfully functionalizes the GQD-surface via amide linkage formation.

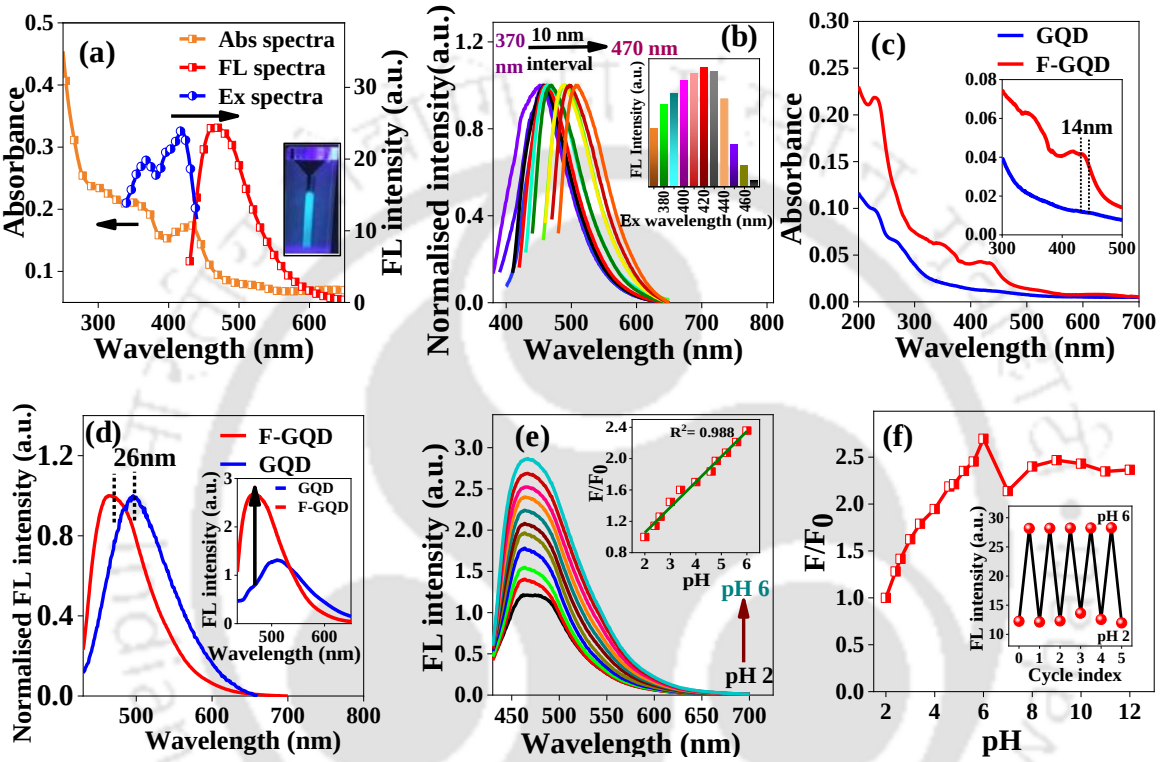

Figure 3.2. (a) Absorption, excitation (λ_{em} = 470 nm), and emission (λ_{ex} = 420 nm) spectra of F-GQD. (b) Normalized FL spectra at different excitation wavelengths (from 370 nm to 470 nm, 10 nm interval) inset plot shows the variation of peak emission intensity at different excitation wavelengths. (c) Absorbance spectra of GQD and F-GQD, (d) Normalised fluorescence spectra of GQD and F-GQD with 420 nm excitation. Inset plot shows difference of emission intensity after functionalization of GQD, (e) Emission spectra at different pH. Inset shows the ratio (F/F_0, where F represents FL intensity at particular pH and F_0, is FL intensity at pH 2) of FL intensity linearly fitted with change of pH. (f) pH dependent FL intensity ratio plot of F-GQD. Inset plot shows cyclic switching of FL intensity of F-GQD under alternating pH 6 and pH 2.

3.2.2. Photophysical Properties of F-GQD

The photophysical properties of the synthesized nanoprobe were explored systematically by UV-vis absorption, excitation, and fluorescence (FL) spectroscopy (**Figure 3.2a**). Two prominent absorption bands at 365 nm and 430 nm denote the higher energy π-π* transition of aromatic sp^2 domains and lower energy n-π* transition involving hetero-atomic surface states containing C=O and C=N moieties, respectively. The emission property of the nanoprobe highly depends on the excitation wavelength (**Figure 3.2b**), indicating multiple

centres arising from variations of the surface states. The F-GQD shows bluish-green colour emission under UV lamp (365 nm**, inset of Figure 3.2a**). The maximum FL intensity occurs at 470 nm wavelength when excited at 420 nm (**inset of Figure 3.2b**). The lowest energy absorption band and FL spectrum of F-GQD were blue-shifted by ~14 nm and ~26 nm, respectively, from the bare GQD (**Figure 3.2c and 3.2d**). Under the same excitation (420 nm), F-GQD shows ~3 times higher FL intensity than normal GQD (**inset of Figure 3.2d**). The QY enhances from 4.7% (GQD) to 13.4% (F-GQD) upon the incorporation of the DAP moiety at the surface of GQD. We also checked the pH sensitivity of the F-GQD in PBS buffer (10 mM) by varying the pH from 2 to 12. The FL property is susceptible to pH change; the fluorescence intensity gradually increases with an increase in the pH from acidic (pH 2) to the neutral condition (pH 6) (**Figure 3.2e**). The intensity variation within the pH range of 3 to 6.5 corresponds to an excellent linear fit with an R^2 of 0.982 (**inset of Figure 3.2e**). Afterward, the FL intensity drops slightly at pH 7 and remains almost invariant from pH 8 to 12 (**Figure 3.2f**). The pH-dependent fluorescence behavior may arise from reversible deprotonation and protonation states of the surface functional groups like pyridinic–N, $–NH_2$, and –OH. In addition, the fluorescence intensity of F-GQD shows excellent reversibility against alteration of pH between 2 and 6, repeatedly (**inset of Figure 3.2f**). Thus, F-GQD can be a suitable pH sensor within this range. The emission property of F-GQD remains almost invariant at temperature variations 5 °C to 90 °C (**Figure A. 3.1b**). Moreover, the measured zeta potential value of F-GQD is -9.93 mV.

3.2.3. Detection of Pb (II)

The exceptional photophysical properties of F-GQDs could be exploited to develop a fluorescence-based sensing platform. At first, various metal ions (Na^+, K^+, Mg^{2+}, Zn^{2+}, Cu^{2+} Co^{2+}, Ni^{2+}, Cr^{3+}, Fe^{2+}) were tested for any alteration of FL of F-GQD (**Figure A. 3.2a**). Interestingly, the emission intensity of F-GQD becomes ~2.8 fold increased after the addition 450 µM of Pb^{2+} (**Figure 3.3a**) in PBS buffer medium (pH 7). Here, we optimized the emission enhancement time in the presence of Pb^{2+}. In **Figure 3.3b**, only 1 min response time was sufficient for the FL intensity enhancement with addition 300 µM of Pb^{2+}. The ratio of FL intensity (F/F_0) was linearly fitted from 0 to 300 µM of Pb^{2+} with R^2 value 0.996 (**Figure 3.3c**). The calculated detection limit was observed to be 1.2 µM.

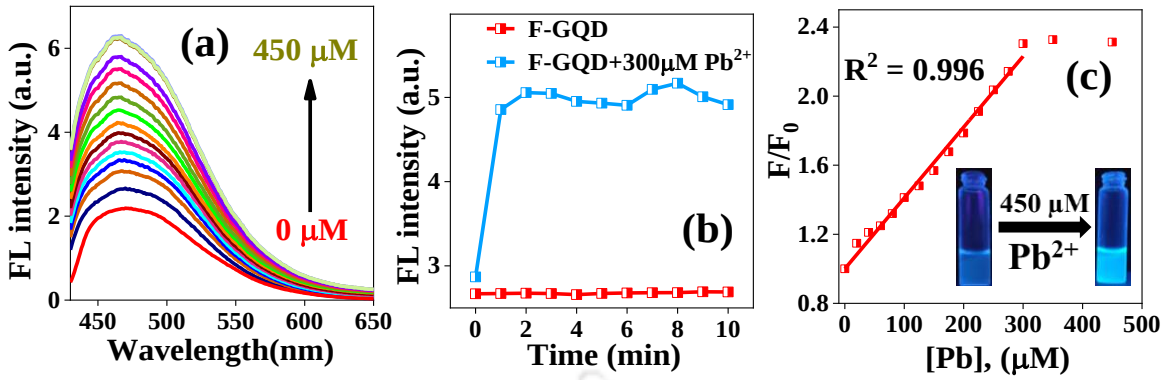

Figure 3.3. (a) Fluorescence enhancement of F-GQD with the gradual addition of Pb^{2+}. (b) FL response time of F-GQD with 300 μM Pb^{2+}. (c) Linearly fitted FL intensity ratio plot (F/F_0, F, and F_0 are fluorescence intensities in the presence and absence of Pb^{2+} respectively). The inset photographs show the visual change of fluorescence of F-GQD and in the presence of 450 μM Pb^{2+}.

2.2.4. Detection of Hypochlorite

For fluorometric recognition of ClO^-, pH becomes a crucial factor for experiments. As specific organelle has particular pH in our cellular systems, it is essential to discriminate ClO^- for a wide range of pH from pH 4 to 8 (**Figure 3.4a**). Interestingly, quenching efficiency was maximum at pH 5, suggesting that slightly acidic to neutral condition is most suitable for detection of ClO^-. Nevertheless, considering the application in living cells, pH 7 was preferred for further studies. **Figure 3.4b** demonstrates the FL kinetics measurement of F-GQD with the addition of 15 μM ClO^-, where a significant reduction of FL intensity (at 470nm) was achieved within 500 sec at pH 7. Therefore, 8 min incubation time was chosen for recording each FL spectrum. **Figure 3.4c** depicts that the emission intensity of F-GQD continuously decreases with the systematic addition of ClO^- up to 30 μM. The intense bluish-green emission of F-GQD is entirely faded out underneath the UV lamp (**inset of Figure 3.4c**). The intensity ratio (F/F_0, where F and F_0 are the FL intensity after and before addition of ClO^-) shows upward curvature nature against ClO^- concentration (**Figure 3.4d**) with a linear relationship from 0 to 8 μM with an R^2 of 0.994 (**inset of Figure 3.4d**). The obtain LOD value was 12.6 nM which is remarkable in nature. The selectivity of F-GQD was further explored by taking other competitive analytes, ROS (H_2O_2, ClO_4^-·OH, O_2^-) and RNS ($NO^·$, $ONOO^-$) species. No obvious alteration of FL property was witnessed in the presence of these analytes (**Figure A. 3.2b**). Hence, F-GQD is highly selective and sensitive for ClO^- detection.

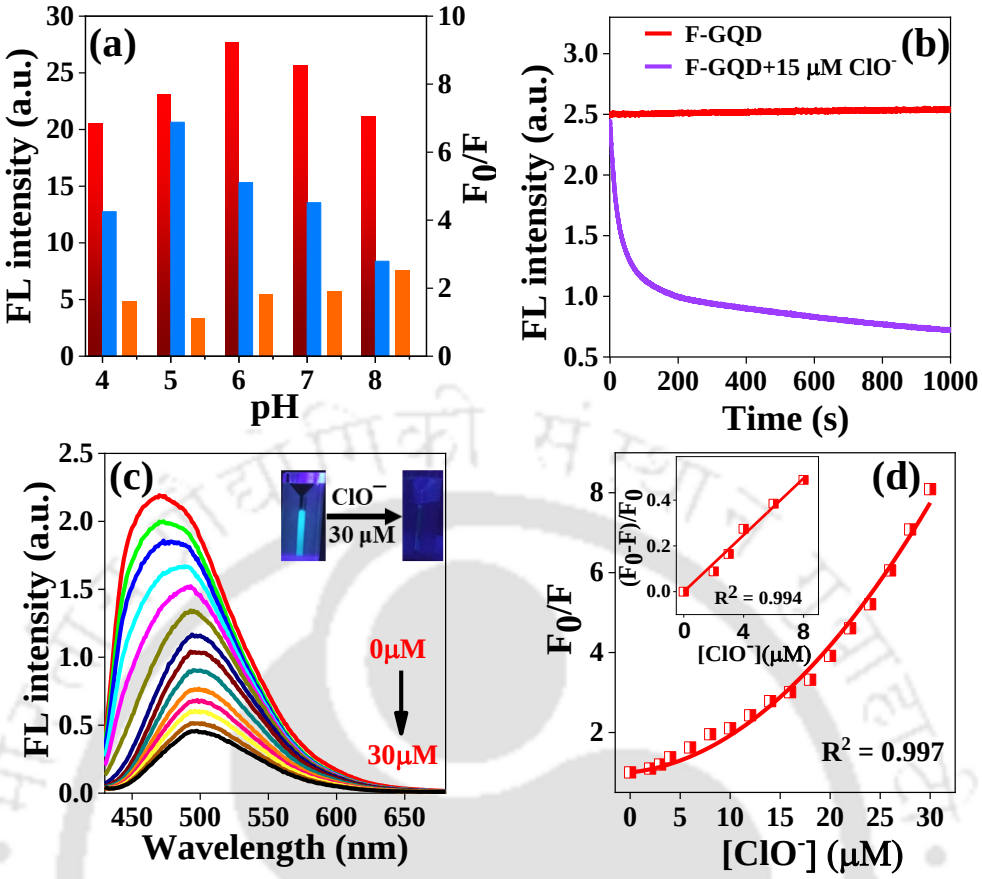

Figure 3.4. (a) pH dependent FL quenching of F-GQD in the presence of ClO^- from pH 4 to pH 8. The red line indicates FL intensity at a particular pH; the orange line shows FL intensity after the addition of 15 μM ClO^-, and the blue line indicates quenching ability at a specific pH. (b) Time-dependent fluorescence kinetics of F-GQD in the absence and presence of 15 μM ClO^-. (c) FL spectra of F-GQD in the presence of various concentrations of ClO^- (0 - 30μM). The inset shows the visual fluorescence of F-GQD and its complete depletion in the presence of 30 μM ClO^-. (d) Ratio of FL intensity with different concentrations of ClO^-. Inset Figure shows ratio of FL intensity linearly plotted with different concentrations of ClO^-.

3.2.5. Mechanism of Fluorescence Enhancement by Pb^{2+}

Various spectroscopic measurements were executed to unravel the Pb^{2+} triggered emission enhancement. The absorbance centre at 430 nm of F-GQDs was slightly blue-shifted upon the addition of $Pb^{2+,}$ suggesting that aggregation may occur via the complex formation (**Figure 3.5a**). For further elucidation of aggregation, TEM analysis of the F-GQD-Pb^{2+} system was carried out. The size of F-GQD increased considerably times after being treated with Pb^{2+} (**Figure 3.5b**). Moreover, fluorescence lifetime measurements were conducted to check the Pb^{2+} induced AIEE mechanism further. **Figure 3.5c and Table A.3.1** denoted a considerable increase in the average lifetime from bare F-GQD (**1.74 ns**) to F-GQD-Pb^{2+} system (**2.29 ns**). The complexation between $Pb^{2+}$and F-GQD may generate rigid conformation, which inhibits the free rotation of F-GQD moiety, resulting in the FL enhancement. Here, the function of the amine group was justified by considering 2AP-

GQD. The FL profile enhanced only 12% in the presence of Pb^{2+} (**Figure A. 3.3**). Thus F-GQD provides a better coordination site for Pb^{2+} through the synergic effect of various heterogenic groups. Thus, we conclude that F-GQD undergoes aggregation in the presence of Pb^{2+} through several intra-extra molecular interactions and complex formation, which successively induced the emission enhancement activity of F-GQD.

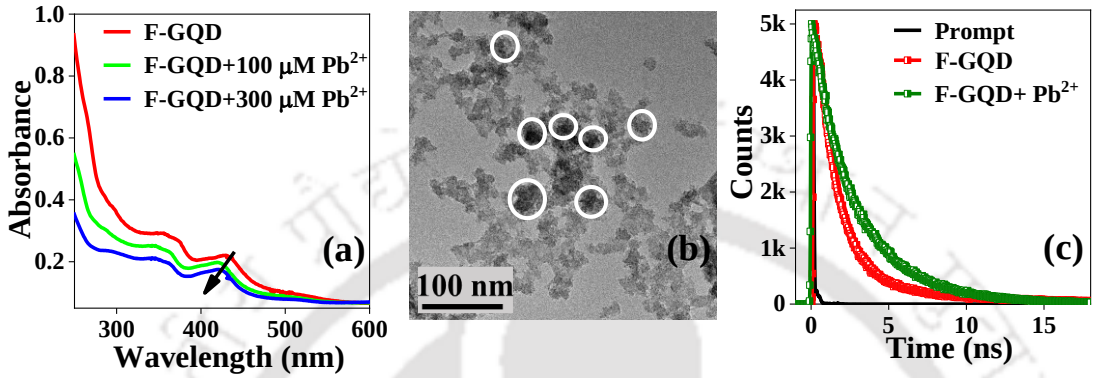

Figure 3.5. (a) Absorption spectra of F-GQD in presence of Pb^{2+}, (b) TEM image of F-GQD-Pb^{2+} system and (b) lifetime analysis of F-GQD and F-GQD-Pb^{2+}.

3.2.6. Mechanism of Fluorescence Quenching by ClO^-

The absorption bands, π-π*(360 nm) and n- π*(430 nm) become slightly red (375 nm) and blue-shifted (418 nm), respectively, after the addition of ClO^- (**Figure 3.6a**), suggesting some interaction between F-GQD and ClO^-. Additionally, TEM analysis reveals that the average diameter of F-GQD increases significantly from 2.9 ± 0.2 nm to 5.8 ± 0.6 nm upon the addition of ClO^- (**Figure 3.6b**). Hence, F-GQD produces small aggregates in contact with ClO^-. XPS analysis was conducted to prove further interaction between the nanoprobe and quencher (ClO^-) (**Figure A. 3.4a**). The deconvoluted Cl 2p XPS spectrum revealed the formation of an organochlorine bond (**Figure 3.6c**). Moreover, FTIR analysis shows that the absorption peaks assigned for -OH/-NH_2 and N-H bending (1554 cm^{-1} for F-GQD) become broader upon the addition of ClO^-. The broadening indicates the formation of hydrogen bonds in the F-GQD-ClO^- system**.** (**Figure 3.6d**). The upward curvature Stern-Volmer plot (**Figure 3.4d**) mentioned earlier points towards the presence of both static and dynamic mechanisms. FL decays were measured to delineate the contribution of the dynamic quenching. The average lifetime of F-GQD reduces drastically with the gradual addition of ClO^- (**Figure 3.6e and Table A. 3.2**). A linear fit to τ_0/τ vs. ClO^- concentration reveals that the dynamic quenching constant is $1.42\pm0.07\times10^5$ M^{-1} (**Figure 3.6f**). The remarkably high value indicates that the dynamic quenching effect (DQE) is very efficient

in F-GQD-ClO^- system. The energy transfer efficiency for the F-GQD-ClO^- system was calculated by equation (1) and found to be 80% at 26 µM ClO^-.

$$\text{Efficiency of DQE} = 1 - \frac{\tau}{\tau_0} \quad \text{equation (1)}$$

The static quenching constant was estimated by following equation 1.[42]

$$\frac{I_0}{I} = K_{SV}[Q]e^{V[Q]} + 1 \quad \text{equation (2)}$$

where [Q], K_{SV}, and V stands for quencher concentration, dynamic and static quenching constants, respectively. The calculated V value is 8.837×10^3 M^{-1}, which is too little compared to the dynamic quenching constant. All the above observations suggest that detection of ClO^- by F-GQD consists of two types of mechanisms, where dynamic quenching (energy transfer) is predominant over the static one (H-bonding). Thus, amine functionalization of F-GQD influences to form a H-bonded network (N−H···O−Cl) through which the nanodot comes closer to form a nanoaggregate and triggers energy migration from F-GQD to ClO^-.

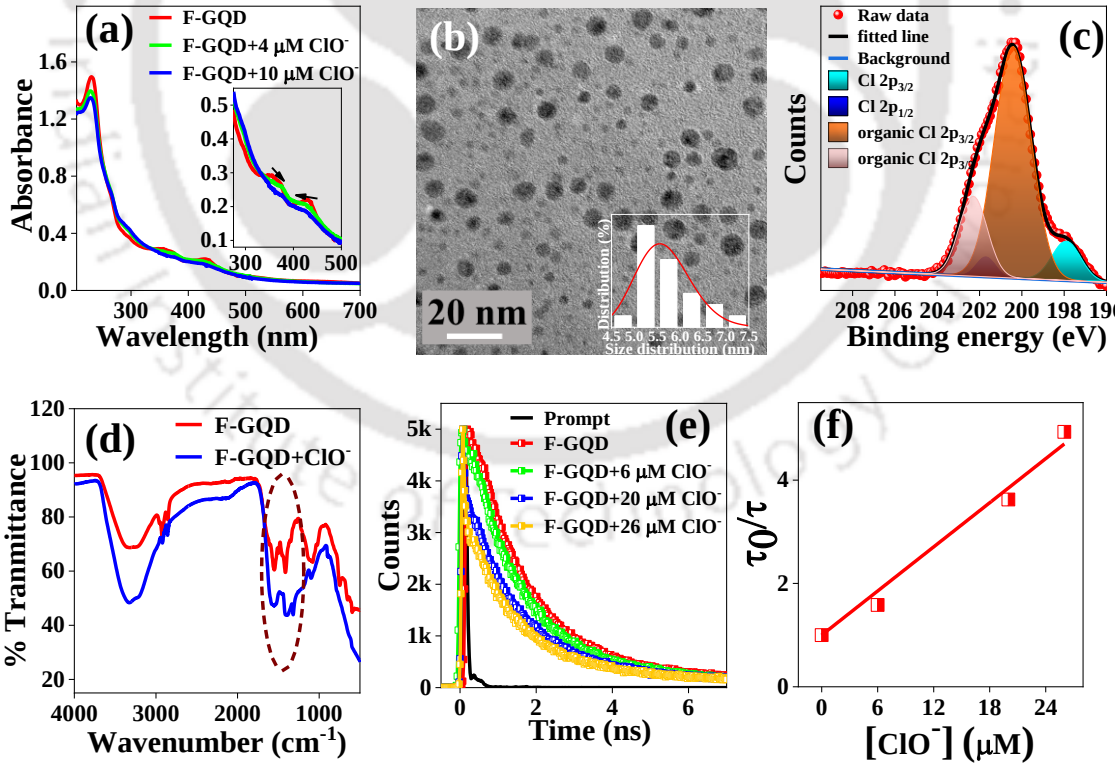

Figure 3.6. (a) Absorption spectra of F-GQD in the presence of ClO^-. The inset shows the spectral change of F-GQD with the addition of ClO^-. (b) TEM images of F-GQD after addition of ClO^-, inset shows size distribution with lognormal fitting. (c) Deconvoluted Cl 2p XPS spectra after the addition of ClO^- (d) FTIR spectra of F-GQD and F-GQD-ClO^- system. (e) FL decays of F-GQD at various concentrations of ClO^-. (f) The ratio of average lifetime linearly fitted against ClO^- concentration.

We also examine the role of the amine group in the sensing process. The 2AP-GQD nanodots show negligible FL quenching towards ClO^- (**Figure A. 3.4b**); only **14 %** quenching was observed in the presence of 100 µM ClO^-. Thus, the amine functionality plays an essential role in producing the H-bonding network and enhances the ClO^- quenching efficiency of F-GQD. In **scheme 3.2**, we represent the pathways for the sensing of both Pb^{2+} and ClO^-.

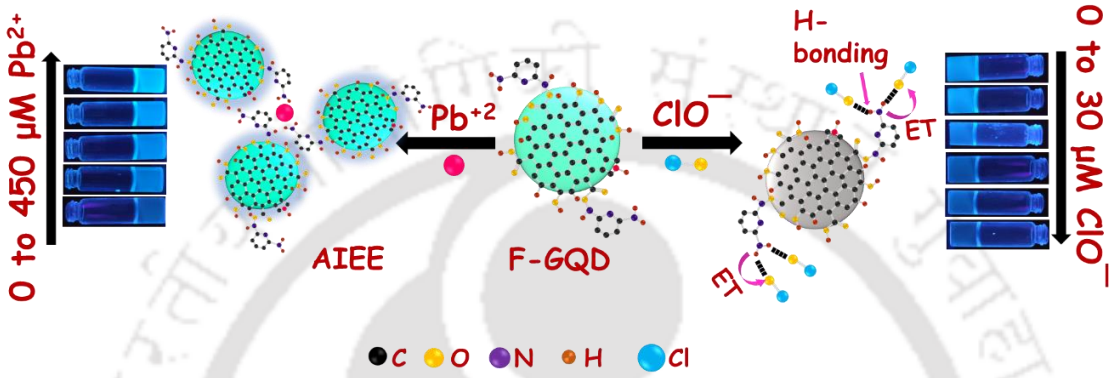

Scheme 3.2. Sensing approach for multimode detection of Pb^{2+} and ClO^-.

3.2.7. Multicolour cell imaging application

The checked cytotoxicity of F-GQD in HeLa cells by MTT assay to explore its biological application. For the cell viability study, the HeLa cells were cultured with different concentrations of F-GQD (50 to 400 µg mL^{-1}). The F-GQD-treated cells exhibited more than 80% viability at all concentrations of F-GQD after 24 h post-treatment suggesting negligible toxicity to cells and good biocompatibility (**Figure A. 3.5**). We also want to check the viability of the F-GQD as a potential multicolor cell imaging probe. For this purpose, HeLa cells were incubated with 100 µg/mL F-GQD for 2 h. The treated cells illuminate bright bluish-green, green, and orange emission under the different excitation laser sources of 405, 488, and 561 nm, respectively (**Figure 3.7a-d**). The FL signal mainly originates from the cytoplasm of the cells without changing any cell morphology. These outcomes accounted that F-GQD could eventually be employed as multicolour fluorescent probes for cellular imaging.

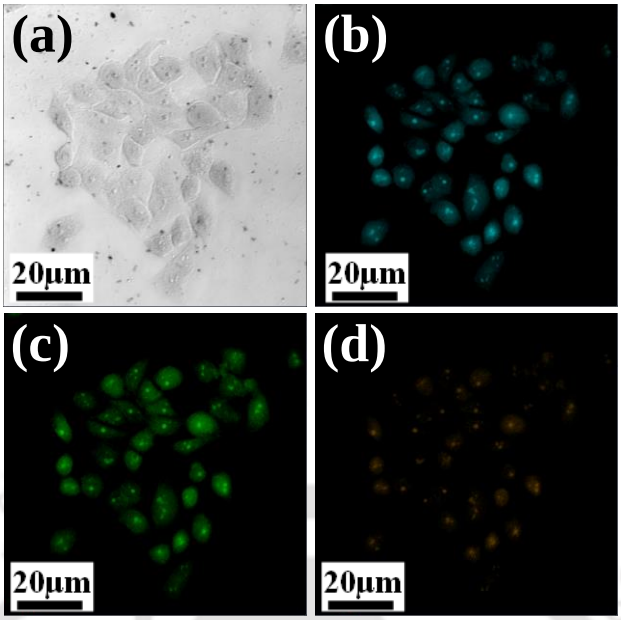

Figure 3.7. Confocal microscopic images of HeLa cells after incubating with 100 µg/mL F-GQD for 2 h, (a) bright field, (b) under 405 nm, (c) 488 nm and (d) 561 nm laser sources.

3.2.8. Recognition of ClO^- in HeLa cells

After treating HeLa cells with 100 µg/mL F-GQD, cells reveal a bright bluish-green FL when excited with a laser source at 405 nm in CLSM (**Figure 3.8d-f**). The FL response significantly diminishes when the cells were treated with 10 µM ClO^- and the emission almost vanishes at 20µM ClO^- (**Figure 3.8g-i and Figure 3.8 j-l**). These results suggest that F-GQD can easily penetrate the cell membrane and successfully detect intracellular ClO^-.

3.3. Conclusion

In summary, we synthesized a novel fluorescent nanoprobe F-GQD via a simple one-step coupling reaction between GQD and DAP moiety. The heterogenous polar groups at the edge makes it intrinsically pH-responsive. The nanoprobe shows multimodal sensing behavior; it is a fluorescence turn-on sensor for Pb^{2+} whereas a fluorescence turn-off sensor for ClO^-. The fluorescence amplification arises through the remarkable AIEE effect upon complexation with Pb^{2+}. The ClO^- recognition mechanism consists of both static and dynamic quenching effects. The dynamics effect arises by energy dissipation from F-GQD to ClO^- via the N−H···O−Cl H-bonding network between amine group in F-GQD and ClO^-. The amine group at the edge of F-GQDs is primarily responsible for the superior binding ability to Pb^{2+} and ClO^-. Moreover, The F-GQD was used as an efficient FL nanoprobe for multicolor HeLa cell imaging due to its excitation-dependent emission

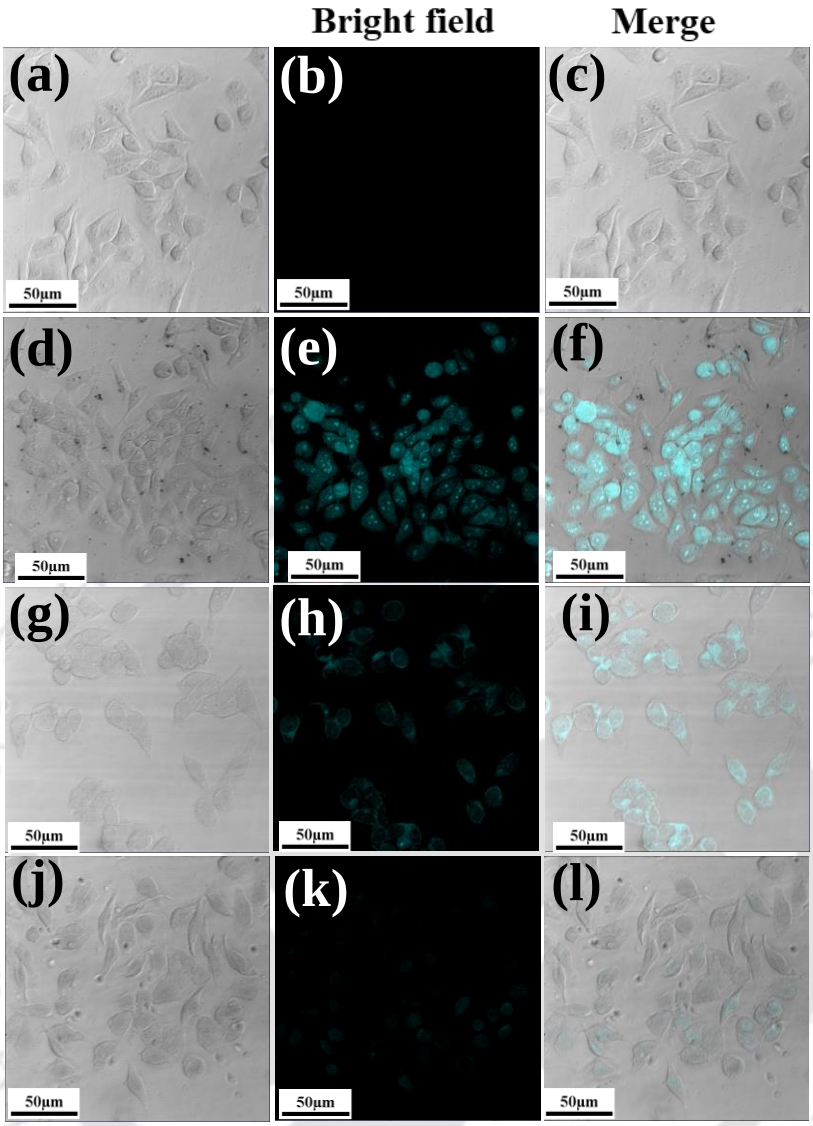

Figure 3.8. The decrease in FL intensity of F-GQD with ClO^-. (a)-(c) cell control (d)-(f) 100µg/mL of F-GQD treated cells. (g)-(i) cells treated with F-GQD +10 µM ClO^- and (j) to (l) cells treated with F-GQD +20 µM ClO^-. The excitation source was 405 nm laser, and the fluorescence signal was recorded in the emission range of 420 nm to 490 nm

property. Besides, F-GQD can efficiently sense the exogenous ClO^- in HeLa cells. This work affords an effective approach for designing efficient fluorescence probes based on the functionalization of GQDs.

References

1. S. Liu, W. Wei, X. Sun and L. Wang, *Biosensors and Bioelectronics*, 2016, **83**, 33-38.

2. U. A. Reddy, P. V. Prabhakar, G. S. Rao, P. R. Rao, K. Sandeep, M. F. Rahman, S. I. Kumari, P. Grover, H. A. Khan and M. Mahboob, *Environmental Science and Pollution Research*, 2015, **22**, 13453-13463.

3. G. Aragay, J. Pons and A. Merkoçi, *Chemical Reviews*, 2011, **111**, 3433-3458.

4. C. C. Winterbourn, *Nat. Chem. Biol.*, 2008, **4**, 278-286.

5. M. O. Breckwoldt, J. W. Chen, L. Stangenberg, E. Aikawa, E. Rodriguez, S. Qiu, M. A. Moskowitz and R. Weissleder, *Proc. Natl. Acad. Sci. U.S.A*, 2008, **105**, 18584-18589.

6. D. L. Lefkowitz and S. S. Lefkowitz, *Free Radic. Biol. Med*, 2008, **45**, 726-731.

7. S. Sugiyama, Y. Okada, G. K. Sukhova, R. Virmani, J. W. Heinecke and P. Libby, *Am. J. Pathol.*, 2001, **158**, 879-891.

8. B. C. Dickinson and C. J. Chang, *Nat. Chem. Biol.*, 2011, **7**, 504-511.

9. R. Wang, R. Wang, D. Ju, W. Lu, C. Jiang, X. Shan, Q. Chen and G. Sun, *Analyst*, 2018, **143**, 5834-5840.

10. Z. Zhang, K. Pei, Q. Yang, J. Dong, Z. Yan and J. Chen, *New J. Chem*, 2018, **42**, 15895-15904.

11. T. A. Bellar, J. J. Lichtenberg and R. C. Kroner, *J Am Water Works Assoc*, 1974, **66**, 703-706.

12. Y. Zhan, F. Luo, L. Guo, B. Qiu, Y. Lin, J. Li, G. Chen and Z. Lin, *ACS Sens.*, 2017, **2**, 1684-1691.

13. R. J. Goiffon, S. C. Martinez and D. Piwnica-Worms, *Nat. Commun*, 2015, **6**, 6271.

14. Y. Wang, S. Gao, X. Zang, J. Li and J. Ma, *Analytica Chimica Acta*, 2012, **716**, 112-118.

15. C. Zheng, L. Hu, X. Hou, B. He and G. Jiang, *Anal. Chem.*, 2018, **90**, 3683-3691.

16. M. Murata, T. A. Ivandini, M. Shibata, S. Nomura, A. Fujishima and Y. Einaga, *J. Electroanal. Chem*, 2008, **612**, 29-36.

17. M. H. Al-Malack, S. Y. Sheikheldin, N. M. Fayad and N. Khaja, *Water Air Soil Pollut.*, 2000, **120**, 195-208.

18. Y. Dong, G. Li, N. Zhou, R. Wang, Y. Chi and G. Chen, *Anal. Chem.*, 2012, **84**, 8378-8382.

19. Q. Wang, C. Tan and W. Cai, *Analyst*, 2012, **137**, 1872-1875.

20. Y. Ye, L. Zhao, S. Hu, A. Liang, Y. Li, Q. Zhuang, G. Tao and J. Gu, *Dalton Trans.*, 2019, **48**, 2617-2625.

21. C. L. Gopu, A. Shanti Krishna and K. Sreenivasan, *Sens. Actuators B Chem.*, 2015, **209**, 798-802.

22. Y. Chong, Y. Ma, H. Shen, X. Tu, X. Zhou, J. Xu, J. Dai, S. Fan and Z. Zhang, *Biomaterial*, 2014, **35**, 5041-5048.

23. Y. Zhou, H. Sun, F. Wang, J. Ren and X. Qu, *Chem. Commun.*, 2017, **53**, 10588-10591.

24. H. Tetsuka, R. Asahi, A. Nagoya, K. Okamoto, I. Tajima, R. Ohta and A. Okamoto, *Adv. Mater.*, 2012, **24**, 5333-5338.

25. B.-P. Qi, H. Hu, L. Bao, Z.-L. Zhang, B. Tang, Y. Peng, B.-S. Wang and D.-W. Pang, *Nanoscale*, 2015, **7**, 5969-5973.

26. W. Kwon, Y.-H. Kim, J.-H. Kim, T. Lee, S. Do, Y. Park, M. S. Jeong, T.-W. Lee and S.-W. Rhee, *Sci. Rep.*, 2016, **6**, 24205.

27. H. Tetsuka, A. Nagoya, T. Fukusumi and T. Matsui, *Adv. Mater.*, 2016, **28**, 4632-4638.

28. S. Bian, C. Shen, H. Hua, L. Zhou, H. Zhu, F. Xi, J. Liu and X. Dong, *RSC Adv.*, 2016, **6**, 69977-69983.

29. L. Ma, S. Sun, Y. Wang, K. Jiang, J. Zhu, J. Li and H. Lin, *Microchim. Acta*, 2017, **184**, 3833-3840.

30. X. Fang, J. Ding, N. Yuan, P. Sun, M. Lv, G. Ding and C. Zhu, *Phys. Chem. Chem. Phys.*, 2017, **19**, 6057-6063.

31. Y. Ding, J. Zheng, J. Wang, Y. Yang and X. Liu, *J. Mater. Chem. C*, 2019, **7**, 1502-1509.

32. S. Sun, L. Zhang, K. Jiang, A. Wu and H. Lin, *Chem. Mater.*, 2016, **28**, 8659-8668.

33. L. Wang, X. Zhang, K. Yang, L. Wang and C.-S. Lee, *Carbon*, 2020, **160**, 298-306.

34. T. Zhang, J. Zhu, Y. Zhai, H. Wang, X. Bai, B. Dong, H. Wang and H. Song, *Nanoscale*, 2017, **9**, 13042-13051.

35. D. Ozyurt, S. Shafqat, T. T. Pakkanen, R. K. Hocking, A. Mouritz and B. Fox, *Carbon*, 2021, **175**, 576-584.

36. Y. Sun, S. Wang, C. Li, P. Luo, L. Tao, Y. Wei and G. Shi, *Phys. Chem. Chem. Phys.*, 2013, **15**, 9907-9913.

37. G. Rajender, U. Goswami and P. K. Giri, *J. Colloid Interface Sci.*, 2019, **541**, 387-398.

38. Z.-L. He, C. Yuan, H. Gao, Z. Mou, S. Qian, C. Zhai and C. Lu, *ACS Sustainable Chem. Eng.*, 2020, **8**, 12331-12341.

39. N. Wang, A.-Q. Zheng, X. Liu, J.-J. Chen, T. Yang, M.-L. Chen and J.-H. Wang, *ACS Appl. Mater. Interfaces*, 2018, **10**, 7901-7909.

40. R. Das, H. Sugimoto, M. Fujii and P. K. Giri, *ACS Appl. Mater. Interfaces*, 2020, **12**, 4755-4768.

41. S. Zhu, Q. Meng, L. Wang, J. Zhang, Y. Song, H. Jin, K. Zhang, H. Sun, H. Wang and B. Yang, *Angew. Chem.*, 2013, **52**, 3953-3957.

42. Z. Huang, W. Song, Y. Li, L. Wang, N. K. Pandey, L. Chudal, M. Wang, Y. Li, L. Zhao, W. Yin and W. Chen, *J. Mater. Chem. C*, 2020, **8**, 12935-12942.

[This page was intentionally left blank]

CHAPTER 4

Multifunctional N-doped Carbon Dots for Bimodal Detection of Bilirubin, Vitamin B_{12}, and Living Cell Imaging

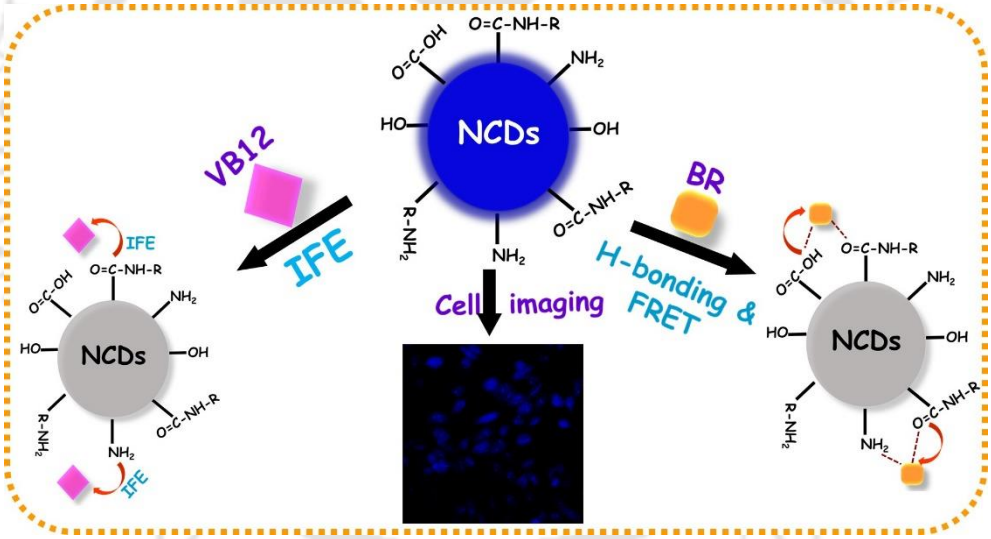

Manuscript: Nilanjana Nandi, Shubham Gaurav, Priyanka Sarkar, Sachin Kumar, and Kalyanasis Sahu, "Multifunctional N-Doped Carbon Dots for Bimodal Detection of Bilirubin and Vitamin B_{12}, and Living Cell Imaging" *ACS Appl. Bio Mater.* 2021, **4**, 6, 5201–5211

[This page was intentionally left blank]

Abstract

A N-doped carbon dot (NCDs) has been synthesized via a simplistic one-step hydrothermal technique using L-aspartic acid and 3,6-diaminoacridine hydrochloride. The NCDs exhibit a high quantum yield (22.7%) and excellent optical stability in aqueous media. Additionally, NCDs display good solid-state yellowish-green emission which is ~ 75 nm red shifted from solution-state emission. The remarkable fluorescence (FL) properties of NCDs were further applied to develop a multifunctional sensor for bilirubin (BR) and vitamin B12 (VB12) via fluorescence quenching. We have systematically studied the FL quenching mechanisms for the two analytes. The primary quenching mechanism of BR was via the FRET pathway facilitated by the H-bonding network between the hydrophilic moieties existing at the surface of BR and NCDs. In contrast, IFE was mainly responsible for the recognition of VB12. The in vitro competency was also verified in the human cervical cancer cell line (HeLa cell) with negligible cytotoxicity and significant biocompatibility. This result facilitates the application of NCDs for bioimaging and recognition of VB12 in a living organism.

4.1 Overview

Over the past few decades, carbon dots (CDs) have magnetized tremendous attention across various interdisciplinary research fields for easy and affordable synthesis, tiny structures, bright and tunable fluorescence (FL), outstanding solubility in various solvents, excellent photostability, low toxicity, and extraordinary biocompatibility.[1-6] Owing to these critical properties, CDs become a forefront practical alternative to organic fluorophores and heavy metal-based quantum dots requiring vigorous synthesis techniques, hazardous conditions, highly toxic, and expensive chemicals.[7, 8] The superior characteristics of CDs have been exploited in various fields such as electrochemical,[9] photovoltaics,[10] catalysis,[11] fluorescent ink,[12] analytical detections of various molecules,[13] drug-loading and photomedicine fields.[14, 15] Recently, non-metallic heteroatom (nitrogen, boron, or phosphorus) doping can tremendously modulate the inherent properties like photophysical property, quantum yield (QY), electronic structure, and surface defects which helps to expand their applicability. [16-18] Several new applications have also been reported exploiting the improved physical and chemical properties properties[19]. Some non-metal doped CDs have the capability of sensing multiple analytes.[20, 21]

The N-doped CDs (NCDs) have been explored for determining several analytes such as metal ions,[22, 23] biomolecules,[24, 25], and other organic molecules.[26] Recently, N-doped red-emitting carbon dot has been synthesized from citric acid and neutral red to detect several metal ions, such as Pt^{2+}, Au^{3+}, and Pd^{2+}. Moreover, the carbon dots have been used for *in vivo* and *in vitro* applications.[27] Liu et al. synthesized N-doped carbon quantum dot from poly(ethyleneimine) by simple hydrothermal technique.[28] The blue FL of the quantum dot was turned off in the presence of Cu^{2+} by efficient electron transfer while the fluorescence signal restores after the addition of L-cysteine. Chang et al. reported the hydrothermal synthesis of blue emissive NCDs using two precursors, folic acid and citric acid.[29] This NCD was further applied for multiple detection platforms, e.g., pH sensing and Hg^{2+} sensing via photoinduced electron transfer.

The jaundice biomarker bilirubin (BR) is a side-product generated by the breakdown of hemoglobin.[30, 31] The average concentration of free BR in human blood is ~25 μM. In the case of jaundice, the concentration of free BR may exceed to 50 μM.[32, 33] The yellowish red-colored BR is excreted by the urine and bile. An excessive amount of free BR in human blood serum can lead to hemolytic anemia and liver dysfunction.[34, 35] Anjana et al. applied

CDs derived from citric acid and L-cysteine to detect BR.[36] The fluorescence was drastically reduced with the addition of Fe^{3+} via static quenching, and subsequently, the emission intensity was regained in the presence of BR. The lone pair electron in the pyrrole ring of BR undergoes complexation with $Fe^{3+,}$ which triggers restoration of the fluorescence signal.[36]

Furthermore, vitamin-B_{12} (VB12) is a crucial micronutrient for developing cells, maintaining the nerve cell function, helping DNA restoration and metabolism of macronutrients (such as carbohydrates, fat) in mammals.[37] Our typical requirement of VB12 is ~0.4 to 2.8 mg/day, while an overdose of VB12 can be harmful to the liver, kidney, and lungs and causes several diseases like asthma, organ failure.[38] Most importantly, deficiency of VB12 can produce pernicious anemia, several neurological and heart problems.[39, 40] Therefore, it is essential to develop an efficient technique for determining VB12 levels precisely. Recently, safranine T and citric acid have been used to obtain multifunctional CDs where safranine T acts as a guest inside the carbon sphere host created by the carbonization of citric acid. This multifunctional CD was further used to detect VB12 by the inner filter effect (IFE) pathway.[41] Du et al. reported a novel CD using a hydrothermal synthesis of two precursors 1,2-ethylenediamine and artemisia annua.[42] The CD was useful to detect VB12 and Co^{2+} based on IFE and static quenching pathways, respectively. Wang et al. developed a CD by a thermal reduction for the sensing of VB12 through Förster resonant energy transfer (FRET)) mechanism.[43] Ding et al. also reported CD derived from citric acid to detect VB12 by the IFE mechanism.[44]

In the present work, we attempt a green hydrothermal synthesis of a highly blue fluorescent NCD nanosensor using L-aspartic acid and 3,6-diaminoacridine hydrochloride as carbon and nitrogen sources, respectively. The NCD displays admirable photostability, negligible cytotoxicity, and excellent biocompatibility. The NCDs also show yellowish-green emission in the solid-state, which is ~75 nm red-shifted from the solution state emission. The blue emission of NCD in the solution state can efficiently disappear in BR and VB12, resulting in good sensitivity and selectivity towards both the analytes. We found that NCD follows a different sensing mechanism for the two analytes (**Scheme 4.1**). BR was detected through the FRET mechanism via the formation of an H-bonding network between hydrophilic moieties existing at the surface of BR and NCDs, whereas the IFE is mainly responsible for VB12 detection. Furthermore, the NCD has been introduced for fluorescence imaging of Hela cells and *in vitro* sensing of VB12.

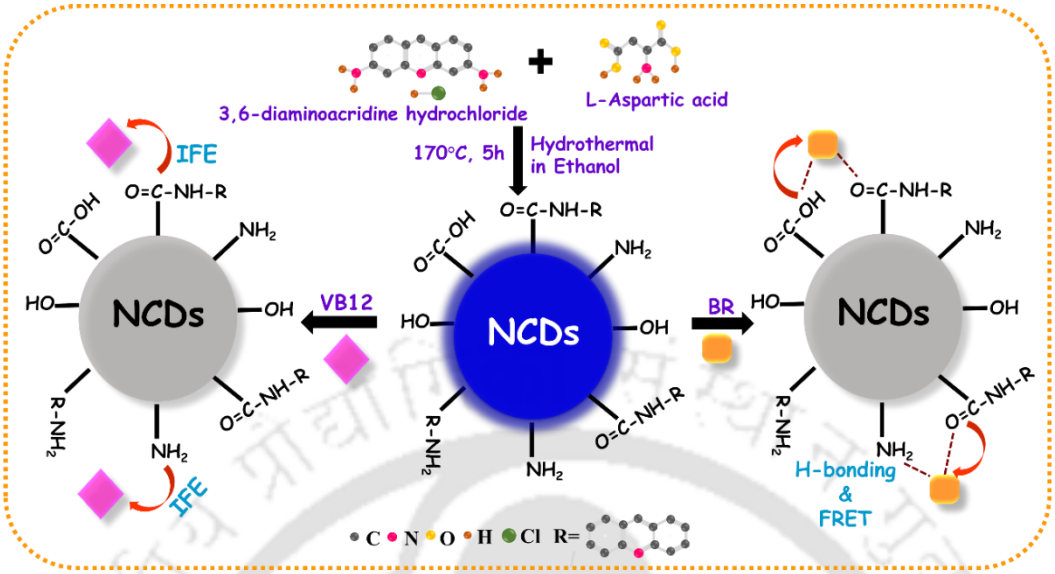

Scheme 4.1. Schematic representation of NCD for the detection of VB12 and BR.

4.2 Results and Discussions

4.2.1 Surface and morphological characterizations

In this work, NCDs were prepared by taking L-aspartic acid and 3,6-diaminoacridine hydrochloride. The reaction was optimized by considering the emission intensity of as-prepared NCD (**Figure A.4.1a and A.4.1b**). Here, the former acts as a carbon source, and the latter helps to increase the heterogenicity at the surface by incorporating N-atom. The microstructure of NCDs was examined by transmission electron microscopy (TEM). **Figure 4.1a** reveals a spherical structure with excellent dispersive nature. High-resolution TEM (HRTEM) depicts a lattice spacing of 0.21 nm (inset of **Figure 4.1a**), denoting the presence of (100) graphitic plane of carbon material. The size distribution histogram shows that the average size of NCDs was 3.8 ± 0.9 nm (inset of **Figure 4.1a)**. Fourier-transformed infrared (FTIR) spectroscopy was also applied to access an overview of the chemical functionality present in the NCD (**Figure 4.1b**). The broad stretching vibrations at 3585-3420 cm^{-1} and 3233-3185 cm^{-1} denote the presence of O-H and N-H groups, respectively. Three vibration peaks at 1780 cm^{-1}, 1706 $cm^{-1,}$ and 1667 cm^{-1} were attributed to the carbonyl group (carboxylic acid and amide C=O) and C-N bond, respectively.[45, 46] The characteristic absorption band at 1538 cm^{-1} indicates N-H bending. The IR peaks at 1448 cm^{-1}, 1394 cm^{-1} (bimodal peak), 1266 cm^{-1}, 1185 cm^{1}, and 1100 cm^{-1} stand for C=C

aromatic frame, N-H, C-O, C-NH-C asymmetric stretching vibration, and C-O-C group at the edge sites of NCD.[47-49] Moreover, the peaks at 2980 cm^{-1} to 2924 cm^{-1} refer to C-H stretching vibration.

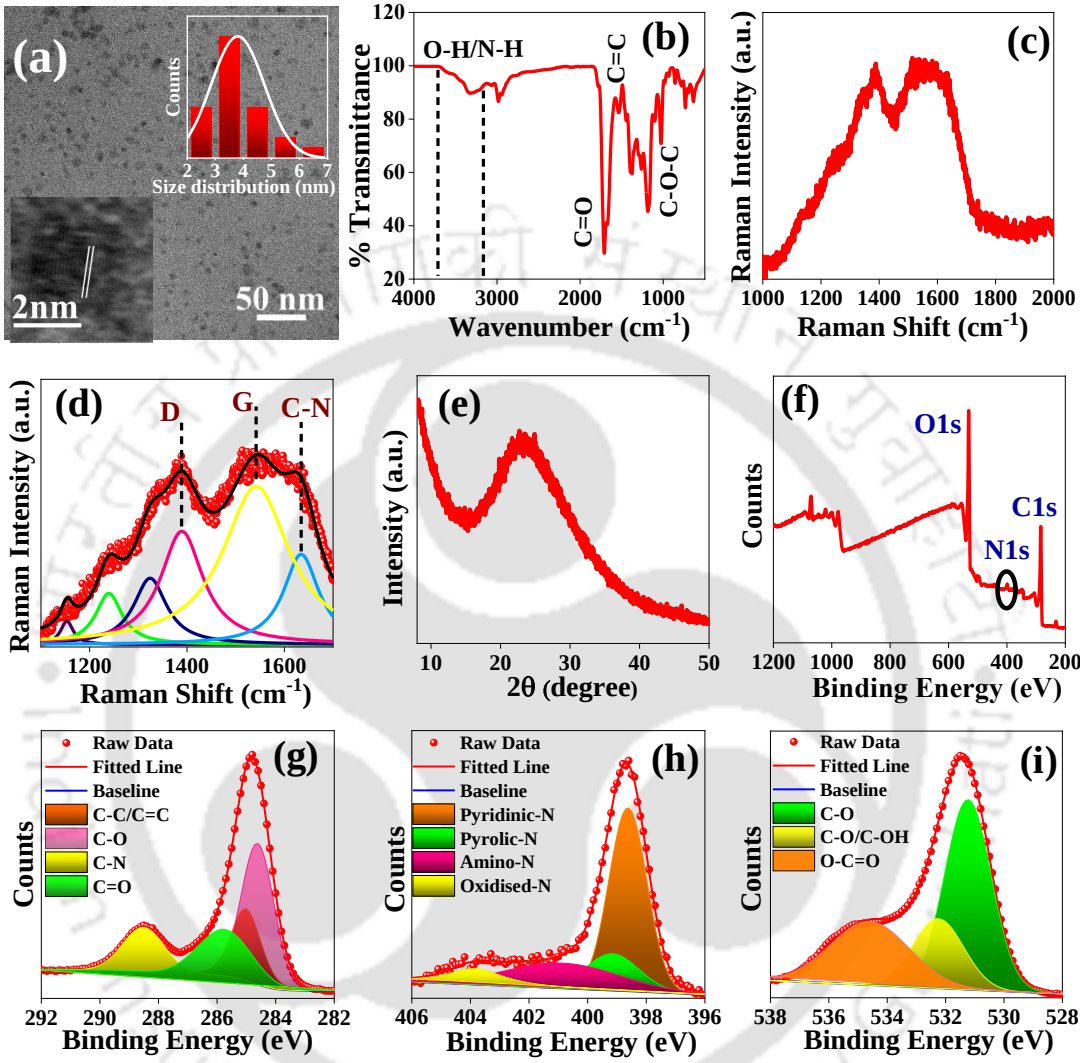

Figure 4.1. (a) TEM image, the upper inset shows size distribution profile, and the lower inset shows HRTEM image depicting the lattice spacing; (b) FTIR spectra; (c) Full range Raman spectra; (d) Deconvoluted of Raman spectra; (f) full range XPS spectra; High-resolution XPS spectra of C 1s (g), N 1s (h) and O 1s (i).

Raman spectroscopy is a potent tool to characterize the surface states and functionality of carbon-based nanomaterials. **Figure 4.1c** depicts the full range Raman spectrum of the synthesized nanodot. The spectrum in the range 1100−1700 cm^{-1} was deconvoluted into six Lorentzian peaks (**Figure 4.1d**). The specification of each peak parameter is supplied in **Table A.4.1.** After deconvolution, the D and G bands appear at 1389 cm^{-1} and 1545 cm^{-1}, respectively, corresponding to defect sites of the carbon network and sp^2 hybridized carbon framework. More precisely, peaks situated at 1320 cm^{-1} and 1630 cm^{-1} correspond to the O=C-N and C-N bond vibrations arising from the amide functionality of NCDs.[50, 51]

The p-XRD diagram of NCDs exhibited a wide peak at 23.2° (**Figure 4.1e**), indicating a disordered graphite structure.[52]

XPS study was executed to validate further the results obtained from FTIR and Raman analysis and understand the composition and various surface states of NCDs. Three prominent peaks at ~284 eV, ~398 eV, and ~531 eV is for C 1s, N 1s, and O 1s, respectively, with atomic contributions of 58.61 % (C 1s), 38.67 % (O 1s), and 2.72 % (N 1s) (**Figure 4.1f**). The high-resolution XPS spectra of the same elements were further deconvoluted for complete functionality analysis (**Figure 4.1 g-i**). In the deconvoluted C 1s spectrum, four apparent peaks at 284.6 eV, 285.1 eV, 285.8 eV, and 288.7 eV indicate C-C / C=C, C-O, C-N, and C=O moieties.[53, 54] For N 1s spectrum, four binding energy bands, are located at 398.6 eV, 399.2 eV, 401.1 eV, and 403.8 eV, which corresponds to pyridinic-N, pyrrolic-N, amino-N (N-H), an oxidized form of N as N-O.[55, 56] These pronounced peaks confirm the existence of multiple N-related functional groups in NCD nanoprobe. Additionally, deconvoluted O 1s spectra also reveal that the oxygen is present in the form of C-O (531.2 eV), C-O-C / C-OH (533.3 eV), and O-C=O (534.6 eV).[57-59] To verify the structure of nanoprobe NCDs ^{1}H NMR was taken in D_2O solvent. Here, we observed the chemical shift value from 1 ppm to 4.5 ppm suggesting some kind of polyamide-polyester type of structure (**Figure A.4.2**). Furthermore, the chemical shift values from 6.3 ppm to 7 ppm also signify the aromatic ring from 3,6-diaminoacridine orange moiety.[60]

4.2.2 Photo-physical characterization

The photophysical properties of NCDs were thoroughly evaluated by UV-vis absorption, fluorescence emission, and excitation spectroscopy. NCDs show a vast absorption spectrum (**Figure 4.2a**), with two dominant broad absorption bands at 285 nm and 360 nm, leading to the π-π* electronic transition of the C=C moieties of the carbon core and n-π* transition of aromatic sp^2 domain consists of C=O or C=N bonds. NCDs display emission maximum at 450 nm when excited at 360 nm.

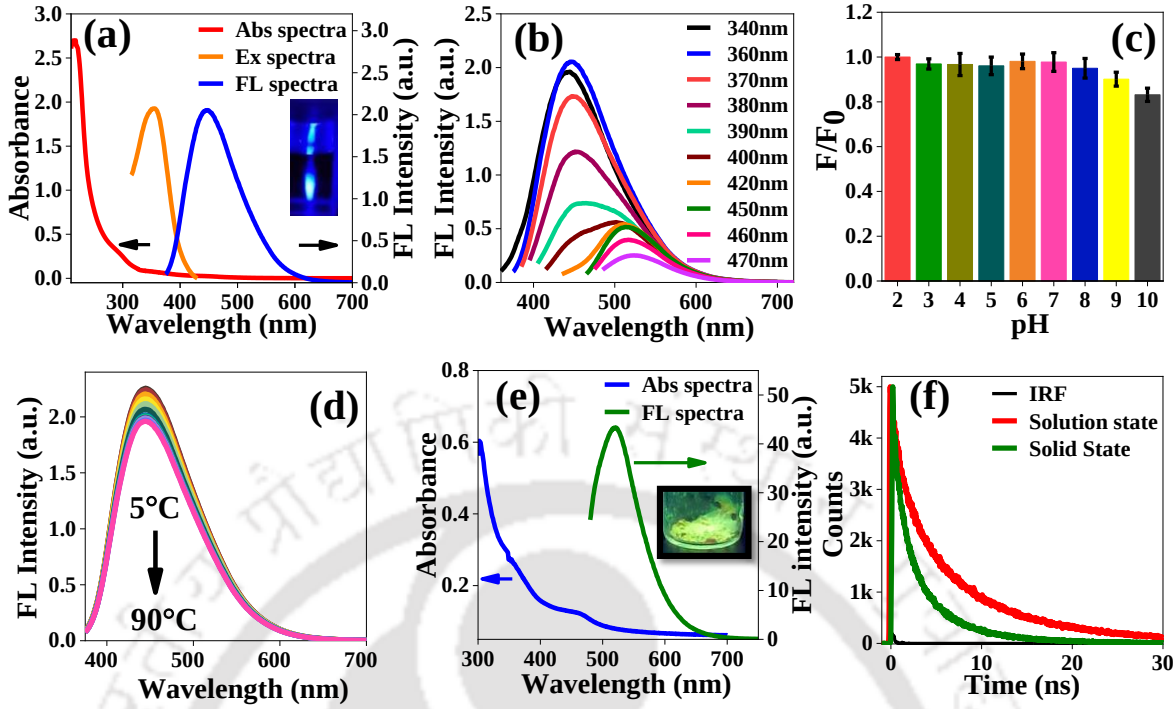

Figure 4.2. (a) UV-vis absorption, fluorescence excitation (λ_{em}= 450 nm), and emission (λ_{ex} = 360 nm) spectra of NCDs (b) Excitation wavelength-dependent emission spectra of NCDs from λ_{ex} from 340 nm to 470 nm with 10 nm interval. (c) pH-dependent fluorescence intensity ratio of NCD where F represents FL intensity at particular pH and F_0 represents FL intensity at pH 2. (d) Temperature-dependent FL spectra; inset shows the ratio of FL intensity change with temperature. (e) Solid-state absorption-emission of NCDs. Inset shows the photograph of the solid-state emission of NCDs under 365 nm UV lamp (f) FL decays of NCDs in solution and solid-state.

The purity of NCDs was also clarified by taking absorption and emission spectra of the 3,6-diaminoacridine molecule (absorption maximum at 445nm, emission maximum at 508 nm, **Figure A.4.3**). In NCDs, no extra peak appears at the mentioned spectral range, confirming the absence of any free 3,6-diaminoacridine molecule. The photograph of NCDs aqueous solution was captured within a spectrofluorometer with an excitation wavelength (λ_{ex}) of 360 nm (inset of **Figure 4.2a**). Like other reported CDs, the emission maximum of NCD also depends highly on the excitation wavelength. When λ_{ex} was varied from 340 nm to 470 nm, the fluorescence (FL) spectrum also shifts towards a higher wavelength indicating the presence of several emissive trap states and size variation (**Figure 4.2b)**. Quantum yield (QY) of the blue-emitting NCD is found to 22.7 % in water at 360 nm excitation, using quinine sulfate (QY = 54.4 % in 0.1 M H_2SO_4) as a reference. The significantly high QY and λ_{ex} –dependent FL behavior may originate from the heterogenic functionality- (such as amino, carboxyl, and hydroxyl groups) induced electronic states. We checked the optical stability under different pH conditions from 2 to 10. We adjust the pH of the PBS medium by adding a diluted solution of NaOH and H_3PO_4. The ratio of FL intensity (F/F_0, where F

represents FL intensity at particular pH and F_0 represents FL intensity at pH 2) remains almost invariable up to pH 8, but decreases by ~10% and ~17%, respectively, at pH 9 and 10 (**Figure 4.2c**), with no recognizable change in the emission maxima. This pH dependency of NCDs may arise due to protonation/deprotonation of the surface functional groups like -COOH/-OH or $-NH_2$. The temperature-dependent FL performance of NCD (**Figure 4.2d**), where we observe only a ~14% reduction of the FL intensity over the 5 – 90 °C temperature range. Thus, the NCD emission profile is quite stable in different challenging environments. Thus, as-prepared NCD is a potential nanoprobe for biomedical applications. Moreover, NCD also exhibits FL in the solid-state displaying absorption and emission maxima at 466 nm and 525 nm, respectively (**Figure 4.2e**). In solid-state the NCDs emit yellowish-green emission (inset of **Figure 4.2e**) which is red shifted by ~75 nm from the solution state.

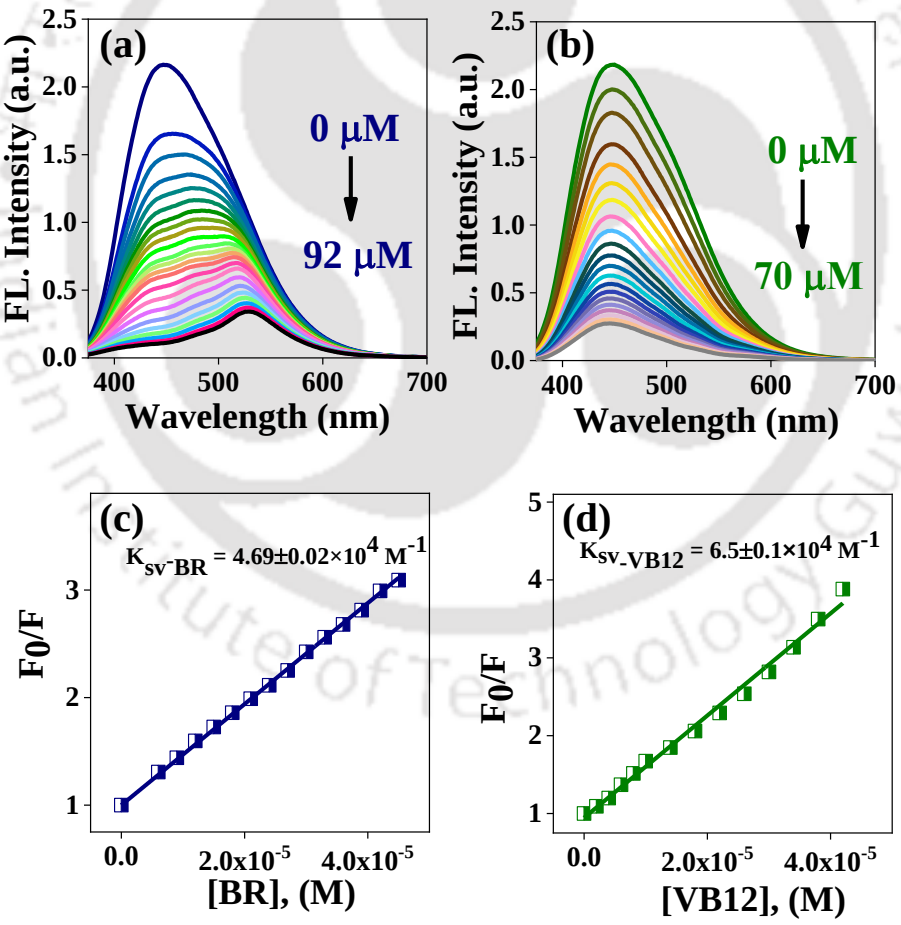

Figure 4.3. Fluorescence response of NCDs toward varying concentrations of (a) BR and (b) VB12 in 10 mM PBS buffer of pH 7.4. Stern–Volmer plots (F_0/F where F_0 and F denotes FL intensity before and after addition of quencher) for the fluorescence quenching of (c) BR and (d) VB12.

The average lifetime of the NCDs in the solution and solid-state are 4.6 ns and 2.0 ns, respectively (**Table A.4.2** and **Figure 4.2f**). The lower lifetime in the solid-state indicates self-quenching, which may occur through the energy-transfer process within the π-π conjugated framework. [61]

4.2.3 Detection of Bilirubin (BR)

The nanoprobe was further introduced for the detection of BR. We checked the time dependence of the fluorescence response towards BR before recording the FL spectrum. **Figure A.4.4a and A.4.4b** show intensity in every 1 min interval up to 10 min, where the intense bluish emission intensity of NCD was diminished instantly after adding BR. The emission intensity (at 450 nm) decreases steadily; quenches up to 24% at 6 μM BR, and further quenches to 85% at 92 μM BR (**Figure 4.3a**). The emission maxima of NCDs were gradually shifted towards a higher wavelength with consecutive additions of BR. The ratio of FL intensity before and after the addition of BR was linearly fitted with Stern-Volmer (S-V) equation up to 45 μM BR concentration (**Figure 4.3c**). The slope obtained from **Figure 4.3c**, denoted as K_{sv} is found to be 4.69×10^4 M^{-1}. The detection limit (LOD) was **89.07 nM** obtained using the standard protocol**,** 3σ/K, where σ is the standard deviation of FL intensity of three blank experiments and K represents the slope**.** This nanomaterial can be utilized for instant detection of free BR.

4.2.4 Detection of Vitamin-B_{12} (VB12)

Furthermore, VB12 was also detected with the NCDs. The emission intensity (at 450 nm) decreases with the subsequent addition of VB12 (0 to 70 μM) without any spectral shift (**Figure 4.3b**). The fluorescence quenching efficiency can be obtained by linearly fitted S-V up to 42 μM VB12 with R^2 value of 0.996 (**Figure 4.3d**). The S-V quenching constant (K_{sv}) was found to be 6.56×10^4 $M^{-1,}$ confirming that NCDs have very high sensitivity towards VB12. The detection limit (LOD) is calculated to be **56.28 nM**.

4.2.5 Selectivity Study

We thoroughly evaluated the selectivity of the nanosensor. In **Figure 4.4a**, the emission signal of NCD remains unchanged after incorporating 1 mM of numerous metal ion (Pb^{2+}, Ag^{+}, Hg^{2+}, Ni^{2+}, Cr^{3+}, Cd^{2+}, Co^{2+}, Cu^{2+}, Fe^{2+}, Fe^{3+}, Zn^{2+}, $S_2O_8^{2-}$, PO_4^{3-}, SCN^{-}, CN^{-}). For BR, we chose a series of biomolecules BSA, HSA, dopamine, levodopa, ascorbic acid, GSH, uric acid, urea, creatinine, hemoglobin, and glucose sucrose for interfering study

(**Figure 4.4b**). The emission intensity of NCDs towards bilirubin co-existing with other congeners (**Figure 4.4c**). Each time the maximum quenching of fluorescence intensity was displayed by free BR. For selectivity of VB12, various competitive vitamins (VB1, VB3, VB5, VB6, VB7, VB9) are checked, but no significant alteration of FL intensity was observed (**Figure 4.4d**). Hence, the nanosensor NCDs was successfully used in the specific recognition of BR and VB12 in the presence of various competitive analytes.

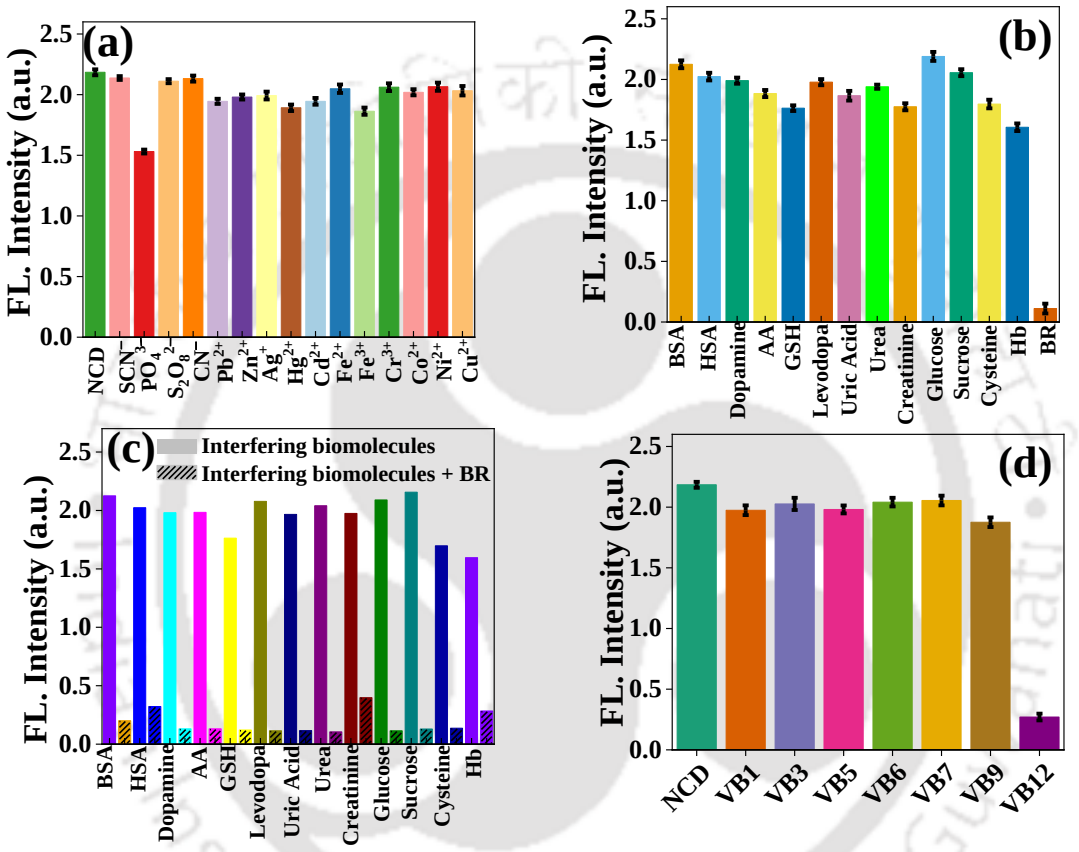

Figure 4.4. (a) Interfering study of NCDs with various metal ions (b) Selectivity study of NCD conducted with different biomolecules along with BR. (c) Fluorescence emission intensity of NCDs towards bilirubin with co-existence of other congeners. (d) Selectivity study of NCDs with various vitamins along with VB12.

4.2.6 Mechanism of detection of BR

Several types of interaction between BR and NCDs may lead to FL quenching, such as ground-state complexation, energy transfer, collision, or through IFE. UV-vis spectroscopy may provide insight into the possibility of any ground-state complex formation between the nanoprobe and quencher. Here, we did not observe any significant spectral change after adding BR (**Figure A.4.5**).

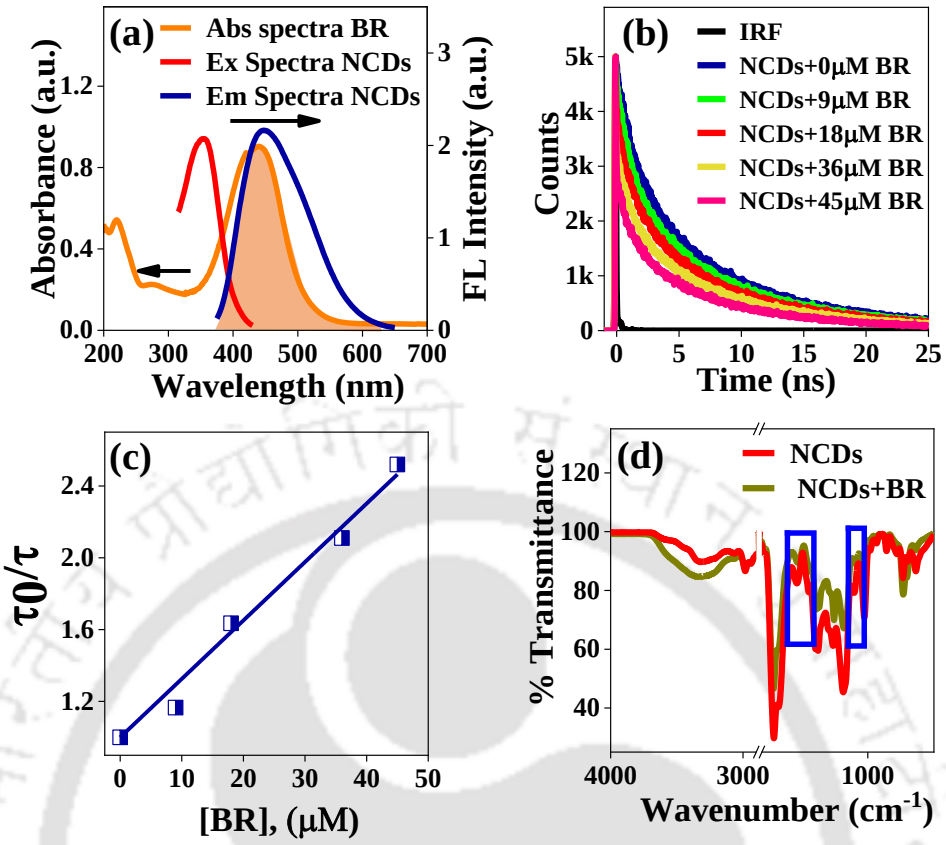

Figure 4.5. (a) Spectral overlap between the absorption spectrum of BR and the excitation and emission spectra of NCDs. (b) Fluorescence decays of NCDs in the presence of various concentrations of BR. (c) The linear relationship between the ratio of the average lifetime (τ_o/τ) against the BR concentration. (d) FTIR spectra of NCDs in the absence and presence of BR.

This result excludes the possibility of any ground-state complexation between NCD and BR. Here, the broad absorption spectrum of BR shows maximum spectral overlap with the emission spectrum of NCD rather than with the excitation spectrum (**Figure 4.5a),** which is the main prerequisite for IFE and FRET to occur. Hence, fluorescence decays were measured in the presence and absence of BR to determine the main reason for the quenching. All decays were fitted in a tri-exponential function (discuss in chapter 1, section).

Figure 4.5b and Table A.4.3 depict a substantial reduction of the average fluorescence lifetime of NCD (τ_{avg} = 4.63 ns) in the presence of 45 μM of BR (τ_{avg} = 1.85 ns), suggesting enhancement of non-radiative pathway or FRET in the NCDs-BR system. Moreover, **Figure 4.5c** shows excellent linearity of the average fluorescence lifetime ratio (τ_o/τ) plot against BR concentration. The slope obtained from the linear fitted plot represents the dynamic quenching constant K_D. The value of K_D is 3.23×10^4 M^{-1} which is remarkably high, confirming that the dynamic quenching is predominant in the fluorescence

suppression process. Bearing in mind the BR's structure, there could be either H-bonding interaction of various hydrophilic groups present in BR moiety and NCD or π–π interaction between NCDs and BR.[62] FTIR analysis was conducted to investigate further molecular interaction between NCDs and BR. The broad peak assigned for -OH and -NH_2 becomes much broader in **Figure 4.5d.** The N-H bending and C-O-C bond vibrations at 1538 cm^{-1} and 1100 cm^{-1} become significantly blue-shifted by 16 cm^{-1} and 12 $cm^{-1,}$ respectively. The shift indicates that the hydroxyl group of BR engages in H-bonding with the surface functional groups of NCDs, which facilitates energy transfer from NCDs (donor) to the acceptor (BR). The emission maxima also shift towards a longer wavelength due to the presence of H-bonding interaction. Considering all the results, we conclude that BR comes at the close proximity of nanoprobe NCDs, facilitating H-bonding between the hydrophilic surface group of the donor-acceptor pair. The extent of overlap between the absorption spectrum of BR and the emission spectrum of NCD was found to be 1.29×10^{13} M^{-1} cm^3 (formula discuss in chapter 1, section)**.** Furthermore, the efficiency of FRET energy transfer was 60.3% in the presence of 45 μM BR. The estimated Förster distance (R_0) and donor-acceptor distance (r_0) values are 4.21 nm and 3.92 nm (section, chapter 1), respectively. The distance between donor-acceptor (r_0) governs the whole FRET process, which falls in the range of 1-10 nm.[63] These results hold an excellent agreement for the FRET process occurring between nanosensor NCD and BR.

4.2.7 Mechanism of detection of VB12

We further used the nanodot for the detection of VB12. The fluorescence intensity was promptly quenched with the subsequent addition of VB12. The UV-vis spectrum of NCD did not alter significantly after adding VB12 (**Figure 4.6a**), nullifying any complex formation between NCD and VB12. Moreover, there is an efficient overlap between the excitation and emission spectra of NCD and the absorption spectrum of VB12 (**Figure 4.6b**), indicating the existence of either the IFE, FRET process, or both.[64, 65] We measured the fluorescence decays to discriminate between the two possibilities (**Figure 4.6c**). The fluoresce decays remain almost invariant in the presence of VB12. The average fluorescence lifetime of the NCD changes from 4.66 ns in the absence of VB12 to 4.40 ns at 70 μM VB12 (**Table A.4.4)**. Thus, we can exclude any possibility of FRET as the contribution is only ~5%. Therefore, IFE is the only possible pathway for the quenching mechanism. The ratio of $F_{corrected}/F_{observed}$ is the correction factor (CF) which was

estimated with various VB12 concentrations and summarized in **Table A.4.5.** The observed quenching efficiency before and after correction of IFE is plotted in **Figure 4.6d**.

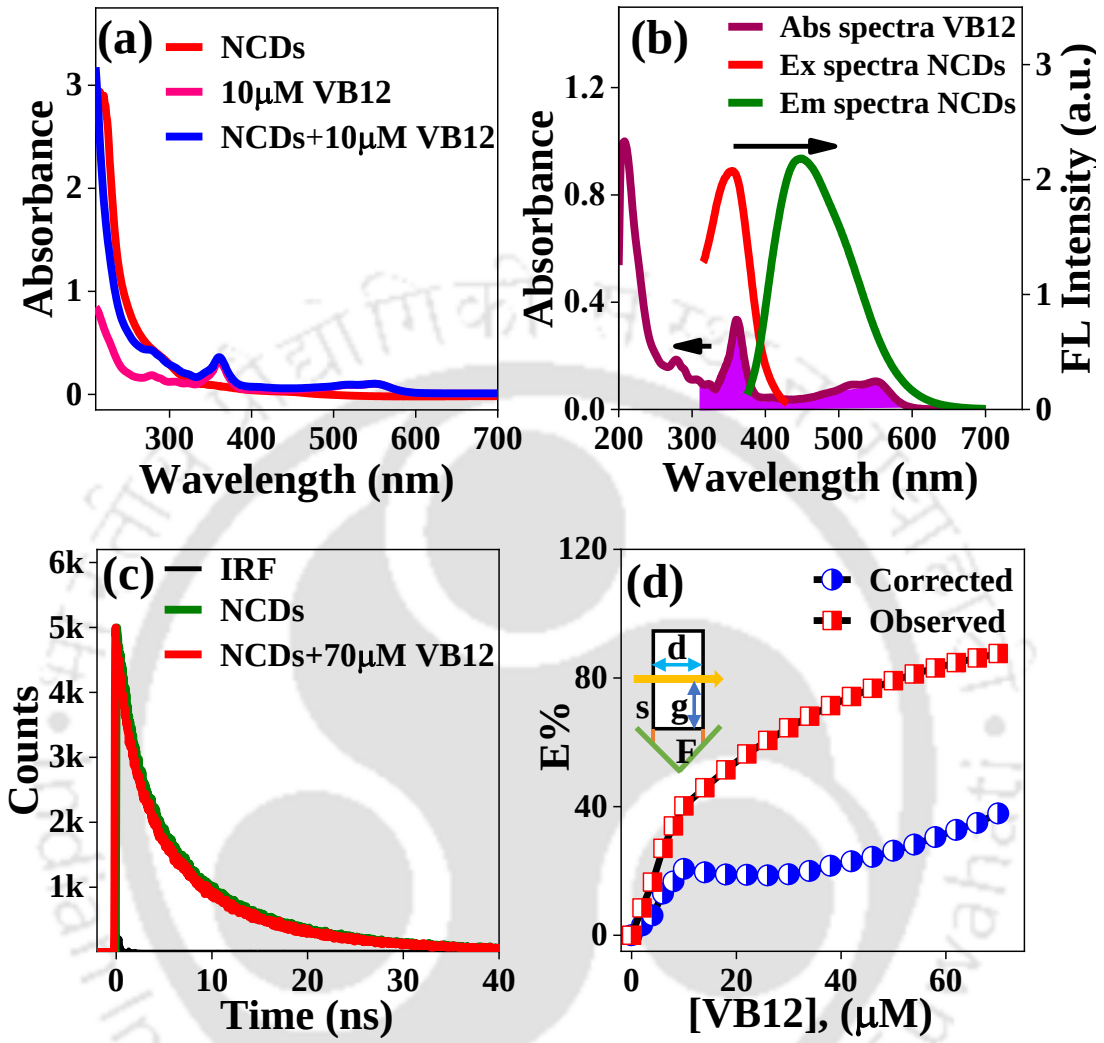

Figure 4.6. (a) Absorption of NCDs, VB12, and NCDs with 10μM VB12. (b) Spectral overlap between absorption spectra of VB12, fluorescence excitation, and emission spectra of NCDs. (c) Fluorescence lifetime curves of NCDs with different concentrations of VB12. (d) Suppressed efficiency (E%) of observed (red curve) and modified (blue curve) measurements for NCDs after each addition of different concentrations of VB12. (inside figure used for IFE equation; described in chapter 1 section).

4.2.8 Biological applications

For potential bio-application of NCDs nanoprobe, the cytotoxicity was vigilantly tested in HeLa cells performing MTT assay. Prior to bio-application studies, the cells were exposed to multiple concentration of NCDs (50, 100, 150, 200, 250, 300, 350, 400, 450, 500 μg/ml) for 12 h for inspection of cell viability. The viability of HeLa cells reduced slowly with increasing concentration of NCD; nevertheless, the overall cell viability remains more than 80% for NCD concentration as high as 500 μg/mL (**Figure 4.7a**). This observation evoked that NCDs exhibit low cytotoxicity and commendable biocompatibility.

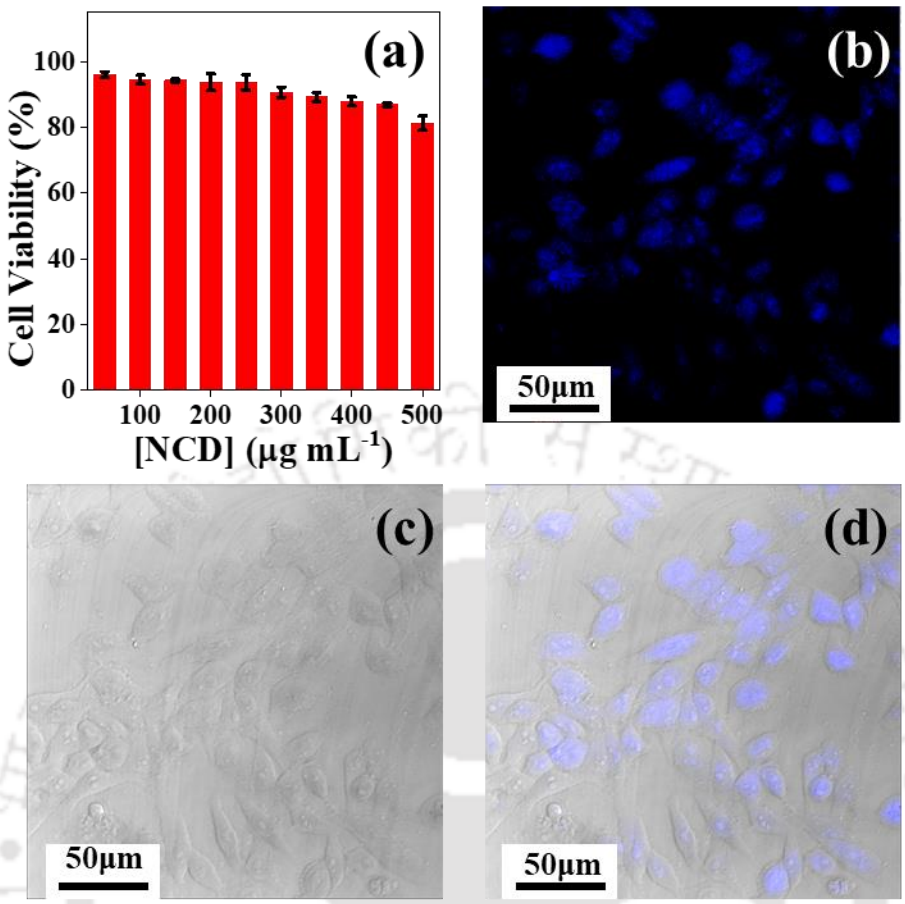

Figure 4.7. (a) Cell viability study of NCDs in HeLa cell for 12 h. (b)Confocal image of HeLa cells in the presence of NCDs (200 μg/mL) under 405 nm laser excitation source. (c) bright field image, (d) Merge image of (b) and (c) in scale bar 50 μm.

After incubating HeLa cells with 200μg/mL NCDs, the cells exhibit a bright blue fluorescence signal when excited with the 405 nm laser excitation source in CLSM (**Figure 4.7b**). In **Figure 4.7c and Figure 4.7d**, it was evident that nanosensor NCDs get preferentially localized into the cytoplasm as well as the nucleus of HeLa cells. When NCD-treated HeLa cells (**Figure 4.8 d-f**) were incubated with two different VB12 concentrations, the fluorescence signal reduces sharply at 24 μM and almost wholly disappears after treating 60 μM VB12 (**Figure 4.8 g-i and Figure 4.8 j-l**). Hence, the NCDs are efficient fluorescent nanoprobes for the recognition of VB12 inside living cells.

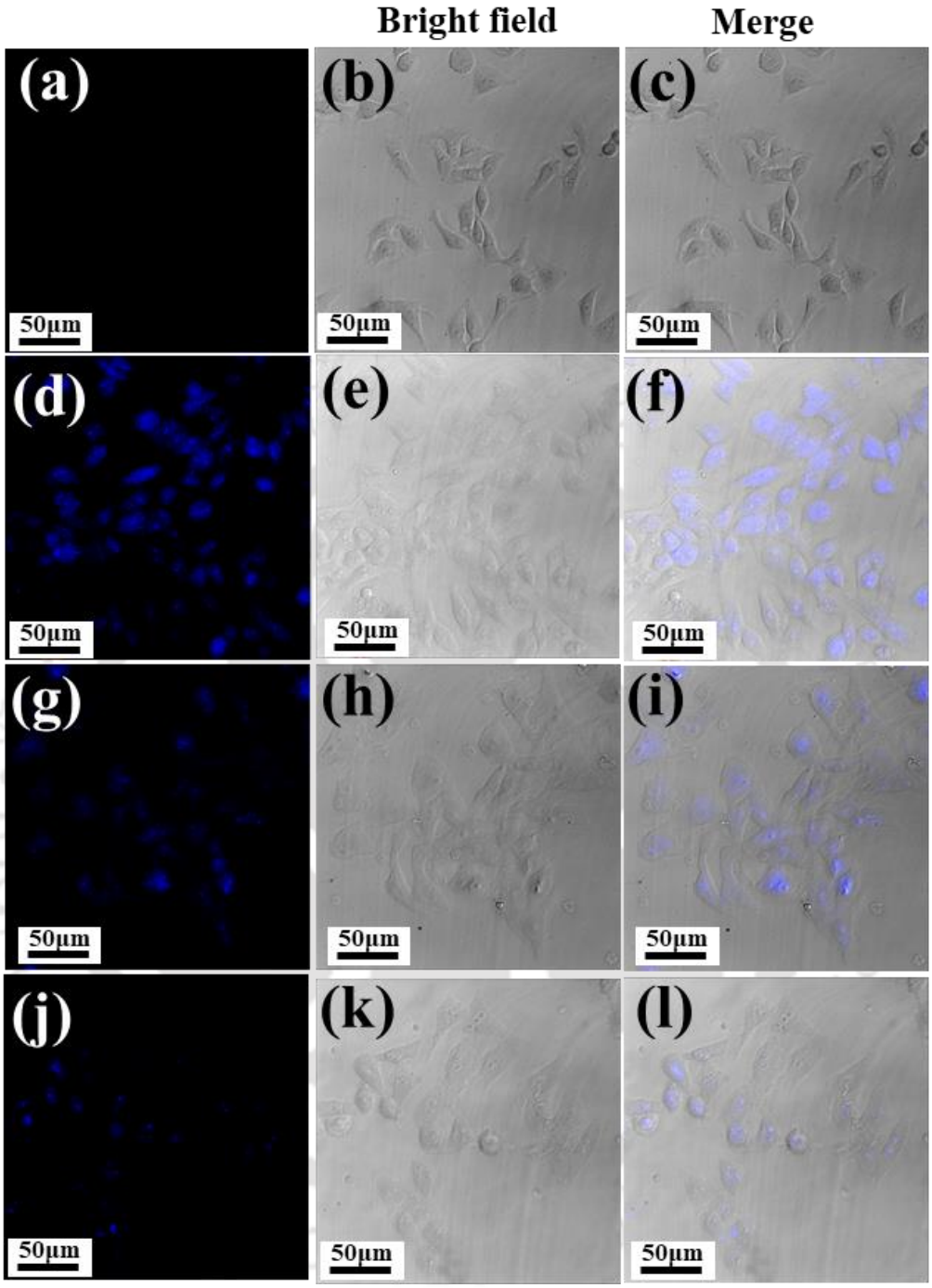

Figure 4.8. Reduction in fluorescence intensity of NCD with VB12. (a)-(c) cell control (d)-(f) 200 µg/mL NCDs treated cells. (g)-(i) cells treated with NCD+24 µM VB12 and (j) to (l) cells treated with NCD+60 µM VB12. The excitation source was 405 nm laser, and the fluorescence signal was recorded in the emission range of 410 nm to 470 nm.

4.3 Conclusion

In summary, a -N functionality incorporated carbon quantum dot was synthesized by adopting inexpensive and simple hydrothermal technique with L-aspartic acid and 3,6-

diaminoacridine hydrochloride used as a precursor. The multifunctional group present at the surface of NCD allows it soluble in both aqueous and organic solvent. NCDs also have solid state luminescence property for which it was applied as security ink application. The NCDs exhibit low cytotoxicity and excellent resistibility under adverse circumstances (pH treatment, UV-irradiation, temperature etc.). The NCD was successfully introduced for very sensitive and highly selective recognition of VB12 and bilirubin in PBS buffer medium; the bright blue fluorescence of NCDs was promptly diminished in the presence of both VB12 and BR with detection limits 56.28 nM and 89.07 nM, respectively. The fluorescence quench follows a very different mechanistic approach for the two analytes. The VB12-induced fluorescence quenching is caused by the IFE phenomenon where BR acts as a favorable FRET acceptor to quench the NCD fluorescence. Moreover, NCDs have also manifested a great potential for cell-imaging in the biological platform.

References

1. H. Li, Z. Kang, Y. Liu and S.-T. Lee, *J. Mater. Chem.*, 2012, **22**, 24230-24253.

2. S. N. Baker and G. A. Baker, *Angew. Chem., Int. Ed.*, 2010, **49**, 6726-6744.

3. V. Singh, K. S. Rawat, S. Mishra, T. Baghel, S. Fatima, A. A. John, N. Kalleti, D. Singh, A. Nazir, S. K. Rath and A. Goel, *J. Mater. Chem. B*, 2018, **6**, 3366-3371.

4. S. Y. Lim, W. Shen and Z. Gao, *Chem. Soc. Rev.*, 2015, **44**, 362-381.

5. Y. Wang and A. Hu, *J. Mater. Chem. C*, 2014, **2**, 6921-6939.

6. S. Mandal, S. R. Prasad, D. Mandal and P. Das, *ACS Appl. Mater. Interfaces*, 2019, **11**, 33273-33284.

7. C. Ji, Y. Zhou, R. M. Leblanc and Z. Peng, *ACS Sensors*, 2020, **5**, 2724-2741.

8. M. J. Molaei, *Talanta*, 2019, **196**, 456-478.

9. B. De and N. Karak, *J. Mater. Chem. A*, 2017, **5**, 1826-1859.

10. V.-D. Dao, P. Kim, S. Baek, L. L. Larina, K. Yong, R. Ryoo, S. H. Ko and H.-S. Choi, *Carbon*, 2016, **96**, 139-144.

11. Z. Li, Q. Chang, C. Xue, H. Wang, N. Li, H. Liu, J. Yang and S. Hu, *Carbon*, 2020, **165**, 175-184.

12. W. U. Khan, D. Wang, W. Zhang, Z. Tang, X. Ma, X. Ding, S. Du and Y. Wang, *Sci. Rep.*, 2017, **7**, 14866.

13. A. Gupta, N. C. Verma, S. Khan, S. Tiwari, A. Chaudhary and C. K. Nandi, *Sensors and Actuators B: Chemical*, 2016, **232**, 107-114.

14. W. Su, R. Guo, F. Yuan, Y. Li, X. Li, Y. Zhang, S. Zhou and L. Fan, *J. Phys. Chem. Lett.*, 2020, **11**, 1357-1363.

15. X. Gong, Q. Zhang, Y. Gao, S. Shuang, M. M. F. Choi and C. Dong, *ACS Appl. Mater. Interfaces*, 2016, **8**, 11288-11297.

16. Y. Li, Y. Zhao, H. Cheng, Y. Hu, G. Shi, L. Dai and L. Qu, *J. Am. Chem. Soc.*, 2012, **134**, 15-18.

17. Q. Xu, T. Kuang, Y. Liu, L. Cai, X. Peng, T. Sreenivasan Sreeprasad, P. Zhao, Z. Yu and N. Li, *J. Mater. Chem. B*, 2016, **4**, 7204-7219.

18. S. Miao, K. Liang, J. Zhu, B. Yang, D. Zhao and B. Kong, *Nano Today*, 2020, **33**, 100879.

19. H. Li, X. He, Z. Kang, H. Huang, Y. Liu, J. Liu, S. Lian, C. H. A. Tsang, X. Yang and S.-T. Lee, *Angew. Chem., Int. Ed.*, 2010, **49**, 4430-4434.

20. Y. Ma, A. Y. Chen, Y. Y. Huang, X. He, X. F. Xie, B. He, J. H. Yang and X. Y. Wang, *Carbon*, 2020, **162**, 234-244.

21. G. Liu, S. Li, M. Cheng, L. Zhao, B. Zhang, Y. Gao, Y. Xu, F. Liu and G. Lu, *New J. Chem.*, 2018, **42**, 13147-13156.

22. J. Liao, Z. Cheng and L. Zhou, *ACS Sustainable Chem. Eng.*, 2016, **4**, 3053-3061.

23. A. Gupta, A. Chaudhary, P. Mehta, C. Dwivedi, S. Khan, N. C. Verma and C. K. Nandi, *Chem. Commun.*, 2015, **51**, 10750-10753.

24. X. Zhu, T. Zhao, Z. Nie, Z. Miao, Y. Liu and S. Yao, *Nanoscale*, 2016, **8**, 2205-2211.

25. Y. Hu, X. Geng, L. Zhang, Z. Huang, J. Ge and Z. Li, *Sci. Rep.*, 2017, **7**, 5849.

26. A. Saravanan, M. Maruthapandi, P. Das, S. Ganguly, S. Margel, J. H. T. Luong and A. Gedanken, *ACS Appl. Bio Mater.*, 2020, **3**, 8023-8031.

27. W. Gao, H. Song, X. Wang, X. Liu, X. Pang, Y. Zhou, B. Gao and X. Peng, *ACS Appl. Mater. Interfaces*, 2018, **10**, 1147-1154.

28. X. Liu, S. Zhang, H. Xu, R. Wang, L. Dong, S. Gao, B. Tang, W. Fang, F. Hou, L. Zhong and A. Aldalbahi, *ACS Appl. Mater. Interfaces*, 2020, **12**, 47245-47255.

29. D. Chang, L. Li, L. Shi and Y. Yang, *Analyst*, 2020, **145**, 8030-8037.

30. T. D. Boyer, K. D. Lindor, A. J. Sanyal and N. A. Terrault, *Zakim and Boyer's Hepatology: A Textbook of Liver Disease E-Book*, Elsevier Health Sciences, 2016.

31. Y.-F. Shen, M.-R. Tsai, S.-C. Chen, Y.-S. Leung, C.-T. Hsieh, Y.-S. Chen, F.-L. Huang, R. P. Obena, M. M. L. Zulueta, H.-Y. Huang, W.-J. Lee, K.-C. Tang, C.-T. Kung, M.-H. Chen, D.-B. Shieh, Y.-J. Chen, T.-M. Liu, P.-T. Chou and C.-K. Sun, *Anal. Chem.*, 2015, **87**, 7575-7582.

32. S.-K. Chou and M.-J. Syu, *Biomaterials*, 2009, **30**, 1255-1262.

33. A. Despopoulos, S. Silbernagl and W. R. Gay, *Color Atlas of Physiology*, G. Thieme, 1991.

34. J. Fevery, *Liver International*, 2008, **28**, 592-605.

35. L. B. VanWagner and R. M. Green, *JAMA*, 2015, **313**, 516-517.

36. R. R. Anjana, J. S. Anjali Devi, M. Jayasree, R. S. Aparna, B. Aswathy, G. L. Praveen, G. M. Lekha and G. Sony, *Microchimica Acta*, 2017, **185**, 11.

37. S. Chakravarty, B. Gogoi, B. B. Mandal, N. Bhardwaj and N. S. Sarma, *Biosensors and Bioelectronics*, 2018, **112**, 18-22.

38. Y. Jia, Y. Hu, Y. Li, Q. Zeng, X. Jiang and Z. Cheng, *Microchimica Acta*, 2019, **186**, 84.

39. P. Berton, R. P. Monasterio and R. G. Wuilloud, *Talanta*, 2012, **97**, 521-526.

40. F. O'Leary and S. Samman, *Nutrients*, 2010, **2**, 299-316.

41. W. He, W. Weng, X. Sun, Y. Pan, X. Chen, B. Liu and J. Shen, *ACS Appl. Nano Mater.*, 2020, **3**, 7420-7427.

42. F. Du, Z. Cheng, M. Kremer, Y. Liu, X. Wang, S. Shuang and C. Dong, *J. Mater. Chem. B*, 2020, **8**, 5089-5095.

43. J. Wang, J. Wei, S. Su and J. Qiu, *New J. Chem.*, 2015, **39**, 501-507.

44. L. Ding, H. Yang, S. Ge and J. Yu, *Spectrochimica Acta Part A: Molecular and Biomolecular Spectroscopy*, 2018, **193**, 305-309.

45. P. D. Khavlyuk, E. A. Stepanidenko, D. P. Bondarenko, D. V. Danilov, A. V. Koroleva, A. V. Baranov, V. G. Maslov, P. Kasak, A. V. Fedorov, E. V. Ushakova and A. L. Rogach, *Nanoscale*, 2021, **13**, 3070-3078.

46. L. Vallan, E. P. Urriolabeitia, F. Ruipérez, J. M. Matxain, R. Canton-Vitoria, N. Tagmatarchis, A. M. Benito and W. K. Maser, *J. Am. Chem. Soc.*, 2018, **140**, 12862-12869.

47. H. Tetsuka, A. Nagoya, T. Fukusumi and T. Matsui, *Adv. Mater.*, 2016, **28**, 4632-4638.

48. J. Yu, C. Xu, Z. Tian, Y. Lin and Z. Shi, *New J. Chem.*, 2016, **40**, 2083-2088.

49. F. Li, J. Zhang, S. Hu and Y. Jia, *ACS Sensors*, 2021, DOI: 10.1021/acssensors.0c02515.

50. T. Zhang, J. Zhu, Y. Zhai, H. Wang, X. Bai, B. Dong, H. Wang and H. Song, *Nanoscale*, 2017, **9**, 13042-13051.

51. L. Wang, X. Zhang, K. Yang, L. Wang and C.-S. Lee, *Carbon*, 2020, **160**, 298-306.

52. Y. Hu, J. Yang, J. Tian and J.-S. Yu, *J. Mater. Chem. B*, 2015, **3**, 5608-5614.

53. F. Arcudi, L. Đorđević and M. Prato, *Angew. Chem., Int. Ed.*, 2016, **55**, 2107-2112.

54. B. Yuan, S. Guan, X. Sun, X. Li, H. Zeng, Z. Xie, P. Chen and S. Zhou, *ACS Appl. Mater. Interfaces*, 2018, **10**, 16005-16014.

55. X. Lu, D. Wang, L. Ge, L. Xiao, H. Zhang, L. Liu, J. Zhang, M. An and P. Yang, *New J. Chem.*, 2018, **42**, 19665-19670.

56. V. D. Dang, A. B. Ganganboina and R.-A. Doong, *ACS Appl. Mater. Interfaces*, 2020, **12**, 32247-32258.

57. X. Ran, Q. Qu, L. Li, L. Zuo, S. Zhang, J. Gui, Y. Kang and L. Yang, *ACS Sustainable Chem. Eng.*, 2018, **6**, 11716-11723.

58. R. Das, A. Bora and P. K. Giri, *J. Mater. Chem. C*, 2020, **8**, 7935-7946.

59. S. R. Anand, A. Bhati, D. Saini, Gunture, N. Chauhan, P. Khare and S. K. Sonkar, *ACS Omega*, 2019, **4**, 1581-1591.

60. S. Pandit, P. Behera, J. Sahoo and M. De, *ACS Appl. Bio Mater.*, 2019, **2**, 3393-3403.

61. Y. Chen, M. Zheng, Y. Xiao, H. Dong, H. Zhang, J. Zhuang, H. Hu, B. Lei and Y. Liu, *Adv. Mater.*, 2016, **28**, 312-318.

62. Y. Du, X. Li, X. Lv and Q. Jia, *ACS Appl. Mater. Interfaces*, 2017, **9**, 30925-30932.

63. K. Shanmugaraj and S. A. John, *Spectrochimica Acta Part A: Molecular and Biomolecular Spectroscopy*, 2019, **215**, 290-296.

64. M. Lin, H. Y. Zou, T. Yang, Z. X. Liu, H. Liu and C. Z. Huang, *Nanoscale*, 2016, **8**, 2999-3007.

65. W. He, Z. Huo, X. Sun and J. Shen, *Microchemical Journal*, 2020, **153**, 104528.

CHAPTER 5

N-Doped Carbon Dots for Visual Recognition of 4-Nitroaniline

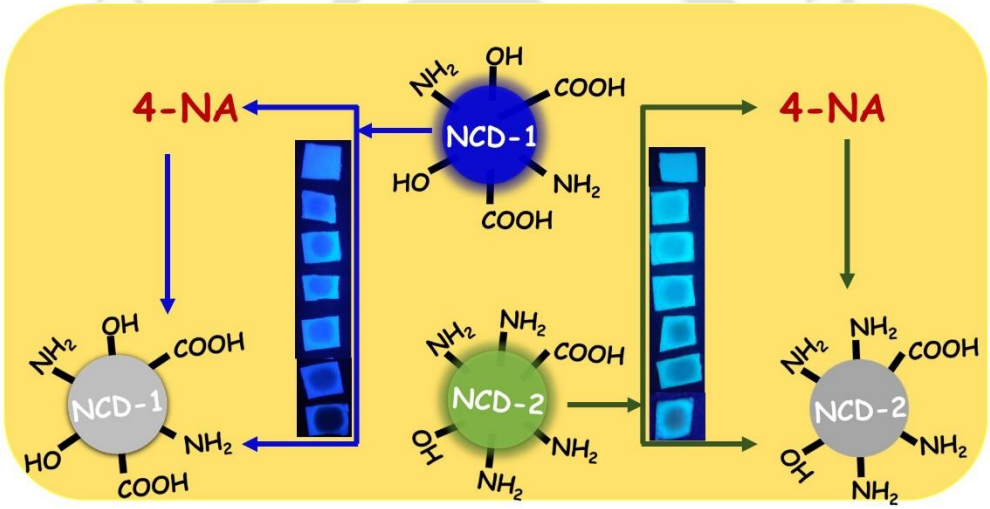

Manuscript: Nilanjana Nandi, Priyanka Sarkar, Kalyanasis Sahu, "N-Doped Carbon Dots for Visual Recognition of 4-Nitroaniline". *ACS Appl. Nano Mater.* 2021, **4**, 9, 9616–9624

[This page was intentionally left blank]

Abstract

Carbon dot (CDs) based fluorometric detection of the industrial pollutant, 4-nitroaniline (4-NA), is a very challenging research arena. Herein, we designed two N-doped CDs (NCDs) with distinct photophysical characteristics by varying the heteroatom percentage. The CD emission color shifts from blue (NCD-1) to green (NCD-2) in water as the heteroatom percentage increases from 8.3 % to 15.8 %. The NCDs also slightly differ in sizes with diameters of 2.5 and 3.6 nm, respectively. In comparison to NCD-2, only NCD-1 exhibits bright green luminescence (521 nm) in solid-state. Besides, the as-prepared NCDs showed excellent solvent-dependent emission behavior; NCD-2 shows a higher spectral shift (76 nm) than NCD-1 (41 nm). NCD-2 displays blue emissions in DMSO and green emissions in water. Both the NCDs perform excellently for discriminative recognition of 4-NA by fluorescence quenching. Detailed investigation revealed that quenching mechanisms depend on the distinct fluorescence properties of NCDs and the solvent medium. In water, NCD-1 fluorescence mainly quenches through inner filter effect (IFE) and photo-induced electron transfer (PET), while a combination of Förster resonance energy transfer (FRET) and PET causes fluorescence quenching for NCD-2. In the DMSO medium, the primary fluorescence quenching of NCD-2 was achieved by FRET, IFE, and a small contribution of PET. Furthermore, an inexpensive portable paper strip was constructed for fast and easy on-site sensing of 4-NA.

5.1 Overview

With the rapid growth of chemical industries, secretion of industrial effluents has increased magnificently and become a burgeoning concern for greenery protection and numerous health issues. Organic amines are extensively preferred intermediate for a wide range of chemical syntheses, such as rubber, dyes, pesticides, pharmaceuticals, and paint.[1, 2] One of the most abundant organic-pollutant, 4-nitroaniline (4-NA), has been found in wastewater and is very poisonous for the aquatic environment, causing hazardous diseases like skin cancer, liver damage, and methemoglobinemia.[3-5] Hence, detection of the lethal 4-NA is very crucial for controlling environmental pollution and several health problems, including aquatic and human bodies.[6]

To date, carbon dots (CDs) are flourishing fluorescent nanosensors because of their tiny size, tunable emission properties, variable solubility in solvents, good quantum yield, and excellent biocompatibility.[7-10] Various heteroatom dopants (boron, nitrogen, and sulfur) can improve their optical properties and quantum yield.[11-14] N-doped CDs (NCDs) are efficient fluorescent nanosensors for various analytes such as metal ions, organic molecules, and bio-molecules via different fluorescence mechanisms.[15-17] Blue emissive NCDs obtained from plant cytoplasm have been employed to recognize 4-NA by hydrogen bonding effect.[1] Recently, CDs derived from oyster mushroom were applied to the detection of nitroarenes, i.e., o-nitroaniline and 4-NA via fluorescence quenching via a combination of different processes, i.e., PET (photo-induced electron transfer) inner filter effect (IFE), PET and Förster resonance energy transfer (FRET).[18]

Herein, we have developed two different N-doped carbon dots with blue (NCD-1) and green (NCD-2) emissions using a simple hydrothermal synthesis of single precursors- 5-aminoisophthalic acid 3,5-diaminobenzoic acid, respectively (**Scheme 5.1**). The variation of the –COOH/-NH_2 ratio from 2:1 (NCD-1) and 1:2 (NCD-2) is a unique way to control the N-content and the surface functionality. The NCD-1 shows substantial solid-state luminescence with an emission maximum at 521 nm, which is ~91 nm red-shifted from the solution state. In addition, NCD-2 possesses different color (green and blue) emissions in two different solvents, water and dimethyl sulfoxide (DMSO). Further, the two nanodots were introduced to recognize 4-NA in an aqueous medium. Most interestingly, the detection mechanism highly depends on the solvent medium and fluorescence property of synthesized nanodots. In NCD-1, the sensing mechanism consists of photo-induced

electron transfer (PET) and the inner filter effect (IFE). However, FRET (Förster resonance energy transfer) and PET were mainly responsible for the quenching of NCD-2 4-NA in aqueous media. All three different processes (IFE, FRET, and PET) operate together for the quenching of NCD-2 emission in the DMSO medium. Moreover, the two nanodots showed excellent sensitivity and selectivity towards other competitive pollutants. Additionally, we have also subsumed paper strip-based detection of 4-NA.

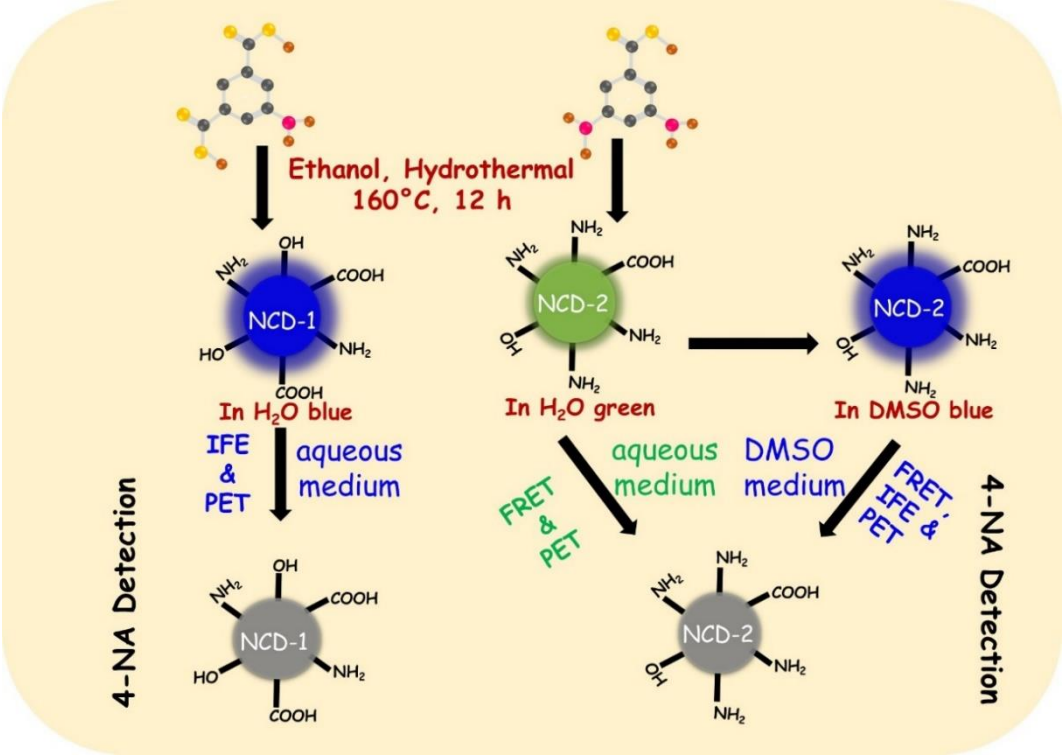

Scheme 5.1. Synthesis route and sensing pathways of 4-NA by NCD-1 and NCD-2

5.2 Results and Discussions

5.2.1. Surface characterization

NCD-1 and NCD-2 were synthesized from 5-aminoisophthalic acid and 3,5-diaminobenzoic acid, respectively adopting a green hydrothermal procedure (see supporting information). The nanodots were spherical with average diameters of NCD-1 and NCD-2 2.5 ± 0.5 nm and 3.6 ± 0.3 nm, respectively, as revealed by transmission electron microscopy (TEM) (**Figure 5.1a and 5.1b**). The HRTEM (high resolution-TEM) image also reveals a lattice spacing of 0.24 nm for both the CDs, which denotes the presence of (100) graphitic plane (inset of **Figure 5.1a** and **5.1b**). XPS analysis reveals an overview of the chemical composition of two nanodots. The nanodots showed dominant XPS peaks

at 284 eV for C 1s, 399 eV for N 1s, and 534 eV for O 1s. The N percentage of NCD-2 (15.8%) is almost double of NCD-1 (8.3%) (**Figure 5.1c and 5.1d**). Detailed deconvolution of high-resolution XPS spectra of C 1s, N 1s and O 1s (**Figure 5.1e to 5.1j**), shows that both the NCDs have similar kind of chemical bonds (**Table A.5.1 and A.5.2**) namely C=C (284.3 ± 0.4 eV), C=O (288.8 ± 0.1 eV), C-N (285.1 ± 0.4 eV), C=N (286±0.2 eV)[19-21], pyridinic-N (398.9 ± 0.2 eV), amino-N (399.2±0.5 eV), pyrrolic-N (400±0.3 eV),[22, 23] C-O (531 eV), C-OH (533.3±0.1 eV), C-O-C (531.8±0.2 eV) and O-C=O (534.1±0.2 eV).[24-26] In comparison to NCD-1, NCD-2 has a higher percentage of amino-N, C=C, and C-O-C chemical bondings, suggesting more heterogeneity at the surface.

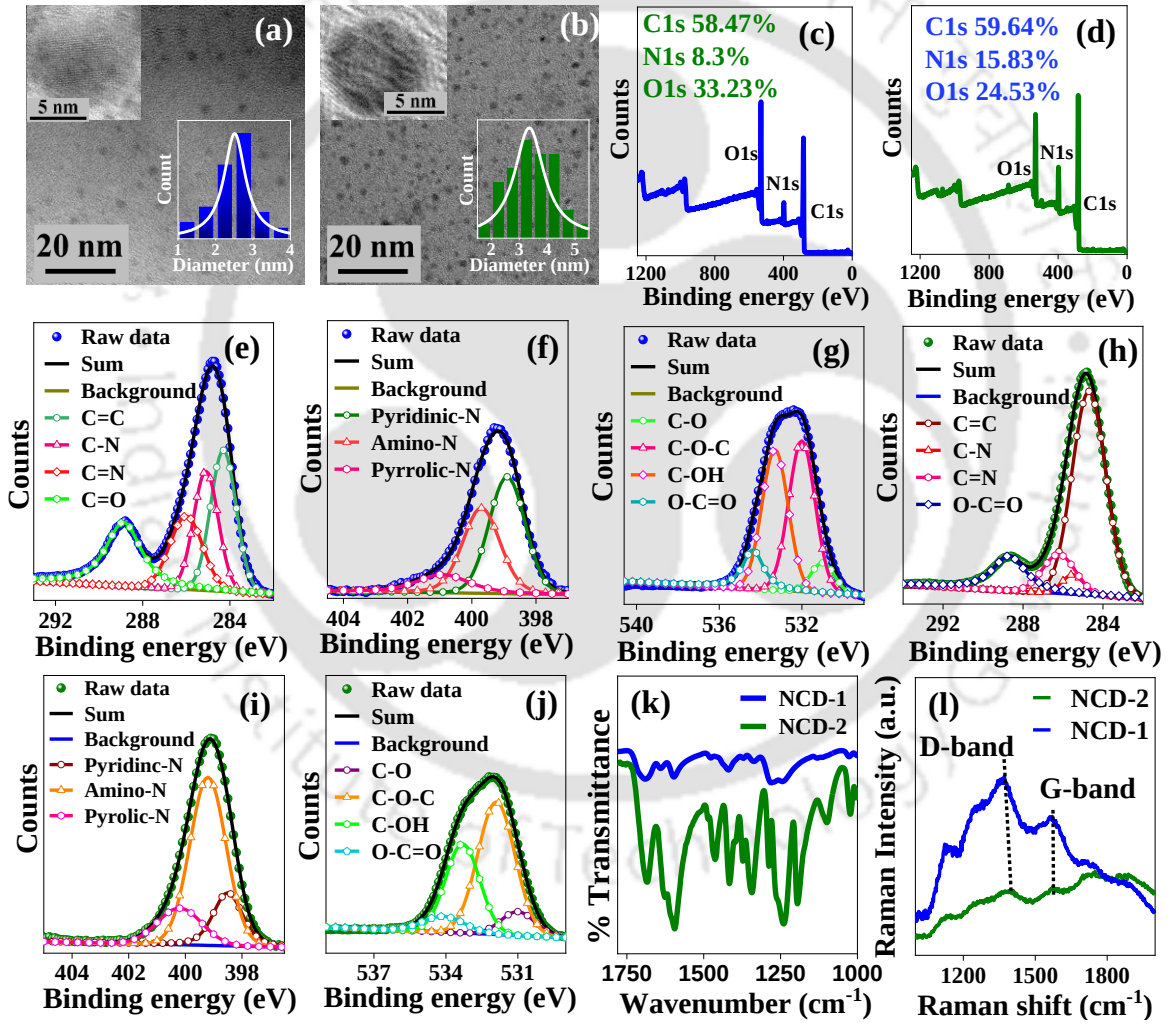

Figure 5.1. (a) TEM image of NCD-1. (b) TEM image of NCD-2. Inset graphs are referred to size distribution curve and HRTEM image.Full range XPS spectra of NCD-1 (c), NCD-2 (d). Deconvoluted XPS spectra of NCD-1 (e) C 1s, (f) N 1s, (g) O 1s. Deconvoluted XPS spectra of NCD-2 (h) C 1s, (i) N 1s, (j) O 1s. (k) IR spectra in the range from 1800-1000 cm^{-1}. (l) Raman spectra of NCD-1 and NCD-2.

The surface functionalities were further examined by Fourier-transformed infrared (FTIR) analysis (**Figure A.5.1 and Figure 5.1k**). Two nanodots exhibit prominent peaks in the

3436-3209 cm^{-1} range for -OH/-NH_2 functional groups and 1691-1596 cm^{-1} range for carbonyl functionalities arising from -COOH and O=C-NH. The N functionality, i.e., C-N and C=N stretching vibrations appear at 1464 to 1417 cm^{-1}, respectively, and the peaks from 1265 cm^{-1} to 1033 cm^{-1} appear because of C-O, C-O-C, C-NH-C bonds.[27-30] Thus, both XPS study and FTIR spectral analysis hold good agreement about the edge functionality of NCDs. For more endorsement about the structural composition, Raman analysis was conducted (**Figure 5.1l**). For NCD-1, the Raman-D and G bands were observed at 1370 cm^{-1} and 1575 cm^{-1}, which denote various vacancy states and sp^2 hybridized carbon frames, respectively. For NCD-2, Raman-D and G bands are located at 1385 cm^{-1} and 1576 cm^{-1}, respectively. In NCD-2, the Raman-D band is blue-shifted by ~15 cm^{-1} from NCD-1, indicating the rise of distortion of the lattice by increasing nitrogen functionality. Moreover, some additional peaks appear at 1120 cm^{-1}, 1245 cm^{-1}, and 1680 cm^{-1} which may be assigned to C-H, C=O and C=N functional groups.[31]

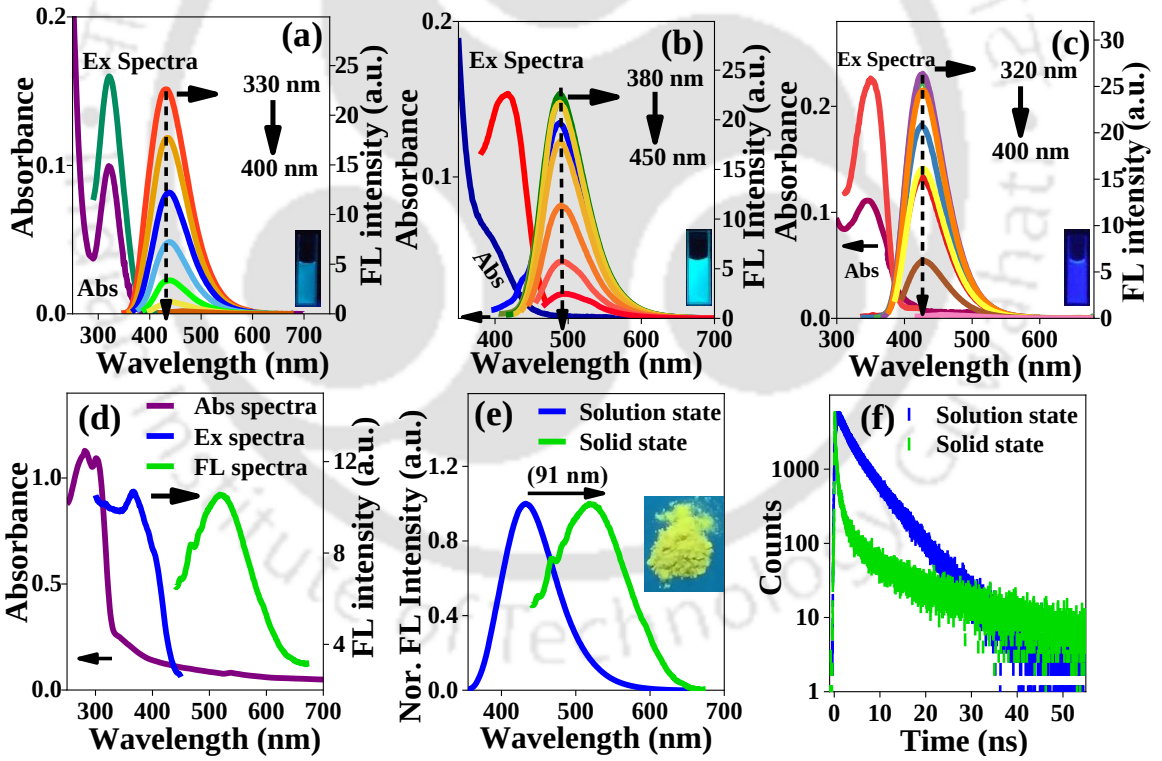

Figure 5.2. (a) UV-vis absorption, excitation (λ_{em} = 430 nm), and emission spectra of NCD-1 in water medium at different excitation wavelengths t. Inset shows a photograph of NCD-1 aqueous solution under 365 nm UV lamp. (b) UV-vis absorption spectra, excitation (λ_{em} = 490 nm) and excitation dependent emission spectra of NCD-2 in the aqueous medium. Inset photograph of NCD-2 aqueous solution under 365 nm UV lamp. (c) Uv-vis absorption spectra, excitation (λ_{em} = 425 nm) and excitation dependent emission spectra of NCD-2 in DMSO solvent. Inset photograph of NCD-2 DMSO solvent under 365 nm UV lamp. (d) Absorption, excitation and fluorescence spectra of NCD-1 in the solid state under 360 nm excitation. (e) Spectral shift between NCD-1 aqueous solution to solid-state. Inset photograph of NCD-1 solid under 365 nm excitation. (f) Fluorescence decays of NCD-1 in aqueous solution and solid-state.

5.2.2. Photo-physical Properties

The optical properties of the synthesized two nanodots were thoroughly investigated by various spectroscopic techniques- UV-vis absorption, excitation, and fluorescence (FL) spectroscopy. In an aqueous medium, the lowest energy absorption bands of NCD-1 and NCD-2 were located at 330 nm and 410 nm, respectively (**Figure 5.2a and 5.2b**), which indicates n-π* transition of C=O, C=N heteroatomic moieties. Both nanodots show excitation wavelength-independent emission behavior which is quite rare and only observed for highly pure CDs. The emission maxima of NCD-1 and NCD-2 in aqueous media were at 430 nm (λ_{ex} = 330nm) and 490 nm (λ_{ex} = 400nm), respectively.

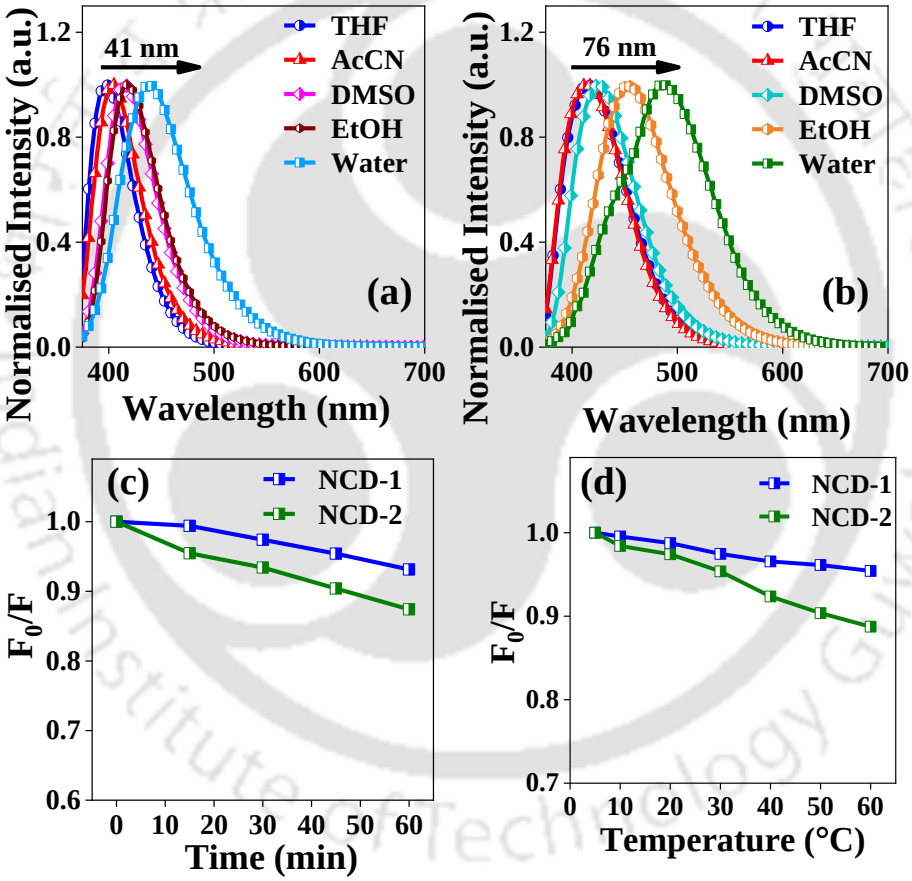

Figure 5.3. Solvent dependent spectral shift (a) NCD-1, (b) NCD-2. (c) UV-irradiation study, (d) Temperature dependent emission stability study.

Interestingly, NCD-2 shows blue emission in DMSO media; the lowest energy absorption band and the FL peak are centered at 350 nm and 425 nm, respectively (**Figure 5.2c**). The measured quantum yield for NCD-1 is 15.6 %, and NCD-2 is 14.7 % in an aqueous medium, whereas NCD-2 shows 22.7 % quantum yield in DMSO.

Interestingly, NCD-1 shows excellent solid-state emission. The solid NCD-1 exhibits green emission at 521 nm when excited at 360 nm (**Figure 5.2d**), independent of excitation wavelength. The FL maximum was dramatically red-shifted by ~91 nm (**Figure 5.2e**) and the average lifetime (0.39 ns) is drastically reduced in comparison to the solution (2.47 ns) state (**Table A.5.3 and Figure 5.2f**) due to aggregation caused quenching.[32, 33]

Both the CDs show solvent-dependent emission property; emission maximum undergoes red-shift with increasing the solvent polarity from tetrahydrofuran (THF) to water. NCD-1 depicts 41 nm, while NCD-2 shows a 76 nm emission shift (**Figure 5.3a and 5.3b**). This solvent-induced spectral shift also inferred that NCD-2 is more polar, containing a more heterogeneous surface than NCD-1. The stability of FL intensity is also verified by changing temperature and UV-light treatment. The ratio of FL intensity remains almost unchanged after UV-light treatment for 1 hour and varying temperature from 5 ¬ 60 °C (**Figure 5.3c and 5.3d**).

5.2.3. Detection of 4-NA

Following the excellent emission properties of the NCDs, their sensing abilities as a fluorescent chemosensor have been investigated for a diverse range of organic amines such as 4-NA, 3-nitroaniline (3-NA), 2-nitroaniline (2-NA), 2,4-dinitroaniline (DNA), aniline, nitrobenzene, triethylamine (TEA) and ethylenediamine (EDA). The FL intensities of NCD-1 and NCD-2 efficiently quench upon successive addition of 4-NA (**Figure 5.4a and 5.4b**). Since the nanodot NCD-2 displays very different emissions in water (green) and DMSO (blue), we checked their sensing efficiency in both media. The sensing ability of NCD-2 in DMSO medium is quite comparable to the aqueous medium (**Figure 5.4c).**

Accordingly, the FL intensity ratio of two nanodots (I_0/I, where I_0 and I symbolize FL intensity before and after addition of 4-NA) enormously increases with increasing concentration of 4-NA (**Figure 5.4d and 5.4e**) in the aqueous medium. At lower concentration, the Stern-Volmer (S-V) plot follows linearity against the concentration of 4-NA (insets of **Figure 5.4d** and **5.4e)**. The K_{SV} (S-V constant) values are $1.4 \pm 0.2 \times 10^4$ M^{-1} and $2.9 \pm 0.1 \times 10^4$ M^{-1} for NCD-1 and NCD-2, respectively. The K_{SV} value for NCD-2 is about double of NCD-1, accounting that NCD-2 is more sensitive towards 4-NA. The detection limit is estimated to be 111.6 nM and 68.9 nM for NCD-1 and NCD-2, respectively in the water medium. Now, the S-V constant for NCD-2 in DMSO medium is $2.7 \pm 0.1 \times 10^4$ M^{-1} which is almost comparable with after linear fitting of the ratio of FL

intensity against concentration of 4-NA up to 48 µM for NCD-2 in DMSO medium (**Figure 5.4f**). The calculated LOD value is 36 nM which is lower than water medium.

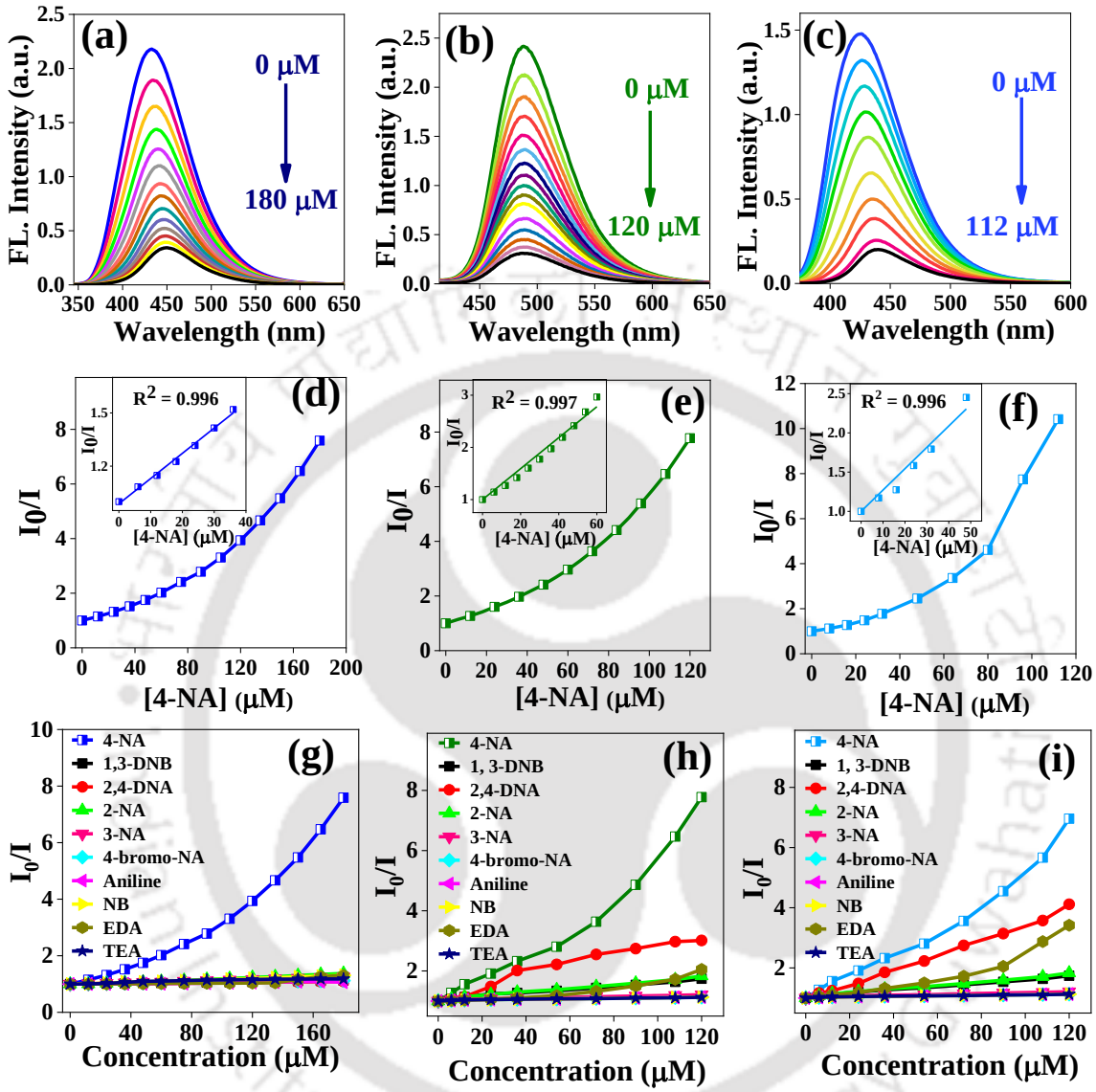

Figure 5.4. (a-c) Quenching of emission spectrum of (a) NCD-1 in aqueous medium, (b) NCD-2 in aqueous medium and (c) NCD-2 in DMSO medium with gradual addition of 4-NA; (d-f) Variations of FL intensity ratio (I_0/I where I_0 and I refer to maximum intensity in the absence and presence of 4-NA) of (d) NCD-1 in aqueous medium, (e) NCD-2 in aqueous medium and (f) NCD-2 in DMSO medium; insets show the linear S-V fitting in the low concentration regime. (g-i) FL quenching plot of different competitive aniline derivatives along with 4-NA and for (g) NCD-1 in the aqueous medium, (h) NCD-2 in the aqueous medium and (i) NCD-2 in DMSO medium.

5.2.4. Selectivity Studies in aqueous and DMSO medium

Several competitive aniline derivatives were examined under the same experimental condition to ascertain the selectivity of the NCDs towards 4-NA. No considerable deviations in the FL intensity of two nanodots were perceived for any derivatives except 4-NA in the aqueous media. However, some derivatives can quench NCD-2 emission in the

DMSO medium, which follows the order 4-NA> 2,4-DNA> EDA. The I_0/I plots for other competitive nitro-compounds are also estimated for the two nanodots (**Figure 5.4g, 5.4h and 5.4i),** which cogently supports that both NCDs are highly selective and drastic quenching of FL intensity was triggered only by 4-NA. Moreover, some other metal ions which might coexist in water samples (e.g., Na^+, K^+, Mn^{2+}, Zn^{2+}, Cr^{3+}, Co^{2+}, CN^-, I^-, Br^-, HCO_3^-, CO_3^{2-}), did not impinge the FL intensity of NCD-1 and NCD-2 in both media (**Figure A.5.2a to A.5.2c**).

5.2.5. Sensing Mechanism in Aqueous Medium

Several mechanistic pathways such as Forster resonance energy transfer (FRET), photo-induced electron transfer (PET), formation of ground-state complex, and inner filter effect (IFE) commonly account for FL quenching. In an aqueous medium, the absorbance value of NCD-1 and NCD-2 is only increased without the appearance of any new peak in the whole UV-vis region (**Figure A.5.3a and Figure A.5.3b**). Hence, we may omit the possibility of ground-state complex formation between the nanodots and 4-NA.

For NCD-1, both the excitation and FL spectra overlap markedly with the absorption spectrum of 4-NA (**Figure 5.5a**), which is the utmost prerequisite for FRET or IFE to operate. Fluorescence decays were subsequently measured to distinguish between the two mechanisms. It is very clear from **Figure 5.5b** that the lifetime of NCD-1 remains almost unchanged after the addition of 180 µM 4-NA (**Table A.5.4**). Thus, the possibility of FRET between NCD-1 and 4-NA can be nullified. Hence, IFE should be a significant FL suppression process in NCD-1 (**Figure 5.5c**). However, IFE correction, suggests that its contribution is ~55 % to the overall quenching process (**Table A.5.5**).

We evaluate the energy value by considering frontier molecular orbitals of the NCDs and 4-NA to determine the other possible quenching mechanisms. Density functional theory (DFT) calculation was conducted for 4-NA and other targeted competitive organic compounds (**Figure A.5.4**) to determine HOMO (highest occupied molecular orbital) and LUMO (lowest unoccupied molecular orbital) energies. The HOMO and LUMO energy levels of NCD-1, and NCD-2, were obtained from UV-onset (**Figure A.5.3d and Figure A.5.3e**) and cyclic voltammetry study (**Figure 5.5d**). A successful PET may occur from LUMO of NCD-1 (-2.08 eV) to LUMO of 4-NA (-2.41 eV) (**Figure 5.5e**). Therefore, we can conclude that there is an almost equal contribution of IFE and PET for diminishing the FL intensity of NCD-1.

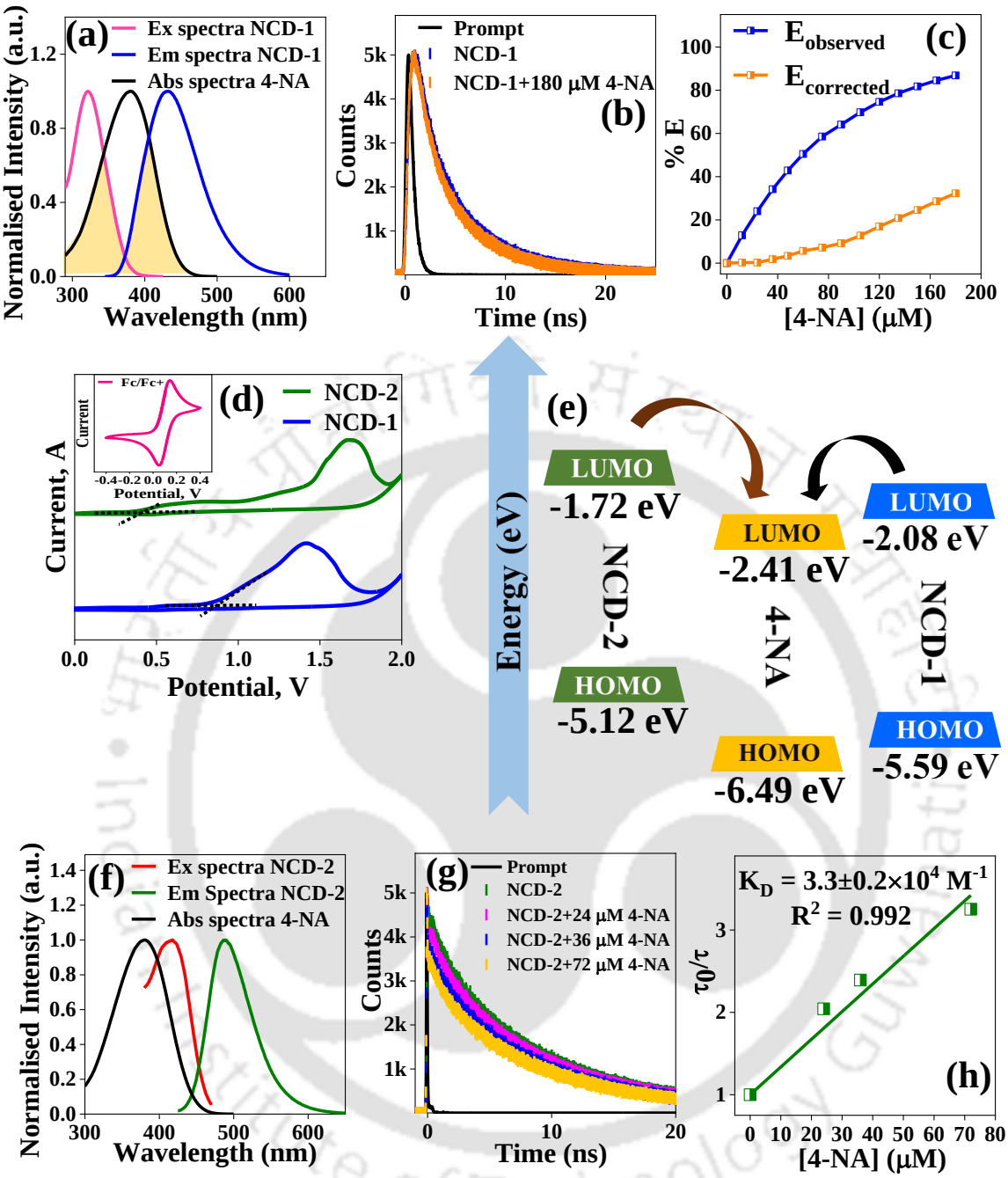

Figure 5.5. (a) Spectral overlap between excitation, emission spectra of NCD-1 with absorption spectrum of 4-NA. (b) FL decays of NCD-1 in the absence and presence of 180 µM of 4-NA. (c) Suppressed FL efficiency (E%) of observed (blue curve) and modified (orange curve) measurements for NCD-1 after each addition of various concentrations of 4-NA. (d) cyclic voltametric study of NCD-1 and NCD-2 on glassy carbon electrode using 0.1 M tetrabutylammonium hexafluorophosphate (TBAF6) as a reference electrolyte in acetonitrile solution . (e) Pictorial representation of PET mechanism from NCD-1 and NCD-2 to LUMO level of 4-NA LUMO level. (f) Spectral overlap between excitation, emission spectra of NCD-2 with absorption spectra of 4-NA. (g) Fluorescence decay curve of NCD-2 aqueous solution with addition different concentration of 4-NA. (h) Linear fitted curve of ratio of changing average lifetime value (τ_0/τ) against 4-NA.

For NCD-2 in the aqueous medium, there is also a considerable spectral overlap (absorption of 4-NA, FL emission, and excitation of NCD-2), as shown in **Figure 5.5f**. Interestingly,

the average lifetime of NCD-2 decreases from 4.61 ns to 1.41 ns after the addition of 72 µM 4-NA (**Table A.5.6 and Figure 5.5g**). This observation points towards the FRET mechanism. Detailed calculation shows that the involvement of FRET between NCD-2 and 4-NA is ~ 69%. The dynamic quenching rate constant (K_D) is $3.3 \pm 0.2 \times 10^4$ M^{-1} obtained by plotting ratio of the average lifetime (τ_0/τ, τ_0, and τ refer lifetime before and after addition of 4-NA) against 4-NA concentration (**Figure 5.5h**). The IFE contribution is too insignificant (2%) in this case (**Figure A.5.3f and Table A.5.7**). Furthermore, to elucidate the remainder quenching effect, HOMO-LUMO calculations of this green emissive nanodot and 4-NA are performed. The LUMO (-1.72 eV) of NCD-2 is lying above the LUMO level of 4-NA (-2.39 eV), which also signifies a quite favorable electron transfer from NCD-2 to 4-NA (**Figure 5.5e**). Hence, the quenching of NCD-2 by 4-NA is driven by the FRET and PET combination. However, the PET contribution in quenching is slightly less than the NCD-1 due to less effective energy level matching.

5.2.6. Sensing Mechanism of NCD-2 in DMSO

Like the aqueous medium, no apparent change of the absorption pattern of NCD-2 was also noticed in DMSO after adding 4-NA (**Figure A.5.3c**), eliminating the scope of ground-state complex formation. Significant spectral overlap of the absorption spectrum of 4-NA with the excitation and emission spectra of NCD-2 gives rise to the possibility of IFE and FRET as possible quenching mechanisms (**Figure 5.6a**). Fluorescence decay measurements showed that the average decay time regularly decreases from 4.93 ns (0 µM 4-NA) to 2.86 ns (112 µM 4-NA), elucidating the FRET possibility in DMSO solvent (**Figure 5.6b and Table A.5.8**). The K_D value in the DMSO medium was found to be $5.9 \pm 0.4 \times 10^3$ M^{-1} in **Figure 5.6c,** which is very low compared to the water medium. Additionally, the IFE effect is also present in DMSO solvent. The estimated contribution of IFE was ~ 37% (**Figure 5.6d and Table A.5.9**). Therefore, in DMSO solvent major FL quenching effect came from FRET (~ 58%), IFE (~ 37%) mechanism, and remaining quenching coming from PET pathways. For better understanding, we provided a table containing solvent dependent detection mechanism pathways for the synthesized nanodot (**Table 5.1**)

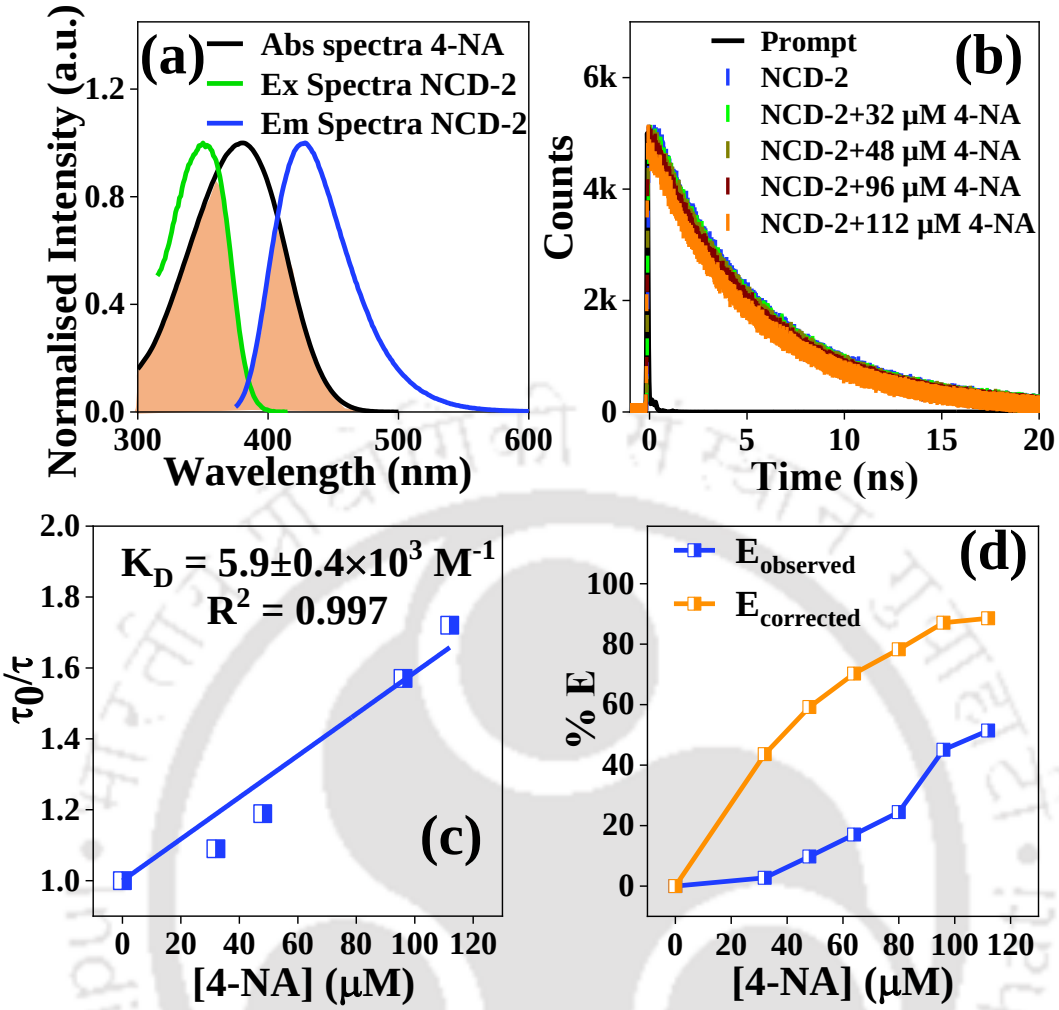

Figure 5.6. (a) Spectral overlap between excitation, emission spectra of NCD-2 with absorption spectra of 4-NA. (b) Decay profile of NCD-2 in DMSO with different concentration of 4-NA. (c) Linear fitted curve of ratio of changing average lifetime value (τ_0/τ) against 4-NA. (d) Suppressed FL efficiency (E%) of observed (sky-blue curve) and modified (orange curve) measurements for NCD-1 after each addition of various concentrations of 4-NA.

5.2.7. Solid State Detection of 4-NA

The application of two nanodots was further extended for paper strip-based detection of 4-NA. Several paper strips were uniformly coated by NCD-1 and NCD-2 aqueous solutions and dried in a desiccator for 24 h. Afterward, 5 µL of several concentrations of 4-NA ranging from 10^{-8} M to 10^{-1} M was dropped on the dried filter paper strips. In normal light no spot is appear in the paper strips, while a visible dark spot appeared underneath the UV lamp (365 nm) at the droplet position (**Figure 5.7a** to **5.7d**). The dark spot can be visibly recognized even at an ultralow concentration of 4-NA (10^{-7} M). Therefore, this can be a facile strategy for the rapid detection of 4-NA.

Table 5.1. List of mechanism pathways followed by NCD-1 and NCD-2 in aqueous and DMSO medium.

Synthesized nanodots	Solvent	FL property	Primary detection mechanism	Secondary detection mechanism	Additional detection mechanism
NCD-1 (Blue emission)	Water	Excitation: 330 nm Emission: 430 nm	IFE (~ 55%)	PET	
NCD-2 (Green emission)	Water	Excitation: 410 nm Emission: 490 nm	FRET (~ 69%)	PET	IFE (~2%)
NCD-2 (Blue emission)	DMSO	Excitation: 350 nm Emission: 425 nm	FRET (~ 58%)	IFE (~ 37%)	PET

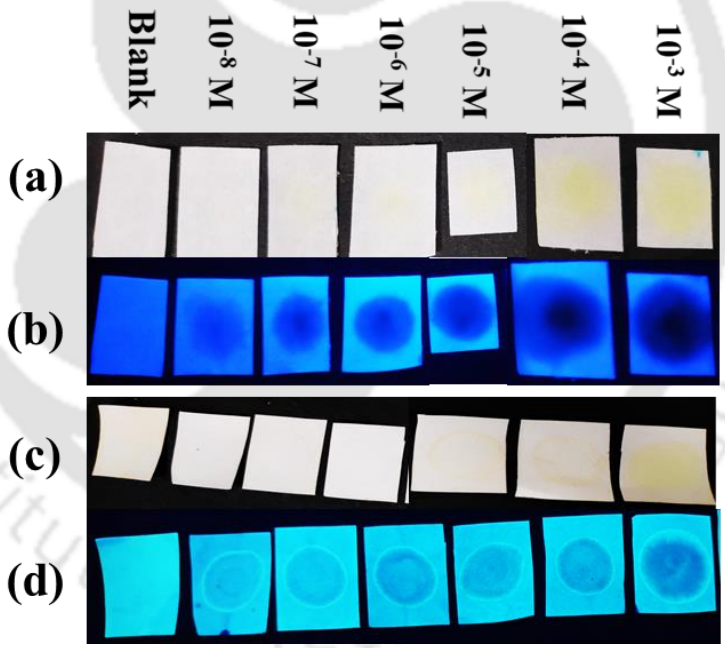

Figure 5.7. (a) NCD-1 paper strips for solid-phase detection of 4-NA. (b) NCD-2 paper strips for on-site recognition of 4-NA.

5.3 Conclusion

In this report, two nanodots NCD-1 and NCD-2, with varying N-content, have been synthesized with blue and green emissions in an aqueous medium through a cost-effective, one-pot hydrothermal method. The FL properties of the NCDs have different prospects; NCD-1 has outstanding solid-state emission properties while NCD-2 exhibits different

color emissions in water (green) and DMSO (blue). Both the NCDs act as excellent fluorescence sensors for 4-NA in water by triggering strong quenching. Moreover, NCD-2 also demonstrates excellent sensing ability in DMSO solvent. Interestingly, the fluorescence quenching mechanisms differ in each case; for NCD-1 in water, PET and IFE dominate, whereas FRET and PET are crucial for NCD-2 in water, and all three FRET, IFE, and PET operate together for NCD-2 in DMSO medium. Additionally, two NCD systems were applied paper strip-based detection of 4-NA, revealing promising results. Finally, it can be concluded that this approach will be very useful for the mechanistic investigation of organic amine detection and a practical solution for the quick sensing of 4-NA.

References

1. H. Yuan, D. Li, Y. Liu, X. Xu and C. Xiong, *Analyst*, 2015, **140**, 1428-1431.

2. C. E. Agudelo-Morales, O. F. Silva, R. E. Galian and J. Pérez-Prieto, *ChemPhysChem*, 2012, **13**, 4195-4201.

3. H. M. Pinheiro, E. Touraud and O. Thomas, *Dyes Pigms.*, 2004, **61**, 121-139.

4. L. M. Games and R. A. Hites, *Anal. Chem.*, 1977, **49**, 1433-1440.

5. J. Wang, G. Wang, G. A. S. Ansari and M. F. Khan, *Toxicol. Appl. Pharmacol.*, 2008, **230**, 227-234.

6. R. Benigni and L. Passerini, *Mutat Res Rev Mutat Res*, 2002, **511**, 191-206.

7. S. Mandal, S. R. Prasad, D. Mandal and P. Das, *ACS Appl. Mater. Interfaces*, 2019, **11**, 33273-33284.

8. S. N. Baker and G. A. Baker, *Angew. Chem., Int. Ed.*, 2010, **49**, 6726-6744.

9. S. Y. Lim, W. Shen and Z. Gao, *Chem. Soc. Rev.*, 2015, **44**, 362-381.

10. Y. Wang and A. Hu, *J. Mater. Chem. C*, 2014, **2**, 6921-6939.

11. N. T. N. Anh, A. D. Chowdhury and R.-a. Doong, *Sens. Actuators B Chem.*, 2017, **252**, 1169-1178.

12. W. Gao, H. Song, X. Wang, X. Liu, X. Pang, Y. Zhou, B. Gao and X. Peng, *ACS Appl. Mater. Interfaces*, 2018, **10**, 1147-1154.

13. A. B. Ganganboina, A. Dutta Chowdhury and R.-a. Doong, *ACS Appl. Mater. Interfaces*, 2018, **10**, 614-624.

14. M. Amjadi, J. L. Manzoori, T. Hallaj and N. Azizi, *J. Lumin.*, 2017, **182**, 246-251.

15. A. Kathiravan, A. Gowri, V. Srinivasan, T. A. Smith, M. Ashokkumar and M. Asha Jhonsi, *Analyst*, 2020, **145**, 4532-4539.

16. N. Nandi, S. Gaurav, P. Sarkar, S. Kumar and K. Sahu, *ACS Appl. Bio Mater.*, 2021, **4**, 5201-5211.

17. X. Liu, S. Zhang, H. Xu, R. Wang, L. Dong, S. Gao, B. Tang, W. Fang, F. Hou, L. Zhong and A. Aldalbahi, *ACS Appl. Mater. Interfaces*, 2020, **12**, 47245-47255.

18. M. Zulfajri, A. Rasool and G. G. Huang, *New J. Chem.*, 2020, **44**, 10525-10535.

19. B. Yuan, S. Guan, X. Sun, X. Li, H. Zeng, Z. Xie, P. Chen and S. Zhou, *ACS Appl. Mater. Interfaces*, 2018, **10**, 16005-16014.

20. X. Lu, D. Wang, L. Ge, L. Xiao, H. Zhang, L. Liu, J. Zhang, M. An and P. Yang, *New J. Chem.*, 2018, **42**, 19665-19670.

21. F. Arcudi, L. Đorđević and M. Prato, *Angew. Chem., Int. Ed.*, 2016, **55**, 2107-2112.

22. V. D. Dang, A. B. Ganganboina and R.-A. Doong, *ACS Appl. Mater. Interfaces*, 2020, **12**, 32247-32258.

23. X. Wu, C. Ma, J. Liu, Y. Liu, S. Luo, M. Xu, P. Wu, W. Li and S. Liu, *ACS Sustain. Chem. Eng.*, 2019, **7**, 18801-18809.

24. S. R. Anand, A. Bhati, D. Saini, Gunture, N. Chauhan, P. Khare and S. K. Sonkar, *ACS Omega*, 2019, **4**, 1581-1591.

25. D. Chang, L. Li, L. Shi and Y. Yang, *Analyst*, 2020, **145**, 8030-8037.

26. R. Das, A. Bora and P. K. Giri, *J. Mater. Chem. C*, 2020, **8**, 7935-7946.

27. P. D. Khavlyuk, E. A. Stepanidenko, D. P. Bondarenko, D. V. Danilov, A. V. Koroleva, A. V. Baranov, V. G. Maslov, P. Kasak, A. V. Fedorov, E. V. Ushakova and A. L. Rogach, *Nanoscale*, 2021, **13**, 3070-3078.

28. J. Yu, C. Xu, Z. Tian, Y. Lin and Z. Shi, *New J. Chem.*, 2016, **40**, 2083-2088.

29. F. Li, J. Zhang, S. Hu and Y. Jia, *ACS Sens.*, 2021, **6**, 1218-1227.

30. L. Vallan, E. P. Urriolabeitia, F. Ruipérez, J. M. Matxain, R. Canton-Vitoria, N. Tagmatarchis, A. M. Benito and W. K. Maser, *J. Am. Chem. Soc.*, 2018, **140**, 12862-12869.

31. T. Zhang, J. Zhu, Y. Zhai, H. Wang, X. Bai, B. Dong, H. Wang and H. Song, *Nanoscale*, 2017, **9**, 13042-13051.

32. Y. Chen, M. Zheng, Y. Xiao, H. Dong, H. Zhang, J. Zhuang, H. Hu, B. Lei and Y. Liu, *Adv. Mater.*, 2016, **28**, 312-318.

33. H. Li, Z. Zhang, J. Ding, Y. Xu, G. Chen, J. Liu, L. Zhao, N. Huang, Z. He, Y. Li and L. Ding, *Carbon*, 2019, **149**, 342-349.

CHAPTER 6

N-doped carbon dots: Triple mode excitation-emission features for dual channel sensing and logic gate application

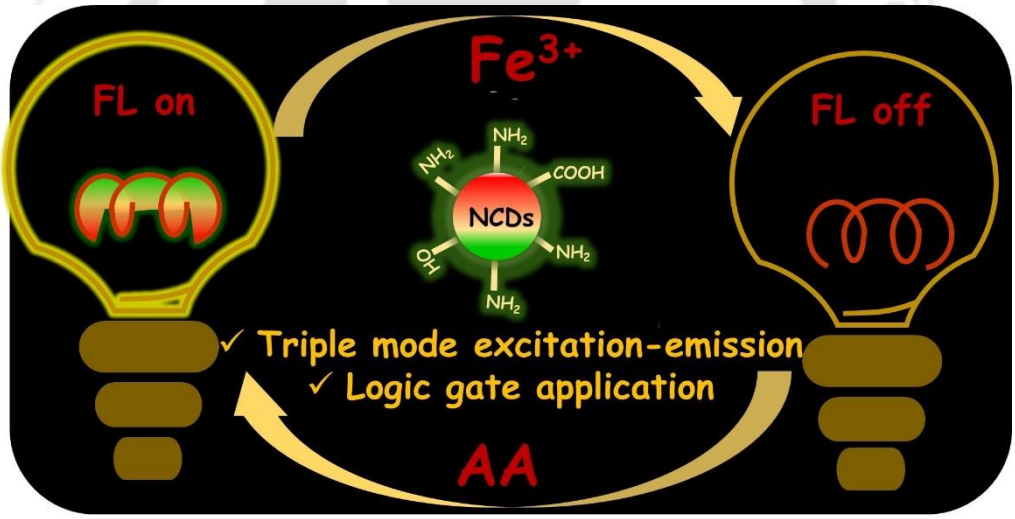

Manuscript: Nilanjana Nandi, Priyanka Sarkar, Kalyanasis Sahu, "N-doped carbon dots: triple mode excitation–emission features for dual channel sensing and logic gate application". *Materials Today Chemistry* , 2022, **26**, 101015

[This page was intentionally left blank]

Abstract

Carbon dots (CDs) have congregated massive opportunities in basic and applied research streams owing to their versatile properties. Herein, a unique N-doped CD (NCD) was synthesized via the hydrothermal technique using 3,5-diaminobenzoic acid and hydrazine hydrate as precursors. The NCDs exhibit exceptional optical properties; they emit very different colors under different excitation windows. The fluorescence maxima were at 404 nm (blue), 506 nm (green), and 605 nm (red), respectively, when the excitation wavelengths fall within 300-340 nm, 380-460 nm, and 500-540 nm. The emission features were drastically different from more straightforward CDs (CD_{Blank}) prepared using 3,5-diaminobenzoic acid only via the same hydrothermal route without hydrazine hydrate. We found that the 506 nm and 605 nm emissions originate from various surface states, while the 404 nm emission comes from the NCD core states. The triple emissive-NCDs were implemented for sensing; Fe^{3+} effectively quenches the green and red emissions through turn-off quenching, while ascorbic acid (AA) successfully recovers the quenched emission in a turn-on manner. Both static and dynamic mechanisms were responsible for quenching green and red emissions and were accounted for by complexation-induced aggregation and electron transition from the electron-rich NCDs to the vacant d orbital of Fe^{3+}, respectively. The detection limits for the green and red regions were 7.9 nM and 12.2 nM, respectively. The AA restores both the emission signals by reducing Fe^{3+} to Fe^{2+}. The calculated detection limits for AA recognition were 0.55 µM and 1.05 µM, respectively, for the green and red emissions. Furthermore, a multi-input logic gate was constructed to convert the molecular information as fluorescence signal outputs.

6.1 Overview

In recent times, carbon dots (CDs) have engrossed incredible attention as a zero-dimensional fluorescent nanomaterial. Outstanding properties including facile synthesis, robust chemical and optical stability, excellent biocompatibility, low cytotoxicity, and good bio-imaging capability propel their applications in vast research areas, such as photocatalysis[1, 2], photosensitizer[3, 4], light-emitting diodes[5, 6], sensing, anti-counterfeiting[7], and biological arena[8-10]. Nowadays, tremendous interest has been developed in modifying and engineering the optical property of CDs, and currently, the focus shifts from single excitation-emission to multiple excitation-emission. The multiple excitation-emission features are incredibly advantageous as multiple fluorescence (FL) emission centers are present in one substance. The origin of multiple emission features of CDs is ambiguous, whether it arises from the carbogenic core[11, 12], multiple surface states[13], solvent relaxation effect[14], supramolecular cross-linked enhanced emission (SCEE)[15], trap carriers[16], or surface fluorophore[17]. Thus, a detailed experimental analysis is imperative to endorse the unique luminescent properties of CDs. In a recent report, the dual fluorescence characteristic was attributed to both carbon-core and molecular states[18]. There are only a few literature reports on multiple excitation-emission features. Some carbonized polymer dots (CPDs) possess dual-channel excitation-emission in blue (Ex: 350 nm, Em: 445 nm) and yellow (Ex: 440 nm, Em: 575 nm) regions [19]. In another report, nitrogen-doped CDs show distinct emissions at different excitation regions, e.g., blue (Ex: 298 nm; Em: 398 nm) and green (Ex: 404 nm: Em: 518 nm) emissions [20]. These multiple excitation-emission probes are incredibly beneficial for sensing applications.

Recognition of metal ions and bioactive molecules is critical for the environmental cause and clinical analysis. Specifically, detecting the ferric (Fe^{3+}) ion in drinking water is crucial. A high Fe^{3+} content can cause gastrointestinal problems and loss of appetite[21]. Contrarily, an insufficient Fe^{3+} is equally harmful and directly inflicts severe physical disorders and biological damages, causing anemina[22], arthritis, osteoporosis[23], heart failure[24], liver problems[25], and other difficulties[26, 27]. Ascorbic acid (AA) is a class of well-known antioxidants, and vitamins used to treat various ailments like cold, infection, mental sickness, and, most importantly, AIDS[28, 29]. People are currently using AA enriched daily diet to boost their immune systems. AA deficiency affects several physiological processes and causes Parkinson's disease, cardiovascular disease, and cancer[30]. Several recognition techniques have been established for the dual-mode quantification of Fe^{3+} and AA, such as

electrochemical methods[31, 32], atomic absorption spectrometry[33], inductively coupled plasma mass spectrometry[34], fluorescence (FL) based detection[35-37]. However, the FL-based detection techniques are more promising due to rapid, simple, sensitive, and visual mode detection. Several FL-based probes, such as small organic molecules[38], lanthanide-doped nanoparticles[39], metal-organic frameworks[40] (MOFs), metal nanoclusters[41] (NCs), carbon dots[42-45] etc., have been reported for the detection of Fe^{3+} and AA. However, FL-based probes often require complex synthesis conditions resulting in low sensitivity, poor stability, and inherent toxicity. Therefore, it is indispensable to develop innovative FL-based materials to recognize Fe^{3+} and AA better.

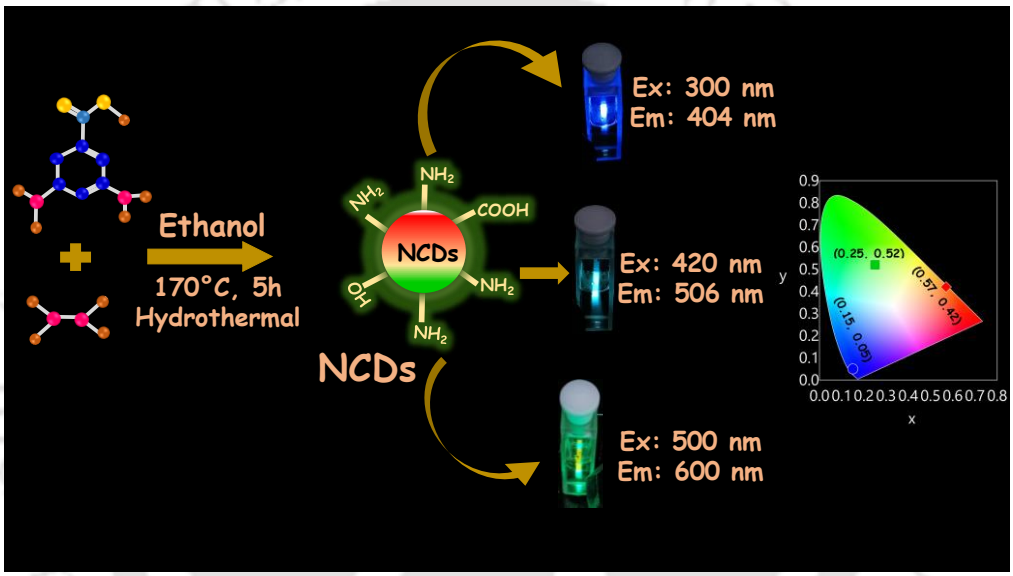

Scheme 6.1. Schematic representation of the synthesis route of NCDs and the triple-mode excitation-emission characteristics.

We establish a simple and innovative sensor for the dual-mode detection of Fe^{3+} and AA using NCDs, which display outstanding triple-mode excitation-emission features having emissions in three distinctive emission regions: blue (Ex: 300 nm, Em: 404 nm), green (Ex: 420 nm., Em:506 nm), and red (Ex: 500 nm, Em: 605 nm). To get more insight into the origin of the tricolor emission, for example, whether it comes from the carbon core or generated from molecular or surface states, we have synthesized a more straightforward CD (CD_{Blank}) from 3,5-diaminobenzoic acid only following the same preparation method. The multi-emissivity feature may originate from the carbon core state and several emissive surface states. We found that the surface-states emissions (green and red) are very sensitive to Fe^{3+}, which selectively quenches the respective emissions. Both static and dynamic quenching mechanisms were responsible for the Fe^{3+} induced quenching—the former

mechanism results from the complexation of active surface functional groups with Fe^{3+}. The emission can be selectively restored by ascorbic acid (AA). The strong binding affinity of AA with Fe^{3+} accounts for the fluorescence intensity recovery of NCDs. Hence, NCDs served as "on-off-on" sensors for the dual-channel detection of Fe^{3+} and AA. In addition, the "on-off-on" strategy successfully attributes designing a multi-input molecular logic gate, which can be very useful for constructing the fluorescence-based smart molecular device.

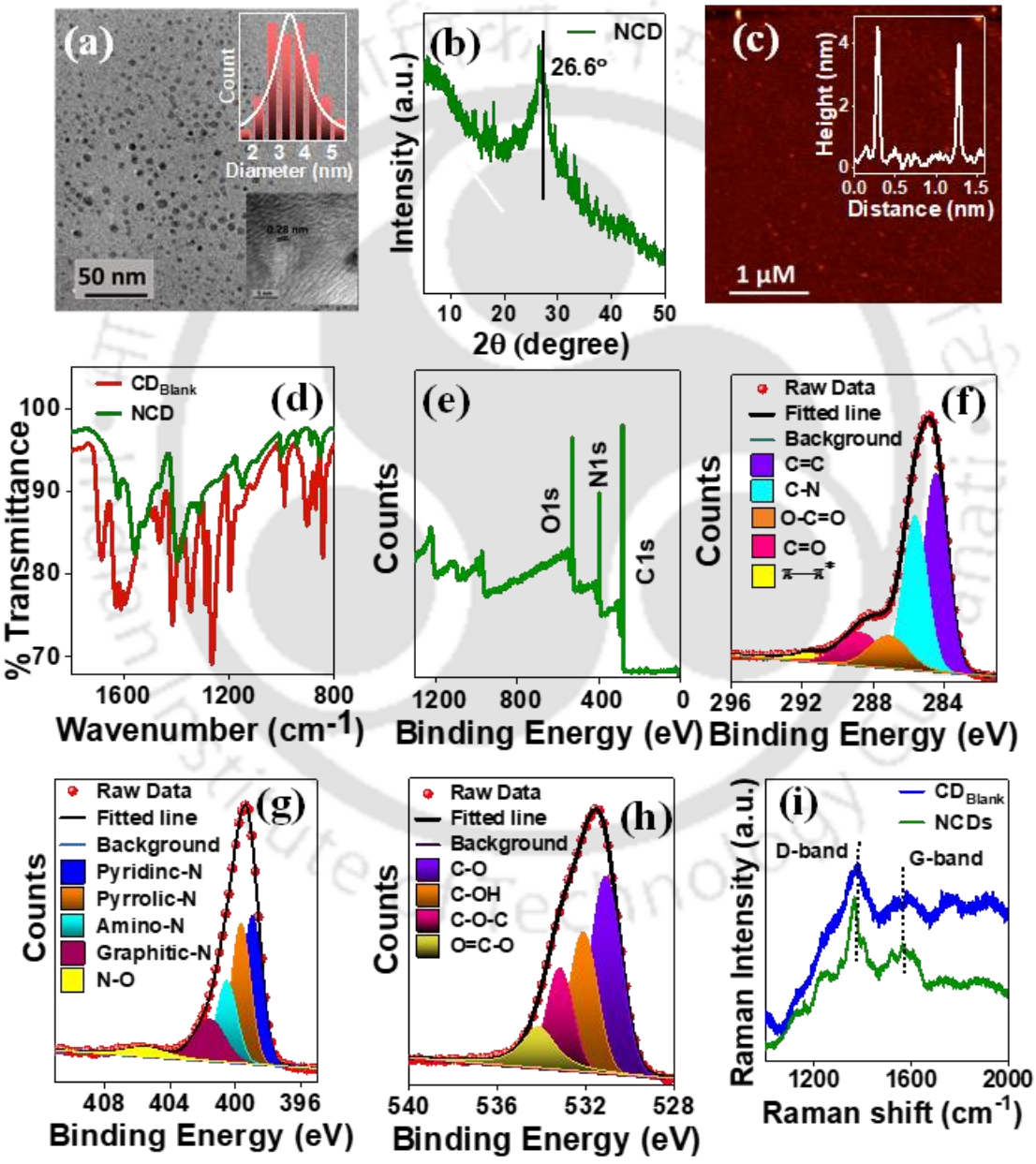

Figure 6.1. (a) TEM image (insets show the size distribution histogram and high-resolution TEM image), (b) pXRD pattern, and (c) AFM image of NCDs; (d) FTIR spectra of NCDs and CD_{Blank}. (e) Full range XPS survey of NCDs. Deconvoluted XPS spectra of C 1s (f), O 1s (g), and N 1s (h). (i) Raman spectra of CD_{Blank} and NCDs.

6.2 Results and Discussions

6.2.1 Surface characterization

The synthesis procedure of the N-doped triple-emitting CDs is represented in **Scheme 6.1**. It was synthesized via the hydrothermal method with 3,5-diaminobenzoic acid and hydrazine hydrate in an ethanol medium at 170 °C for 5 hours. **Figure 6.1a** reveals the perfectly monodispersed sphere-shaped morphology of NCDS with an average diameter of 4.1 ± 0.7 nm. The synthesized CDs exhibit 0.28 nm lattice space (inset of **Figure 6.1a**), belonging to the (002) plane[46], which is revealed by HRTEM images. **Figure 6.1b** depicted powder XRD depicted a distinct peak at 26.6° corresponding to the (002) plane. The AFM images of NCDs reveal typical topographic heights ranging from 2.5 to 6.5 nm (**Figure 6.1c**). The investigation of various chemical components was carried out by Fourier-transformed infrared (FTIR) spectroscopy. The full FTIR spectrum is represented in **Figure A.6.1a.** The characteristic stretching vibration from 3350 cm^{-1} to 3319 cm^{-1} indicates the presence of N-H/O-H functional groups. The other characteristic vibration band located at 2450 cm^{-1}, 1623 cm^{-1}, 1560 cm^{-1}, 1521 cm^{-1}, 1398 cm^{-1} implied for N=C=O, C=O in amide linkage, C=N bending vibration, C-N stretching band of amide-II, C-N bond, respectively (**Figure 6.1d**). Moreover, FTIR band ranging from 1301 cm^{-1} to 1147 cm^{-1} belongs to the C-O bond of –COOH, C-O-C groups, etc. The C=O of amide linkage of CD_{Blank} (1685 cm^{-1}) was shifted to a lower wavenumber than in NCDs (1623 cm^{-1}). Another noticeable observation is that no peak appears at 2450 cm^{-1} and in the range of 1250 to 1287 cm^{-1} in NCDs[47-49]. These observations suggested that the addition of hydrazine hydrate changes the surface functionality of NCDs, which are distinctly different from $CD_{Blank.}$

The XPS is the utmost essential characterization for determining the chemical composition of NCDs. Three typical peaks at 283.6 eV, 398 eV, and 530.3 eV are clearly located in the full range XPS scan (**Figure 6.1e**), and the contribution of each element are 64.77 %, 19.27 %, 15.97 % for C 1s, N 1s, and O 1s, respectively (**Figure A.6.1b**). **Figure 6.1f-6.1h** demonstrated high-resolution XPS spectra of C 1s, N 1s, and O 1s, respectively. The high-resolution C 1s XPS scan is fitted into five peak parameters: C=C (284.5 eV), C-N (285.7 eV), O=C-O (287.1 eV), C=O (288.8 eV), (291.8 eV)[49, 50]. Similarly, high-resolution N 1s and O 1s XPS scan entirely deconvoluted into five and four peak parameters which show the existence of numerous surface functionalities like pyridinic-N (398.9 eV), pyrrolic-N (399.7 eV), amino-N (400.6 eV), graphitic-N (401.6 eV), N-O (405.6 eV), C-O (531.1 eV),

C-OH (532.2 eV), O-C-O (533 eV) and O-C=O (534.1 eV)[51-53]. The contribution of each bond was thoroughly calculated and presented in **Table A.6.1 and A.6.2.** The percentage of graphitic-N and oxidized N in NCDs is much higher than in CD_{Blank} (**Figure A.6.1c**). Hence, the FTIR and XPS analyses show good concurrence about the chemical constituents of newly synthesized NCDs. Furthermore, Raman spectroscopy is a unique characterization technique for CD-based materials. The Raman-D and Raman-G bands emerge at 1367 cm^{-1} and 1563 cm^{-1}, respectively (**Figure 6.1i**), arising due to the surface defect and E_{2g} vibration mode of graphite related to the vibration of sp^2 carbon atoms present in a hexagonal lattice. In contrast to CD_{Blank}, both the Raman-D and G band is red-shifted by 15 cm^{-1} and 12 cm^{-1}, respectively, suggesting alteration of the electronic environment by hydrazine hydrate. Moreover, the Raman intensity (I_D/I_G) ratio of the D and G bands increases from 1.08 in CD_{Blank} to 1.19 in NCDs, revealing that the NCDs have a much higher degree of Raman active sites and subsequent increase of the amorphous nature of the NCDs.

6.2.2 Photo-physical Properties

The photophysical properties of newly developed CDs were thoroughly investigated with different optical techniques such as absorption, excitation, and emission spectroscopy. Interestingly, the CDs exhibit a unique tri-color emission when excited with three different excitation channels. As depicted in **Figure 6.2a**, the CDs reveal a broad absorption spectrum from 400 nm to 600 nm along with a high energy band allocated at 310 nm due to n-π* and π-π* electronic transitions, respectively, which arise from various heteroatomic surface functionalities (C=N, C=O, etc.) and sp^2 bonded C=C carbon core, respectively. The emission spectra of CDs were recorded in three different ranges of excitation wavelengths: 300-360 nm, 370-460 nm, and 500-540 nm. Three distinct emission spectra with maxima at blue (404 nm), green (506 nm), and red (605 nm) wavelengths were observed with no apparent excitation-dependent emission with the specific excitation windows (**Figure 6.2b, 6.2c, and 6.2d**). Moreover, **Figure 6.2e** also clearly shows that emission maxima are independent of excitation wavelengths within the specified range. Here, we denote the blue, green, and red emission spectra as FL_B, FL_G, and FL_R, respectively. The tricolor emission may originate from the carbon core or generate from the surface state. To get further insights, we have synthesized CDs (denoted as CD_{Blank}) from 3,5-diaminobenzoic acid only following the same preparation method. The TEM images of CD_{Blank} are displayed in **Figure A.6.2a and A.6.2b**.

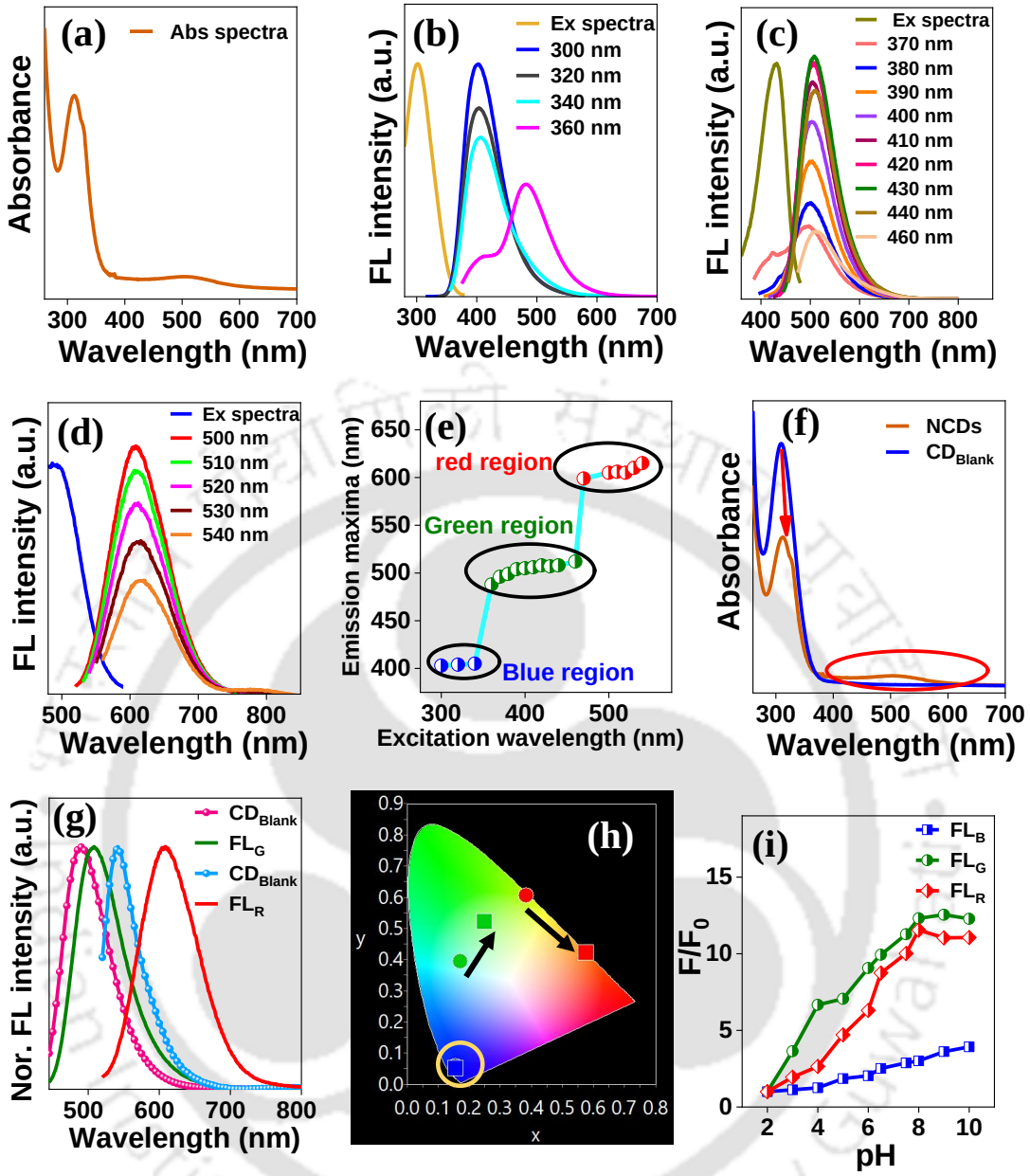

Figure 6.2. (a) The absorption spectrum of NCDs. Excitation and emission spectra of NCDs in the range of (b) 300 nm to 360 nm, (c) 370 nm to 460 nm, (d) 500 nm to 540 nm. (e) Various emission maxima plotted against their excitation wavelength, (f) Comparison of the absorption spectra of NCDs, and CD_{Blank}. (g) Comparison of FL spectra of NCD's green and red region with the corresponding FL spectra of CD_{Blank} under 420 nm and 500 nm excitation. (h) Shifting of CIE coordinate of CD_{Blank} and NCDs multiple emissions. (i) pH stability study of NCDs. Blue lines indicate stability under 300 nm excitation, the green line indicates stability under 420 nm excitation, and the red line indicates stability under 500 nm excitation. F_0 is FL intensity at pH 2, and F is FL intensity at other pH values.

The absorption profile of CD_{Blank} (**Figure 6.2f**) is distinct from the NCDs, with no broad absorption band in the range of 400-550 nm. Interestingly, the emission diagram of CD_{Blank} only shows two distinct emission wavelengths: blue (λ_{em}^{max} = 405 nm) and green (λ_{em}^{max} = 485 nm) (**Figure A.6.2c),** but no emission signal appeared on the red side. Furthermore, as we introduced hydrazine hydrate into the reaction medium, the green region peak (Ex: 420 nm)

was shifted to 11 nm higher wavelength side from $CD_{Blank,}$ which is shown by normalized FL spectra (**Figure 6.2g**). However, under 500 nm excitation CD_{Blank} and FL_R emission maxima are located at 540 nm and 605 nm, respectively. This observation is also evident by calculating CIE coordinates. The green ((0.25, 0.52), green square) and red ((0.57, 0.42), red square) regions of NCDs show a distinct shift from the green ((0.17, 0.39), green circle) and red ((0.38, 0.60), orange circle) regions of CD_{Blank}. But the coordinates of the blue region of NCDs and CD_{Blank} remain exactly the same ((0.15, 0.05), blue square and circle) (**Figure 2h**). Recent work reported that with an increase in the N-functionality, the emission wavelength shifts to the red side[54, 55]. The XPS shows that the graphitic-N percentage increases from CD_{Blank} to NCDs, shifting the FL maximum to a higher wavelength [56]. Thus, we can conclude that both the green and red emissions may originate from multiple surface functional states of NCDs, while the blue emission emanates from the graphitic sp^2-network carbon core of NCDs.

Furthermore, the photobleaching analysis accomplished the accreditation of the surface state and core state emission as the photostability of as-prepared NCDs is related to their different FL origins[57]. The intensity of both the green and red components was reduced significantly to 48 % and 40 %, respectively, compared to the negligible reduction of the blue part (3 %) in **Figure A.6.2d**. To further evaluate the emission origin, emission spectra of the different regions (blue, green, and red) were recorded by varying pH. The multiple hydrophilic surface functionalities present on the surface of carbon dots may show a better ability pH-dependent FL performance via protonation/deprotonation[58, 59]. As expected, the surface state emissions (green and red) are more pH-sensitive rather than the core state (blue) emissions. The intensity of both FL_G and FL_R increases markedly with pH increment, but the intensity FL_B does not change much with pH (**Figure 6.2i**). The robust resistance against photobleaching and pH supports that the blue component arises from the carbon-core states or hole-electron recombination, while green and red emissions originate from the surface states. The assignment agrees with the former reports that the carbon-core states typically exhibit a shorter emission wavelength than the surface-state emission[18, 60, 61]. The calculated quantum yields of the NCDs are 27.5 %, 31.9 %, and 10.4 %, respectively, for the blue, green, and red emissions. We also checked the effect of temperature (**Figure A.6.2e**); emission intensities of all the three regions do not show any robust changes with alteration of temperature. The FL lifetimes of the different emission regions of NCDs were quite distinct (**Figure A.6.2f** and **Table A.6.3**). These special spectral features comprising

triple mode-excitation to triple mode-emission allow NCDs to generate unique research interests.

6.2.3 Dual-mode detection of Fe(III) and AA

The potential of the newly synthesized CDs having multiple heterogeneous functional groups was tested for the FL-based metal ion sensing. Initially, the FL quenching efficacy of FL_B, FL_G, and FL_R was evaluated by adding 100 µM Fe^{3+}. In contrast to FL_B, the higher wavelength emissions (FL_G and FL_R) were much more sensitive to Fe^{3+} (**Figure 6.3a-c**).

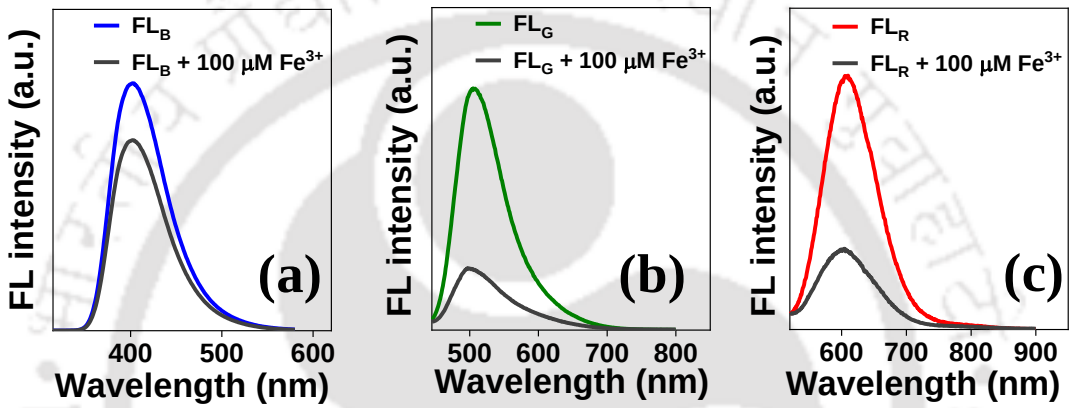

Figure 6.3. Differential quenching efficacy of NCDs in three different emission regions toward a specific concentration (100 µM) of Fe^{3+}: (a) blue region (Ex: 300 nm) (b) green region (Ex: 420 nm), and (c) red region (Ex: 500 nm).

Since the blue emission is less susceptible to Fe^{3+}, we have performed the rest of the studies considering only green and red-channel emissions. **Figure 6.4a** shows that the luminescence intensity (E_x: 420 nm, E_m: 506 nm) gradually decreases upon sequential addition of Fe^{3+}, and ~82 % of the initial fluorescence was quenched at 140 µM Fe^{3+}. The strong quenching makes CDs effective "turn off" sensors for Fe^{3+}. The plot of the emission intensity ratio (F_0/F) against Fe^{3+}concentration diverges from linearity at higher concentrations (**Figure 6.4b**), while the low concentration region (0 to 25 µM) follows a linear Stern-Volmer pattern (inset of **Figure 6.4b**). The calculated S-V constant (K_{SV}) value was **$1.43 \pm 0.08 \times 10^4$ M^{-1}**. The calculated detection limit (LOD) was **7.9 nM**.

Now, the fluorescent of CDs was successfully reestablished with the addition of AA to the Fe^{3+}-induced quenched-state. **Figure A.6.3a-b** demonstrated that only 3 min incubation time is sufficient for recovering the green FL intensity, establishing an effective "turn on" FL-based approach for recognizing AA. **Figure 6.4c** depicts the increment of green FL intensity with the gradual addition of AA from 0 to 600 µM from the FL off-state of the

FL_G-Fe^{3+} system. The linear relationship was obtained at low concentration regimes (0 to 120 µM) (**Figure 6.4d**). The detected LOD value is **0.55 µM**. The CIE coordinates of FL_G, FL_G-$Fe^{3+,}$ and FL_G-Fe^{3+}-AA are represented in **Figure 6.4e** ((0.25, 0.52), green color), ((0.26, 0.45), black color) and ((0.24, 0.0.47), red color) respectively. The quenched and recovered FL intensity is detectible in the naked eye under the same 420 nm excitation wavelength (**Figure 6.4f**).

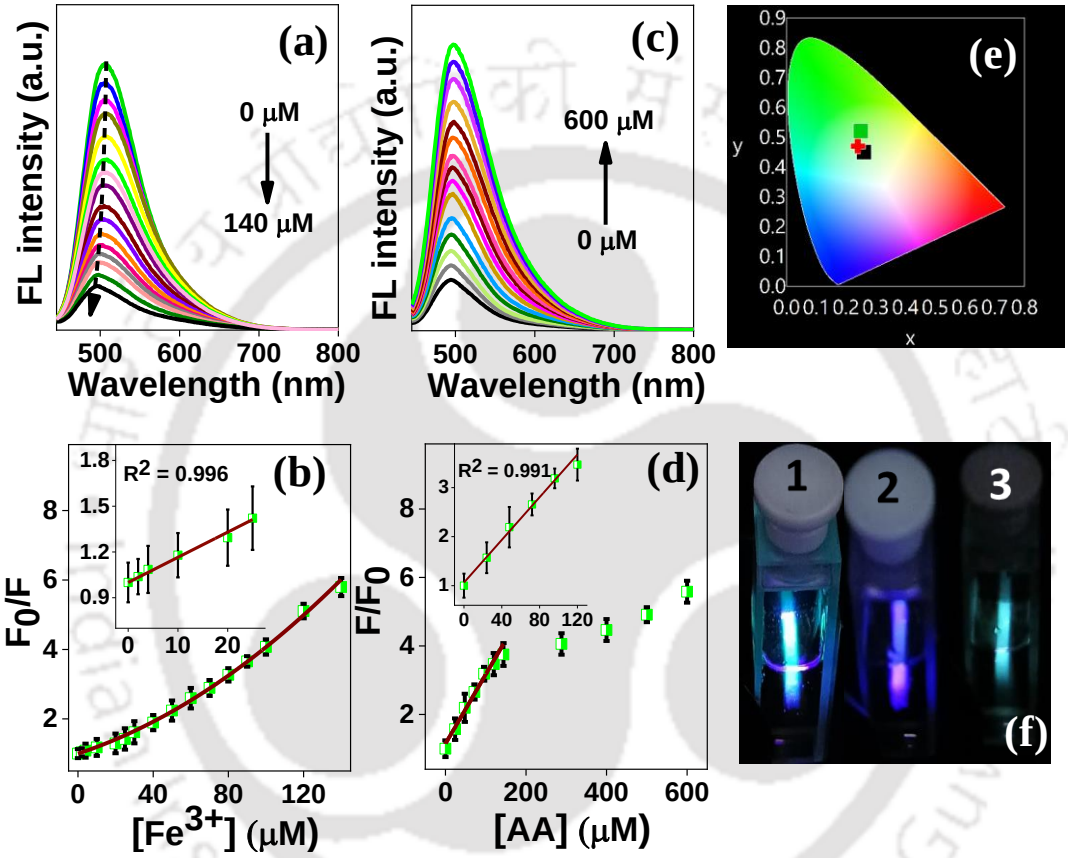

Figure 6.4. (a) Fluorescence quenching titration of NCDs by Fe^{3+} under 420 nm excitation. (b) Intensity ratio (F_0 and F are the FL intensities in the absence and presence of Fe^{3+}, respectively). Inset graph shows S-V linear plot. (c) Turn-on FL intensity from by AA under excitation of 420 nm. (d) Intensity ratio plot (F_0 and F is the FL intensity of NCDs+Fe^{3+} system and NCDs+Fe^{3+}+AA systems respectively). (e) CIE coordinates NCDs green emission (square green color), NCDs+Fe^{3+} (Square black color) and NCDs+Fe^{3+}+AA (plus red color). (f) photograph of the samples under 420 nm excitation wavelength inside FL spectrometer: (1) NCDs-FL on state (FL_G), (2) NCDs+Fe^{3+} (FL quenched state, FL_G with 140 µM Fe^{3+}) and NCDs+ Fe^{3+}+AA (FL recovered state, with FL_G, 140 µM Fe^{3+} and 600 µM AA).

Similarly, the red emission intensity (Ex: 500 nm, Em: 605 nm) was also sensitive towards Fe^{3+} and resulted in the quenching of FL intensity. The addition of Fe^{3+} up to 250 µM concentration entirely diminishes the luminescence intensity (**Figure 6.5a**). Also, F_0/F vs. Fe^{3+} concentration plot shows a slightly concave upward instead of a straight line at higher concentrations (**Figure 6.5b**). The S-V plot fitted to a straight line from 0-100 µM concentration of Fe^{3+} leads to K_{SV} value of **$1.83 \pm 0.02 \times 10^4$ M^{-1}** (inset of **Figure 6.5b**).

The calculated LOD value of 12.2 nM is comparable with the green emission region. Furthermore, the addition of AA to FL_R-Fe^{3+} system also recovered the FL intensity (turn on) of NCDs. As shown in **Figure 6.5c**, the FL intensity effectively recovered with a substantial addition of AA up to 1400 µM. The straight line was fitted from 0 to 144 µM concentration of AA (**Figure 6.5d**). From **Figure 6.5e**, the obtained CIE coordinates for red channel are ((0.58, 0.42), red colour), ((0.53, 0.46), black colour) and ((0.57, 0.42), blue colour) which stands for FL_R, FL_R-Fe^{3+} and FL_R-Fe^{3+}-AA, respectively. For the red-emission, the calculated LOD value of AA was 1.05 µM.

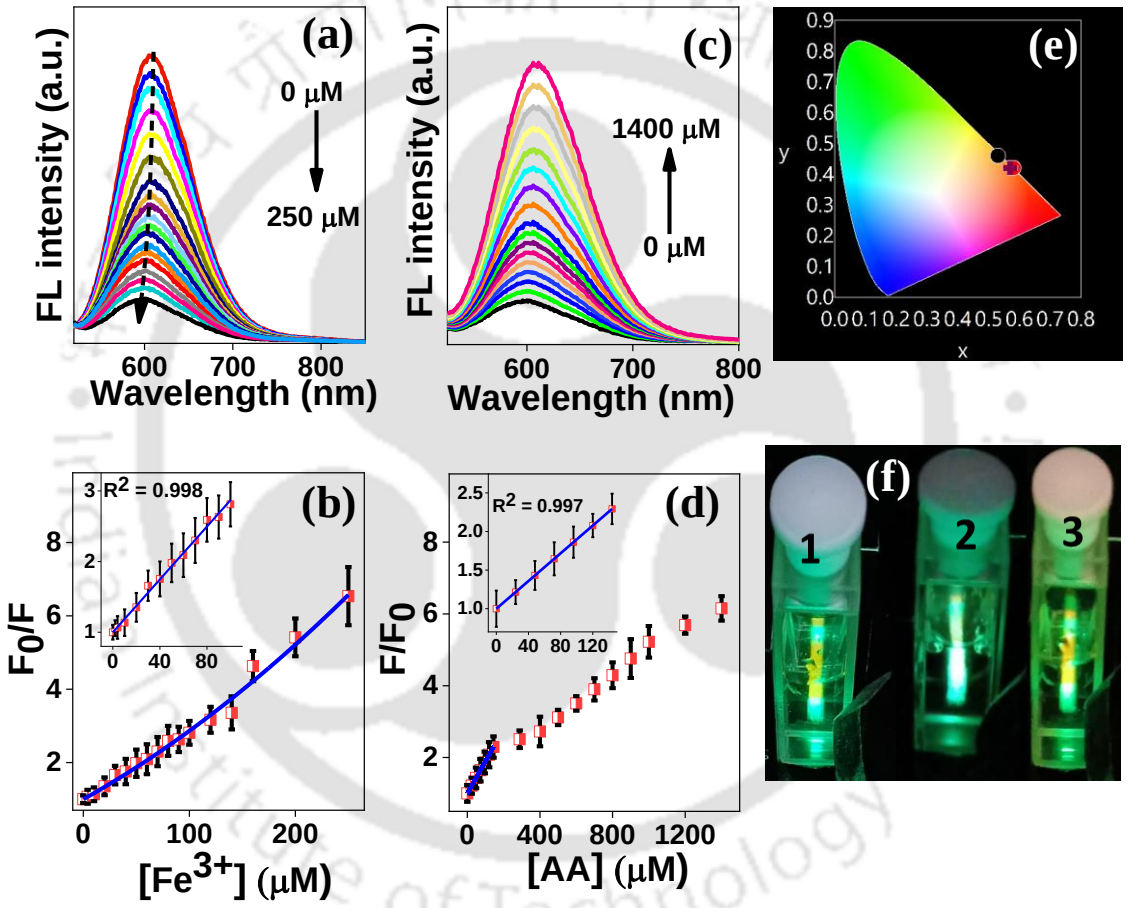

Figure 6.5. (a) Fluorescence quenching titration of NCDs by Fe^{3+} under excitation of 500 nm. (b) Intensity ratio (F_0 and F is the FL intensity absensce and presence of Fe^{3+} respectively). Inset graph shows S-V linear plot. (c) Turn-on FL intensity from by AA under excitation of 500 nm. (d) Intensity ratio plot (F_0 and F is the FL intensity of NCDs+Fe^{3+} system and NCDs+Fe^{3+}+AA systems respectively). (e) CIE coordinates NCDs red emission (circle red colour), NCDs+Fe^{3+} (black circle shape) and NCDs+Fe^{3+}+AA (plus purple colour). (f) digital photograph under 500 nm excitation wavelength in FL instrument. (1) NCDs-FL on state (FL_R), (2) NCDs+Fe^{3+} (FL quenched state, with FL_R and 250 µM Fe^3) and NCDs+Fe^{3+}+AA (FL recovered state, with FL_R, 250 µM Fe^{3+} and 1400 µM AA).

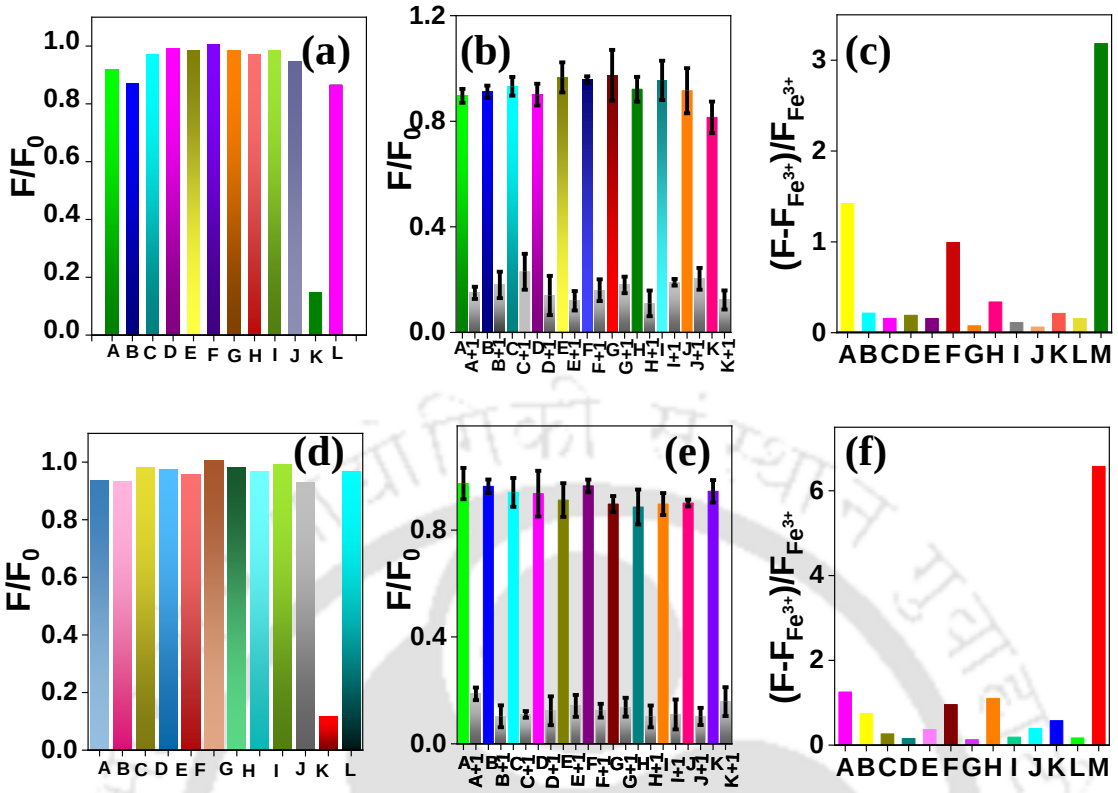

Figure 6.6. (a) Selectivity study of FL_G in the presence of various metal ions (A, B, C, D, E, F, G, H, I, J, K are K^+, Ag^+, Cd^{2+}, Co^{2+}, Cr^{3+}, Fe^{2+}, Ni^{2+}, Pb^{2+}, Zn^{2+}, $Ca^{2+,}$ and H_2O_2 respectively), (b) Selectivity study of FL_G in the presence of various metal ions (A, B, C, D, E, F, G, H, I, J, K are K^+, Ag^+, Cd^{2+}, Co^{2+}, Cr^{3+}, Fe^{2+}, Ni^{2+}, Pb^{2+}, Zn^{2+}, $Ca^{2+,}$ and H_2O_2 respectively, 1 represents Fe^{3+}). (c) Selectivity study of FL_G in the presence of various competitive bio-analytes (A, B, C, D, E, F, G, H, I, J, K, L, M, N, O, and P are glutathione, lysine, threonine, urea, glutamic acid, cysteine, L-aspartic acid, dopamine, methionine, glycine, citric acid, glucose, ascorbic acid, thiourea, urea, and histidine respectively). (d) Selectivity study of FL_R in the presence of various metal ions (A, B, C, D, E, F, G, H, I, J, K are K^+, Ag^+, Cd^{2+}, Co^{2+}, Cr^{3+}, Fe^{2+}, Ni^{2+}, Pb^{2+}, Zn^{2+}, $Ca^{2+,}$ and H_2O_2 respectively) (e) Selectivity study of FL_R in the presence of various metal ions (A, B, C, D, E, F, G, H, I, J, K are K^+, Ag^+, Cd^{2+}, Co^{2+}, Cr^{3+}, Fe^{2+}, Ni^{2+}, Pb^{2+}, Zn^{2+}, $Ca^{2+,}$ and H_2O_2 respectively, 1 represents Fe^{3+}). (f) Selectivity study of FL_R in the presence of various competitive bio-analytes. (A, B, C, D, E, F, G, H, I, J, K, L, M, N, O, and P are glutathione, lysine, threonine, urea, glutamic acid, cysteine, L-aspartic acid, dopamine, methionine, glycine, citric acid, glucose, ascorbic acid, thiourea, urea, and histidine respectively).

6.2.4 Selectivity Study

Specificity is highly recommended for a good nanosensor. Therefore, a comparative analysis was executed by taking 10 metal ions (K^+, Ag^+, Cd^{2+}, Cr^{3+}, Ni^{2+}, Zn^{2+}, Co^{2+}, Fe^{2+}, Pb^{2+}, Ca^{2+}), and each of the ion's concentration was kept at 180 µM and some vitamins were selected for green channel. The effect of metal ions and co-existing effect of Fe^{3+} in presence of other competitive metal-ion and some biomolecules are investigated (**Figure 6.6a, 6.6b, and 6.7b**). For AA, 15 competitive analytes were chosen (700 µM concentration of each analyte) for performing the selectivity study. No noticeable alteration of FL was observed for any of the metal ions other than Fe^{3+}, while glutathione and cysteine can relatively recover the FL intensity to some extent, but maximum increment was noticed for

AA (**Figure 6.6c**). For red region, 300 µM of each metal ion and 1500 µM of each competitive analyte was used added to check the interfering effect (**Figure 6.6d to 6.6f**). Here also, cysteine and glutathione affect recovery, which is very nominal responses.

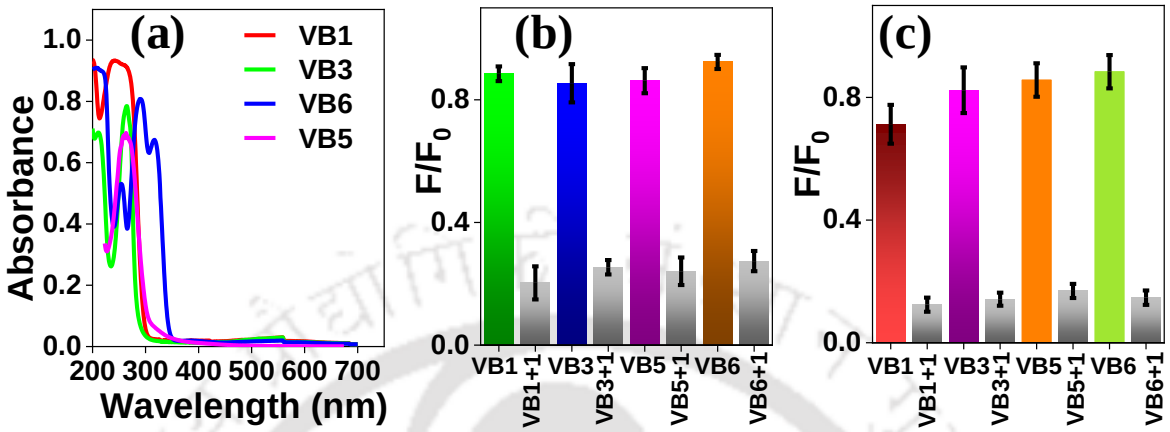

Figure 6.7. (a) Absorption spectra of different vitamins. The selectivity study of NCDs with different vitamins co-existing with Fe^{3+} under (b) 420 nm, and (c) 500 nm excitation wavelengths. Here 1 represents Fe^{3+}.

The effect of some vitamins [vitamin B1 (VB1), vitamin B3 (VB3), vitamin B5 (VB5) and vitamin B6 (VB6)] on emission signal was also examined. **Figure 6.7a** depicted absorbance spectra of the considered vitamins. **Figure 6.7b-c** shows that no noticeable FL signal alteration in green and red region was witnessed. Hence, both the green and red channels of NCDs effectively serve as good sensor for dual recognition of Fe^{3+} and AA.

6.2.5 "Turn-Off" mechanism of FL_G-FL_R by Fe(III):

The major plausible reasons behind diminishing fluorescence of a nanosensor are (1) complexation via coordination between various surface functionalities and positively charged metal ion, which may lead to aggregation, (2) electron transfer from the electron-rich NCDs to positively charged metal ions, (3) Förster resonance energy transfer (FRET) and (4) inner filter effect (IFE) where metal ion has absorption spectrum overlapped with the excitation of the emission spectrum of NCDs. The heteroatomic surface moieties of NCDs play a great role in sensing metal ions. The fluorescence quenching mechanism was thoroughly evaluated by UV-Vis absorption and lifetime analysis and further supported by TEM and XPS to detect accompanied structural and composition changes of the NCDs. **Figure 6.4b** and **6.5b** indicates that the quenching mechanism is not entirely static or dynamic but a combination of both.

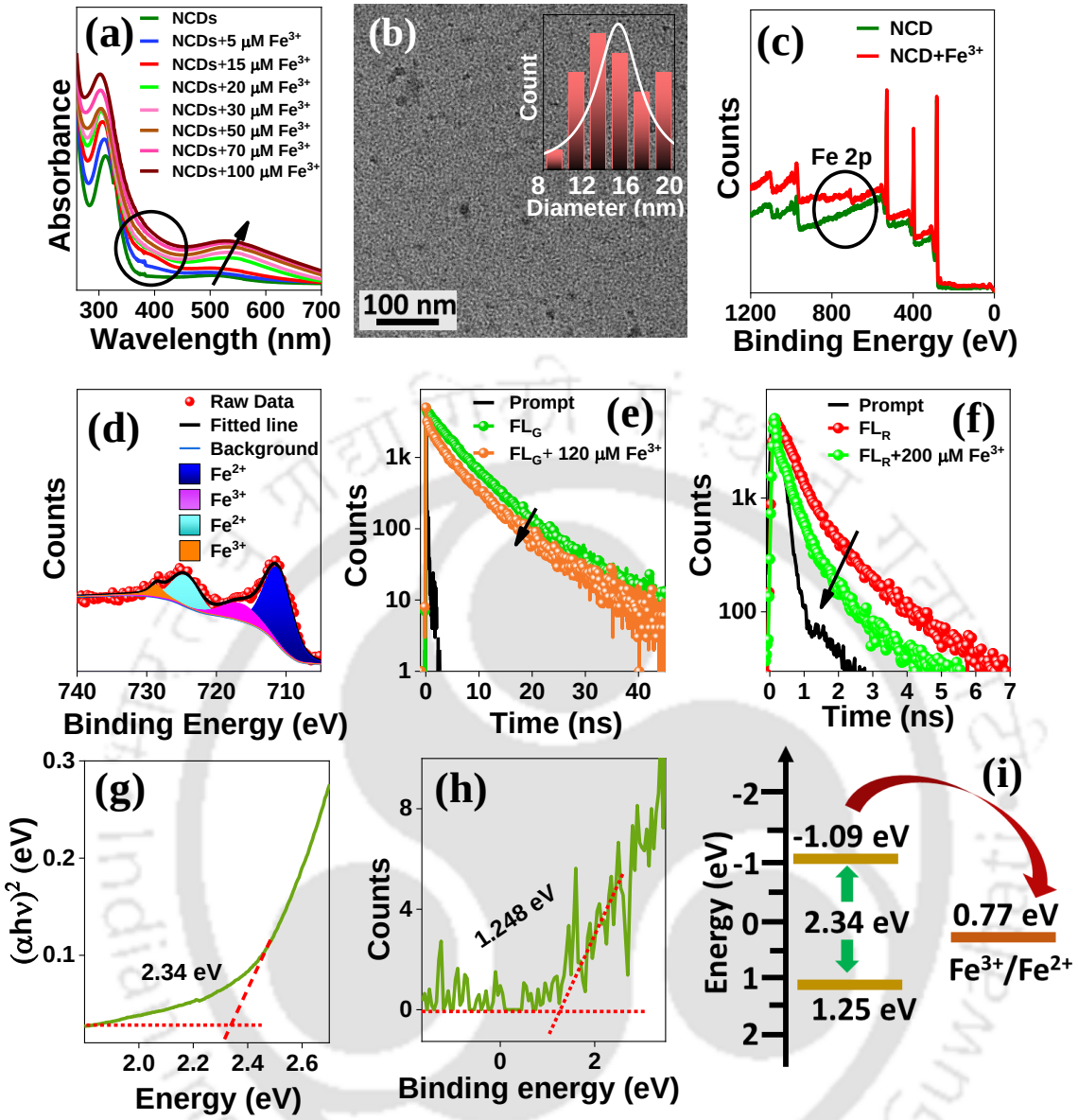

Figure 6.8. (a) Absorbance spectra of NCDs in the presence of different concentrations of Fe^{3+}. (b) TEM images of the NCDs-Fe^{3+} systems. (c) Deconvoluted XPS spectrum of Fe 2p in NCDs-Fe^{3+} system. (d) Fluorescence decays of FL_G and FL_G-Fe^{3+} (λ_{ex} = 405 nm, λ_{em} = 506 nm). (e) Fluorescence decays of FL_R and FL_R-Fe^{3+} (λ_{ex} = 510 nm, λ_{em} = 605 nm). (f) Pictorial representation of excited-state electron transfer phenomena from NCDs to Fe^{3+}.

The absorption spectra of NCDs in the presence of several concentrations of Fe^{3+} showed that the longer wavelength broad absorption band of NCDs shifts to the red-side, and a new prominent peak at 540 nm emerged, signifying the complexation between Fe^{3+} and heterogeneous surface functionality (**Figure 6.8a**). TEM analysis of the NCDs-Fe^{3+} system was carried out to check any kind of complexation-induced aggregate formation. **Figure 6.8b** revealed that the average size (4.12 ± 0.7 nm) of NCDs increased about 3.2 times from the initial size supporting the aggregation. Moreover, the complex formation mechanism

was further verified by XPS analysis. XPS characterization of the NCDs-Fe^{3+} system accounted a distinctive peak of which can be deconvoluted into Fe^{3+} (714.2 eV, 728.2 eV) and Fe^{2+} (709.8 eV, 723.2 eV) in **Figure 6.8c and 6.8d** [62]. After treatment with Fe^{3+}, peak positions of the amino-N, oxidized-N shift to lower binding energy side by 0.4 and 0.3 eV. Moreover, the characteristic peak for C-OH and O=C-O also shift to lower binding energies by 0.3 and 0.5 eV (**Figure A.6.4a-f** and **Table A.6.4**). This spectral specification evidenced that some Fe^{3+} ions reduce to Fe^{2+} after complexation with NCDs via electron transfer, reflecting the dynamic quenching process. The FL decays were monitored in the presence and absence of Fe^{3+} for both the regions (green and red) separately using 405 nm and 510 nm excitation diodes to decipher the involvement of the dynamic quenching in the overall FL suppression process (**Figure 6.8e and 6.8f**). For FL_G, the average lifetime decreased from 2.4 ns to 0.6 ns, and a similar trend was also observed for FL_R, where the FL lifetime declined from 0.7 ns to 0.2 ns (**Table A.6.5** and **Table A.6.6**). For more exploration of mechanism, we measured the bandgap (E_g) and valence band (E_{VB}) of NCDs from Tauc plot and XPS, respectively (**Figure 6.8g and 6.8h**), and put them in the renowned equation (2) to get the value of conduction band (E_{CB}).

$$E_{CB} = E_{VB} - E_g \text{ ----} \quad (2)$$

The obtained conduction band energy is -1.09 eV. The excited electrons from NCDs initially go to the conduction band and are then transferred to unfilled d orbital of Fe^{3+}, ensuing suppressing the FL property as depicted in **Figure 6.8i**. Therefore, the above observations clearly proved that the combination of static-dynamic quenching processes are responsible for the "turn off" fluorescence in both emission regions (green and red).

6.2.6 "Turn-on" mechanism of FL_G-FL_R by AA

It is well known that Fe^{3+} can bind strongly with AA via complexation, which can further lead to the redox reaction. To validate the oxidation-reduction occurring between Fe^{3+} and AA, 1,10-phenanthroline was introduced in NCDs-Fe^{3+} and NCDs-Fe^{3+}-AA systems. The photographs display obvious reddish-orange color in the NCDs-Fe^{3+}-AA system because of the complexation of Fe^{2+} with 1,10-phenanthroline (**Figure 6.9a**). Hence, fluorescence recovery from the quenched state might be ascribed as a redox reaction. Besides, two more competitive reducing agents, glutathione (GSH) and L-cysteine (L-cys), were added to the NCDs-Fe^{3+} system, but no substantial color difference was recognized by the interfering materials (**Figure 6.9a**). For further support the redox reaction, absorption spectra were

taken in the presence of AA in NCDs-Fe^{3+} system (**Figure 6.9b**). The absorption peak positioned at 540 nm due to NCDs-Fe^{3+} complexation gradually faded out and finally enforced the reoccurrence of the NCDs absorption spectrum. The XPS spectra also evidenced that after addition of AA to NCD-Fe3+ system, the Fe 2p peak is entirely diminished (**Figure 6.9c**). These observations completely support that the AA consumes Fe^{3+} via its good binding and reducing ability. The very strong reducing and binding capability of AA in contrast to other competitive interference, allows it to bind straightforwardly to Fe^{3+} for which NCDs become free and the FL signal is restored.

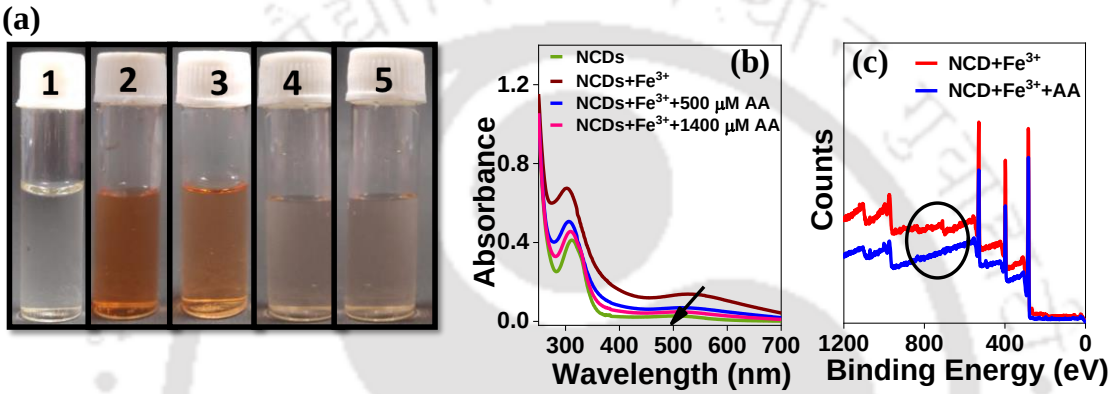

Figure 6.9. (a) Digital photographs NCDs+ Fe^{3+} (1), 1,10-phenanthroline-Fe^{2+} (2), NCDs+ Fe^{3+} + AA + 1,10-phenanthroline (3), NCDs+ Fe^{3+} + GSH + 1,10-phenanthroline (4), NCDs+ Fe^{3+} + L-cysteine + 1,10-phenanthroline (5). (b) Absorbance spectra of NCDs, NCDs+ Fe^{3+} and NCDs+ Fe^{3+} + 500 µM AA and NCDs+ Fe^{3+} + 1400 µM AA.

Scheme 6.2 demonstrates the FL quenching-restoring steps by Fe^{3+} and AA where FL quenching occurs via complexation-induced aggregation assisted by excited-state electron transfer from NCD to Fe^{3+} and reestablishment of emission intensity occurs by the redox reaction between Fe^{3+} and AA.

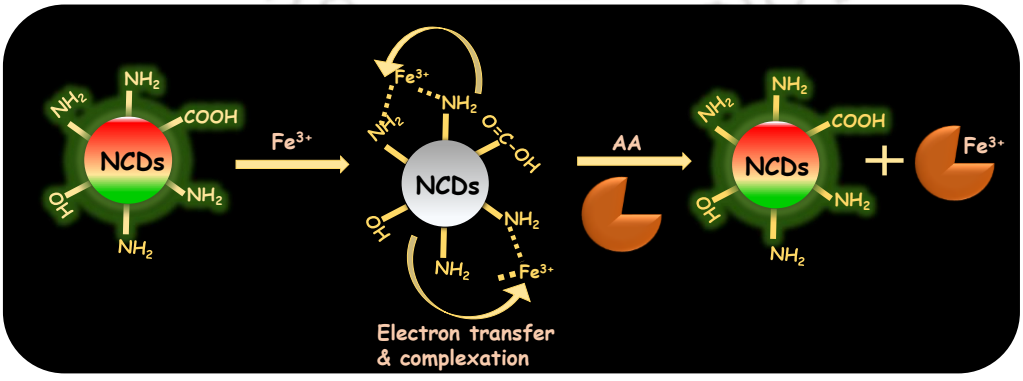

Scheme 6.2. Schematic representation of whole sensing mechanism of Fe^{3+} and AA by NCDs.

6.2.7 Design of Molecular Logic gates

The impact of various chemicals like Fe^{3+} and AA on the FL spectra of NCDs prompted the designing of molecular logic gate. For developing multiple input single output logic gates, we have considered simple chemistry that in presence of H_2O_2, the Fe^{2+} is oxidized to Fe^{3+} via Fenton reaction in equation (3)

$$Fe^{2+} + H_2O_2 \rightarrow Fe^{3+} + OH^{\cdot} \quad \text{------ (3)}$$

We have utilized this knowledge and the effect of Fe^{2+}, (Fe^{2+}+H_2O_2), and (Fe^{2+}+ H_2O_2+AA) on the NCD emission signal was thoroughly investigated.

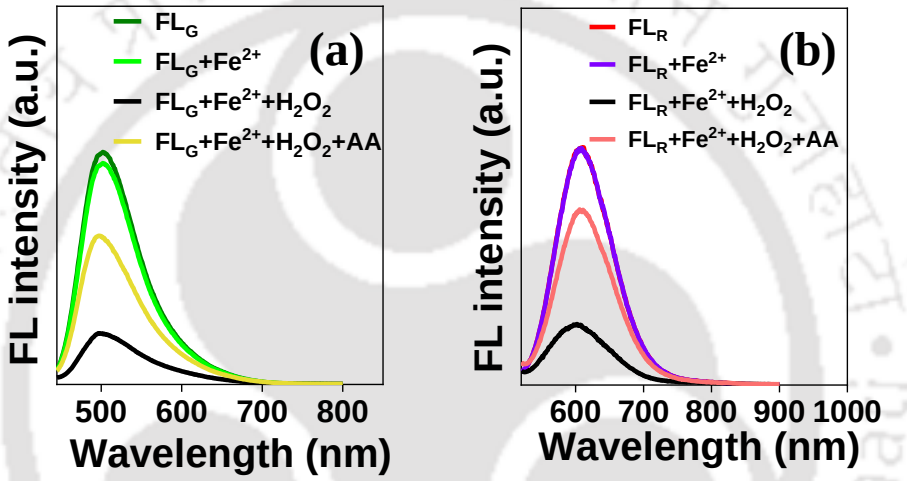

Figure 6.10. (a) and (b) are the emission spectra of NCD in the presence of Fe^{2+}, (Fe^{2+} and H_2O_2), and (Fe^{2+}+H_2O_2+AA) under 420 nm and 500 nm excitation, respectively.

From **Figure 6.10a** and **6.10b** it can be seen that the generation of Fe^{3+} from the direct addition of Fe^{2+} and H_2O_2 leads to the FL quenching, however, the subsequent addition of AA on the NCD-Fe^{2+}-H_2O_2 solution recovers the FL intensity.

The state of the analyte defines the input signal; the presence of the analyte is "1", and the absence of the analyte is "0". The output signal designates the fluorescence state; the normal fluorescence intensity represents "1", and the quenched fluorescence signifies "0". A single-input NOT gate is designed when only a single analyte Fe^{3+} is considered as input, and the FL intensity of the NCDs is taken as output (**Figure 6.11a and 6.11b**). The presence of Fe^{3+} analyte in the NCDs system (input ''1'') converts the logical negation ''1''into ''0'', and the absence of the analyte (input ''0'') leads to an output ''1''. Recalling that AA addition can recover the fluorescence of the NCDs-Fe^{3+} system, a two-input logic gate is constructed where the input-1 is Fe^{3+}, and input-2 is AA (**Figure 6.11c and 6.11d**).

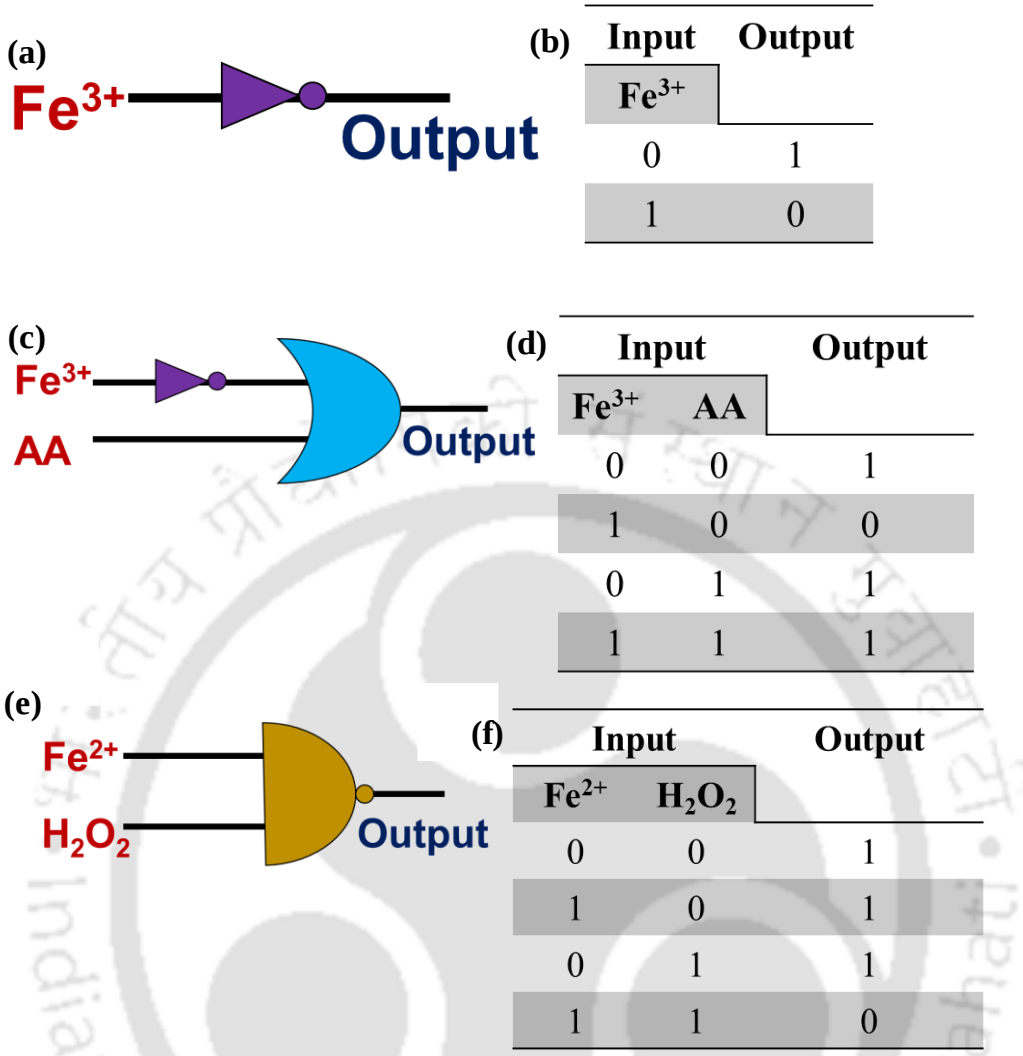

Figure 6.11. (a) NOT GATE with a single input. (b) Corresponding truth table from (a). (c) Two input logic gates by considering Fe^{3+} and AA. (d) Corresponding truth table from (c). (e) NAND input logic gate by considering Fe^{3+} and H_2O_2. (f) Corresponding truth table from (e).

The presence of only Fe^{3+} (input "1 0") reveals a low output (output ''0''), and for all other inputs, the output fluorescence remains high (output ''1''). Another molecular logic gate was designed with Fe^{2+} and H_2O_2 as two inputs that provide information regarding the oxidation process of Fe^{2+} to Fe^{3+}. In the presence of only Fe^{2+} or H_2O_2, NCD fluorescence remains unchanged but quenches severely when both are present due to the formation of Fe^{3+}. According to the outputs, a NAND gate can be constructed as shown in **Figure 6.11e and 6.11f**. Furthermore, a triple input logic gate is designed using Fe^{3+} as the 1st input, Fe^{2+} as the 2nd input, and H_2O_2 as the 3rd input (**Figure 6.12a**). The corresponding truth table is shown in **Figure 6.12b** which reveals that the fluorescence probe (NCDs) is highly sensitive towards Fe^{3+} and insensitive to Fe^{2+}. This can evidently differentiate Fe^{3+} and Fe^{2+}.

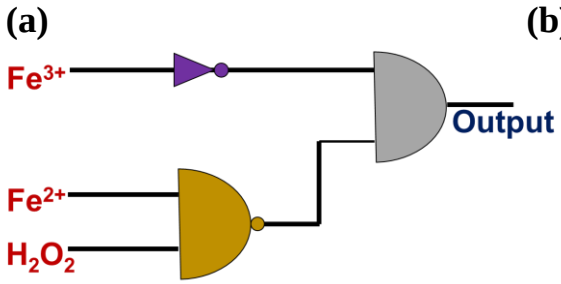

(b)

Input			Output
Fe^{3+}	Fe^{2+}	H_2O_2	
0	0	0	1
0	0	1	1
0	1	0	1
0	1	1	0
1	0	0	0
1	0	1	0
1	1	0	0
1	1	1	0

Figure 6.12. Construction of three input (Fe^{3+}, Fe^{2+} and H_2O_2) logic gate. (b) Corresponding truth table from (a).

Finally, a four-input logic gate is designed with Fe^{3+}, AA, Fe^{2+}, and H_2O_2 as 1st, 2nd, 3rd, and 4th inputs (**Figure 6.13a**). The corresponding fluorescence results are presented as a truth table in **Figure 6.13b.** The multi-input logic gate can be beneficial for designing fluorescence-based smart molecular devices.

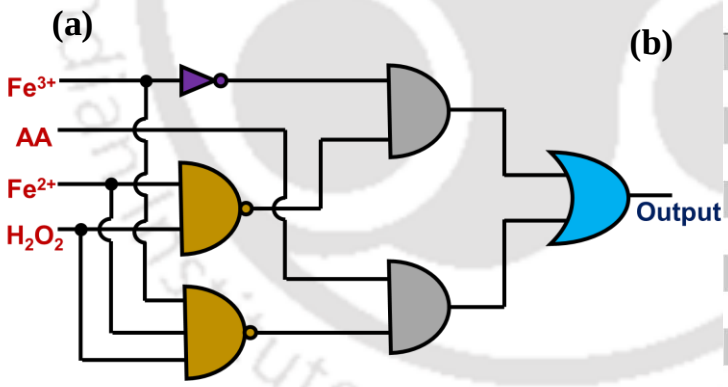

(b)

Input				Output
Fe^{3+}	AA	Fe^{2+}	H_2O_2	
0	0	0	0	1
0	0	0	1	1
0	0	1	0	1
0	0	1	1	0
0	1	0	0	1
0	1	0	1	1
0	1	1	0	1
0	1	1	1	1
1	0	0	0	0
1	0	0	1	0
1	0	1	0	0
1	0	1	1	0
1	1	0	0	1
1	1	0	1	1
1	1	1	0	1
1	1	1	1	0

Figure 6.13. (a) NCDs-based four-input molecular logic gate with Fe^{3+}, AA, Fe^{2+}, and H_2O_2 act as inputs. (b) Truth table corresponding gate.

6.3 Conclusion

In summary, we reported a unique NCD displaying triple mode excitation-emission features. The NCDs exhibit emission at three diverse ranges depending on specific excitation wavelengths. The NCDs exhibits blue (λ_{em}^{max}: 404 nm), green (λ_{em}^{max}: 506 nm) and red (λ_{em}^{max}: 600 nm) emissions when excited at 300-340 nm, 380-460 nm, and 500-540 nm, respectively. We also synthesized a carbon dot (CD_{Blank}) without the additional nitrogen source (hydrazine hydrate), which shows much simpler photophysics than the NCDs. From a detailed comparison between the NCD and CD_{Blank} emission characteristics, we proposed that the blue emission from NCDs originates from the carbon-core, while the other two emission centers arise due to multiple surface functional groups. The assignment was further evaluated by a group of experiments, including pH variation and photostability of different emission colors. Furthermore, the NCDs serve as a potential nanoprobe for the rapid dual-mode detection of Fe^{3+} and AA. The surface-states emissions (green and red) are highly susceptible to quenching by Fe^{3+} through synergic static and dynamic quenching processes. The static quenching effect was mediated by aggregation via complexation between NCDs and Fe^{3+}. The dynamic quenching, manifested by the decrease of the average lifetime, occurs through electron transfer from NCDs to vacant d of Fe^{3+}. The quenched emission of NCDs was restored by AA addition by the redox reaction process between Fe^{3+} and AA. Moreover, a multi-input molecular logic gate is also constructed from the obtained fluorescence results, which opens up the possibility of designing fluorescence-based smart molecular devices.

References

1. N.-N. Chai, H.-X. Wang, C.-X. Hu, Q. Wang and H.-L. Zhang, *J. Mater. Chem. A*, 2015, **3**, 16613-16620.

2. D. Han, M. Ma, Y. Han, Z. Cui, Y. Liang, X. Liu, Z. Li, S. Zhu and S. Wu, *ACS Sustain. Chem. Eng.*, 2020, **8**, 534-542.

3. S. Deshmukh, A. Deore and S. Mondal, *ACS Appl. Nano Mater.*, 2021, **4**, 7587-7606.

4. P. M. Olmos-Moya, S. Velazquez-Martinez, C. Pineda-Arellano, J. R. Rangel-Mendez and L. F. Chazaro-Ruiz, *Carbon*, 2022, **187**, 216-229.

5. X. Wang, B. Wang, H. Wang, T. Zhang, H. Qi, Z. Wu, Y. Ma, H. Huang, M. Shao, Y. Liu, Y. Li and Z. Kang, *Angew. Chem., Int. Ed.*, 2021, **60**, 12585-12590.

6. T. Yuan, T. Meng, P. He, Y. Shi, Y. Li, X. Li, L. Fan and S. Yang, *J. Mater. Chem. C*, 2019, **7**, 6820-6835.

7. J. Guo, H. Li, L. Ling, G. Li, R. Cheng, X. Lu, A.-Q. Xie, Q. Li, C.-F. Wang and S. Chen, *ACS Sustain. Chem. Eng.*, 2020, **8**, 1566-1572.

8. I. Srivastava, S. K. Misra, S. Bangru, K. A. Boateng, J. A. N. T. Soares, A. S. Schwartz-Duval, A. Kalsotra and D. Pan, *ACS Appl. Mater. Interfaces*, 2020, **12**, 16137-16149.

9. S. Anwar, H. Ding, M. Xu, X. Hu, Z. Li, J. Wang, L. Liu, L. Jiang, D. Wang, C. Dong, M. Yan, Q. Wang and H. Bi, *ACS Appl. Bio Mater.*, 2019, **2**, 2317-2338.

10. M. J. Molaei, *RSC Adv.*, 2019, **9**, 6460-6481.

11. X. Miao, D. Qu, D. Yang, B. Nie, Y. Zhao, H. Fan and Z. Sun, *Adv. Mater.*, 2018, **30**, 1704740.

12. F. Yuan, T. Yuan, L. Sui, Z. Wang, Z. Xi, Y. Li, X. Li, L. Fan, Z. a. Tan, A. Chen, M. Jin and S. Yang, *Nat. Commun.*, 2018, **9**, 2249.

13. F. Yuan, Y.-K. Wang, G. Sharma, Y. Dong, X. Zheng, P. Li, A. Johnston, G. Bappi, J. Z. Fan, H. Kung, B. Chen, M. I. Saidaminov, K. Singh, O. Voznyy, O. M. Bakr, Z.-H. Lu and E. H. Sargent, *Nat. Photonics*, 2020, **14**, 171-176.

14. S. Khan, A. Gupta, N. C. Verma and C. K. Nandi, *Nano Lett.*, 2015, **15**, 8300-8305.

15. L. Vallan, E. P. Urriolabeitia, F. Ruipérez, J. M. Matxain, R. Canton-Vitoria, N. Tagmatarchis, A. M. Benito and W. K. Maser, *J. Am. Chem. Soc.*, 2018, **140**, 12862-12869.

16. L. Xiao, Y. Wang, Y. Huang, T. Wong and H. Sun, *Nanoscale*, 2017, **9**, 12637-12646.

17. Y.-P. Sun, B. Zhou, Y. Lin, W. Wang, K. A. S. Fernando, P. Pathak, M. J. Meziani, B. A. Harruff, X. Wang, H. Wang, P. G. Luo, H. Yang, M. E. Kose, B. Chen, L. M. Veca and S.-Y. Xie, *J. Am. Chem. Soc.*, 2006, **128**, 7756-7757.

18. J.-R. Macairan, T. V. de Medeiros, M. Gazzetto, F. Yarur Villanueva, A. Cannizzo and R. Naccache, *J. Colloid. Interf. Sci.*, 2022, **606**, 67-76.

19. Y.-T. Gao, B.-B. Chen, L. Jiang, J. Lv, S. Chang, Y. Wang, R.-C. Qian, D.-W. Li and M. E. Hafez, *ACS Appl. Mater. Interfaces*, 2021, **13**, 50228-50235.

20. O. Xu, S. Wan, Y. Zhang, J. Li and X. Zhu, *Sens. Actuators B Chem.*, 2021, **340**, 129904.

21. Z. Huang, W. Song, Y. Li, L. Wang, N. K. Pandey, L. Chudal, M. Wang, Y. Li, L. Zhao, W. Yin and W. Chen, *J. Mater. Chem. C*, 2020, **8**, 12935-12942.

22. R. D. Baker, F. R. Greer and T. C. o. Nutrition, *Pediatrics*, 2010, **126**, 1040-1050.

23. H. Cai, H. Xu, H. Chu, J. Li and D. Zhang, *J. Mater. Chem. B*, 2021, **9**, 767-782.

24. Y. Shizukuda and D. R. Rosing, *J Arrhythm*, 2019, **35**, 575-583.

25. Y. W. Kim, S. M. Lee, S. M. Shin, S. J. Hwang, J. S. Brooks, H. E. Kang, M. G. Lee, S. C. Kim and S. G. Kim, *Free Radic. Biol. Med.*, 2009, **47**, 1082-1092.

26. X. Wang, H. Wang and S. Feng, *Sens. Actuators B Chem.*, 2017, **241**, 65-72.

27. R. Cui, K. Zhang, X. Wu, H. Zhang and C. Wang, *ACS Omega*, 2019, **4**, 9918-9924.

28. A. S. Pires, C. R. Marques, J. C. Encarnação, A. M. Abrantes, A. C. Mamede, M. Laranjo, A. C. Gonçalves, A. B. Sarmento-Ribeiro and M. F. Botelho, *Eur. J. Cell Biol.*, 2016, **95**, 208-218.

29. M. Fiorani, C. Azzolini, A. Guidarelli, L. Cerioni and O. Cantoni, *Pharmacol. Res.*, 2014, **84**, 12-17.

30. C. Li, J. Zeng, D. Guo, L. Liu, L. Xiong, X. Luo, Z. Hu and F. Wu, *ACS Appl. Mater. Interfaces*, 2021, **13**, 49453-49461.

31. L. R. Kindra, C. J. Eggers, A. T. Liu, K. Mendoza, J. Mendoza, A. R. Klein Myers and R. M. Penner, *Anal. Chem.*, 2015, **87**, 11492-11500.

32. Z. Wang, M. Shoji and H. Ogata, *Analyst*, 2011, **136**, 4903-4905.

33. B. Paz-Rodríguez, M. R. Domínguez-González, M. Aboal-Somoza and P. Bermejo-Barrera, *Food Chem.*, 2015, **170**, 492-500.

34. A. Spolaor, P. Vallelonga, J. Gabrieli, G. Cozzi, C. Boutron and C. Barbante, *J. Anal. At. Spectrom.*, 2012, **27**, 310-317.

35. X. Luo, W. Zhang, Y. Han, X. Chen, L. Zhu, W. Tang, J. Wang, T. Yue and Z. Li, *Food Chem.*, 2018, **258**, 214-221.

36. S. Lunvongsa, M. Oshima and S. Motomizu, *Talanta*, 2006, **68**, 969-973.

37. Z.-Q. Liang, C.-X. Wang, J.-X. Yang, H.-W. Gao, Y.-P. Tian, X.-T. Tao and M.-H. Jiang, *New J. Chem.*, 2007, **31**, 906-910.

38. L. Long, L. Zhou, L. Wang, S. Meng, A. Gong and C. Zhang, *Anal. Chim. Acta*, 2014, **812**, 145-151.

39. L. Zhang, B. Ling, L. Wang and H. Chen, *Talanta*, 2017, **172**, 95-101.

40. L. Guo, Y. Liu, R. Kong, G. Chen, Z. Liu, F. Qu, L. Xia and W. Tan, *Anal. Chem.*, 2019, **91**, 12453-12460.

41. S. Zhang, C. Zhang, X. Shao, R. Guan, Y. Hu, K. Zhang, W. Liu, M. Hong and Q. Yue, *RSC Adv.*, 2021, **11**, 17283-17290.

42. M. Shamsipur, K. Molaei, F. Molaabasi, M. Alipour, N. Alizadeh, S. Hosseinkhani and M. Hosseini, *Talanta*, 2018, **183**, 122-130.

43. Y. Huang, N. He, Q. Kang, D. Shen, X. Wang, Y. Wang and L. Chen, *Analyst*, 2019, **144**, 6609-6616.

44. C. Wang, H. Lin, Z. Xu, Y. Huang, M. G. Humphrey and C. Zhang, *ACS Appl. Mater. Interfaces*, 2016, **8**, 6621-6628.

45. X. Sun, Q. Zhang, K. Yin, S. Zhou and H. Li, *Chem. Commun.*, 2016, **52**, 12024-12027.

46. J. Weerasinghe, J. Scott, A. D. K. Deshan, D. Chen, A. Singh, S. Sen, P. Sonar, K. Vasilev, Q. Li and K. Ostrikov, *Adv. Mater. Technol.*, **n/a**, 2100586.

47. V. D. Dang, A. B. Ganganboina and R.-A. Doong, *ACS Appl. Mater. Interfaces*, 2020, **12**, 32247-32258.

48. F. Arcudi, L. Đorđević and M. Prato, *Angew. Chem., Int. Ed.*, 2016, **55**, 2107-2112.

49. N. Nandi, P. Sarkar and K. Sahu, *ACS Appl. Nano Mater.*, 2021, **4**, 9616-9624.

50. I.-A. Baragau, Z. Lu, N. P. Power, D. J. Morgan, J. Bowen, P. Diaz and S. Kellici, *Chem. Eng. J.*, 2021, **405**, 126631.

51. N. Nandi, S. Gaurav, P. Sarkar, S. Kumar and K. Sahu, *ACS Appl. Bio Mater.*, 2021, **4**, 5201-5211.

52. N. Nandi, S. Gaurav, P. Sarkar, S. Kumar and K. Sahu, *ACS Appl. Bio Mater.*, 2021, **4**, 7605-7614.

53. Y. Liu and P. Wu, *ACS Appl. Mater. Interfaces*, 2013, **5**, 3362-3369.

54. L. Zhu, D. Shen, C. Wu and S. Gu, *Ind. Eng. Chem. Res.*, 2020, **59**, 22017-22039.

55. S. Sarkar, M. Sudolská, M. Dubecký, C. J. Reckmeier, A. L. Rogach, R. Zbořil and M. Otyepka, *J. Phys. Chem. C*, 2016, **120**, 1303-1308.

56. K. Holá, M. Sudolská, S. Kalytchuk, D. Nachtigallová, A. L. Rogach, M. Otyepka and R. Zbořil, *ACS Nano*, 2017, **11**, 12402-12410.

57. M. Shamsipur, A. Barati, A. A. Taherpour and M. Jamshidi, *J. Phys. Chem. Lett.*, 2018, **9**, 4189-4198.

58. J. Xia, S. Chen, G.-Y. Zou, Y.-L. Yu and J.-H. Wang, *Nanoscale*, 2018, **10**, 22484-22492.

59. M. Moniruzzaman and J. Kim, *Sens. Actuators B Chem.*, 2019, **295**, 12-21.

60. W. Wang, C. Damm, J. Walter, T. J. Nacken and W. Peukert, *Phys. Chem. Chem. Phys.*, 2016, **18**, 466-475.

61. L. Bao, Z.-L. Zhang, Z.-Q. Tian, L. Zhang, C. Liu, Y. Lin, B. Qi and D.-W. Pang, *Adv. Mater.*, 2011, **23**, 5801-5806.

62. X.-Y. Zhang, Y. Li, Y.-Y. Wang, X.-Y. Liu, F.-L. Jiang, Y. Liu and P. Jiang, *J. Colloid. Interf. Sci.*, 2022, **611**, 255-264.

CHAPTER 7

Dual-emitting anti-cancerous N-doped carbon dots for ratiometric detection of pH, Fe^{3+} and white-light generation

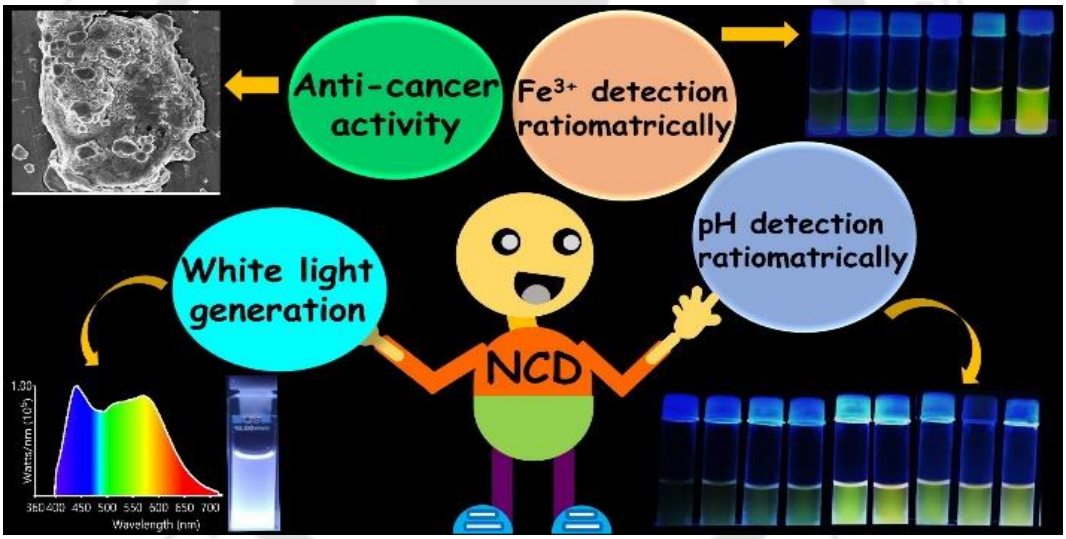

Manuscript: Nilanjana Nandi, Konika Choudhury, Priyanka Sarkar, Neha Barnwal, Kalyanasis Sahu, "Dual-emitting anti-cancerous N-doped carbon dots for ratiometric detection of pH, Fe^{3+} and white-light generation". *(ACS Appl. Nano Mater. 2022, **5**, 11, 17315–17324)*

[This page was intentionally left blank]

Abstract

Carbon dots (CDs) with dual emission features are highly desirable for various applications. Nitrogen-doped carbon dots (NCDs), synthesized hydrothermally, adopting 3,4-diaminobenzoic acid and hydrazine hydrate as precursors, display dual emissions, green (490 nm) and yellow (570 nm), which depend markedly on pH. The ratio of the two bands changes upon changing the pH from 2.1 to 7.6, favoring ratiometric detection of pH, and color variation can be visualized under UV light. Moreover, NCDs can effectively recognize Fe^{3+} in a ratiometric manner. The green emission drops gradually with simultaneous amplification of the yellow emission by adding Fe^{3+} due to complexation occurring between NCD and Fe^{3+}. The color change from light green to bright yellow with increasing Fe^{3+} concentrations was evident under a UV lamp. The NCDs show anticancer properties and effectively recognize pH and Fe^{3+} inside breast cancer cells (MCF-7). By exploiting the bi-color emissions of the nanoprobe, a solution-phase white light emitter was devised by incorporating another blue emissive carbon dot. Thus, the newly prepared NCDs are promising nanomaterials for versatile applications.

7.1 Overview

Fluorescence-based ratiometric chemo and biosensors have engrossed immense attention in modern research offering extraordinary advantages such as improved accuracy, detectability of low levels of analytes, and high reliability.[1-4] Ratiometric sensing provides the advantage of visual detection because one emission band grows up at the expense of another band. The self-calibration is due to the double emission at the different wavelengths, dramatically reducing interference and increasing sensitivity.[5, 6] Still, obtaining a ratiometric fluorescence probe is challenging as it requires suitable fluorophores with varied emissions at the same excitation wavelength.

Carbon dots (CDs) have demonstrated widely distributed excitation-emission wavelength, high solubility in the aqueous phase, chemical-physical inertness, and excellent biocompatibility.[7-9] These excellent photophysical properties mainly stem from the presence of the heterogeneous surface-passivated states.[10-12] These CDs can be functionalized with other CDs[13], metal nanoclusters,[14] metal-organic frameworks (MOF),[15] or other fluorophore units[16] to generate a ratiometric fluorescence property for the detection of pH, temperature, metal ion, and biomolecules.[17-21] Moreover, CDs are also often useful for anticancer agents,[22-24] antibacterial activity,[25, 26] and cell labeling.[27] However, it is scarce that a simple CD can ratiometrically detect metal ions and pH and act as an anti-cancerous agent.

In this report, we have synthesized a simple dual emitting NCD from 3,4-diaminobenzoic acid and hydrazine hydrate through the hydrothermal technique. The novel NCDs is endowed with multiple features, (1) highly pH-responsiveness, (2) visual detection of Fe^{3+} through ratiometric sensing, and (3) efficient destruction of the cancerous cell. The intensities of the two emission bands (490 nm and 570 nm) are gradually increased when the pH value is varied from 2 to 12. The multiple nitrogens and oxygen-containing heterogeneous functional groups are responsible for the pH switching behavior of NCDs. A reverse trend was observed for Fe^{3+} detection; the 490 nm emission decreases, and the 570 nm peak intensity increases gradually with the addition of Fe^{3+}. Additionally, a solution-phase white light can effectively be produced by simply tuning the emission of NCD by adding another blue-emitting CD. Moreover, NCDs also have remarkable anticancer activity and can successfully detect pH and Fe^{3+} inside the MCF-7 cell line.

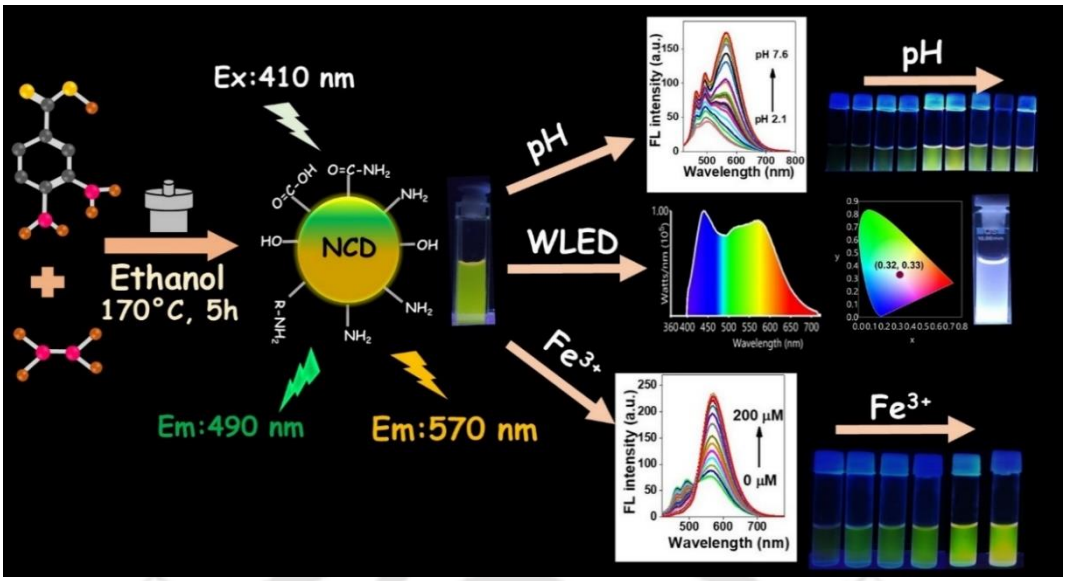

Scheme 7.1. Schematic representation of the synthesis route and various applications.

7.2 Results and Discussions

7.2.1 Surface characterization

The synthesis procedure of the N-doped dual-emitting CDs is represented in **Scheme 7.1** where the novel bi-color emitting NCDs was synthesized from 3,4-diaminobenzoic acid and hydrazine hydrate via hydrothermal methodology. The diameter of NCDs falls in the range of 3.5 to 10.5 nm, with an average diameter of 7.1± 0.9 nm (**Figure 7.1a**). The HRTEM (high-resolution TEM) shows a well-resolved lattice plane of a typical graphitic core with 0.27 nm spacing (**Figure A.7.1a**). The AFM characterization (**Figure 7.1b**) confirms the overall quasi-spherical morphology with a height distribution pattern corroborating the TEM analysis. XPS and FTIR studies further ascertained the chemical composition and multiple functionalities. The FTIR spectra (**Figure 7.1c)** shows peaks at 1612 cm^{-1}, 1512 cm^{-1}, 1434 cm^{-1}, 1364 cm^{-1}, and 1290 to 1140 cm^{-1} corresponds to stretching vibration of amide linkage (NH-C=O), C=N, C=C. N-H, and C-O related functional groups.[24, 28-30] The XPS (**Figure A.7.2)** disclosed three main elements C, N, and O, with the peak positioned at 284, 399, and 530 eV, respectively, with atomic percentages 66.0 (C1s), 19.2 (N1s), and 14.8 (O1s). The deconvoluted XPS peaks of C1s were at 284.4, 285.2, 286, 287.9, and 289.8 eV, which linked to C–C/C=C, C–N, C=N, C=O, and O-C=O respectively (**Figure 7.1d**).[31-33] The deconvoluted XPS spectrum for O1s exhibited well-defined peaks at 530.8, 531.3, 532.1, 533, and 533.8 eV corresponding to O-C/C-O-C,

O=C-N, C=O, C-OH, and O-C=O bond, respectively (**Figure 7.1e**).[32, 34] Similarly, the high-resolution N1s spectrum reveals the existence of four kinds of N-functionality[29, 35] - pyridinic-N (398.8 eV), pyrrolic-N (399.5 eV), amino-N (400.2 eV), and graphitic-N (401.7 eV) (**Figure 7.1f)**. The detailed percentage of contribution calculated from XPS analysis is presented in **Table A.7.1**. Thus, the above analyses support a high degree of heterogeneity within the NCDs.

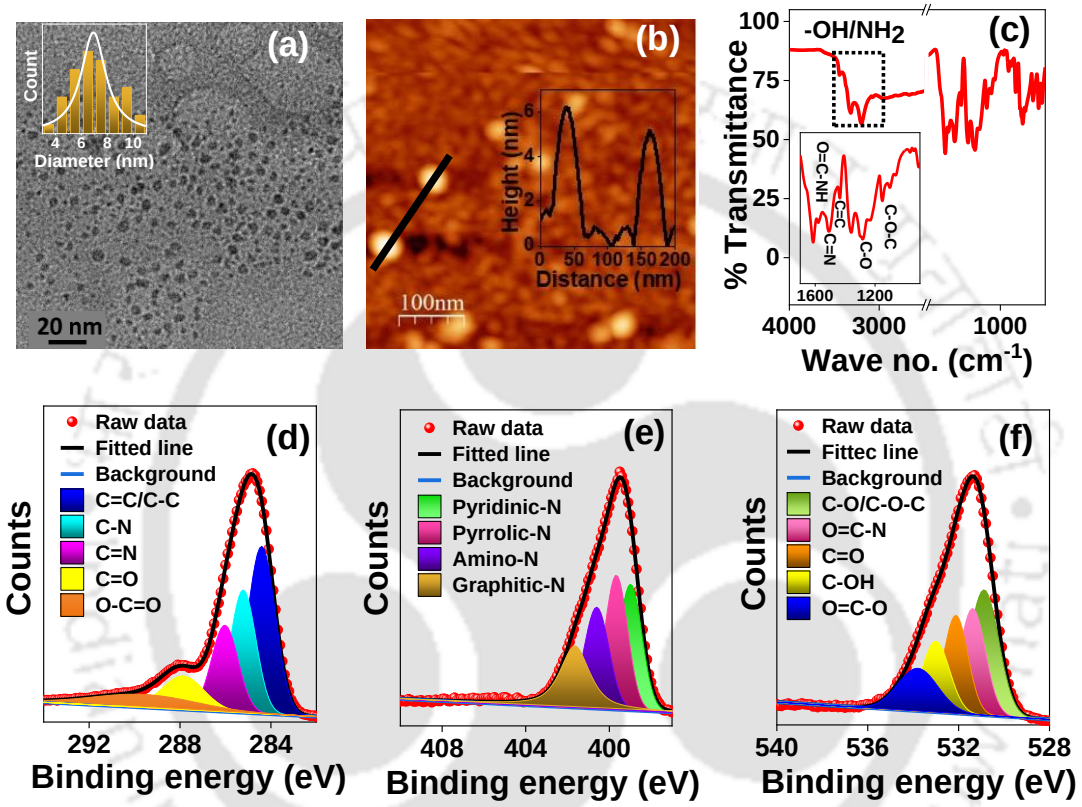

Figure 7.1. (a) TEM image (inset shows size distribution), (b) AFM image (inset shows height distribution) (c) FTIR spectrum (inset spectrum shows FTIR spectrum in the range from 900-1700 cm^{-1}); deconvoluted X-ray photoelectron spectra of (d) C 1s, (e) N 1s, and (f) O 1s.

7.2.2 Photo-physical Properties

The UV-vis absorption spectrum of NCD (**Figure 7.2a**) shows a strong band at 310 nm characteristics of $\pi \rightarrow \pi^*$ transitions involving the carbogenic core and a relatively broad tail, ranging from 400 nm to 500 nm, representing $n \rightarrow \pi^*$ transition of carbon bonded with other heteroatoms (N and O). The NCDs emission spectra are not dependent on excitation wavelengths and show an excitation maximum at 420 nm (**Figure 7.2b**). The NCD exhibits two overlapped FL emission bands at 490 nm and 570 nm and shows bright yellowish-green color underneath a 365 nm UV lamp (inset of **Figure 7.2a**) with a relative quantum

yield of 18.2 %. The calculated CIE coordinate of NCD is (0.33, 0.42) (**Figure 7.2c)**. The NCDs exhibits zeta potential value -7.71 mV.

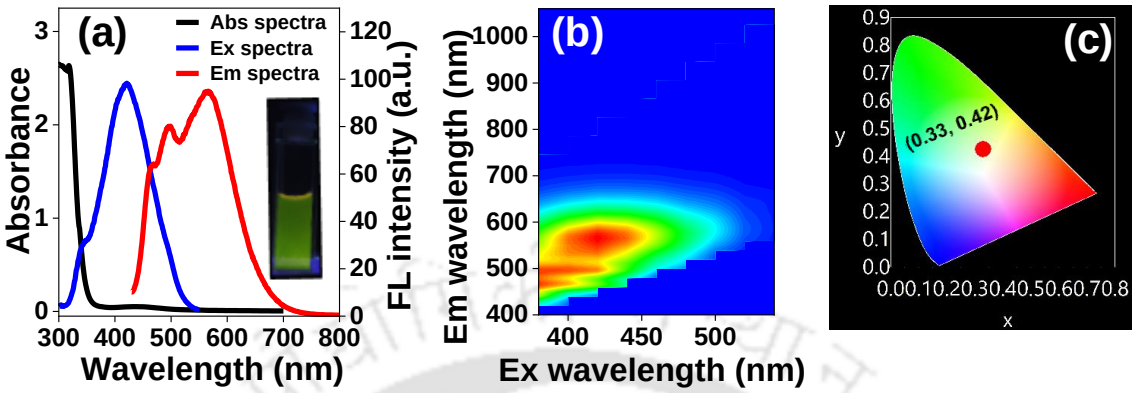

Figure 7.2. (a) UV–vis absorption, FL excitation (λ_{em} 570 nm), and emission (λ_{ex} 410 nm) spectra of NCDs, (b) contour plot for excitation dependent emission, (c) CIE coordinate under 410 nm excitation.

The characteristic of the emission spectrum becomes interesting when recorded at various pH. Especially with changing the pH value from acidic to alkaline, the intensities of the two emission bands gradually increase (**Figure 7.3a and Figure A.7.2a**), but the relative increment of the 570 nm peak is much more than the 490 nm peak. The intensity ratio (F_{490}/F_{570}) plot against pH followed a sigmoidal pattern (**Figure 7.3b**). Moreover, some changes were also observed in the absorption spectra (**Figure 7.3c**), especially the lower energy absorption peak shifts to the blue side with altering the pH value from 2 to 7.6, signifying that the variation of pH may also change the surface-state electronic transitions of NCDs. However, in the basic medium (8 to 12), absorption spectra coincide (**Figure A.7.2b**). Although the solution colors appear the same in daylight, they change remarkably from light-green to yellowish-green under a UV lamp (365 nm), with the pH variation from acidic to basic (**Figure 7.3d and 7.3e**). The calculated CIE coordinate value from pH 2 to 12 was represent in **Figure A.7.2c and Table A.7.2**. The absorbance ratio plot also shows a sigmoidal fit resulting in a pKa value of 5.6 (**Figure 7.3f**). The FL decays of the green and yellow emissions vary with pH (**Figure 7.3g and 7.3h**). The average lifetime of green (490 nm) and yellow (570 nm) shows dramatic changes with changing pH from 2 to 7.5 (**Table A.7.3**). Hence, the pH-sensitive emission stems from both the ground-state and excited-state processes. Earlier literature reports proposed that the pH sensitivity of carbon dots originated from the association and dissociation of H^+ of some acidic and alkaline groups present at the surface of CDs, which directly induces FL signal alteration.[36-39] It is

challenging to develop a CD with inherent ratiometric performance to different pHs with accompanying visual color changes.

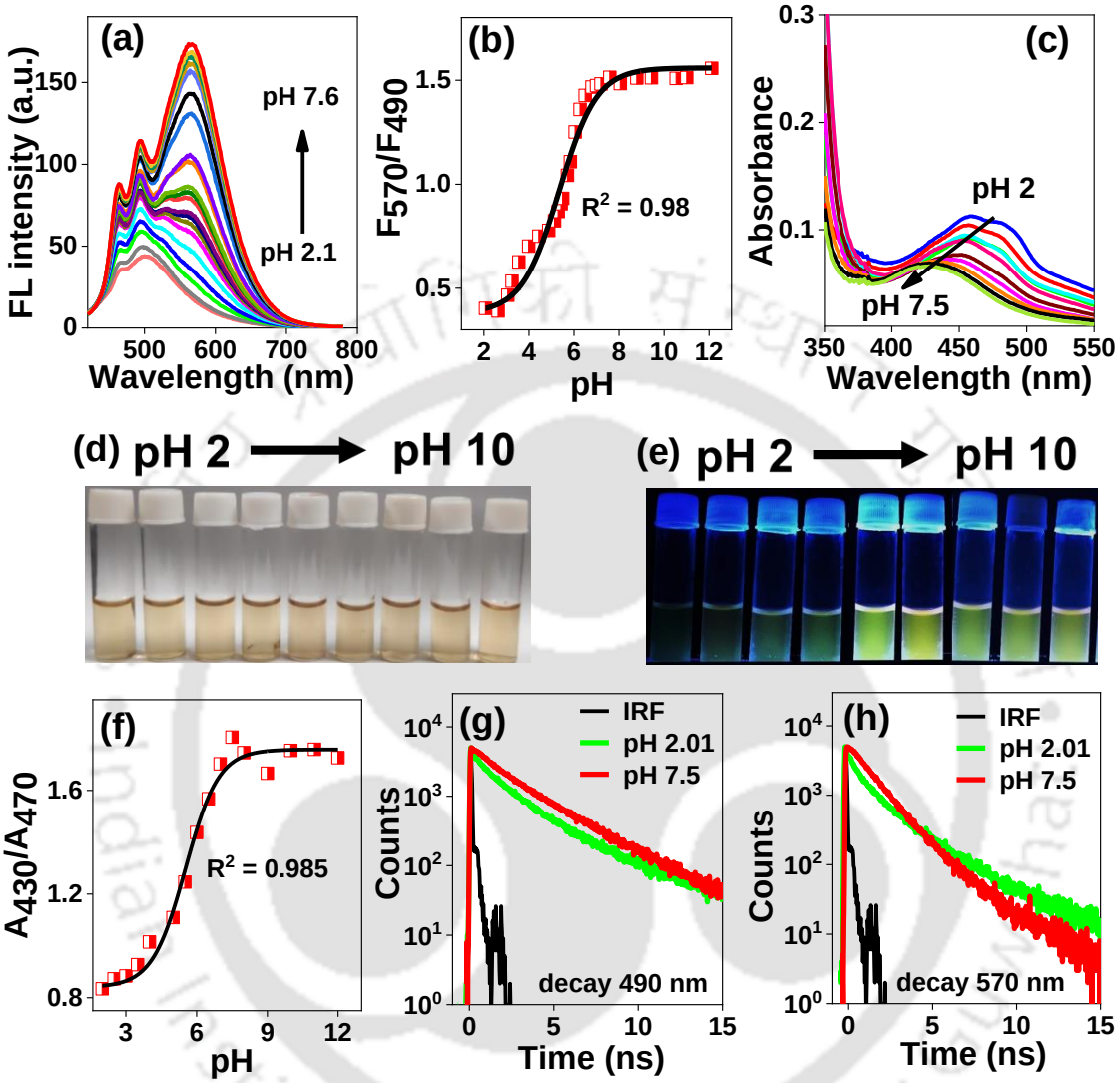

Figure 7.3. (a) pH dependent emission profile (pH 2.1 to 7.6), (b) Intensity ratio (F_{570}/F_{490}) vs. pH plot, (c) pH dependent absorption spectra, Photograph of pH variation under (d) daylight, (e) 365 nm UV lamp, (f) Absorbance ratio (A_{430}/A_{470}) plot under different pH values. Fluorescence decays monitored at (g) 490 nm and (h) 570 nm wavelengths (λ_{ex} = 405 nm).

7.2.3 Fe^{3+} detection and its mechanism

The medium pH and incubation duration are crucial factors in achieving better analytical performance. Here 25 μM Fe^{3+} was incorporated into the NCDs solution to check the response time and find the optimal pH. Here, only 4 min is required to change the emission peaks in a ratiometric manner (**Figure 7.4a**). The sensing study was performed in the pH

range of 3.4 to 8, with the maximum change occurring at pH 3.4 and 5.5 (**Figure 7.4b-7.4f**). We chose the less acidic pH of 5.5 for further study.

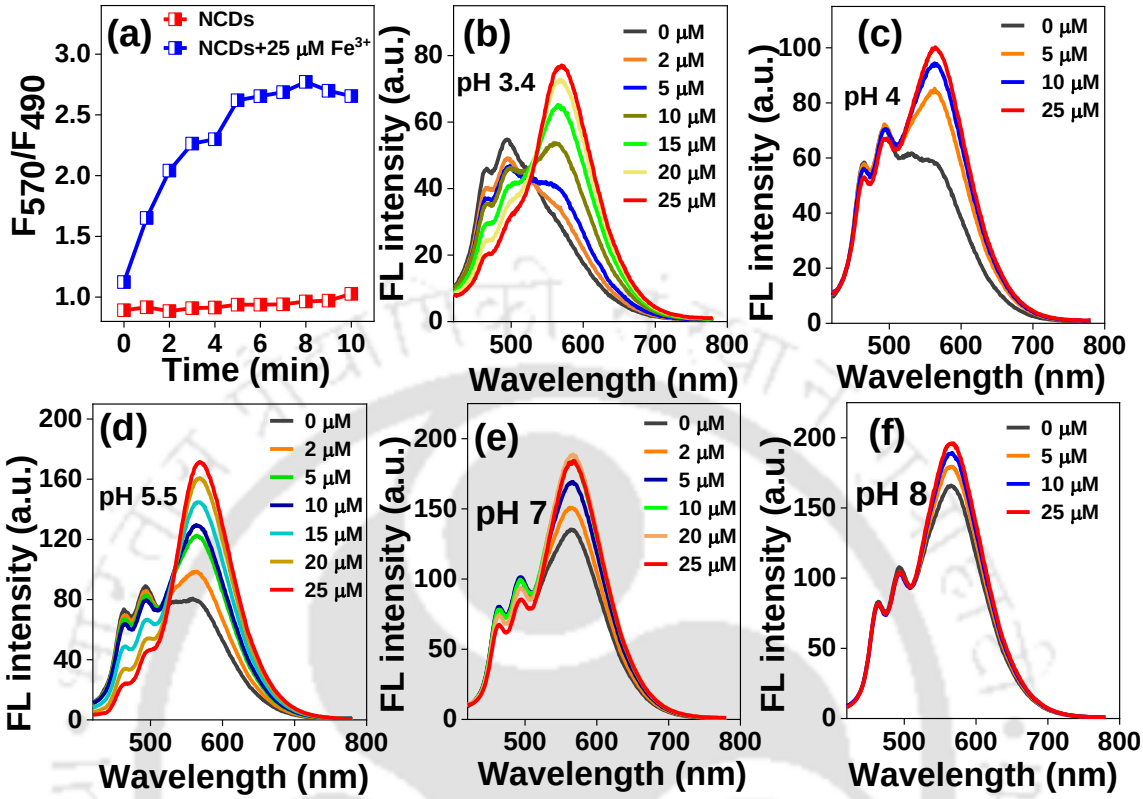

Figure 7.4. (a) time –dependent Fe^{3+} sensing, (b)-(f) pH-dependent Fe^{3+} detection

With the subsequent addition of Fe^{3+} up to 200 μM, the NCDs show ratiometric changes in emission intensity, i.e., the 490 nm peak gradually decreases, and the 570 nm peak gradually increases (**Figure 7.5a**). The F_{570}/F_{490} plot shows a linear response up to 10 μM concentration (**Figure 7.5b)** with a 0.88 μM detection limit. The shifting of the CIE coordinate value from [red; (0.33, 0.43)] to [blue; (0.47, 0.50)] was also observed with the regular addition of Fe^{3+} (**Figure 7.5c**). This color variation is evident in the naked eye under normal light and a 365 nm UV lamp (**Figures 7.5d and 7.5e**). The selectivity of NCD was measured by taking various metal ions (**Figure A.7.4**), but NCDs are pretty selective and sensitive toward Fe^{3+} only.

Various surface groups may interact with Fe^{3+} causing such ratiometric change in FL intensities. UV-vis absorption and XPS analysis were undertaken to support the formalism. The absorption peak at 444 nm gradually increases with the subsequent addition of Fe^{3+}, indicating the complexation between NCDs and Fe^{3+}. (**Figure 7.5f**). The complexation was

also corroborated further by XPS characterization, where a distinct peak for Fe 2p was observed (**Figure A.7.4a**).

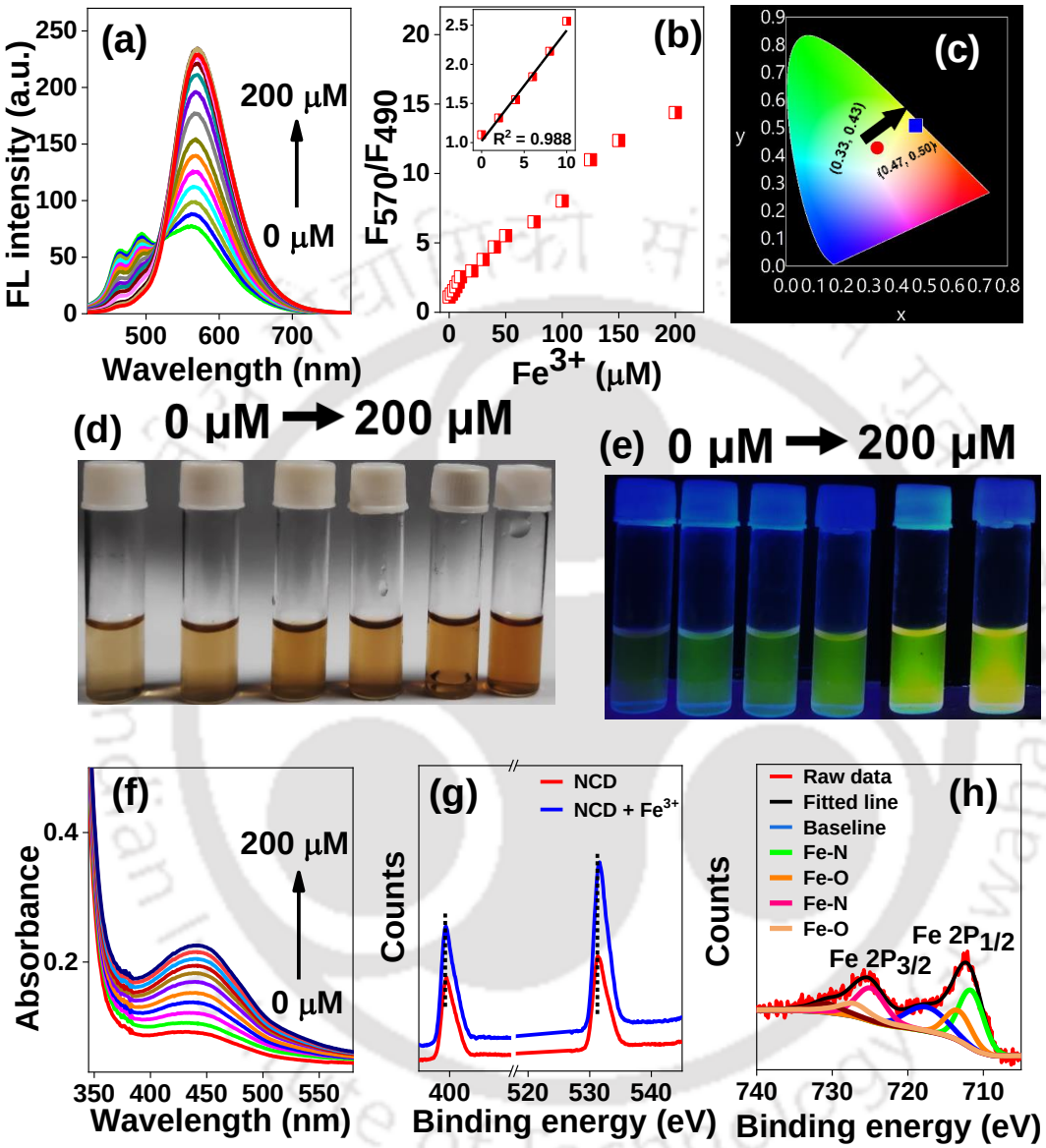

Figure 7.5. (a) Emission spectra of NCD in the presence of Fe3+ displaying ratiometric changes at pH 5.5, (b) Intensity ratio (F570/F490) against Fe^{3+} concentration plot (inset shows linear response up to 10 µM). (c) CIE coordinate of NCDs and NCDs-Fe^{3+}, digital photograph of NCDs with different concentration of Fe^{3+} under normal light (d) and (e) UV light. (f) Absorbance spectra of NCDs with various concentrations of Fe^{3+}, (g) XPS peak shifting for N 1s and O 1s with Fe^{3+} addition, (h) deconvoluted XPS spectra of Fe 2p.

Moreover, there are apparent shifting of N 1s and O 1s spectra by ~ 0.3 eV and 0.4 eV, respectively (**Figure 7.5g and 7.5h**). After deconvolution of N1s and O1s spectra (**Figure A.7.4b, A.7.4c and Table A.7.4**), the significant shift of binding energy value for amino-N, graphitic-N, C-OH, C=O, and O-C=O bonds. Furthermore, the high-resolution XPS

spectra of Fe 2p suggested the formation of Fe-O and Fe-N bonds[40] (**Figure 7.5h**). Hence, it can be stated that Fe^{3+} may interact with oxygen and nitrogen-containing functional groups and form the NCDs-Fe^{3+} complex. Thus, it can be concluded that the Fe^{3+} forms complex with NCDs leading to aggregation, which is responsible for ratiometric changes in FL behavior.

7.2.4 Biological applications

The effect of NCD on MCF-7 and noncancerous HEK-293 cells was assessed via an MTT-based assay where cell viability is expressed quantitatively with respect to half-maximal inhibitory concentration (IC_{50}). Cellular proliferation in the case of MCF-7 following NCD-treatment decreases in a concentration-dependent manner (**Figure 7.6a**). The corresponding IC_{50} value for NCD-treated MCF-7 cells was found to be 452 µg/ml. Even though a dose-dependent reduction was observed in HEK-293 cells, the viability remained over 60% within the tested range (**Figure 7.6b**).

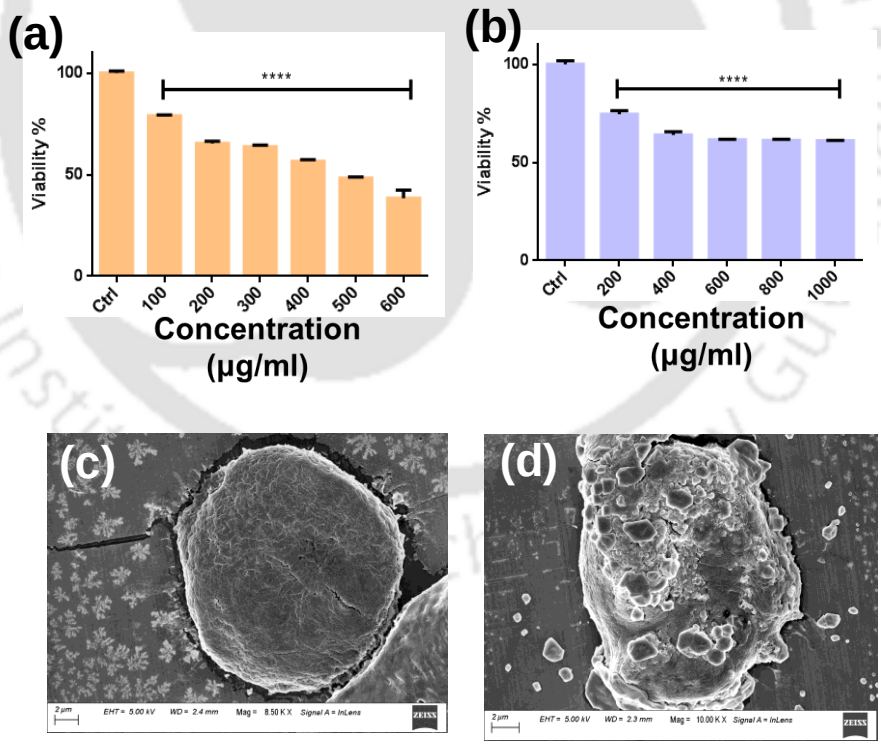

Figure 7.6. MTT assay of NCDs (a) MCF-7 and (b) HEK-293 cell-line, (c) and (d) are the FESEM images of untreated and treated MCF-7 cells, respectively.

To study the morphology of the NCD-treated MCF-7 cells, FESEM was conducted (**Figures 7.6c and 7.6d)**. The MCF-7 cells treated with NCDs at IC_{50} concentration for 12

h show visible blebbing, damaged cell surface, in coherence with apoptotic pathway initiators (**Figure 7.6d**). Apoptosis is characterized by a distinct set of morphological alterations synchronizing with programmed cell death. These include loss of focal adhesion, cell membrane blebs or bud formation, and cell shrinkage.[41, 42] The mechanism behind such an alteration can be due to cell stress following treatment that disrupts protein and lipid bilayer, leading to a loss of cell membrane integrity. Thus, it may be concluded that treating NCDs on luminal breast cancer cells (MCF-7) can deregulate cellular pathways manifested through morphological degradation.

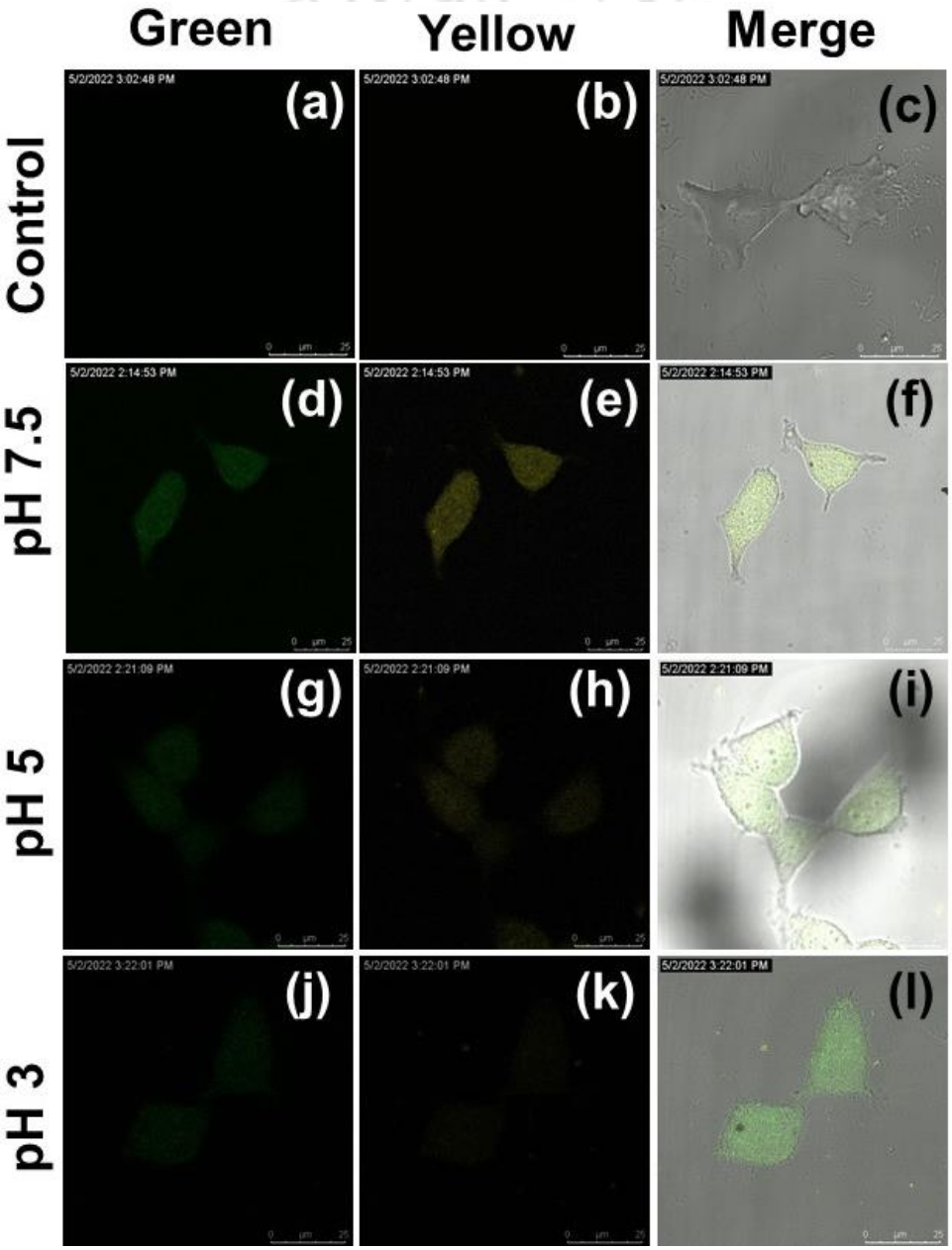

Figure 7.7. Decrease of FL intensity with gradual change of pH, (a)-(c) cell control, (d)-(f) pH 7.5, (g)-(i) pH 5 and (j)-(l) pH 3.

The NCDs were also useful for bioimaging; MCF-7 cells were visualized under the confocal microscope following treatment for 7 h. The microscopy images confirmed the uptake of the NCDs into the breast cancer cells as indicated by the green (490 nm) and yellow (570 nm) luminescence under the 405 laser source. **Figures 7.7d-7.7l** depicted that as the pH increases from 3 to 7.5, both the emission (green and yellow channels) intensities increase, demonstrating that the NCDs have a superior ability to detect intracellular pH.

Moreover, **Figure 7.8a-7.8f** shows NCDs-treated MCF-7 cells under pH 5.5. The figures show that NCDs are well-dispersed throughout the cytoplasm, exhibiting a bright green and yellow emission. Interestingly, as exogenous 200 µM Fe^{3+} is incorporated into the cell line, the yellow emission increases with the concomitant diminishing of the green emission further confirming the ratiometric detection of Fe^{3+}. This outcome confirms that NCD has the superior cell-penetrating ability making it an ideal bioimaging tool.

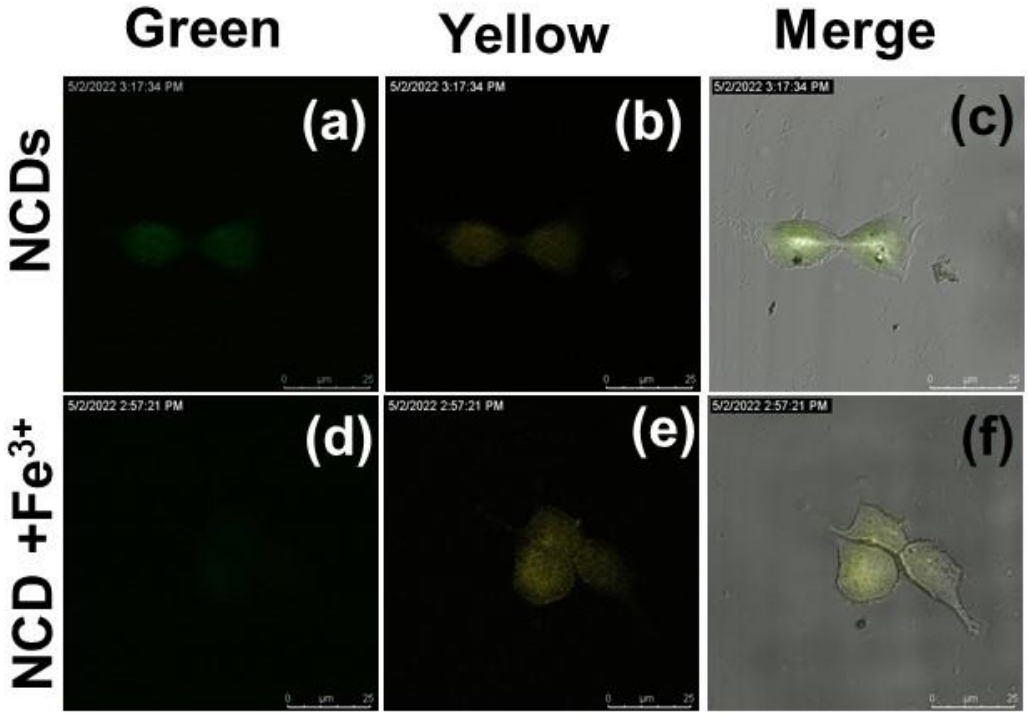

Figure 7.8. Ratiometric change of FL intensity in MCF-7 cell line at pH 5.5 (a) only NCDs and (b) NCDs treated with Fe^{3+}.

7.2.5 Solution phase white light (WL) generation

The demand for nature-friendly WL systems is rapidly growing. The challenge for researchers is to prepare WL using non-toxic and bio-friendly material.[43] In the current scenario, WL has been generated simply by mixing various colors (blue, green, red, and

yellow) emitting fluorophores with low toxic behavior.[44] To generate WL, the contribution of three crucial colors (blue, green, and red) or two colors with a similar FL intensity that almost covers the entire visible range (400nm to 700 nm) is essential.[45] Here, two different CDs - as-prepared NCDs (pH 6, 150 µg/ml, **Figure 7.9a**) and previously reported blue emissive NCD-1[29] (50 µg/ml, **Figure 7.9b**) was taken two produce WL (**Figure 7.9c**). The mixture produces perfect WL with the CIE coordinate value (0.32, 0.33) under excitation of 390 nm. in **Figure 7.9d**. The solution can effectively produce white light under a 365 nm UV lamp (**Figure 7.9f**).

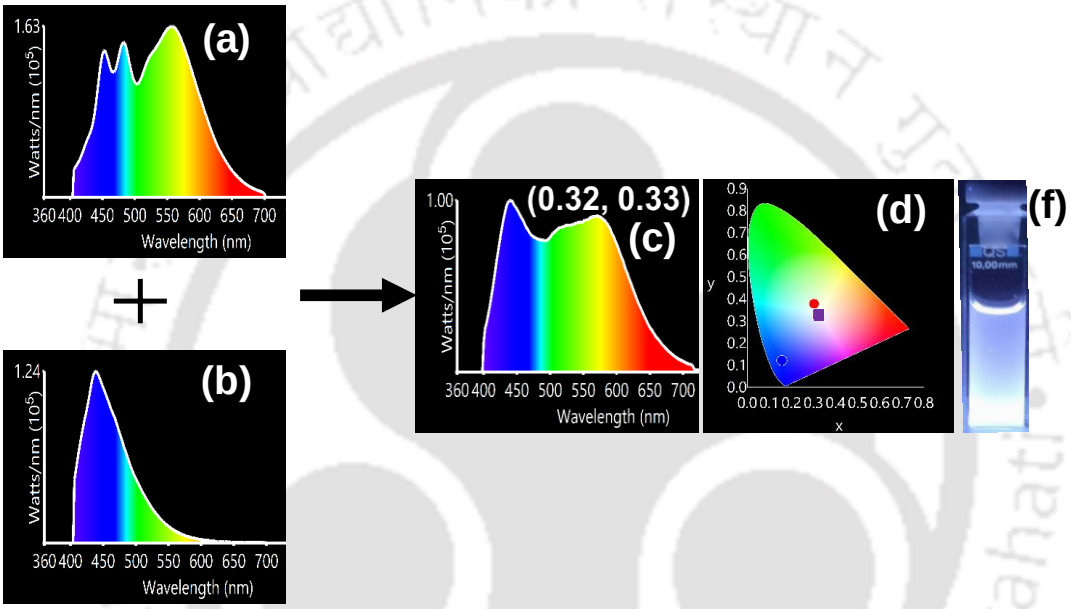

Figure 7.9. Emission spectra of (a) NCDs at pH 6, (b) NCD-1 (excitation 390 nm), (c) combined white light emission spectrum, (d) CIE coordinate diagram of NCDs [red circle; (0.30, 0.37)], NCD-1 [red circle; (0.0.15, 0.12)], white light spectrum [purple square; (0.32, 0.33)], (f) digital photograph of white light emission under a 365 nm UV lamp.

7.3 Conclusion

In summary, a dual-emissive nanoprobe was designed with emission at green (490 nm) and yellow (570 nm) to successfully detect pH and Fe^{3+} in a sensitive, rapid, and ratiometric manner. The alteration of protonation-deprotonation equilibrium of various nitrogen and oxygen-containing surface functional with H^+ concentrations are responsible for the pH-dependent emission response. The nanoprobe undergoes complexation with Fe^{3+} through surface heteroatomic functionality and exhibits a ratiometric change of emission bands enabling visual detection of Fe^{3+}. Finally, white light emission was generated by combining the broad emission of the NCD with the blue emission of another NCD. The biocompatible

NCD displays anticancer activity in the breast cancer cell (MCF-7). The NCDs can efficiently recognize intracellular pH and Fe^{3+} in the MCF-7 cell line, which can be important in the clinical platform.

References

1. Z.-X. Han, X.-B. Zhang, Z. Li, Y.-J. Gong, X.-Y. Wu, Z. Jin, C.-M. He, L.-X. Jian, J. Zhang, G.-L. Shen and R.-Q. Yu, *Anal. Chem.*, 2010, **82**, 3108-3113.

2. Y. Kubo, M. Yamamoto, M. Ikeda, M. Takeuchi, S. Shinkai, S. Yamaguchi and K. Tamao, *Angew. Chem. Int. Ed.*, 2003, **42**, 2036-2040.

3. M. A. Haidekker, T. P. Brady, D. Lichlyter and E. A. Theodorakis, *J. Chem. Soc.*, 2006, **128**, 398-399.

4. J. Yao, K. Zhang, H. Zhu, F. Ma, M. Sun, H. Yu, J. Sun and S. Wang, *Anal. Chem.*, 2013, **85**, 6461-6468.

5. J. Hou, P. Jia, K. Yang, T. Bu, S. Zhao, L. Li and L. Wang, *ACS Appl. Mater. Interfaces*, 2022, **14**, 13848-13857.

6. X. Han, J. Liu, K. Yu, Y. Lu, W. Xiang, D. Zhao and Y. He, *Inorg. Chem*, 2022, **61**, 5067-5075.

7. G. Ge, L. Li, D. Wang, M. Chen, Z. Zeng, W. Xiong, X. Wu and C. Guo, *J. Mater. Chem. B*, 2021, **9**, 6553-6575.

8. V. Sharma, *J. Mater. Chem. C*, 2021, **9**, 16828-16842.

9. M. Li, T. Chen, J. J. Gooding and J. Liu, *ACS Sens.*, 2019, **4**, 1732-1748.

10. P. Zhao and L. Zhu, *Chem. Commun.*, 2018, **54**, 5401-5406.

11. L. Li and T. Dong, *J. Mater. Chem. C*, 2018, **6**, 7944-7970.

12. J.-R. Macairan, T. V. de Medeiros, M. Gazzetto, F. Yarur Villanueva, A. Cannizzo and R. Naccache, *J. Colloid Interface Sci.*, 2022, **606**, 67-76.

13. C. Wang, H. Lin, Z. Xu, Y. Huang, M. G. Humphrey and C. Zhang, *ACS Appl. Mater. Interfaces*, 2016, **8**, 6621-6628.

14. S. Kundu, M. Ghosh and N. Sarkar, *Langmuir*, 2021, **37**, 9281-9301.

15. H. Tan, X. Wu, Y. Weng, Y. Lu and Z.-Z. Huang, *Anal. Chem.*, 2020, **92**, 3447-3454.

16. J. S. Sidhu, A. Singh, N. Garg and N. Singh, *ACS Appl. Mater. Interfaces*, 2017, **9**, 25847-25856.

17. Y. Ding, Y. Lu, K. Yu, S. Wang, D. Zhao and B. Chen, *Adv. Opt. Mater.*, 2021, **9**, 2100945.

18. R. Jiang, Y. Zhang, Q. Zhang, L. Li and L. Yang, *ACS Appl. Nano Mater.*, 2021, **4**, 9760-9767.

19. C. Yao, Y. Xu and Z. Xia, *J. Mater. Chem. C*, 2018, **6**, 4396-4399.

20. Y.-S. He, C.-G. Pan, H.-X. Cao, M.-Z. Yue, L. Wang and G.-X. Liang, *Sens. Actuators B: Chem.*, 2018, **265**, 371-377.

21. X. Yu, C.-X. Zhang, L. Zhang, Y.-R. Xue, H.-W. Li and Y. Wu, *Sens. Actuators B: Chem.*, 2018, **263**, 327-335.

22. M. Chowdhury and P. Kumar Das, *ACS Appl. Bio Mater.*, 2021, **4**, 5132-5144.

23. Y. Han, H. Liu, M. Fan, S. Gao, D. Fan, Z. Wang, J. Chang, J. Zhang and K. Ge, *J. Colloid Interface Sci.*, 2022, **616**, 595-604.

24. T. Boobalan, M. Sethupathi, N. Sengottuvelan, P. Kumar, P. Balaji, B. Gulyás, P. Padmanabhan, S. T. Selvan and A. Arun, *ACS Appl. Nano Mater.*, 2020, **3**, 5910-5919.

25. R. Su, H. Yan, X. Jiang, Y. Zhang, P. Li and W. Su, *J. Mater. Chem. B*, 2022, **10**, 1250-1264.

26. Q. Luo, K. Qin, F. Liu, X. Zheng, Y. Ding, C. Zhang, M. Xu, X. Liu and Y. Wei, *Analyst*, 2021, **146**, 1965-1972.

27. J. Chen, W.-R. Liu, Y. Li, X. Zou, W. Li, J. Liang, H. Zhang, Y. Liu, X. Zhang, C. Hu and B. Lei, *Chem. Eng. J.*, 2022, **428**, 131168.

28. P. Sarkar, M. Saha, N. Nandi, D. K. Sahu and K. Sahu, *ACS Appl. Nano Mater.*, 2022, DOI: 10.1021/acsanm.1c04496.

29. N. Nandi, P. Sarkar and K. Sahu, *ACS Appl. Nano Mater.*, 2021, **4**, 9616-9624.

30. F. Arcudi, L. Đorđević, S. Rebeccani, M. Cacioppo, A. Zanut, G. Valenti, F. Paolucci and M. Prato, *Adv. Sci.*, 2021, **8**, 2100125.

31. S. Pandit, S. Mondal and M. De, *J. Mater. Chem. B*, 2021, **9**, 1432-1440.

32. N. Nandi, S. Gaurav, P. Sarkar, S. Kumar and K. Sahu, *ACS Appl. Bio Mater.*, 2021, **4**, 5201-5211.

33. N. Nandi, P. Sarkar and K. Sahu, *Materials Today Chemistry*, 2022, **26**, 101015.

34. W. Tomal, T. Świergosz, M. Pilch, W. Kasprzyk and J. Ortyl, *Polym. Chem.*, 2021, **12**, 3661-3676.

35. N. Nandi, S. Gaurav, P. Sarkar, S. Kumar and K. Sahu, *ACS Appl. Bio Mater.*, 2021, **4**, 7605-7614.

36. J.-L. Zhao, Q.-Y. Luo, Q. Ruan, K. Chen, C. Liu, C. Redshaw and Z. Jin, *Chem. Mater.*, 2021, **33**, 6091-6098.

37. E. Liu, T. Liang, E. V. Ushakova, B. Wang, B. Zhang, H. Zhou, G. Xing, C. Wang, Z. Tang, S. Qu and A. L. Rogach, *J. Phys. Chem. Lett.*, 2021, **12**, 604-611.

38. C. Liu, M. Yang, J. Hu, L. Bao, B. Tang, X. Wei, J.-L. Zhao, Z. Jin, Q.-Y. Luo and D.-W. Pang, *J. Phys. Chem. Lett.*, 2021, **12**, 2727-2735.

39. S. Dutta Choudhury, J. M. Chethodil, P. M. Gharat, P. P. K and H. Pal, *J. Phys. Chem. Lett.*, 2017, **8**, 1389-1395.

40. R. Maity, D. Chakraborty, S. Nandi, A. K. Yadav, D. Mullangi, C. P. Vinod and R. Vaidhyanathan, *ACS Appl. Nano Mater.*, 2019, **2**, 5169-5178.

41. G. Häcker, *Cell Tissue Res.*, 2000, **301**, 5-17.

42. B. FADEEL and S. ORRENIUS, *J. Intern. Med.*, 2005, **258**, 479-517.

43. S. Shekhar, P. Mahato, R. Yadav, S. D. Verma and S. Mukherjee, *ACS Sustain. Chem. Eng.*, 2022, **10**, 1379-1389.

44. N. Muhamad Sarih, P. Myers, A. Slater, B. Slater, Z. Abdullah, H. A. Tajuddin and S. Maher, *Sci. Rep.*, 2019, **9**, 11834.

45. F.-Z. Li, L.-L. Zhou and G.-C. Kuang, *Chem.: Asian J.*, 2021, **16**, 97-101.

CHAPTER 8

Summary and Prospects

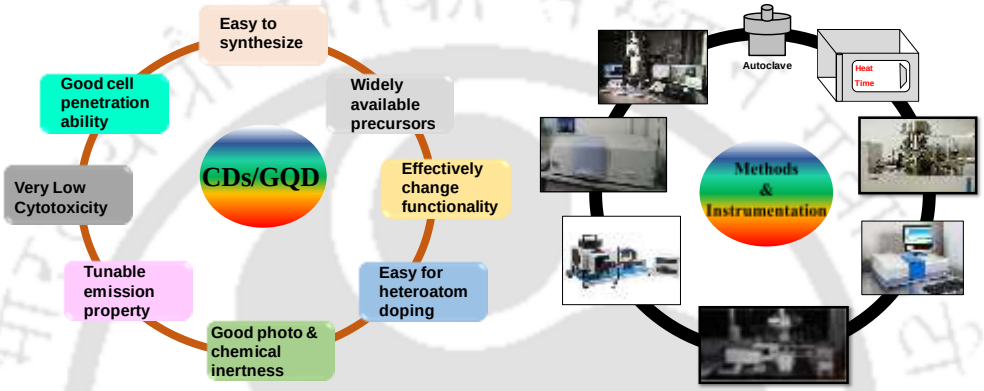

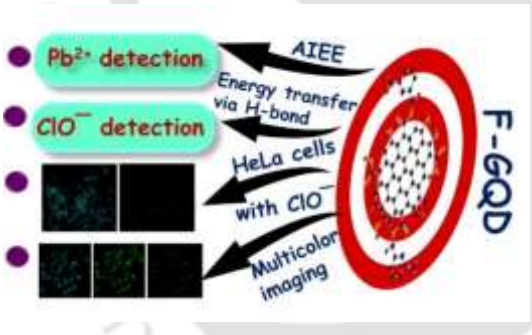

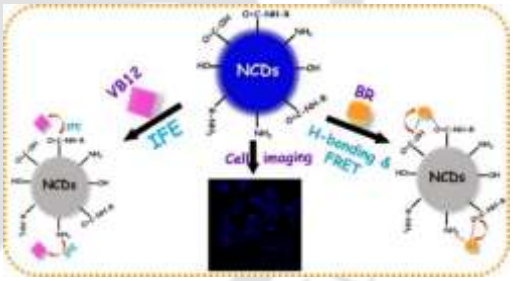

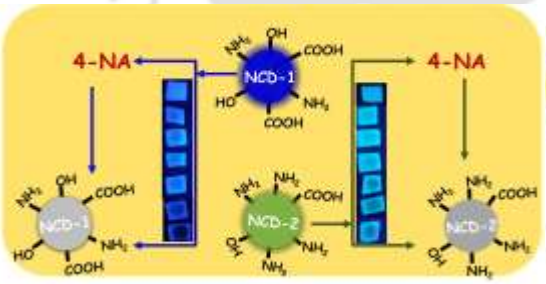

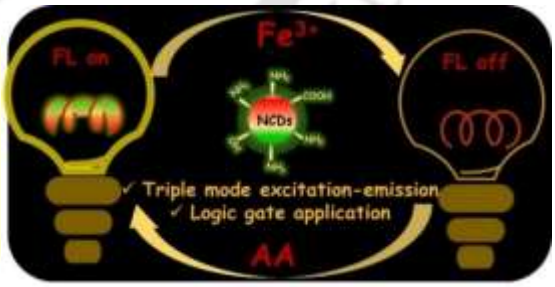

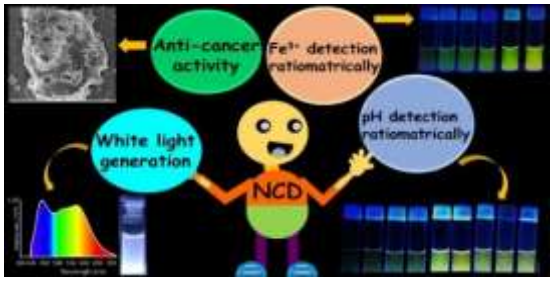

[This page was intentionally left blank]

8.1 Summary

Carbon dot is become an excellent nanoprobe due to its easy synthesis techniques, tiny size, and eco-friendly nature allow it as a promising material for versatile application fields. In the present thesis, a detailed discussion on the the synthesis strategy of various carbon dots with a thorough investigation of their photophysical properties as well as various applications have been presented. The thesis starts with an introduction which describes about the evolution of carbon dots, its exclusive properties, its applications etc. The second chapter of the thesis is about experimental methods describing the instrumentation and research methodologies used. After this there are five working chapters are summarized below.

In chapter three, an edge-functionalized graphene quantum dot was synthesized from graphene quantum dot and 2,6-diaminopyridine moieties. After introducing 2,6-diaminopyridine molecule the quantum yield was increased about 3 times. The sensing performance also improves after functionalization.

In chapter four, the novel highly blue emissive multifunctional N-doped carbon dot was developed by hydrothermal methods for the detection of two bio-analytes i.e., bilirubin and vitamin-B_{12}. was achieved via totally opposite sensing mechanism. Moreover, the carbon dot was also applied in HeLa cell line for the successful detection of vitamin-B_{12} in the living cell.

In chapter five, the hydrothermally-assisted two different percentage heteroatom-containing N-doped carbon dot was prepared. The optical characteristics of the two carbon dots are also different, one is blue emissive and another one is green emissive in nature. Both the synthesized nanodot exhibits high sensitivity toward 4-nitroaniline. Interestingly, the sensing mechanism is depending on the emission of carbon dot and solvent system.

In chapter six, a N-doped carbon dot was hydrothermally synthesized with some unique optical properties i.e., three different emission characteristics under three different excitation windows. This novel nanodot exhibits blue, green and red emission under particular exciatation wavelengths. From our spectroscopic analysis, it has been found that the core state and the surface state emission are responsible for this kind of emissions. The blue emission comes from the core-state while other two emissions come from the surface states. The surface state emissions (green and red) are highly sensitive towards Fe^{3+} via turn-off manner. Later, the off-state fluorescence easily recovered by adding ascorbic acid.

In chapter seven, a dual-emitting carbon dot was synthesized which is highly sensitive to pH and Fe^{3+} with two distinct ratiometric features. Here the nanodot also exhibits anti-cancerous property in the MCF-7 cell line. Moreover, the nanodot also recognizes the intracellular pH changes and exogenous Fe^{3+} in MCF-7 cell lines.

Finally, the thesis is concluded with a summary and future plan which explained the future prospects of these works presented in this thesis.

8.2 Prospects

In recent times, several studies have been performed on carbon dot synthesis, and applications to resolve many issues in terms of achieving high selectivity as well as sensitivity. The present thesis demonstrated the design and development of several novel carbon dots with superior optical properties. The photo-physical properties of these carbon dots have been studied systematically. Furthermore, these carbon dots have been applied as multimode sensing platform. I definitely believe that the advances presented in this thesis will inspire the future researchers to contribute towards highly efficient carbon dots. The optical properties of carbon dot can be further investigated by utilizing ultrafast spectroscopic techniques which can provide some idea about the generation of emission. Being a non-toxic carbon dot can be alternative for photodynamic and photothermal therapy.

Appendix Chapter 3

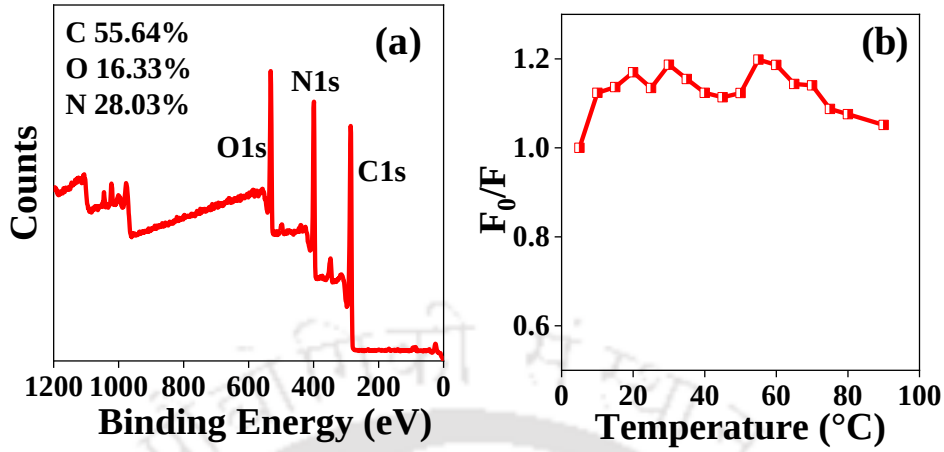

Figure A. 3.1. (a) Full range XPS spectra of F-GQD, (b) Temperature-dependent emission stability of F-GQD

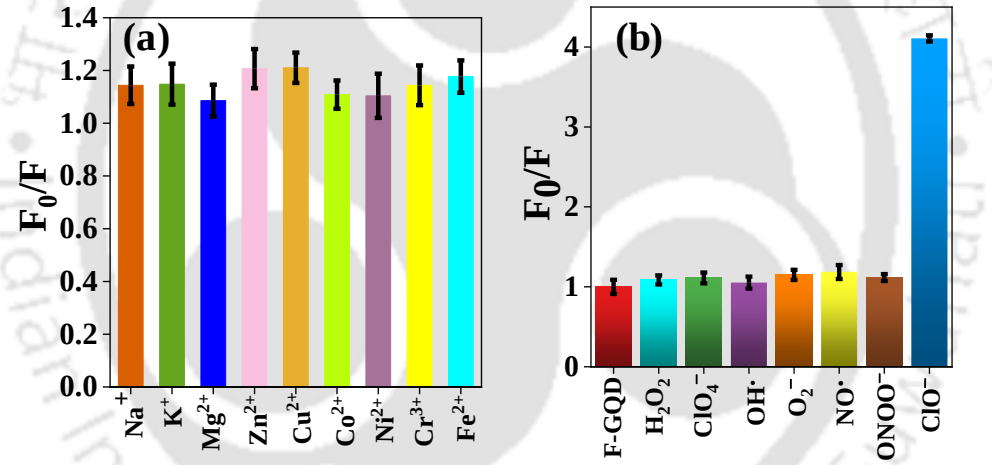

Figure A. 3.2. (a) Selecitivity study of F-GQD in presence of (a) metal ion, (b) other oxidative agents.

Table A. 3.1. FL decay fitting parameters of F-GQD the absence and presence Pb^{2+}.

	A_1	A_2	A_3	τ_1 (ns)	τ_2 (ns)	τ_3 (ns)	τ_{avg} (ns)	χ^2
F-GQD	0.16	0.02	0.86	3.05	17.93	1.04	1.74	1.21
F-GQD +450 µM Pb^{2+}	0.45	0.30	0.25	1.00	1.20	0.09	2.30	1.048

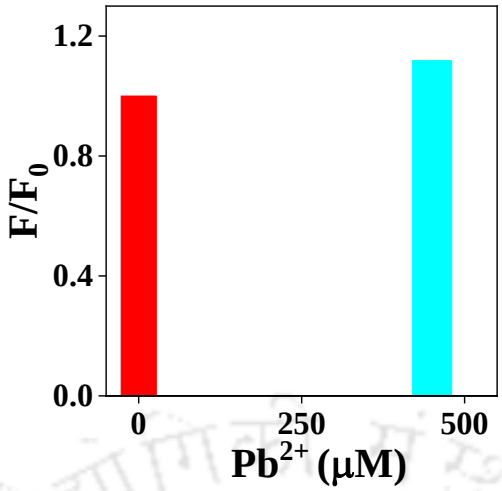

Figure A. 3.3. Fluorescence ratio of 2AP-GQD in presence of 450 mM of Pb^{2+}.

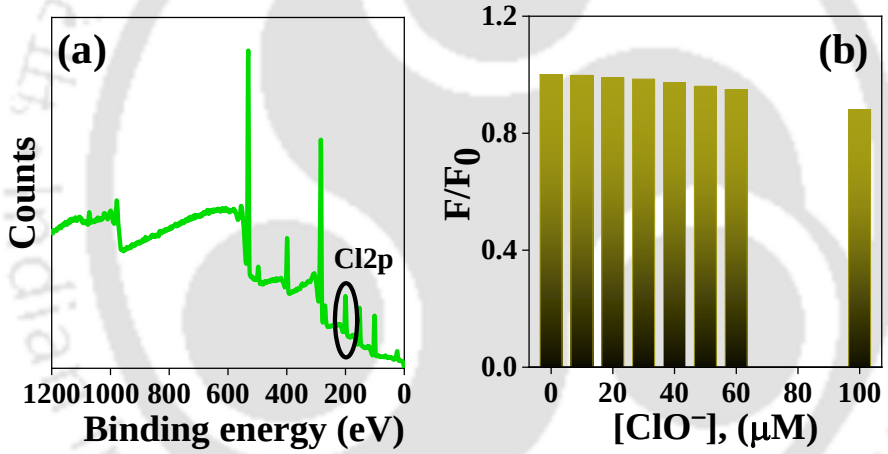

Figure A. 3.4. (a) XPS spectra of F-GQD in the presence of ClO^-, (b) fluorescence ratio of 2AP-GQD in presence of several concentrations of ClO^-.

Table A. 3.2. FL decay fitting parameters of F-GQD at different concentrations of ClO^-.

[ClO^-] (μM)	A_1	A_2	A_3	τ_1 (ns)	τ_2 (ns)	τ_3 (ns)	τ_{avg} (ns)	χ^2
0	0.16	0.02	0.86	3.05	17.93	1.04	1.74	1.21
6	0.2	0.05	0.75	1.84	7.66	0.46	1.10	1.109
20	0.22	0.02	0.76	1.30	8.50	0.031	0.48	1.207
26	0.14	0.02	0.84	1.23	7.91	0.026	0.35	1.26

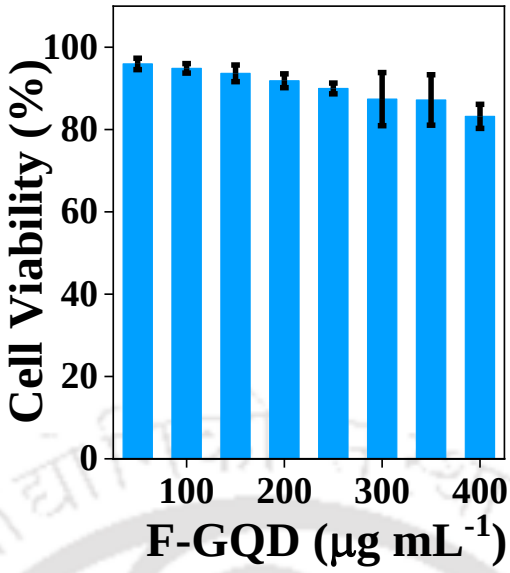

Figure A. 3.5. cell viability study of F-GQD in HeLa cells.

Appendix Chapter 4

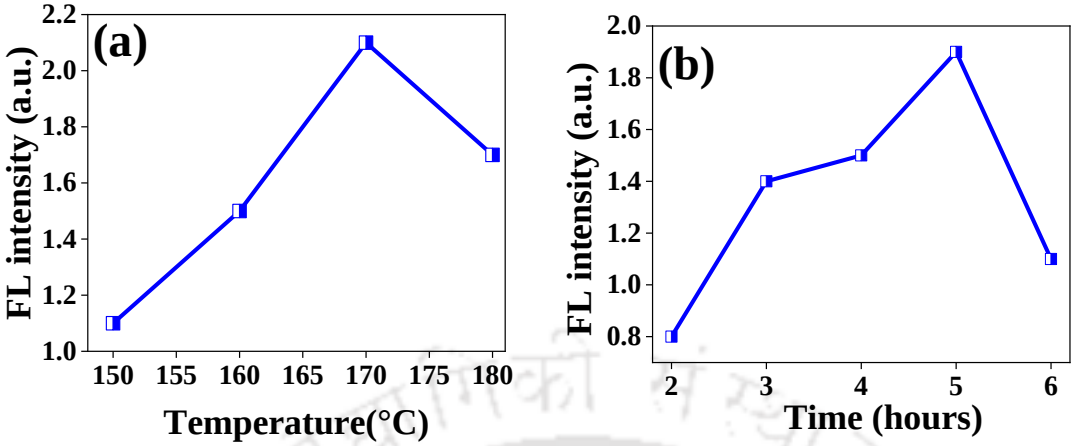

Figure A.4.1. Optimisation of synthesis procedure of NCDs by (a) temperature and (b) time.

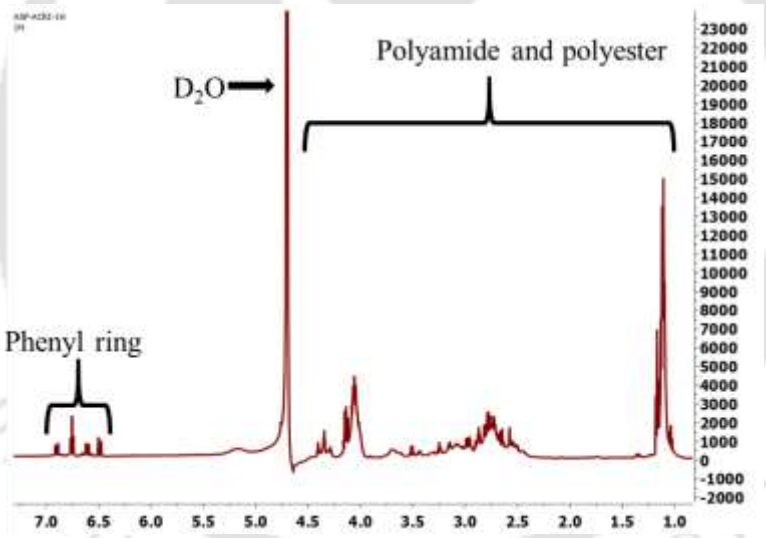

Figure A.4.2. ^{1}H-NMR of NCDs in D_2O

Table A.4.1. Deconvolution and peak assignment of Raman spectra of NCDs

Sample	Raman bands (cm^{-1})					
NCDs	1154	1238	1322	1387	1545	1632
Peak identity	C-C bond stretching of sp^2-sp^3 carbon	C-O-C	O=C-N bond	D band	G band	C-N bond

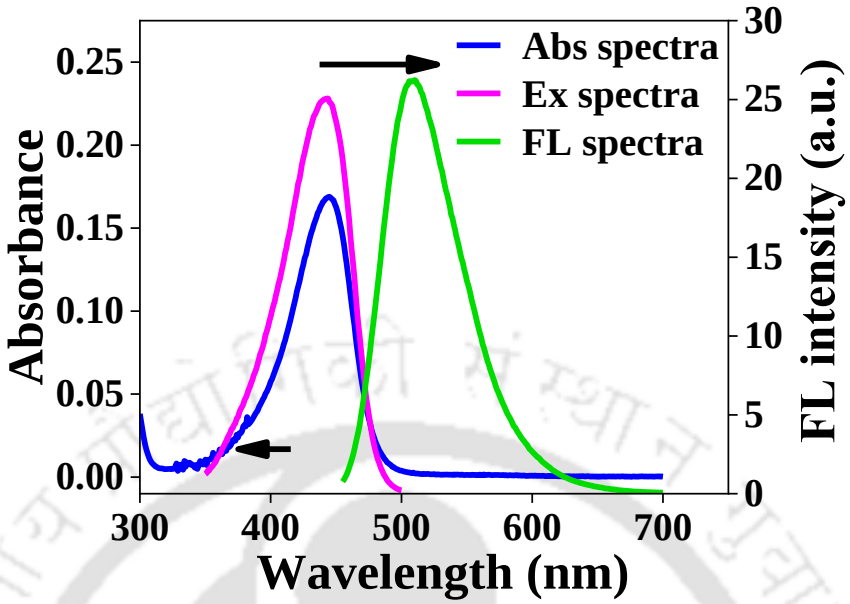

Figure A.4.3. Absorption, excitation and emission spectra of pure 3,6-diaminoacridine hydrochloride in water

Table A.4.2. Fitting parameters of solid state and solution state decay curve of NCDs

Samples	A1	A2	A3	T1 (ns)	T2 (ns)	T3 (ns)	T_{avg} (ns)	χ^2
NCDs-solution	0.36	0.27	0.37	3.90	11.38	0.500	4.66	1.134
NCDs Solid state	0.36	0.49	0.15	2.394	0.4565	6.3878	2.043	1.16

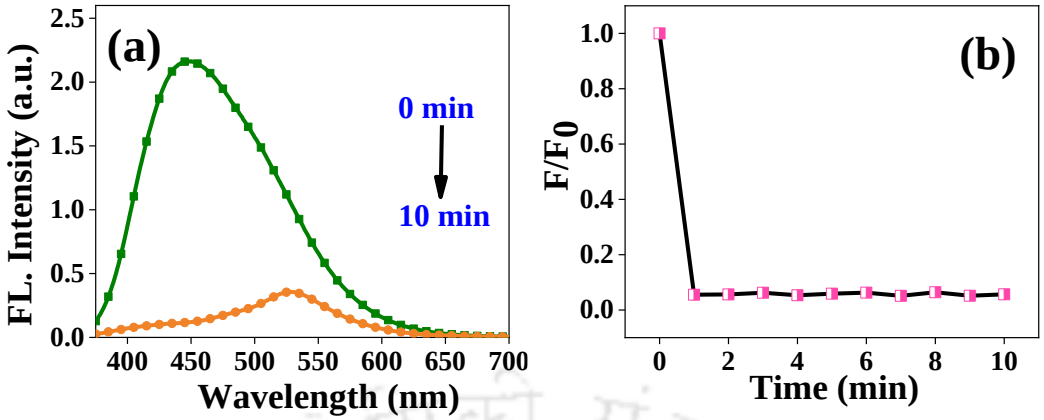

Figure A.4.4 (a) Fluorescence quenching response of NCDs after addition of 100μM bilirubin from 0 min to 10 min. (b) the suppression of FL intensity with time (excitation at 360nm).

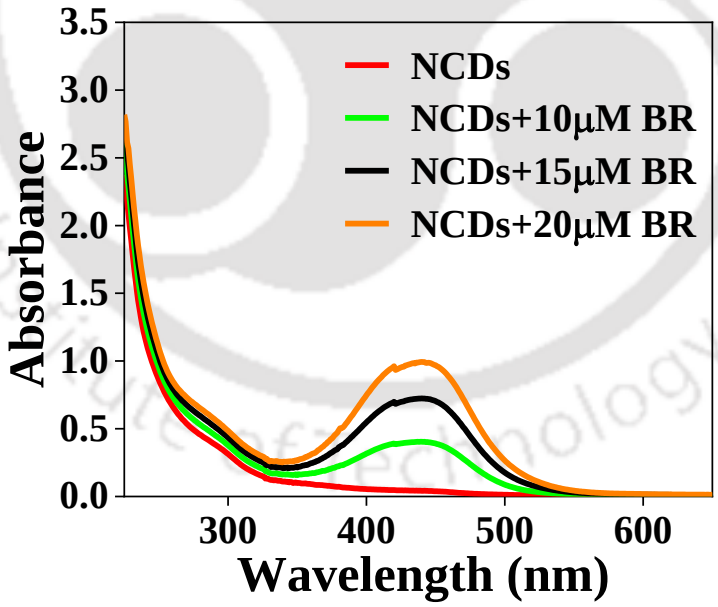

Figure A.4.5. UV-vis absorption spectra of NCDs with different concentrations of BR.

Table A.4.3. Fluorescence decay fitting parameter of NCDs with different concentration of BR.

Samples	A_1	A_2	A_3	τ_1 (ns)	τ_2 (ns)	τ_3 (ns)	τ_{av} (ns)	χ^2
NCDs	0.36	0.27	0.37	3.90	11.38	0.500	4.66	1.134
NCDs + 9μM BR	0.31	0.25	0.44	3.51	10.9	0.38	4.00	1.18
NCDs + 18μM BR	0.25	0.2	0.55	2.72	10.46	0.14	2.85	1.21
NCDs + 36μM BR	0.18	0.17	0.65	2.27	10.26	0.08	2.21	1.23
NCDs + 45μM BR	0.16	0.14	0.7	2.36	10.14	0.07	1.85	1.24

Table A.4.4. Fluorescence decay parameters of NCDs at different concentrations of VB12.

Samples	A_1	A_2	A_3	τ_1 (ns)	τ_2 (ns)	τ_3 (ns)	τ_{av} (ns)	χ^2
NCDs	0.36	0.27	0.37	3.90	11.38	0.500	4.66	1.134
NCDs + 70μM of VB12	0.34	0.35	0.31	2.62	9.7	0.29	4.40	1.10

Table A.4.5. IFE correction table for VB12

Conc. of VB12 (μM)	A_{ex}	A_{em}	CF	$F_{observed}$	$F_{corrected}$	$F_{corrected\ (0)}/F_{corrected}$
0	0.0516	0.02001	1.080371	2.18E+06	2359866	1.000000178
2	0.09912	0.0245	1.144634	2.00E+06	2.29E+06	1.031359785
4	0.14801	0.02999	1.214575	1.82E+06	2.22E+06	1.065299342
6	0.19762	0.03554	1.288504	1.59E+06	2.05E+06	1.148557202
8	0.24501	0.04135	1.362671	1.44E+06	1.97E+06	1.200667214
10	0.29069	0.04546	1.434654	1.31E+06	1.87E+06	1.259505908
14	0.39109	0.05678	1.605243	1.18E+06	1.90E+06	1.242970829
18	0.4995	0.069028	1.803654	1.06E+06	1.91E+06	1.232867317
22	0.60564	0.080389	2.01083	953420.8	1.92E+06	1.230913095
26	0.71115	0.09242	2.232028	860740.7	1.92E+06	1.228330881
30	0.81683	0.10457	2.467516	775154.5	1.91E+06	1.233783743

34	0.92059	0.116	2.710453	696749.3	1.89E+06	1.249593998
38	1.02206	0.12784	2.962121	624713.6	1.85E+06	1.275274031
42	1.12589	0.139525	3.230612	562580.2	1.82E+06	1.298428863
46	1.23165	0.151825	3.517875	507372.6	1.78E+06	1.322147492
50	1.33982	0.164221	3.823734	455150.5	1.74E+06	1.355952793
54	1.44436	0.176696	4.1333	410071.2	1.69E+06	1.392294714
58	1.54678	0.189091	4.448717	368615.9	1.64E+06	1.439058741
62	1.64747	0.201756	4.771994	332567.5	1.59E+06	1.486988816
66	1.74442	0.215381	5.10108	301153.5	1.54E+06	1.536162883

Appendix Chapter 5

Table A.5.1. Deconvoluted fitting parameter of XPS spectra of NCD-1

Sample	Spectrum	Peak position (eV)	Peak identity	% Of contribution
NCD-1	C1s	284.3	C=C	30
		285.1	C-N	24
		286	C=N	20
		288.8	C=O	26
	N 1s	398.9	Pyridinic-N	48
		399.7	Amino-N	39
		400.9	Pyrrolic-N	13
	O 1s	531	C-O	7
		532	C-O-C	42
		533.3	C-OH	39
		534.3	O=C-O	12

Table A.5.2. Deconvoluted fitting parameter of XPS spectra of NCD-2

Sample	Spectrum	Peak position (eV)	Peak identity	% Of contribution
NCD-2	C1s	284.7	C=C	67
		285.5	C-N	4
		286.2	C=N	13
		288.7	C=O	16
	N 1s	398.5	Pyridinic-N	19
		399.2	Amino-N	64
		400.2	Pyrrolic-N	17
	O 1s	531	C-O	9
		531.8	C-O-C	52
		533.3	C-OH	32
		534.1	O=C-O	7

Table A.5.3. Solid and solution state decay curve fitting parameter for NCD-1.

Sample	A_1	A_2	A_3	τ_1 (ns)	τ_2 (ns)	τ_3 (ns)	τ_{avg} (ns)	χ^2
FL_G	0.52	0.3	0.18	0.067	3.507	7.256	2.387	1.17
NCD-1 Solid state	0.07	0.06	0.87	1.701	6.9024	0.0342	0.5629	1.4

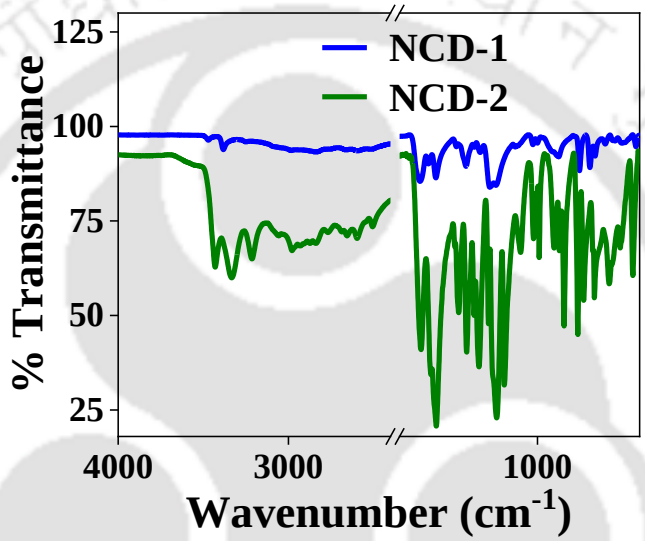

Figure A.5.1. Full range FTIR spectra

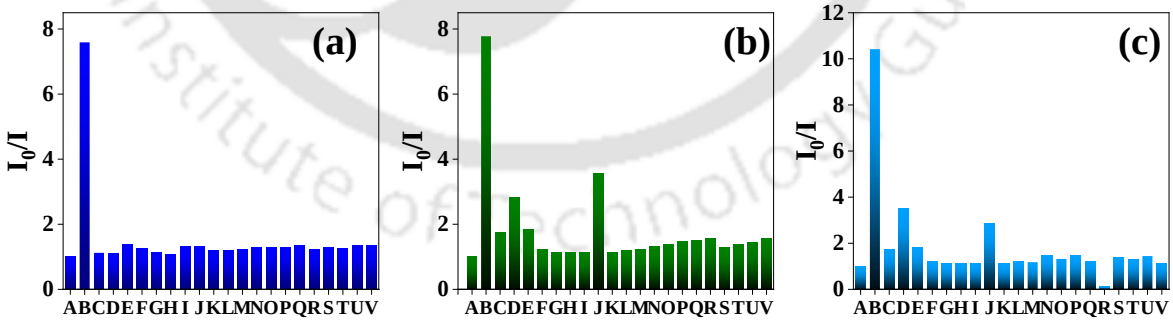

Figure A.5.2. Selectivity study of NCD-1 (a) and NCD-2 (b) in aqueous medium. (c) Selective study of NCD-2 in DMSO medium. Here, A, B, C, D, E, F, G, H, I, J, K, L, M, N, O, P, Q, R, S, T, U, V refers to blank, 4-NA, 1, 3-DNB, 2,4-DNA, 2-NA, 3-NA, 4-bromo-NA, Aniline, NB, EDA, TEA, Na^+, K^+, Mn^{2+}, Zn^{2+}, Cr^{3+}, Co^{2+}, CN^-, I^-, Br^-, HCO_3^-, CO_3^{2-} respectively.

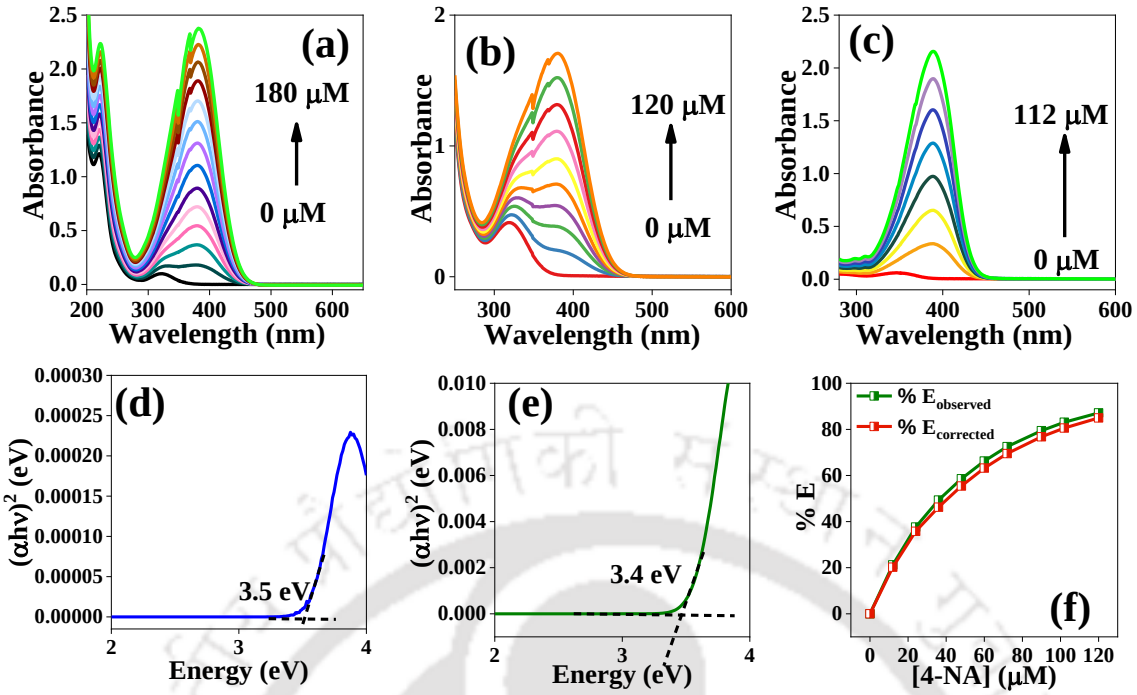

Figure A.5.3. UV-vis absorption spectra after addition of several concentration of 4-NA (a) NCD-1, (b) NCD-2 in aqueous solution and (c) NCD-2 DMSO solvent. (d) and (e) UV-onset graph of NCD-1 and NCD-2 respectively, (f) IFE plot of NCD-2 in aqueous medium.

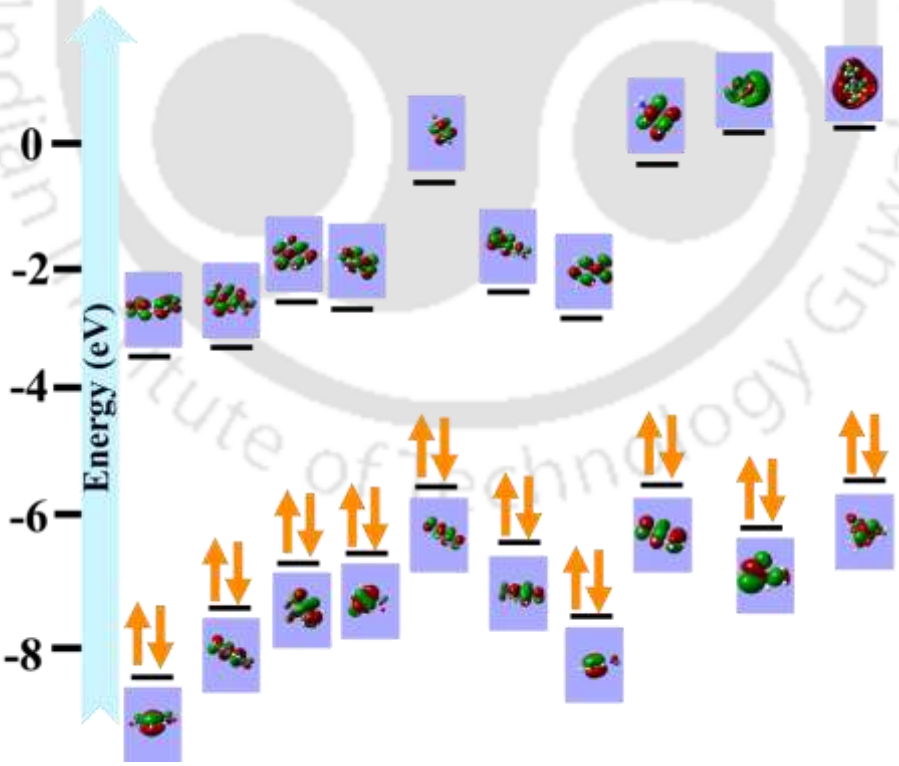

Figure A.5.4. HOMO−LUMO energy diagram based on DFT analysis of nitro-compounds

Calculation of HOMO LUMO energies of NCDs

Using the UV onset method, the calculated HOMO level is −5.12 and −5.59 eV for NCD-1 and NCD-2[2-3].

$$\text{band gap, } E_g\ (\text{eV}) = \frac{1240}{UV_{onset}\ (in\ nm)}$$

E_{HOMO} (eV)= − [E (onset,ox vs Fc +/Fc) + 4.8]

$E_{Fc/Fc+} = 0.09$ eV

$$E_{LUMO} = E_g + E_{HOMO}$$

Parameters	NCD-1	NCD-2
Eg (eV)	3.51	3.40
Oxidation potential Eox (eV)	0.88	0.41
E_{HOMO} (eV)	-5.59	-5.12
E_{LUMO} (eV)	-2.08	-1.72

Table A.5.4. Decay curve fitting parameter of NCD-1 and after addition of 180 µM 4-NA in NCD-1 aqueous solution.

Sample	A_1	A_2	A_3	τ_1 (ns)	τ_2 (ns)	τ_3 (ns)	τ_{avg} (ns)	χ^2
NCD-1	0.31	0.32	0.37	1.88	5.51	0.33	2.47	1.14
NCD-1 + 180 µM 4-NA	0.3	0.26	0.44	2.41	5.69	0.47	2.41	1.09

Table A.5.5. IFE parameter of NCD-1 and 4-NA system in aqueous solution.

Conc. of 4-NA (μM)	A_{ex}	A_{em}	CF	$F_{observed}$	$F_{corrected}$	$F_{corrected}/F_{corrected(0)}$
0	0.089842	0.00033	1.104892	2.17E+06	2.40E+06	1
12	0.171027	0.044859	1.264502	1.89E+06	2.39E+06	1.002804
24	0.255033	0.09121	1.449958	1.65E+06	2.39E+06	1.002792
36	0.335467	0.135703	1.6484	1.43E+06	2.35E+06	1.018266
48	0.415677	0.180366	1.868718	1.24E+06	2.32E+06	1.034723
60	0.493502	0.223482	2.104627	1.07E+06	2.26E+06	1.060017
75	0.609769	0.277292	2.474639	899454.4	2.23E+06	1.07731
90	0.686555	0.329602	2.793844	779317.2	2.18E+06	1.101324
105	0.779074	0.381666	3.187319	656353	2.09E+06	1.146221
120	0.870686	0.431589	3.613791	551078.1	1.99E+06	1.20408
135	0.961627	0.481057	4.080736	465142.9	1.90E+06	1.263301
150	1.046728	0.528266	4.564451	396277	1.81E+06	1.325697
165	1.133454	0.576349	5.103376	335407.6	1.71E+06	1.400881
180	1.218748	0.622775	5.676775	285981.5	1.62E+06	1.477039

Table A.5.6. Decay curve fitting parameter of NCD-2 and after addition of several concentration of 4-NA in NCD-2 aqueous solution.

Sample	**A_1**	**A_2**	**A_3**	**τ_1 (ns)**	**τ_2 (ns)**	**τ_3 (ns)**	**τ_{avg} (ns)**	**χ^2**
NCD-2	0.17	0.42	0.41	2.60	9.81	0.105	4.606	1.05
NCD-2 + 24 µM 4-NA	0.09	0.21	0.7	2.15	9.69	0.034	2.25	1.14
NCD-2 + 36 µM 4-NA	0.08	0.17	0.75	2.56	9.95	0.037	1.92	1.14
NCD-2 + 72 µM 4-NA	0.06	0.13	0.81	2.079	9.69	0.037	1.41	1.19

Table A.5.7. IFE parameter of NCD-2 and 4-NA system in aqueous solution.

Conc. of 4-NA (µM)	A_{ex}	A_{em}	CF	$F_{observed}$	$F_{corrected}$	$F_{corrected}/F_{corrected(0)}$
0	0.0113	0.00277	1.013698	241724.5575	245035.7	1.000435
12	0.02264	0.00319	1.027379	190408.5609	195621.7	1.253145
24	0.03675	0.00594	1.04699	150796.5613	157882.6	1.552688
36	0.05674	0.01036	1.075839	122510.9491	131802.1	1.859928

48	0.06924	0.01206	1.092978	100146.7455	109458.2	2.239599
60	0.08191	0.00985	1.106033	81530.55565	90175.51	2.718502
72	0.09723	0.0097	1.124858	66466.96062	74765.87	3.2788
90	0.11296	0.00965	1.144519	49706.84054	56890.45	4.309024
102	0.12877	0.00987	1.164826	40862.45028	47597.64	5.150304
120	0.14413	0.01118	1.186121	31084.91939	36870.47	6.648744

Table A.5.8. Decay curve fitting parameter of NCD-2 and after addition of several concentration of 4-NA in NCD-2 DMSO solution

Sample	**A_1**	**A_2**	**A_3**	**τ_1 (ns)**	**τ_2 (ns)**	**τ_3 (ns)**	**τ_{avg} (ns)**	**χ^2**
NCD-2	0.03	0.83	0.14	2.27	5.53	1.91	4.93	1.07
NCD-2 + 32 µM 4-NA	0.06	0.78	0.16	2.40	5.58	0.164	4.52	1.009
NCD-2 + 48 µM 4-NA	0.06	0.71	0.23	2.671	5.576	0.125	4.148	1.05
NCD-2 + 96 µM 4-NA	0.07	0.52	0.41	2.79	5.60	0.073	3.14	1.14
NCD-2 + 112 µM 4-NA	0.05	0.5	0.45	1.61	5.52	0.050	2.86	1.111

Table A.5.9. IFE parameter of NCD-2 and 4-NA system in DMSO solution.

Conc. of 4-NA (μM)	A_{ex}	A_{em}	CF	$F_{observed}$	$F_{corrected}$	$F_{corrected}/F_{corrected(0)}$
0	0.050933	0.004847	1.062729	1476520	1569141	1
16	0.241759	0.0782	1.410895	1159870	1636455	1.042898
32	0.428723	0.149617	1.833152	832423.1	1525958	0.97248
48	0.617598	0.221001	2.350878	602263.3	1415847	0.902307
64	0.803443	0.292618	2.96542	438969.2	1301728	0.82958
80	0.991509	0.364819	3.70074	320364.5	1185586	0.755563
96	1.170627	0.433579	4.517987	190776.9	861927.4	0.549299
112	1.333301	0.497966	5.378456	141742.8	762357.4	0.485844

Appendix Chapter 6

Table A.6.1. Deconvoluted fitting parameters of XPS spectra of NCD.

Sample	Spectrum	Peak position (eV)	% contribution	Peak identity
NCD	C 1s	284.4	41.13	C=C
		285.6	32.79	C-N
		287.1	10.52	O-C=O
		288.6	12.5	C=O
		291.6	3.06	Π- Π*
	N 1s	398.9	32.24	Pyridinic-N
		399.6	29.38	Pyrrolic-N
		400.5	18.8	Amino-N
		401.5	14.12	Graphitic-N
		405.4	5.46	N-O
	O 1s	531.1	41.58	C-O
		532.1	26.68	C-OH
		533.2	18.22	C-O-C
		534.1	13.52	O=C-O

Table A.6.2. Deconvoluted fitting parameter of XPS spectra of CD_{Blank}

Sample	Spectrum	Peak position (eV)	% contribution	Peak identity
CD_{Blank}	N 1s	398.6	42.22	Pyridinic-N
		399.3	34.95	Pyrrolic-N
		400.1	17.15	Amino-N
		401.3	3.07	Graphitic-N
		405	2.61	N-O

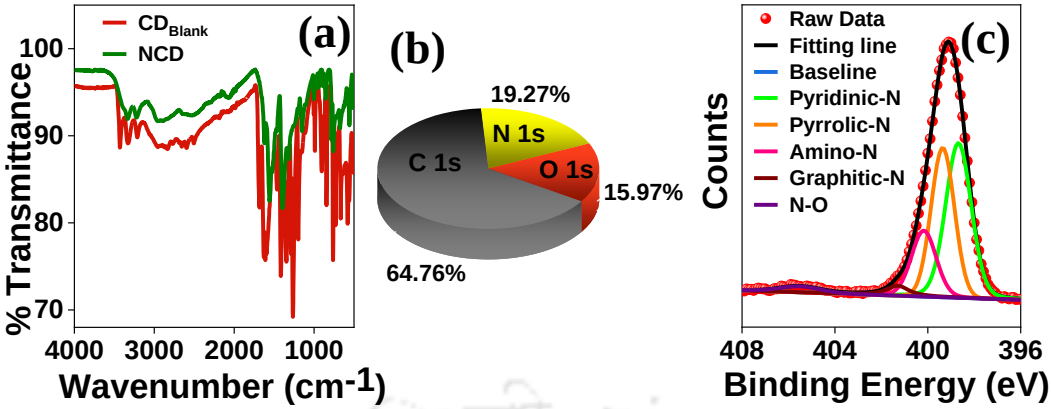

Figure A.6.1. (a) FTIR spectra of as-prepared NCDs and CD_{Blank}. (b) The elemental percentage of NCDs. (c) Deconvoluted XPS spectra of N 1s of CD_{Blank}

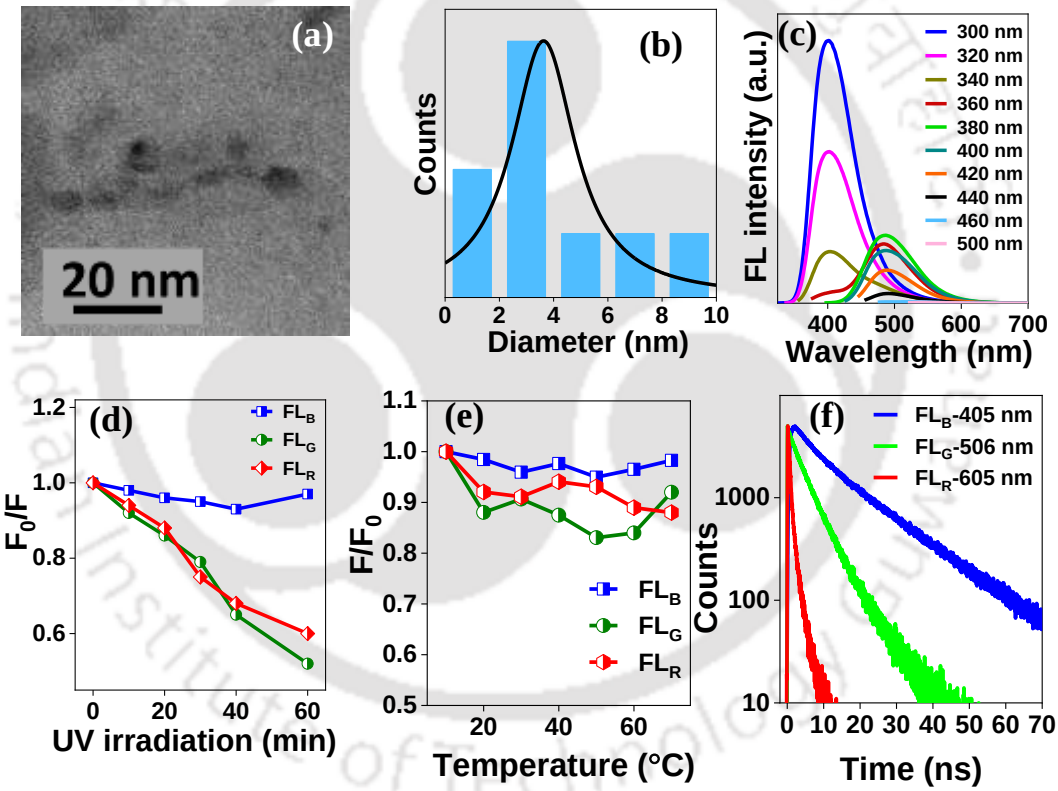

Figure A.6.2. (a) TEM images of CD_{Blank}. (b) Size distribution pattern of CD_{Blank}. (c) excitation-dependent emission plot of CD_{Blank}. (d) UV-radiation stability of NCD. (e) effect of temperature of green and red emission intensity. F is the emission intensity at different temperatures, and F_0 is the emission intensity at 10 °C. (f) Fluorescence decays of the NCDs at blue (405 nm), green (506 nm), and red (605 nm) regions at 292 nm, 375 nm and and 510 nm excitations, respectively.

Table A.6.3. Fluorescence decay parameters of different emissions (FL_B, FL_G and FL_R) of NCDs.

Emission	**Source**	**A_1**	**A_2**	**A_3**	**τ_1 (ns)**	**τ_2 (ns)**	**τ_3 (ns)**	**τ_{avg} (ns)**	**χ^2**
FL_B	292 nm LED	0.09	0.39	0.52	0.10	5.04	17.0	10.8	0.98
FL_G	375 nm Laser diode	0.52	0.30	0.18	0.07	3.50	7.3	2.4	1.17
FL_R	510 nm Laser diode	0.89	0.10	0.01	0.55	2.00	5.0	0.7	1.10

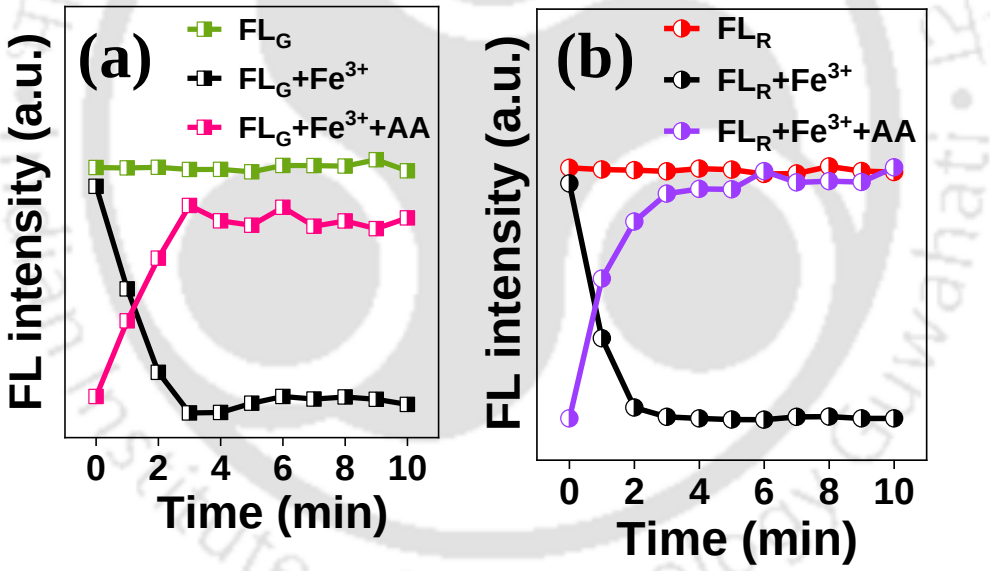

Figure A.6.3. Variation of fluorescence intensities in (a) green and (b) red regions with time in the absence and presence of Fe^{3+} and AA. The zero time indicates the time of addition of the additive, and the time lag to attain a stable fluorescence intensity defines the response time of the analyte.

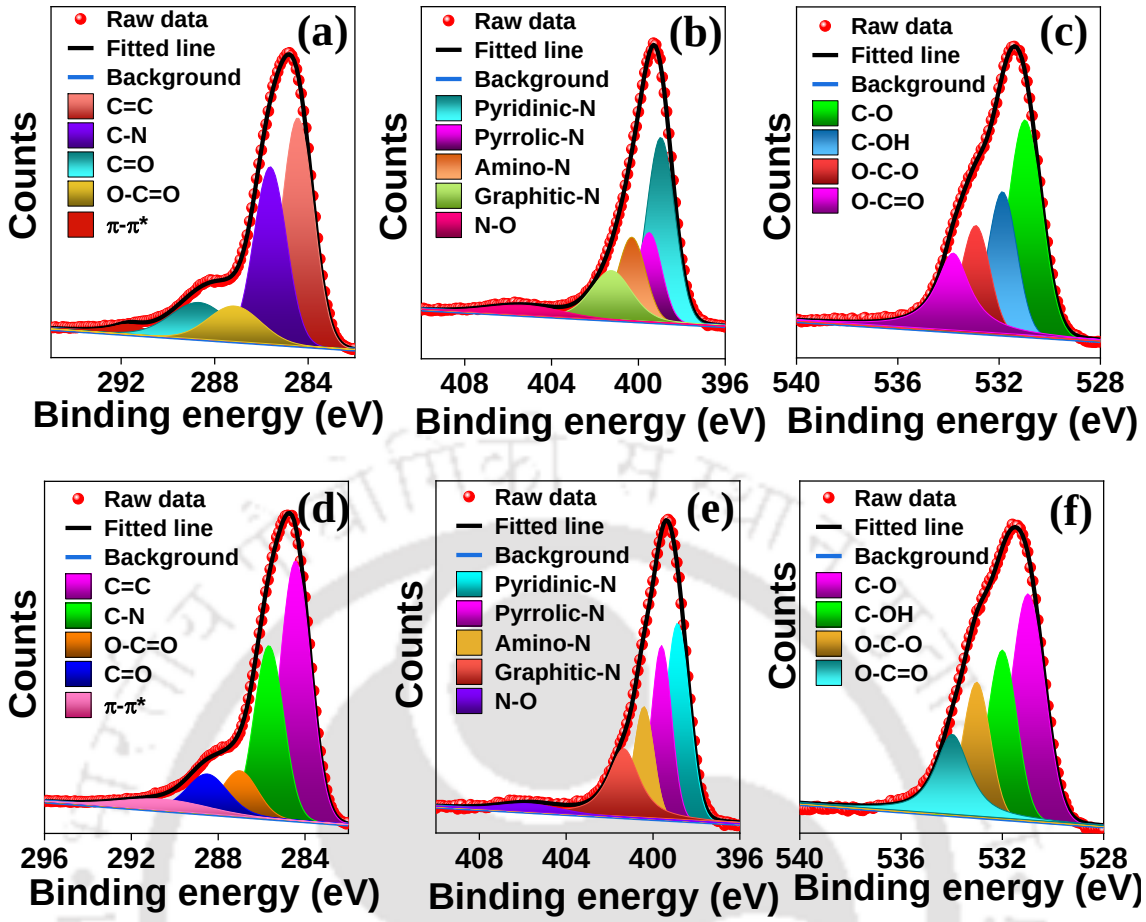

Figure A.6.4. (a) to (c) deconvoluted XPS spectra NCD-Fe^{3+} C1s, N1s, and O 1s, respectively. (d)- (f) deconvoluted XPS spectra NCD-Fe^{3+} +AA C1s, N1s, and O 1s, respectively.

Table A.6.4. Deconvoluted fitting parameter of XPS spectra of NCD, NCD+Fe^{3+} and NCD+Fe^{3+} +AA.

Sample	Spectrum	Peak identity	Peak position (eV)	Peak position (eV) after treating with Fe^{3+}	Peak position (eV) after treating with Fe^{3+}+AA
NCD		C=C	284.4	284.6	284.5
		C-N	285.6	285.7	285.6

	C1s	O-C=O	287.1	287	287
		C=O	288.6	288.6	288.7
		Π- Π*	291.6	291.5	291.4
	N 1s	Pyridinic-N	398.9	398.9	398.8
		Pyrrolic-N	399.6	399.6	399.6
		Amino-N	**400.5**	**400.1**	400.5
		Graphitic-N	401.5	401.4	401.5
		N-O	**405.4**	**405.1**	405.7
	O 1s	C-O	531.1	531.1	531
		C-OH	**532.1**	**531.8**	532.1
		C-O-C	533.2	532.1	533
		O=C-O	**534.1**	**533.6**	534.05
	Fe 2P	Fe^{3+}		714.2	NA
				728.2	NA
		Fe^{2+}		709.8	NA
				723.2	NA

Table A.6.5. Decay curve fitting parameter of FL_G and after addition of 120 µM Fe^{3+}.

Sample	**A_1**	**A_2**	**A_3**	**τ_1 (ns)**	**τ_2 (ns)**	**τ_3 (ns)**	**τ_{avg} (ns)**	**χ^2**
FL_G	0.52	0.30	0.18	0.07	3.50	7.23	2.4	1.17
FL_G + 120 µM Fe^{3+}	0.07	0.06	0.87	1.70	6.9024	0.03	0.6	1.4

Table A.6.6. Decay curve fitting parameter of FL_R and after addition of 200 µM Fe^{3+}.

Sample	**A_1**	**A_2**	**A_3**	**τ_1 (ns)**	**τ_2 (ns)**	**τ_3 (ns)**	**τ_{avg} (ns)**	**χ^2**
FL_R	0.1	0.89	0.01	1.99	0.55	4.99	0.7	1.106
FL_R + 200 µM Fe^{3+}	0.22	0.01	0.77	0.51	3.9	0.11	0.2	1.06

Appendix Chapter 7

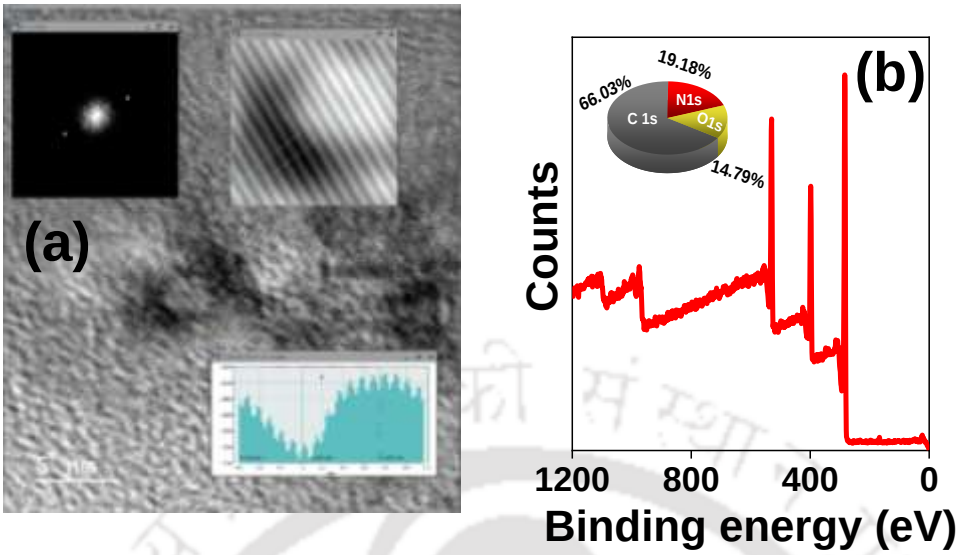

Figure A.7.1. (a) HRTEM image of NCD, (b) Full-range XPS spectra of NCD, inside graph shows the atomic percentage of each element.

Table A.7.1. Deconvoluted XPS parameter of NCDs

Sample		Spectrum	Peak position (eV)	% contribution	Peak identity
NCD		C 1s	248.4	35.8	C=C/C-C
			285.2	24.6	C-N
			286	18	C=N
			287.9	11.2	C=O
			289.8	10.4	O-C=O
		N 1s	398.9	26.8	Pyridinic-N
			399.5	28	Pyrrolic-N
			400.6	23	Amino-N
			401.7	22.2	Graphitic-N
		O 1s	530.8	29.7	C-O/C-O-C
			531.3	21.9	O=C-N
			532.1	18.9	C=O
			533	15.7	C-OH
			533.8	13.8	O=C-O

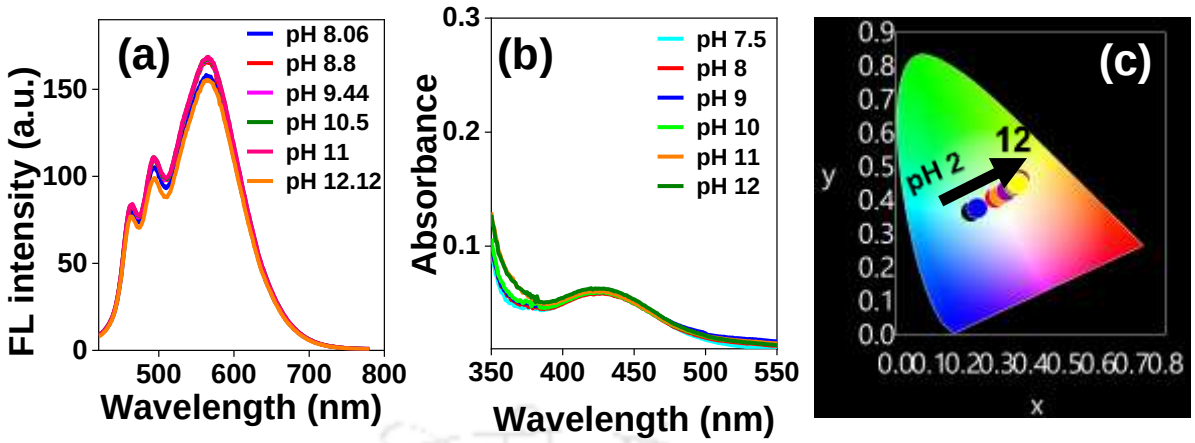

Figure A.7.2. (a) pH-dependent emission at the basic region, (b) pH-dependent absorbance at the basic region, (c) pH-dependent CIE coordinate value from pH 2 to 12.

Table A.7.2. CIE coordinate values of different pH

pH of the medium	X-coordinate value	Y-coordinate value
2.06	0.22	0.37
3.06	0.24	0.38
4.44	0.29	0.41
5.3	0.31	0.42
5.71	0.33	0.43
6.27	0.35	0.44
7.5	0.37	0.46
8.06	0.36	0.45
8.8	0.36	0.45
9.44	0.36	0.45
10.5	0.36	0.45
11	0.36	0.45
12	0.36	0.45

Table A.7.3. Fluorescence decay parameters of NCD under 405 laser diode source

		B_1	B_2	B_3	A_1	A_2	A_3	T_1	T_2	T_3	T_{avg}	χ^2
570 nm	pH 2.01	0.097	0.16	0.019	0.35	0.58	0.07	1.52	0.29	4.11	0.98	1.07
	pH 7.5	0.103	0.15	0.00644	0.4	0.58	0.02	1.01	1.54	4.32	1.38	1.3
490 nm	pH 2.01	0.42	0.141	0.021	0.72	0.24	0.04	0.052	1.69	5.87	0.68	1.17
	pH 7.5	0.23	0.35	0.029	0.37	0.58	0.05	1.36	3.01	5.71	2.53	1.12

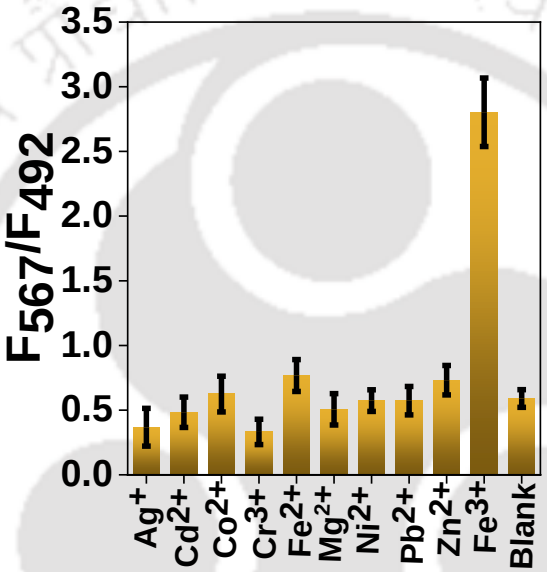

Figure A.7.3. Interfering study of NCD with various metal ions

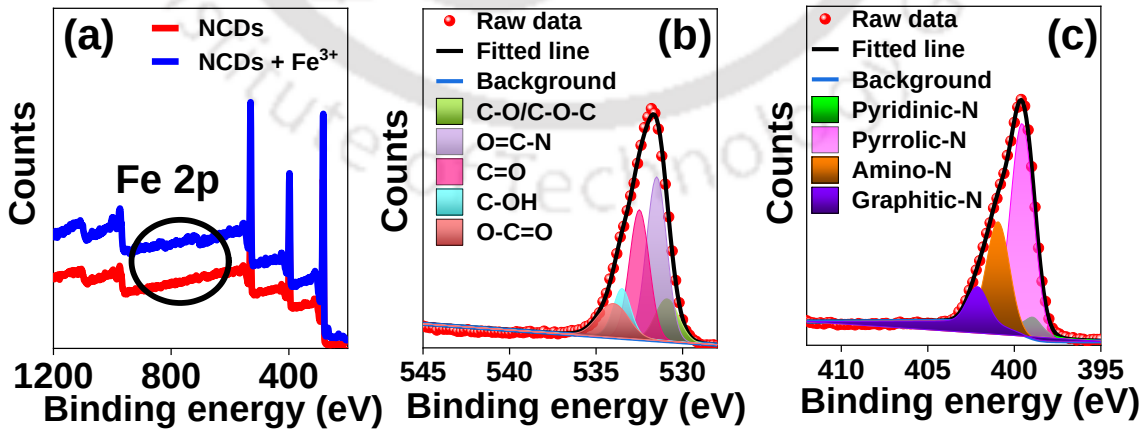

Figure A.7.4. Full range XPS spectra of NCD and NCD+Fe^{3+}, Deconvoluted XPS spectra of NCD treated with Fe^{3+} (b) O1s, (c) N1s

Table A.7.4. Deconvoluted XPS parameter of NCDs-Fe^{3+} system.

	Peak position (eV)	Peak position (eV) after treating with Fe^{3+}	High-resolution peak position (eV)	High-resolution peak position (eV) after treating with Fe^{3+}	Designation
N 1s	399.5	399.2	399	398.9	Pyridinic-N
			399.5	399.5	Pyrrolic-N
			400.6	401	Amino-N
			401.7	402.2	Graphitic-N
O 1s	531.2	531.6	530.8	530.9	-C-O/C-O-C
			531.3	531.5	O=C-N
			532.1	532.5	C=O
			533	533.5	C-OH
			533.8	534	O-C=O

[This page was intentionally left blank]

Publications

1. **Nilanjana Nandi**, Konika Choudhury, Priyanka Sarkar, Neha Barnwal, Kalyanasis Sahu, "Dual-emitting anti-cancerous N-doped carbon dots for ratiometric detection of pH, Fe^{3+} and white-light generation". (*ACS Appl. Nano Mater*. 2022, **5**, 11, 17315–17324)
2. **Nilanjana Nandi**, Priyanka Sarkar, Kalyanasis Sahu, "N-doped carbon dots: triple mode excitation–emission features for dual channel sensing and logic gate application". *Materials Today Chemistry,* 2022, **26**, 101015
3. **Nilanjana Nandi**, Priyanka Sarkar, Kalyanasis Sahu, "N-Doped Carbon Dots for Visual Recognition of 4-Nitroaniline and Use in Fluorescent Inks". *ACS Appl. Nano Mater*. 2021, **4**, 9, 9616–9624.
4. **Nilanjana Nandi**, Shubham Gaurav, Priyanka Sarkar, Sachin Kumar and Kalyanasis Sahu* "Multifunctional N-Doped Carbon Dots for Bimodal Detection of Bilirubin and Vitamin B12, Living Cell Imaging, and Fluorescent Ink." *ACS Appl. Bio Mater*. 2021, **4**, 6, 5201–5211.
5. **Nilanjana Nandi**, Shubham Gaurav, Priyanka Sarkar, Sachin Kumar and Kalyanasis Sahu* "Hit Multiple Targets with One Arrow: Pb^{2+} and ClO^- Detection by Edge Functionalized Graphene Quantum Dots and Their Applications in Living Cells." *ACS Appl. Bio Mater*. 2021, **4**, 10, 7605–7614.
6. Priyanka Sarkar, **Nilanjana Nandi**, Kalyanasis Sahu* Red-Emitting Silver Nanoclusters for Dual-Mode Detection of Cu^{2+} and Vitamin B12 in Living Cell". *ACS Appl. Nano Mater.* 2022, **5**, 6, 7670-7678
7. **Nilanjana Nandi**, Kalyanasis Sahu* "Analysis of excited state proton transfer dynamics of HPTS in methanol-water mixtures from time-resolved area-normalised emission spectrum (TRANES)" *Journal of Photochemistry & Photobiology A: Chemistry,* 2019, **374**, 138–144.
8. Kalyanasis Sahu* **Nilanjana Nandi**, Suman Dolai and Avisek Bera "A Ratio-Analysis Method for the Dynamics of Excited State Proton Transfer: Pyranine in Water and Micelles". *J. Phys. Chem. B* 2018, **122**, 25, 6610–6615.
9. Aparajita Phukon, **Nilanjana Nandi** and Kalyanasis Sahu "Pre-micellar interaction or direct monomer to micelle transition for zwitterionic sulfobetaine surfactant in water? A comparative fluorescence study with cationic surfactant" *Journal of Photochemistry and Photobiology A: Chemistry,* 2018, **357**, 140–148.

[This page was intentionally left blank]

Conferences

1. North-East Research Conclave and Assam Biotech Conclave 2022, May 20-22nd 2022, (Oral presentation)
2. Research Conclave'22 held at IIT Guwahati, Guwahati, Assam, 20-23rd January 2022. (Poster Presentation)
3. The ChemSci2021: Leaders in the Field Symposium organised by RSC's flagship journal Chemical Science & JNCASR Bangalore, 13th to 15th December 2021. (Poster Presentation)
4. International Conference on Progress and Challenges in Modern Day Science (PCMDS-2021) organized by B. Barooah College, Guwahati, Assam, India during 17-18 June, 2021 (Poster Presentation)
5. 6th International Conference on Advanced Nanomaterials and Nanotechnology (ICANN2019) held at Indian Institute of Technology Guwahati, Assam, India December 18-21, 2019. (Poster Presentation)
6. Frontiers in Chemical Sciences 2018 held at Indian Institute of Technology Guwahati, Assam, 6-8th December 2018. (Poster Presentation)

[This page was intentionally left blank]